HAL
open science

Terahertz wave-guided reflectometry system

Mingming Pan

To cite this version:

Mingming Pan. Terahertz wave-guided reflectometry system. Electronics. Université de Bordeaux, 2020. English. NNT : . tel-02926290v1

HAL Id: tel-02926290

https://hal.science/tel-02926290v1

Submitted on 31 Aug 2020 (v1), last revised 26 Oct 2020 (v2)

HAL is a multi-disciplinary open access archive for the deposit and dissemination of scientific research documents, whether they are published or not. The documents may come from teaching and research institutions in France or abroad, or from public or private research centers.

L'archive ouverte pluridisciplinaire **HAL**, est destinée au dépôt et à la diffusion de documents scientifiques de niveau recherche, publiés ou non, émanant des établissements d'enseignement et de recherche français ou étrangers, des laboratoires publics ou privés.

THÈSE PRESENTEE
POUR OBTENIR LE GRADE DE

DOCTEUR DE L'UNIVERSITÉ DE BORDEAUX

Département des sciences physiques et de l'ingénieur

Spécialité électronique

Présentée et soutenue publiquement par

Mingming PAN

Terahertz wave-guided reflectometry system

Directeur de thèse : **Patrick MOUNAIX**
Co-directeur : **Dean Lewis**
Co-encadrant : **Jean-Paul GUILLET**

Soutenue le 2 juillet 2020

Membres du Jury

Mme. MANEUX Cristell	Professeur Université de Bordeaux	Président
M. LAMPIN Jean-François	Directeur de recherche Université de Lille	Rapporteur
M. BLIN Stéphane	Maître de conférences (HDR) Université de Montpellier	Rapporteur
M. HUMBERT Georges	Chargé de recherche XLIM, Limoges	Examinateur
M. ROUX Jean-François	Maître de conférences(HDR) Université de Savoie Mont-Blanc	Examinateur
M. BIGOURD Damien	Chargé de recherche IMS (HDR), Bordeaux	Invité
M. GUILLET Jean-Paul	Maître de conférences Université de Bordeaux	Co-encadrant
M. LEWIS Dean	Professeur Université de Bordeaux	Co-directeur de thèse
M. MOUNAIX Patrick	Directeur de recherche Université de Bordeaux	Directeur de thèse

Réflectométrie dans le domaine temporal pour l'optique guidée terahertz

Résume : Ce travail vise à construire un système compact et facile à mettre en œuvre de réflectométrie guidée par ondes térahertz (TGR) en tirant parti de l'émetteur-récepteur térahertz et des guides d'ondes pour diverses applications. Par rapport aux systèmes conventionnels utilisant une méthode quasi-optique, le nouveau concept a une configuration beaucoup plus simple et permet des applications de sondage à distance.

Après des études sur le développement de la technologie térahertz, un émetteur-récepteur à double ACP à pompage optique et deux émetteurs-récepteurs radar à ondes continues modulées en fréquence (FMCW) ainsi que des guides d'ondes à parois minces à noyau creux sont sélectionnés pour mettre en œuvre le premier système TGR en mode impulsionnel et en mode FMCW. Les deux expériences et la simulation 3D pleine onde sont exploitées pour étudier les comportements de propagation des ondes à l'intérieur du système et pour évaluer les performances du système. Les systèmes TGR créés font l'objet d'une démonstration à des fins d'imagerie et de détection. Grâce à la capacité de guidage du guide d'ondes, ces installations présentent un potentiel dans certaines conditions de mesure difficiles, comme dans un environnement étroit et semi-fermé ou dans le liquide. En particulier, la lentille d'immersion solide insérée à l'extrémité du guide d'ondes s'est avérée être une méthode efficace pour améliorer la capacité d'imagerie du système TGR en mode FMCW, donnant lieu à une résolution de sous-longueur d'onde dans la bande de fréquences autour de 100 GHz.

En plus des études sur les systèmes TGR, un système de réflectométrie sur plaquette exploitant des sources à pompage optique est également proposé pour bénéficier de la large bande de fréquences des sources photoniques. Comme première tentative, des sondes RF associées à un émetteur-récepteur à double ACP sont utilisées pour délivrer le signal d'impulsion dans des échantillons sur la tranche et les signaux temporels obtenus sont analysés. D'autres propositions sont faites pour pousser plus loin cette étude.

Mots-clés : guide d'onde, émetteur-récepteur térahertz, guide d'ondes, système de réflectométrie, simulation 3D pleine onde, FMCW, télédétection, sonde haute fréquence de mesure sur plaquette, test non destructif.

Laboratoire IMS, UMR CNRS 5218, Université de Bordeaux,
351 Cours de la Libération, 33405 Talence Cedex, FRANCE

Terahertz wave-guided reflectometry system

Abstract: This work aims to build up a compact easily-implemented terahertz wave-guided reflectometry (TGR) system by taking advantage of the terahertz transceiver and waveguides for diverse applications. Compared to conventional systems using a quasi-optical method, the new concept has a much simpler configuration and allows for remote probing applications.

After reviews on the development of terahertz technology, an optical-pumped double-PCA transceiver and two frequency-modulated continuous-wave (FMCW) radar transceivers together with hollow-core thin-wall waveguides are selected to implement the first TGR system in pulse mode and in FMCW mode. Both experiments and 3D full-wave simulation are exploited to investigate the propagation behaviors of waves inside the system and to evaluate the system performance. The created TGR systems are demonstrated for imaging and sensing purposes. Thanks to the guiding capacity of the waveguide, these setups show potential in some difficult measurement conditions, such as in a narrow semi-enclosed environment or the liquid. In particular, the solid immersion lens inserted at the end of the waveguide has been proved as an efficient method to enhance the imaging capacity of the TGR system in FMCW mode, giving rise to a subwavelength resolution at the frequency band around 100 GHz.

In addition to the studies of TGR systems, an on-wafer reflectometry system exploiting optical-pumped sources is as well proposed to benefit from the wide frequency band of photonic sources. As the first attempt, RF probes in association with double-PCA transceiver are used to deliver the pulse signal into samples on-wafer and the obtained time signals are analyzed. More propositions are given to push further up this study.

Keywords: wave-guided, terahertz transceiver, waveguide, reflectometry system, 3D full-wave simulation, FMCW, remote sensing, on-wafer measurement high-frequency probe, non-destructive test.

IMS Laboratory, UMR CNRS 5218, University of Bordeaux,
351 Cours de la Libération, 33405 Talence Cedex, FRANCE

Acknowledgments

First of all, I would like to thank my supervisor, M. Patrick Mounaix, for his support during my PhD. I also wish to thank my co-supervisor M. Jean-Paul Guillet for providing me the opportunity to be one part of this great Laser & Terahertz team. Thank you both for your reassuring advice in moments of doubt and for the confidence and trust that you have placed in me.

I would like to thank my jury members: M. Stéphane Blin, M. Jean-François Lampin, M. Jean-François Roux, M. Georges Humbert, Ms. Cristell Maneux and M. Bigourd Damien for accepting to evaluate my work. In particular, I would like to thank M. Georges Humbert for hosting me in the XLIM research institute and showing me the fabrication process of optical fibers. I would like to thank M. Blin for comprehensive and illuminating comments.

I would like to thank my wonderful colleagues in the IMS laboratory. Frédéric, a great engineer, you helped me a lot during my work, and you also gave me some great life advice. Sébastien, Serge, Marina, Magali, Simone, Fabienne, Nicolas, Laëtitia, thanks all of you, it was a pleasure to work with you.

Thanks to Jean-Paul, I have gained valuable teaching experience at IUT of Bordeaux during my PhD thesis. Thank you, Jean-Luc, David, Florent, Simon Joly and Simon Hemour for making this experience very pleasant.

Apart from the work in the laboratory, I had a great time in the UCB1 dive club and Dany's painting studio, where I could take a rest, change my mind and enjoy the sport and art for a while. A big thanks to my monitors Jacques, Christine, and beloved Dany.

During my PhD thesis, I have obtained precious friendship: dear Marine, Thomas, Florent, Nolwen, Djeber, Marco, Margaux, Romain, Joyce, Yuanci, Xue Ma, Feixue, Nicolas and Joyce. Thanks all you guys, we have so much fun together!

A special thanks to Miguel and Jean-Baptist, you two encouraged me from the beginning of my PhD thesis. I am so grateful to have you two as my friends. Thanks for your support and the great time that we had together.

I also thank you, my beautiful, strong girl, Isabel. We started the PhD together and you gave me a great positive model. This young lady is a great fighter and a strong woman. Thank you for all that, you are a great inspiration for me.

No matter where I am, I always know that my parents always support me. A heartfelt thanks to my Dad and Mom, thanks for your unconditional love and trust in me. I'd also like to thank my big family, my aunts, uncles, and cousins. Thanks for your support from China.

Finally, I would like to thank Quentin for everything that you have done for me. I cannot finish my PhD without you, thanks for all your support, patience and love. It was not an easy task, but you helped me to get through it all. You are a wonderful person and I am so lucky to have you. I love you!

Table of contents

ACKNOWLEDGMENTS ..... **III**

TABLE OF CONTENTS ..... **V**

LIST OF FIGURES ..... **VII**

LIST OF TABLES ..... **XVII**

ACRONYMS ..... **XIX**

GENERAL INTRODUCTION **1**

CHAPTER I. GENERAL TERAHERTZ TECHNOLOGY **5**

I.1. Introduction 6
I.2. Terahertz active devices and system configurations 6
I.2.1. Terahertz sources 6
I.2.2. Terahertz detectors 14
I.2.3. Terahertz measurement systems 16
I.2.4. Developments of optical-pumped pulsed transceivers 18
I.3. Terahertz waveguides 22
I.3.1. Metallic terahertz waveguides 22
I.3.2. Developments of dielectric waveguides 26
I.3.3. Conclusion 33
I.4. Terahertz applications 33
I.5. Conclusion 35

CHAPTER II. TERAHERTZ WAVE-GUIDED REFLECTOMETRY QUALIFICATION **37**

II.1. Introduction 38
II.2. Double-PCA free-lens transceiver probe 38
II.2.1. Design of a double-PCA lens-free transceiver 39
II.2.2. Imaging capacity of double-PCA lens-free transceiver 51
II.2.3. Conclusion 61
II.3. Terahertz FMCW radar transceiver units 61
II.3.1. FMCW radar working principle 62
II.3.2. SynView FMCW radar module 63
II.3.3. Silicon radar chip 66
II.3.4. Conclusion 68
II.4. Thin-wall hollow-core waveguides 68
II.4.1. Fused silica hollow-core waveguide 70
II.4.2. Plastic thin-wall waveguide 73
II.5. 3D printed negative-curvature waveguide 75

II.5.1. State-of-the-art of negative curvature waveguides 75
II.5.2. 3D printed fabrication techniques 77
II.5.3. 3D printed negative curvature waveguide 78
II.6. Conclusion 81

CHAPTER III. TERAHERTZ WAVE-GUIDED REFLECTOMETRY SYSTEMS 83
III.1. Introduction 84
III.2. Terahertz wave-guided reflectometry systems in pulse mode 87
III.2.1. Global experimental setup 87
III.2.2. TGR-P system I with a silica waveguide 88
III.2.3. TGR-P system II with a plastic waveguide 97
III.3. Terahertz wave-guided reflectometry system in FMCW mode 107
III.3.1. TGR-FMCW system I using SynView transceiver unit 108
III.3.2. TGR-FMCW system II using Silicon Radar transceiver chip 118
III.4. Conclusion 126

CHAPTER IV. ON-WAFER REFLECTOMETRY SYSTEM: FIRST TESTS 129
IV.1. Development of TMIC technology 130
IV.1.1. On-wafer measurements 130
IV.1.2. Non-destructive fault isolation techniques 133
IV.2. Attempt to an on-wafer reflectometry system 137
IV.2.1. Experimental setup 138
IV.2.2. Reflected time signal I (Model 220) 141
IV.2.3. Reflected time signal II (Model 500) 142
IV.3. Conclusion 144

CONCLUSION AND PERSPECTIVES 145

BIBLIOGRAPHY 149

INTRODUCTION IN FRENCH 169

AUTHOR CONTRIBUTION 173

List of Figures

Figure I.1: Terahertz region in the electromagnetic spectrum, covering frequencies from 100 GHz to 10 THz. 6

Figure I.2: Photoconductive antenna illuminated by a femtosecond laser beam for terahertz wave generation. 9

Figure I.3: Novel antenna designs proposed to improve PCA performance. (a) Mesa-structured InGaAs/InAsAl PA layer, from [43]. (b) LT-GaAs logarithmic spiral antenna with 3D plasmonic contact electrode [36]. (c) Bowtie antenna incorporating with plasmonic contact electrodes [33]. (d) Large area interdigitated PCA antenna allowing a broadband terahertz wave generation [30]. (e) High–Power large-area PC emitter exploiting plasmonic contact electrodes [37]. (f) Ag-nanoantenna coupled PCA, from [39]. 12

Figure I.4: Logarithmic plot of the emitted power of different terahertz technologies sources as a function of frequency and wavelength. 14

Figure I.5: Progress of terahertz detectors over recent years. It includes single detectors and the same technology-based focal-plane arrays (FPAs). 16

Figure I.6: Terahertz measurement systems (a) in transmission mode, (b) and (c) in reflection geometries. To avoid the space congestion issue between the emitter and detector, measurements in reflection mode can be performed with a small incident angle (b) or a normal incidence with a beam splitter or coupler to separate the incident and reflected signals (c). 17

Figure I.7: Typical THz-TDS transmission setup. (OAPM: off-axis parabolic mirror, BS: beam splitter, M: mirror.) A femtosecond laser is used to excite and gate photoconductive antennas to generate and to detect terahertz waves. OAPM is employed to focus the terahertz beam on the sample. 18

Figure I.8: Photographs of different types of terahertz waveguides. (a) Metallic rigid rectangular waveguide (WR-3 band). (b) 3D printed dielectric waveguide. (c) Dielectric porous waveguide. 22

Figure I.9 : (a) Millimeter-wave reflectometry used for the investigation into skin burn injuries [67]. (b) FMCW radar in oil-filled waveguides for position detection [68]. 23

Figure I.10: (a) Terahertz endoscopy experiment setup using a metal wire [76]. (b)Near-field imaging setup using a tapered Sommerfeld wire [77]. (c) Continuous-wave near-field imaging setup using tapered wire as a probe [78]. 24

Figure I.11: (a) Dual-wire coupling configuration used in the proposed terahertz endoscope system setup [76]. (b) Experimental setup using milled grooves on a metal wire to couple incident radiation to a propagating surface wave [79]. (c) Differential phase element, used to improve the coupling efficiency between the linearly polarized beam and Sommerfeld waves on the metal [80]. 25

Figure I.12: Different methods to improve coupling efficiency. (a) Experimental setup including a metal wire as the waveguide, a transmitter with radial symmetric contact geometries, and a receiver [82]. (b) Experimental setup to forward a pulse signal along the metal wire, including a radical symmetric PCA transmitter and a PC-probe [70]. (c) Segmented half wave-plate (HWP) mode converter, consisting of eight pieces of HWP for controlling the spatial polarization mode of the incident laser beam [86]. 25

Figure I.13: Schematic diagram of a thin-wall waveguide exploiting the anti-resonant reflections as the guiding mechanism. At non-resonant frequencies, most of the incident power propagate inside the low-index core, resulting in a high transmission band. The resonant frequencies of the cladding correspond to the dips displayed in the transmission spectrum. 32

Figure I.14: Applications of terahertz technology. (a) Histology image and terahertz image of breast cancer tissue [177]. (b) Optical and terahertz images of an oil painting, the latter providing information for the art reconstruction (from [54]). (c) Image of weapons concealed in a box obtained in the terahertz band, benefiting the security inspection applications (from [6]). (d) Both simulation and experimental time responses of a terahertz pulse reflected from a multilayer structure, allowing for the material analysis (from [166]). 34

Figure II.1: (a) Photograph of double-PCA lens-free transceiver probe. (b) Close-up view of the slim PET cantilever of the transceiver, including an LT-GaAs layer and fed lines. (c) Schematic diagram of the double-PCA design on the apex of the transceiver probe. (d) Photograph of the feed lines on the PET cantilever. To suppress the internal reflections from the probe base, a special “wave-trap” design composed of different perpendicular lines along the feed lines are added. 40

Figure II.2: (a) Yagi-Uda antenna for television reception. (b) Photograph of an X-band prototype planar Yagi antenna. (c) Optical Yagi antenna. 40

Figure II.3: (a) Simplified model of double-PCA transceiver probe. Discrete ports 1 and 3 are used to excite the antenna and to detect signals. Two waveguide ports (port 2 and 4) are placed at the end of CPS-fed lines to absorb the waves propagating towards the probe base. (b) S_{11} and radiation efficiency of the emitter antenna as a function of frequency. (c) Total efficiency of the emitter as a function of frequency. (d) S_{21} and S_{31} curves. While S_{21} indicates the cross-talking signal between two PCAs, S_{31} represents the crosstalk signal between two antennas. 43

Figure II.4: (a) 3D plot of radiation pattern (based on gain) of the emitter of the transceiver at a frequency of 400 GHz. (b) Polar diagram based on the gain value of emitter of the transceiver in the xy-plane with $\theta = 90$ °. The main lobe points to the direction of $\theta = 27$ ° and its angular width (3dB) is 85 °. (c) Polar diagram based on the gain value of emitter of the transceiver in the xz-plane with $\phi = 0$ ° The main lobe points to the direction of $\phi = 96$ ° and its angular width (3dB) is 127.5 °. (d) and (e) 3D plots of radiation pattern at frequencies of 475 GHz and 550 GHz respectively. (f) Polar diagram of radiation patterns of the

transceiver at θ = 90 ° at different frequencies . The main lobes at different frequencies (400/475/550 GHz) point to the direction of θ = 27/41/16 ° and their angular width (3dB) are 85/70.9/50.9 ° respectively. (g) Transceiver model in CST. 45

Figure II.5: (a) Simulation model consisting of a simplified transceiver probe and an air block (blue one) of 4*4*2 mm. (b), (c) and (d) Electric field distribution in the yz-plane, xz-plane and xy-plane respectively. 46

Figure II.6: Photographs of the whole system setup. (a) A laser source and optical components (mirrors, BS:beam splitter, ND: neutral density filter) are placed on the optical table to send the pump beam and probe beams to the transceiver. (b) Apart from all the aforementioned components, the system can be divided into two parts. The first subsystem system is fixed on a vertical breadboard, consisting of a double-PCA transceiver and required optical components such as mirrors and lens to excite the transceiver. The second part is a horizontal platform equipped with three-dimension linear translation stages, acting as the sample support. 47

Figure II.7: Two different configurations for two laser beam excitation. (a) Both laser beams excite the PCAs from the front side of the probe. (b) Laser beams excite two PCAs from both sides of the transceiver probe. 48

Figure II.8: (a) Photograph of the experimental setup, including transceiver probe, lenses, sample's support and two cameras. (b) Schematic diagram of the experimental setup. A metallic sheet was used as the sample. During the measurements, the distance between the transceiver tip and the metallic sheet varied. 48

Figure II.9: (a) Recorded signal by the transceiver probe. The distance between the probe tip and the metallic sheet was around 2 mm. (b) Crosstalk signal between two PCAs on the transceiver. (c) Reflections from the sample. It was obtained by removing crosstalk between two PCAs from the detected signal. (d) Spectra of the cross-talk signal and pure reflected signal from the perfect mirror. 49

Figure II.10: (a) Nine recorded waveforms. A metallic sheet was placed right below the probe tip with a varied distance (distance step =1 mm). Here, d represents a small distance between the probe tip and metallic sheet, less than 1.5 mm. (b) Reflected signals from the metallic sheet. They were obtained by removing the crosstalk signal. (c) Spectra of reflected signals. 49

Figure II.11: (a) Three waveforms of reflected signals obtained with a working distance of 50 µm, 70 µm and 110 µm. It should be noted that even with 0 µm working distance, there is a minimum distance d between the probe tip and sample to prevent the mechanical damage to the transceiver probe. (b) Absolute value of the amplitude of peaks as a function of the distance between transceiver probe and sample. The positive peak is the first maximal peak lying around the optical delay of -49.2 mm. The negative peak is the minimum peak lying around the optical delay of -49 mm. (c) Locations of peaks as a function of the distance between transceiver probe and sample. Here, optical delay in mm represents the peak location in the time domain. 50

Figure II.12: (a) 1951 USAF resolution test chart, in which group 1 was scanned. (b) Table of spatial resolution indicated by each element in group 1. 52

Figure II.13: (a) Image of a1951 USAF resolution test chart, in which two scan zones in group 1 are marked by red rectangles. (b) Reconstructed images of scanned zones at a frequency of 791 GHz. (c) Line profiles of different elements in group1, corresponding to the red line noted in the (b). 53

Figure II.14: Contrast versus spatial frequency at frequencies of 300 GHz, 500 GHz, 700 GHz and 790 GHz respectively. E1 to E6 represent the element 1 to 6 in group 1 of the test chart. 54

Figure II.15: (a) Simulation model in CST, including a simplified transceiver model (2*0.77*0.18 mm^3) and a 0.3*3 mm^2 metallic sheet in front. (b) Side view of the model in the xz-plane, illustrating the metallic sheet moving up with respect to the transceiver. The relative distance between the transceiver and the metal plate can be calculated based on their center position. Left: the relative distance between two objects is negative. Right: the relative distance in the x-direction is positive. (c) and (d) show the time responses when the relative distance between them is positive and negative respectively. (f) Line profiles obtained at different frequencies, corresponding to 425 GHz, 544 GHz, and 568 GHz. 56

Figure II.16: (a) Reconstituted image in the frequency domain. (b) Line profile of vertical bars in element 1 in the y-direction. Top: profile obtained at a frequency of 424 GHz. Top figure: profile obtained at a frequency of 424 GHz. Bottom figure: profile obtained at a frequency of 717 GHz. (c) Line profile of vertical bars in element 2 in the y-direction. Top: at a frequency of 424 GHz. Bottom: at a frequency of 717 GHz. 58

Figure II.17: (a) Simulation model in CST, including a simplified transceiver model and a metallic sheet with a varying length from 2750 µm to 100 µm. (b) Waveforms of reflected signals from the metal sheet with a length of 1200/100/800 µm. (c) Waveforms of reflected signals from the metal sheet with a length of 700/500/300 µm. (d) Magnitude of reflected signal as a function of sheet length at frequencies of 377 GHz, 425 GHz, and 544 GHz, respectively. 59

Figure II.18: (a) Simulation model in CST, including a simplified transceiver probe and a metallic sheet mowing in the y-direction. (b) View of the model in the xy-plane during the movement of the metallic sheet. The relative distance Δy in the y-direction between the metallic sheet and the transceiver probe tip is calculated with reference to the center of the transceiver probe. (c) and (d) Time responses of the transceiver when the metallic sheet is in different relative positions ($\Delta y = \pm 200, \pm 400$ µm respectively). (e) Line profiles obtained at different frequencies varying from 352 GHz to 543 GHz. 60

Figure II.19: (a) Image of element 1 to 4 in group 1 of 1951 USAF test resolution chart obtained at a frequency of 659 GHz (b) Line profiles corresponding to marked color lines in the left. 61

Figure II.20: Simplified architecture of a monostatic FMCW radar transceiver. 62

Figure II.21: Working principle of distance detection using frequency modulation continuous wave radar signal. While the solid line represents the reference radar signal, the dashed line denotes the reflected signal from the sample. 63

Figure II.22: (a) Photograph of SynView system setup. (b) Schematic diagram of Synwiew radar system in reflection configuration with 100 GHz head. The closeup view illustrates the conical horn antenna used as Tx and Rx in the 100 GHz transceiver head. 64

Figure II.23: (a) Simulation model of the conical horn antenna integrated in the 100 GHz synView radar head and its dimensions (b). (c) shows the excitation mode by the waveguide mode through a circular waveguide interface. (TE mode). 65

Figure II.24: Directivity-based radiation pattern of the conical horn antenna at a frequency of 100 GHz. It includes (a) a 3D plot, (b) a 2D polar diagram in the xz-plane at ϕ= 0°, and (c) a polar diagram in the yz-plane at ϕ= 90°. 65

Figure II.25: Electric field energy density distribution inside the horn antenna at a frequency of 100 GHz (nearfield distribution). (a) E-energy density on the yz-plane and xz-plane. (b) E-energy density in the xy-plane at the position of z = 10, 15, 20 and 25 mm. (c) and (d) Beam profiles in x and y directions at the position of z = 10 (Position II) and 25 mm(Position IV) respectively. While FWHM at z = 10 mm is around 4 mm in both directions, 8 mm width in the x-direction and 5mm width in the y-direction are obtained in the xy-plane of z = 25 mm. 66

Figure II.26: (a) Photography of a 122 GHz radar transceiver chip. (b) Photograph of a 122 GHz radar transceiver in conjunction with the HDPE lens, proposed by Silicon Radar GmbH. (c) Photograph of a 122 GHz radar transceiver chip with an adapted objective composed of two 3D printed lens, proposed by the research team in IMS laboratory. 67

Figure II.27: (a) Schematic of 2x2 patch antennas acting as Tx and Rx on the radar transceiver front-end. (b) S-parameter S_{11} of patch antenna Tx as a function of frequency. (c) 3D emission pattern of Tx antenna at the frequency of 122 GHz. The maximum directivity is 11.4 dBi, while the angular width in the xz-plane and yz-plane is 48.4 and 46.7° respectively. 68

Figure II.28: (a) Microscope photograph of the silica hollow-core thin-wall waveguide. (b) Extracted material properties of the fused silica as a function of the frequency. 70

Figure II.29: Transmitted signals (a) and corresponding spectra (b) through silica hollow-core pipe waveguides with different lengths. Blue curves: silica waveguide with a length of 201 mm. Red curves: silica waveguide with a length of 301 mm. 71

Figure II.30: (a) Photographs of experimental setup in reflection, without sample (left) and with a plastic hollow-core waveguide (right). (b) Simplified schematic diagrams of the experimental setup. 72

Figure II.31: Spectrum of the reflected signals via a silica hollow-core waveguide. 73

Figure II.32: (a) Microscope photograph of the hollow-core thin-wall waveguide. (b) Extracted material properties (refractive index and extinction coefficient) of the plastic as a function of the frequency. (c) Transmitted signals through a 54 cm-long-waveguide and (d) its corresponding transmission spectrum. (e) Reflected signals through an 8 cm-long-waveguide and (f) its corresponding spectrum. 74

Figure II.33: (a) Photographs of 3D printed hollow-core waveguide with negative curvature. (b) Microscopy photo of the waveguide. (c) Material properties of the bulk material used for 3D printing. ... 79

Figure II.34: (a) Photograph of the experimental setup. (b) Transmitted signal and (c) the corresponding spectrum. (d) The normalized transmittance as a function of the frequency. 80

Figure II.35: (a) Normalized transmission spectrum obtained by the simulation and experiment with initial design dimensions. (b) Normalized transmission spectrum obtained by increasing the web size by a factor of 1.2. (c) Schematic of the waveguide design and the microscopy photos of two half-ellipse webs. It can be seen that the thickness of the web varies with the position. 81

Figure III.1: Schematic diagram of a terahertz wave-guided reflectometry system demonstrated in the literature. 84

Figure III.2: (a) Schematic diagram of a guided terahertz pulse reflectometry system setup, including the double-PCA transceiver probe and dielectric hollow-core waveguide. (b) Schematic diagram of the propagation process from the transceiver to waveguide and then back to the transceiver. 88

Figure III.3: Full simulation of the setup. (a) Scheme of the model including the transceiver, a 5 cm-long silica waveguide and a metal plate placed at the output. (b) E-field distribution (based on the absolute value) on the xz cross-section along the waveguide at different times. (c) Reflected signal detected by the Rx antenna on the transceiver. Two small figures below provide a close-up view on the waveform in the zone I and II. (d) X component of the electric field detected at the center of the core and in the cladding at the cutplane of z = 40 mm. 90

Figure III.4: 3D full-wave simulation results obtained at the frequency of 450 GHz. (a) Numerical model including a transceiver probe, a 10 cm long waveguide and an air-block. (b-d) Power flow distribution on different cutplanes. Position I to VI correspond to z = 2/5/25/50/75/102.5 mm respectively. In the position I, strong power density displays at the right-down side of cutplane, which is related to the emission pattern of the antenna on the transceiver. In position II, while part of the energy is radiated out of waveguide as coupling loss, part of the energy is coupled inside the waveguide. From the position III, guided power in mixed propagation modes along the waveguide can be observed. (e) Power passing through cross-section as a function of distance. Based on the simulation data, the attenuation coefficient of the waveguide is deduced (red curve with $\alpha = 0.0036$ cm^{-1}). (f) Close-up in the zone of 20-50 mm and 30 to 80 mm. 91

Figure III.5: (a) Power outgoing through cross-section as a function of position at a frequency of 450 GHz. Blue curve: power crossing over the whole cross-section. Red curve: power propagating through air core. Yellow curve: power transmitting in the cladding. The beam profile at the output of waveguide is as well provided in the figure, in which power passes through air core and cladding. (b) Remained power at the output of waveguide as a function of frequency. The blue curve represents the power passing through the whole cross-section and the red curve denotes the power crossing the air-core. Beam profile at frequencies of 400 GHz and 475 GHz are given. 93

Figure III.6: (a) Detected signals by the terahertz transceiver. Blue curve: signal propagating through the waveguide. Red curve: signal propagating in free space. This signal can be divided into three zones.

First, the zone I (t = [0-30] ps) corresponds to the crosstalk signal between the two photoconductive antennas on the transceiver. Then waveform in zone II (t=[30 -250] ps) corresponds to the reflection signal coming from probe-mount and imperfection of wave trapping design. Finally, the reflected signal from the sample at the end of the waveguide (blue curve) and a weak reflected signal by freely propagation (red curve) can be seen in zone III (after 340 ps). (b) Reflections from the metal propagating through a waveguide and in free space respectively. (c) Spectrum of reflection signals obtained at (b). Compared to the propagation in free space, more signal power is transmitted through waveguide owning to its guiding capacity. 95

Figure III.7: (a) Left: Photograph of the experimental setup. The silica hollow-core waveguide is placed below the terahertz transceiver and a 1951 USAF test target as the sample is mounted on the multi-directional linear translation stages. Right: 1951 USAF resolution test target, in which the scanned areas are marked by the red rectangles. (b) and (c) Two images of the scanned areas (elements in group -1 and in group -2 respectively) are obtained from the trapezoidal integration over frequencies from 400 GHz and 500 GHz. (d) and (e) The line profiles of terahertz field magnitude along the solid line AB in group -2 and solid line A'B' in group -1. 96

Figure III.8: Full-wave simulation result obtained at the frequency of 450 GHz. (a) Numerical model including a transceiver probe, a 10 cm long plastic waveguide and an air-block. (b-d) Power flow distribution on the cutplanes (V.A/m²). I to VI correspond to cutplanes of z = 2/10/40/75/90/100 mm respectively. (e) Power passing through cross-section as a function of distance. Blue curve: surface integral over the whole cross-section. Red curve: surface integral of the Poynting vector over the air-core section. Yellow curve: surface integral of the Poynting vector inside the cladding. 99

Figure III.9: Power passing through cross-section as a function of the propagation distance at the frequency of 450 GHz (blue curves) and 550 GHz (red curves). Solid curves represent the power crossing the whole cross-section while dash-dot curves denote the power passing through the center area of the waveguide's core (radius < 1 mm). 100

Figure III.10: (a) Photograph of experimental setup exploiting a plastic hollow-core waveguide as the single communication channel between the transceiver and sample. A metal plate acting as a perfect mirror is placed at the output of the waveguide to obtain the maximum reflected energy. (b) Time signals reflected by the metal, in the free space (blue curve) and though a plastic hollow-core waveguide (red curve). According to the origins of reflections, the waveform of time signal can be divided into three zones. The waveform in zone I corresponds to the crosstalk signal between two antennas and the one in zone II originates from the internal reflection from the probe-base. Signals reflected by the metal lie in zone III, a close-up view is given in (d), in which the amplitude of the signal passing through the waveguide is much stronger than that propagates in free space. 100

Figure III.11: (a) Reflected signals from metal placed at the output of plastic waveguide. In each measurement, the plastic hollow-core waveguide has a different length. While the crosstalk signals in different measurements are overlapped (zone I), reflections from the sample have different features (zone II). (b) Reflections from metal after removing the crosstalk signal induced by the probe itself. (c) Spectra of reflections shown in (b). 101

Figure III.12: (a) Photograph of the experimental setup. A metal plate is placed at the bottom of the container to maximize the reflected power. (b) Schematic diagram of two different measurement configurations. Left one represents the measurement performed without liquid, providing a time signal reference. Right one depicts the measurement in the liquid with a depth of h. (c) Time signals detected by the transceiver in two experimental conditions. Red curve: reference signal obtained with an empty container. Blue curve: Detected reflections from the liquid surface and the metal placed at the bottom..... 103

Figure III.13: (a) Schematic diagram of the experimental setup. (b) Recorded time signals reflected by the liquid paraffin. While the quantity of paraffin in the container remains the same, the container is raised up twice during the experiment. (c) Arrival time (given as optical delay in mm) of the first peak in reflections from liquid surface and container bottom. 104

Figure III.14: (a) Experimental setup. While the liquid container is fixed, liquid paraffin is added after each measurement. (b) Recorded waveforms of time signal reflected by the liquid paraffin. (c) Arrival time (given as optical delay in mm) of the first peak in reflections from liquid surface and container bottom. Based on the time delay between two reflections, liquid depth and level change between measurements are given in the table. 106

Figure III.15: Photograph of experimental setup by combining the SynView 100 GHz head with a hollow-core waveguide. 108

Figure III.16: (a) Simulation model of terahertz wave-guided reflectometry system consisting of a horn antenna and plastic pipe waveguide. (b) and (c) E-field distribution ($Emax$) at frequency of 100 GHz on the cutplant of x = 0 and y = 0 respectively. (d) E-field on the xy-planes (18*18 mm²) at different positions of z = 10 mm (I, the entrance of waveguide), 40 mm (II), 180 mm (III), 310 mm (IV, the output of waveguide), 315 mm (V, 5 mm after the output), 330 mm (VI, 20 mm after the waveguide). 109

Figure III.17: Beam profile evolution in free space. (a) 2D beam profiles and (b) line profiles in the x- (blue curve) and y-direction (red curve) obtained at a distance of 0/3/6/9 mm from the output facet of the waveguide respectively. 110

Figure III.18: Power propagating through the cross-section as a function of distance at the frequency of 88/94/100/106 GHz respectively. 111

Figure III.19: Energy remained in the simulation box during the transmission and reflection under the condition that a perfect mirror (metal) is placed at the end of the waveguide with different distances. At the time of around 1300 ps, guided waves encounter the perfect mirror and then are reflected back through the waveguide. After 2500 ps, the reflected waves are detected and absorbed by the waveguide port..... 112

Figure III.20: (a) Photograph of a 1951 USAF test chart. (b) Raster scan acquired image using the regular far-field 100 GHz SynView unit at NA=0.5 (a 50 mm diameter dielectric lens with a focus distance of 50 mm was used to focuse the incident beam) for reference. (c) Raster scan acquired image using the guided 100 GHz Synwiew probing system in optic-free geometry at 1 mm imaging distance..... 113

Figure III.21: Simulation results. (a) Schematic diagram of the terahertz wave-guided reflectometry system setup including a SynView 100 GHz head, a waveguide and a HDPE lens inserted in the output of

the waveguide. (b) and (c) Electric field energy density distribution in the yz-and xz-plan respectively. (d) Beam profile in the xy-plane at a distance of 3 mm to the output of the waveguide. 2D beam profiles (e) and corresponding line profiles in the x and y directions (f) are given to highlight the improvement that is brought about by the solid immersion lens to the guided reflectometry systems. While I. and II. represent the beam profiles obtained in the original setup without the lens, (at the output, and at a distance of 5 mm after the output of the waveguide respectively), III. depicts the beam profile obtained in the position of 2.7 mm after the PE lens. 115

Figure III.22: Simulation results. (a) Beam size and power intensity as a function of distance after the PE lens. Bleu and red curve denote the FWHMs in the x- and y-directions respectively. The yellow curve represents the maximum power intensity as a function of distance. When d = 2.7 mm, the maximum power flow is obtained, corresponding to the focal plane of the lens. (b) Reflections detected by the conical horn antenna in different configurations. Blue curve: open-end configuration. Red curve: a metal is placed at the output of the lens. Yellow curve: a metal plate is placed at a distance of 2.7 mm after the lens. (c) Field energy contained in the simulation box as a function of time in different configurations. 116

Figure III.23: Raster scan acquired image of a test chart using the guided terahertz FMCW radar reflectometry system with the help of an HDPE lens. 117

Figure III.24: (a) Simulation model of the TGR-FMCW system, consisting of a 122 GHz Silicon radar chip and a plastic waveguide. (b) and (c) E-field distribution on the yz-plane and xz-plane at a frequency of 122 GHz. (d) E-field distributions on the xy-plane at different z positions (xy-cutplane surface: 20*20 mm²). I to VI represent the cutplane of z =1/130/170/300/302/ 320 mm respectively..... 119

Figure III.25: Power passing through cross-section as a function of distance at two different frequencies (122 GHz and 126 GHz respectively). The couped power ratio is around 20% at the frequency of 122 GHz. 120

Figure III.26: Image of a test chart using terahertz wave-guided reflectometry system setup..... 120

Figure III.27: E-energy density distribution on different cutplanes at a frequency of 122 GHz. (a) Simulation model including an equivalent field source of 122 GHz transceiver chip, a 30 cm long waveguide, a solid immersion HDPE lens and a 15 mm air block. (b) and (c) E-energy density on the yz-plane and xz-plane respectively. (d) E-energy density on the xy-planes (20*20 mm²) at the positions of z = 300 mm (Position I, in the vicinity of the output of the waveguide, inside the PE lens),304 (Position II, nearby the output of PE lens), 307 (Position III, after PE lens) and 310 mm (Position IV, after PE lens) respectively. 121

Figure III.28: (a) and (b) Schematic diagram and photograph of the experimental setup. The sample is placed at a distance of 3 mm after the HDPE lens. (c) Raster scan acquired image of the test target from the front face. (d) Raster scan acquired image of the test target from the backside. 122

Figure III.29: (a-c) E-energy density distribution on different cutplanes (yz-plane, xz-plane and xy-palne respectively) at a frequency of 122 GHz in a reflectometry system in conjunction with a silicon bullet lens. I-V corresponds to the position of z = 300/ 305.5/ 306/307/308 mm respectively. The output facet of

the silicon lens lies at the position of z = 306.55 mm. (d) 2D beam profile obtained on the xy-plane of z = 306.7 mm, (0.15 mm after bullet silicon) and the corresponding line profiles in the x-and y-direction. The FWHM in the x- and y-direction is 0.6 mm and 0.66 mm respectively. 123

Figure III.30: (a) Analysis of beam profile after the silicon lens. Bleu and red curves represent the FWHM of the beam in the x- and y-direction as a function of distance. Yellow curve: the electric field energy density at the beam center as a function of distance. (d = 0 mm the focal plan with an FWHM of 0.6 mm and 0.66 mm are achieved in two directions.) (b) Difference of the electric field (Y component) detected by the probe in the receiver's position in two different configurations (reflected by the air and perfect mirror respectively). (c) E-field energy remained in the simulation box as a function of the time. 124

Figure III.31: (a) Experimental setup and (b) image of the test chart obtained using the reflectometry system in combination with a bullet silicon lens. 125

Figure IV.1: Photograph of the TeraProbe testbed. 132

Figure IV.2 : (a) Schematic diagram of an EOTPR system developed by the Teraview Ltd. company. The terahertz pulses are coupled into the device under test (DUT) via a semi-rigid coaxial cable connected to a high-frequency probe. (b) References signals from different levels (from the top die to the substrate) of a packaging. At the left side, there is a photograph of EOTPR 2000 system. 136

Figure IV.3: Photographs of two available high-frequency probes. (a) Model 220. (b) Model 500 B in combination with waveguide transition. They are to couple a pulse signal, which is genrated by a double-PCA lens-free terahertz transceiver, into a sample on–wafer. 138

Figure IV.4: (a) Photograph of the experimental setup. (b) Optical paths on the vertical subsystem to excite the PCAs of the transceiver. Two laser paths correspond to pump and probe laser beams. 140

Figure IV.5: Photographs of the on-wafer reflectometry setup, displaying the details of different parts. As shown in (a) and (b), the transceiver probe is placed in the vicinity of the entrance of the high-frequency probe to achieve proper coupling. (c) Sample support equipped with 3D translation stages and a chuck with vacuum holes to hold the wafer during the measurement. (d) Manual probe positioner installed on an optical table. (e) Two microscope systems, providing machine visions for optical alignment and wafer alignment, respectively. 141

Figure IV.6: (a) Recorded waveforms of time signals reflected from samples on-wafer using the experimental setup with a 220 GHz high-frequency probe. In addition to the measurement in the air, other signals are recorded in the case that the high-frequency probe is in contact with the calibration kit, including short, load, open and Thru. (b) Close-up views of the waveform in zones I and II. It is known that zone (I) corresponds to the reflections induced at the entrance of the probe. 142

Figure IV.7: (a) Recorded waveforms of time signals reflected from the calibration kit using a 500 GHz high-frequency probe and a waveguide transition. In addition to the measurement in the air (open), other signals are recorded in the case that the high-frequency probe is in contact with the calibration kit, including short, load. (b) Close-up views of the waveform in zones I and II. The zones I and II correspond to the reflections from at the entrance of the probe and the end of transitions. 143

List of Tables

Table 1. Novel designs of photoconductive antennas 13

Table 2. Optical-pumped transceivers 20

Table 3. Terahertz negative curvature waveguides 76

Table 4. 3D printed terahertz dielectric waveguides 78

Table 5. Review of Guided reflectometry systems 86

Table 6. On-wafer probes from different companies 131

Table 7. Non-destructive fault isolation techniques for 3d packaged devices 135

Acronyms

BPM	Beam Propagation Method
BWO	Backward-Wave Oscillator
CMOS	Complementary Metal Oxide Semiconductor
COC	Cyclic Olefin Copolymer
CPS	Coplanar Stripline
CPW	Coplanar Waveguide
CW	Continuous-Wave
DFG	Difference-Frequency Generation
DUT	Device Under Test
EBM	Electron Beam Melting
EIK	Extended-Interaction Klystrons
FA	Failure Analysis
FDM	Fused Deposition Modeling
FEL	Free-Electron Lasers
FEM	Finite Element Method
FET	Field-Effect Transistor
FIT	Finite Integration Technique
FMCW	Frequency-Modulated Continuous-Waves
FWHM	Full Width At Half Maximal
GSG	Group-Signal-Group
TGR	Terahertz wave-guided Reflectometry
TGR-FMCW	Terahertz wave-guided Reflectometry in FMCW mode

TGR-P	Terahertz wave-guided Reflectometry in Pulse mode
HBT	Heterojunction Bipolar Transistor
HDPE	High-Density Polyethylene
HEB	Hot-Electron Bolometer
HEMT	High Electron-Mobility Transistor
IMPATT diode	Impact Ionization Avalanche Transit-Time Diode
KGD	Known Good Device
LAPCA	Large Area Photoconductive Antenna
LT-GaAs	Low-Temperature Grown Gaas
MBE	Molecular Beam Epitaxy
MFT	Modulation Transfer Function
MMIC	Monolithic Microwave Integrated Circuit
MTIR	Modified Total Intern Reflection
NEP	Noise Equivalent Power
OR	Optical Rectification
PCA	Photoconductive Antenna
PCS	Photoconductive Switch
PM	Phase-Match
Polyjet	Polymer Jetting
PoP	Package On Package
PPCW	Parallel-Plate Waveguide
QCL	Quantum Cascade Laser
RF	Radiofrequency
SAM	Scanning Acoustic Microscopy
SBD	Schottky Barrier Diode

SIS	Superconductor-Insulator-Superconductor
SLA	Stereolithography
SLS	Selective Laser Sintering
SNR	Signal-To-Noise Ratio
SOI	Silicon On Insulator
SoS	Silicon-On-Sapphire
SPP	Surface Plasma Polariton
SPS	Stimulated Polariton Scattering
TDS	Time Domain Spectroscopy
TLM	Transmission Line Matrix Method
TMIC	Terahertz Monolithic Integrated Circuit
TPO	Terahertz Parametric Oscillator
TSV	Through Silicon Via
TUNNETT diode	Tunnel Injection Transit Time Negative Resistance Diode
TWT	Traveling-Wave Tube
VED	Vacuum Electronic Device
VKGD	Virtual Known Good Device
VNA	Vector Network Analyzer

General Introduction

Lying between two well-developed domains, namely the microwaves and infrared, terahertz radiations have attracted considering attention for their *a priori* seducing properties, among which can be sorted their non-ionizing nature, their ability to penetrate through optically opaque materials, or even their sensitivity to dielectric discontinuities. The development of spectroscopic techniques in the terahertz regime has gradually extended to imaging, which nowadays allows both the academic and the industrial fields to perform a wide panel of non-destructive tests ranging from quality control, to security inspection and through other areas as heritage science.

It is clear that system configurations play an important role in practical uses, impacting the application scope of terahertz technology. From a practical point of view, a compact terahertz measurement system in reflection mode rather than in transmission geometry is more advantageous. More precisely, compared to the transmission configuration that imposes restrictions on the form and properties of an object under test, a reflection geometry requiring only the access to one surface of a sample is more suitable to a wide variety of objects. This being said, although more likely to be used for diverse applications, the complexity and the response understanding that accompany a setup in reflection configuration is consequently higher. In fact, reflection geometries usually require the implementation of additional quasi-optics elements such as lenses or beam splitters. More than inducing further work to achieve proper alignment along the propagation path, these additions concomitantly hinder the possibilities towards reaching compactness and integration of such systems.

To address this issue, terahertz wave-guided implementation is proposed in the present work as a promising solution to conduct interrogative signals to the targeted zone of a sample. Once an optic-free single communication channel is established by a waveguide between the transceiver and the sample, the structure of waveguides directly stipulates the propagation path, reducing the difficulties in alignment. The entire system configuration is simplified since no beam splitter or lens is required to enable the coupling. The main objective of the present work is to implement a compact terahertz wave-guided reflectometry (TGR) system following a demanding selection over the vast library of existing components.

Apart from the construction of a TGR system for sensing and imaging purposes, on-wafer/package-level measurements in the terahertz band are of great interest due to the rapid development of terahertz monolithic integrated circuit (TMIC). Indeed, prompted by the advances of semiconductor technologies and 3D packaging techniques, numerous high-speed devices have been proposed over the last decade. To verify and to validate the novel designs prior to mass production, the research and development process of TMIC must include on-wafer measurements. Compared to conventional tunable continuous-wave sources, a pulse signal generated by an optoelectronic source covers a larger frequency region in the spectrum, making it possible to obtain the scattering parameters in an extra-wide band via a single measurement. Not only the measurement process can be simplified by the deployment of an optoelectronic source, but also the cost of the measurement platform in an extreme-large frequency range can be reduced. Consequently, one part of

this manuscript is focused on the implementation of an on-wafer reflectometry system by using an RF on-wafer probe in association with a wideband double-PCA transceiver. Being the first attempt to deliver a pulse signal into a sample on-wafer, the main challenges to face are how to couple efficiently a pulse signal into a sample on-wafer and how to interpret the time signal with the presence of higher propagation modes.

Based on the aforementioned purposes, the whole manuscript is composed of four chapters that are hereafter succinctly described. The first chapter offers an overview of the developments of terahertz technology, including the advances in terahertz devices (sources, detectors and waveguides), system configurations and applications. Compared to two distinct source and detector, a compact transceiver lightens the system configuration by removing the beam splitter or coupler used to separate the incident beam and the reflected one. Consequently, studies about terahertz transceivers are thoroughly reviewed. To select a suitable waveguide to cooperate with transceivers, an overall account of the advances in terahertz waveguides and their applications are provided. The state-of-the-art about waveguides is divided into two parts: metal waveguides and dielectric ones. In addition to their working principles and propagation properties, the coupling issue taking place in previous studies are especially reviewed with details.

In the second chapter, three selected transceiver units, i.*e.*, a double-PCA lens-free transceiver, an III-V technology-based FMCW module, and a Si-based radar unit, are tested separately to assess their performances. In particular, performances of the double-PCA transceiver including its operating frequency band and imaging capacity are more detailed. Based on the preliminary studies, hollow-core anti-resonant waveguides are considered as a suitable candidate to ensure the signal transmission between the transceivers and a sample. Their transmission bands are verified through THz-TDS measurements, corresponding to an optimized operating frequency band of the double-PCA transceiver (from 400 GHz to 500 GHz), both in transmission and reflection mode. The additive manufacturing (3D printing) technique, that allows fast cost-efficient waveguide development chain, is presented at the end of this chapter.

The third chapter reports the constructed TGR systems and their corresponding performances by taking advantage of the aforementioned transceivers and waveguides. According to the selected transceiver unit, this chapter is divided into two main parts: (i) terahertz wave-guided reflectometry systems in pulse mode (TGR-P), and (ii) terahertz wave-guided reflectometry system in FMCW mode (TGR-FMCW) systems. With respect to TGR-P systems, two selected hollow-core dielectric waveguides are tested to establish an optic-free single communication channel between the double-PCA transceiver and a sample. In addition to the time-domain waveform characterization, the imaging and sensing applications of the systems are also delineated. While the TGR-G system exploiting a 3 mm diameter silica hollow-core waveguide displays a resolution power around 700 μm, the other TGR-G system including a 6 mm diameter plastic waveguide display the potential for liquid depth detection. In regard to TGR-FMCW systems, 100 GHz SynView head and 122 GHz Silicon Radar transceiver chip are separately tested with a plastic hollow-core waveguide. The unwanted ghosting effect is then corrected by the integration of an extra termination hemispherical lens, resulting in the imaging capacity improvement. In addition to experimental setups and applications, investigations into the field properties inside the system are conducted with the help of the 3D full-wave simulation, allowing the analysis of propagation behaviors of waves along the waveguide. The parameters such as coupling efficiency, propagation modes, dynamic range are evaluated and discussed.

The last chapter, more prospective, begins by introducing the rapid development of the TMIC, offering the background of the increasing need for on-wafer measurements. Different methods to improve the reliability and repeatability of on-wafer measurements at high frequencies are reviewed, including the Z-travel control approach and non-contact probes. Apart from the on-wafer measurements, packaging level default detection has benefited from the advances of optoelectronic devices. The EOTPR (Electro-Optical Terahertz Pulse Reflectometry) technique exploiting PCA devices along with an RF probe, is particularly detailed. Inspired by the EOTPR system, two RF probes in the frequency band of 140-220 GHz and 330 GHz to 500 GHz are separately deployed to direct a pulse signal from the double-PCA transceiver to a sample on–wafer. Both system configurations give rise to ring-like shape signals, and the origins of reflections are discussed.

The work reported in this manuscript was realized within a collaboration that gathered several research teams. The implementation and analysis of guided terahertz reflectometry systems were accomplished in IMS laboratory under the supervision of Dr. Patrick Mounaix and Dr. Jean-Paul Guillet while on-wafer measurements were conducted under the guidance of Dr. Sebastien Fregonese (Bordeaux, France). The hollow-core thin-wall waveguides were provided by Dr. Georges Humbert from XLIM research Institute (Limoges, France). The design and the fabrication of 3D printed negative curvature waveguides were carried out by Prof. Cristiano M.B. Cordeiro from UNICAMP (Brazil) and Marcos A. R. Franco from IEAv (Brazil).

Chapter I.

General terahertz technology

I.1. INTRODUCTION **6**

I.2. TERAHERTZ ACTIVE DEVICES AND SYSTEM CONFIGURATIONS **6**

I.2.1. Terahertz sources 6

I.2.2. Terahertz detectors 14

I.2.3. Terahertz measurement systems 16

I.2.4. Developments of optical-pumped pulsed transceivers 18

I.3. TERAHERTZ WAVEGUIDES **22**

I.3.1. Metallic terahertz waveguides 22

I.3.1.1. Rigid metallic waveguides 22

I.3.1.2. Metal wires 23

I.3.1.3. Other metallic waveguides 26

I.3.2. Developments of dielectric waveguides 26

I.3.2.1. (Modified) Total internal reflection waveguides 27

I.3.2.2. Hollow-core waveguides 30

I.3.3. Conclusion 33

I.4. TERAHERTZ APPLICATIONS **33**

I.5. CONCLUSION **35**

I.1. Introduction

An overview of the developments of terahertz technology is provided at the beginning of this chapter, including the advances in terahertz devices, system configurations. Studies about terahertz transceivers and waveguides are then thoroughly reviewed to provide valuable information to select suitable components to implement a compact terahertz wave-guiding reflectometry system. At last, a great amount of terahertz applications is given, proving the potentials of terahertz in different domains.

I.2. Terahertz active devices and system configurations

As shown in Figure I.1, the terahertz frequency band spans from 100 GHz to 10 THz, corresponding to a wavelength range from 3 mm to 30 µm. It lies between two well-developed domains, namely the microwave and infrared bands. Due to the lack of efficient sources and detectors, terahertz radiations took several decades to complete the transition from a newly defined portion of the electromagnetic spectrum to a widely studied topic. Since the 1980*s*, the progressive developments of terahertz devices, both active components and passive ones, contribute to the advances of terahertz technology. Increasing attention from the academic and industrial fields has been drawn to the terahertz region [1].

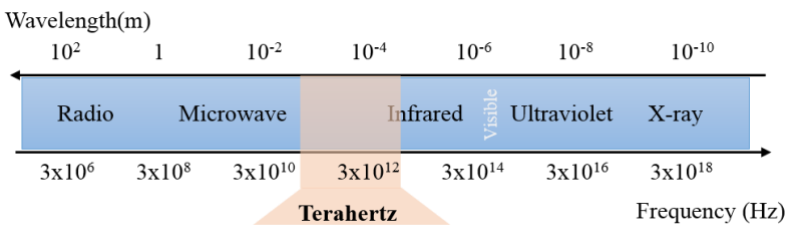

Figure I.1: Terahertz region in the electromagnetic spectrum, covering frequencies from 100 GHz to 10 THz.

I.2.1. Terahertz sources

The burst of terahertz technology is tightly linked to the technical advances of terahertz sources. At the very beginning of the research stage, apart from radiations received from the astronomic objects, the black body was the primary terahertz source. The absence of a convenient and powerful source limited the research work to specialized laboratories. In the *1980s*, new types of terahertz emitters, such as photoconductive antenna (PCA), were developed. Since then, a great deal of effort has been made to improve consistently the performances of existing sources and to develop novel effective ones [2]. According to the generation principle, terahertz sources can be classified into five distinct types: thermal sources, vacuum electron device sources, terahertz lasers, solid-state devices, and laser-pumped sources [3]. The working principle and main features of each kind of source are briefly described below. In particular, developments of photoconductive antennas are more detailed with novel designs.

Thermal sources

Thermal sources such as globar sources [4] and mercury lamps [5] can emit an extremely broadband signal, but they provide a weak output power of the order of picowatts. Low output power, high-temperature requirements prevent this type of source from industrial applications. It is worth noting that all the objects

with a temperature above 10 K radiate terahertz waves naturally. On this basis, the feasibility of the passive imaging technique is ensured [6].

Vacuum electron devices

Unlike thermal sources, vacuum electronic devices (VED) can obtain a remarkable high output power in the terahertz region, from mW up to GW, showing great importance to fundamental science. This type of source can operate either in pulse or continuous-wave mode by converting the kinetic energy of an accelerated electron beam to electromagnetic energy within the interaction zone [3]. The commonly used VED sources include the backward-wave oscillator (BWO), extended-interaction klystrons (EIK), traveling-wave tubes (TWT), gyrotrons, free-electron lasers (FEL) and synchrotrons [7]. Although these high-power sources are beneficial for applications such as terahertz imaging, remote sensing, their bulky size and high cost limit their use outside laboratories. With the effort brought in this domain, further progress toward compact, low-weight, reliable, cost-efficient terahertz VED sources is expected.

Solid-state sources

As integrated circuit technologies continue to develop, the high-speed device is pushing the operating frequency up from microwave to the terahertz range. Thanks to the advances in semiconductor materials (mainly III-V based transistors), the limitation of output power associated with frequency is further reduced [8]. On this basis, more performant solid-state sources are developed in the terahertz band. They can be divided into two types: diode-based sources (*e.g.*, Gunn diode [9], IMPATT diodes, TUNNETT diode and resonant tunneling diodes) and transistor-based ones (*e.g.*, CMOS or HEMT) [10], [11]. Considering their reasonable cost, easy usage, compact size, various frequency choice and excellent power performances, they have been widely used in academic researches and for commercial applications. For these exact reasons, two frequency-modulated continuous-waves (FMCW) radar units were investigated and selected to construct a guided terahertz reflectometry system, more details are given in Chapter I.4. If readers are interested in the developments of solid-state sources, an overall review concerning their performances is provided in [12].

Terahertz lasers

Among all terahertz lasers, gas lasers are considered as the first one in use. They can generate a coherent signal in a wide spectral range with an output power reaching several hundreds of mW [13]. In 2019, a terahertz molecular laser (ML) pumped by a mid-infrared quantum cascade laser was reported, which can emit 1 mW at 1.1 THz in continuous wave [14]. However, their bulky volumes reduce the potential application scope in industrials. Recently, a new member was introduced into the terahertz laser family, quantum cascade laser (QCL). It can provide a more powerful output within a compact size. The concept of QCL was firstly carried out in the mid-infrared (mid-IR) region before extending to the terahertz band in 2002 [15]. Different from a conventional semiconductor laser, which generates photons by exploiting the drop of the electron from the conduction band to the valence band, there is no recombination between the electron and hole during the QCL generation process. Instead, transitions between electronic subbands in a series of quantum wells, formed by the band structure of semiconductor material, give rise to the emission of terahertz radiation. The characteristics of the laser are determined by the band structures and

semiconductor properties. Currently, QCLs fill the gap of terahertz sources at frequencies between 1 and 5 THz with relatively high power output (>1 W) in a compact size, including narrow-line CW or pulse mode [16]. Although the cryogenic cooling system is still required, QCLs remain attractive due to their powerful output and compact volume. Researchers continue to explore the possibilities to reduce the operating temperature, to extend the frequency band and to increase the dynamics of the output power in pulse mode.

Laser-pumped sources

Optical rectification

Optical rectification (OR) is one of the most widely used approaches to generating terahertz radiations. Triggered by a short pulse laser (femtosecond laser beam), non-linear crystals such as LiNbO3, organic crystal DAST and ZnTe generate terahertz waves efficiently if the phase-match (PM) condition in materials is satisfied [17]. This method is frequently used for time domain spectroscopy owing to its extremely broad spectrum capacity. Novel non-linear materials are proposed and tested to improve the generation efficiency of terahertz waves. PM methods, including tilted-pulse-front geometry or Cherenkov geometry, continue to be investigated for further improvement [17].

Photoconductive antenna

Thanks to the novel antenna designs and advances in semiconductor technology, the performances of photoconductive switch (PCS) sources and detectors have been improved during the last decade. It has become one of the most frequently used devices due to its simplicity, low cost, compact volume and steadily improved fabrication process. It can work in two modes, either pulsed mode or continuous-wave (CW) mode [18]. In combination with a dual-wavelength laser source, a photoconductive switch acts as a photomixer to generate a CW signal [19]. Different kinds of photo-mixers have been developed, including ErAs:GaAs inter-digitated photo-mixer, uni-traveling-carrier photo-diode (UTC-PD) [20], [21], *etc*. Compared to photoconductive antennas, photo-mixers show more advantage in terms of output power at frequencies below several THz. Considering the scope of the present work, the working principle of a photoconductive antenna (PCA) in the pulsed mode (both generation and detection) is introduced in the following part [22].

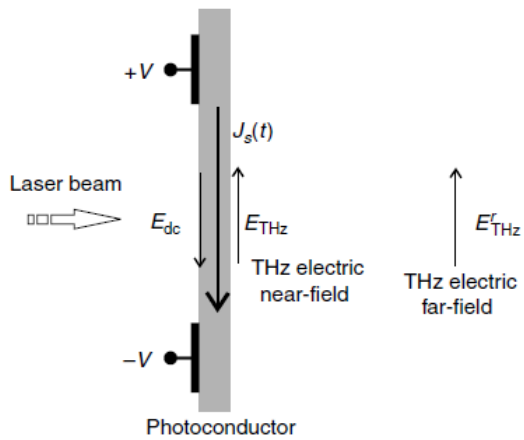

Figure I.2: Photoconductive antenna illuminated by a femtosecond laser beam for terahertz wave generation.

As depicted in Figure I.2, a PCA is biased with a DC voltage to generate a bias electric field E_{DC} between two electrodes. Irradiated by a femtosecond laser carrying photon energy higher than the semiconductor's bandgap, photo-excited carriers are then created in the active zone of the substrate. These photo-generated carriers may recombine, be trapped, or form momentum scatter, leading to a time-dependent conductivity $\sigma(t)$ of the semiconductor layer, which can be expressed as :

$$\sigma(t) = \frac{1}{\alpha} e\mu N(t) \tag{1}$$

where α represents the optical absorption coefficient, e denotes the elementary charge, μ is the mobility of electron and $N(t)$ is the density of photocarrier depending on carrier lifetime in the semiconductor layer and the properties of laser pump. This sudden change of conductivity in the material gives rise to a transient current $J(t)$ under the bias field E_{DC}, which is given in Equation (2).

$$J(t) = \sigma(t) E_{DC} \tag{2}$$

This transient current $J(t)$ further leads to electromagnetic waves, *i.e.*, terahertz radiations E_{THz}. The whole generation principle can be described as below:

$$E_{THz} = -\frac{1}{4\pi\varepsilon_o}\frac{A}{c^2 z}\frac{\partial J(t)}{\partial t} = -\frac{Ae}{4\pi\varepsilon_0 c^2 z} E_{DC} \frac{\partial \sigma(t)}{\partial t} \tag{3}$$

where A is the gap area illuminated by the laser light, z is the distance between the field point, ε_0 is vacuum permittivity, and c is the speed of light in vacuum. It reveals that the generated terahertz waves depend on the bias field, the properties of the semiconductor substrate and the laser pump. If the given energy of bias field and laser excitation are too strong, the generated terahertz field may not respect Equation (3) anymore, more deeper explanations can be found in [23].

On the contrary of generation principle, photo-excited carriers in a PCA detector are accelerated by the transient terahertz field, leading to photocurrent between two electrodes. If the carrier lifetime in the semiconductor is much shorter than the pulse duration, the produced photocurrent can be considered

proportional to the instantaneous electric field of terahertz waves. The relation between the current density J and terahertz field E_{THz} can be described by Equation (4):

$$\bar{J} = \bar{N} e \mu E_{THz}(\tau) \quad \textbf{(4)}$$

where $\bar{N}$ denotes the average electron density, and τ is the temporary delay between probe pulse and terahertz pulse. By varying the time difference between laser pump and probe beams, a time-dependent waveform can be obtained, *i.e.*, both phase and amplitude information are obtainable. Hence, the photoconductive sampling technique is a coherent detection method.

Semiconductor materials used for PCA

The aforementioned photocurrent formulas reveal that the properties of the substrate have a significant impact on the final performances of PCA. A semiconductor material possessing high mobility, short lifetime and low dark conductivity, allows to obtain broadband emission and high SNR detection. However, it is difficult to find a substrate fulfilling all the requirements. While a short lifetime is an essential condition to achieve broadband terahertz signal detection, high carrier mobility allows providing an intense terahertz field. In the *1980s*, silicon-on-sapphire (SoS) was first used for PCA generation. It was then replaced by GaAs with more suitable properties in terms of bandgap, carrier mobility and lifetime. Up to date, high-quality low-temperature grown GaAs (LT-GaAs) fabricated by molecular beam epitaxy (MBE) technique, has become the most widely used PCA substrate due to its improved high resistivity, carrier mobility and shorter lifetime. It can be used as the substrate for the PCA emitter and detector. However, the current fabrication technique cannot guarantee the reproducibility, and it remains expensive for large-scale industrial production. To circumvent the need for low-temperature growth, various approaches have been proposed to obtain semiconductors with a decreased carrier lifetime whilst maintaining its carrier mobility. The use of ion implementation in materials has been demonstrated efficient, including GaAs:C, GaAs:Fe and InP:Fe [22].

Considering the bandgap of GaAs (~1.42 eV), Ti:sapphire laser in the vicinity of 800 nm (~1.55 eV) is usually used as the excitation source. By using a narrower bandgap substrate, well-developed telecom-band laser sources (such as Er:fiber 1550 nm and Yb:fiber 1050 nm) can help to construct a more compatible, low-cost and robust photoconductive system. Therefore, increasing attention has been focused on the InGaAs/InAlAs heterostructure with a 0.8-1.2 eV bandgap. In 2014, by using Be-doped InGaAs/InAlAs multilayer PCA, Schell *et al.* have obtained a terahertz pulse signal covering the frequency band in excess of 6 THz with a dynamic range up to 90 dB [24]. Apart from the alloy of InAlAs, ZnSe, HgCdTe, graphene and other 2D materials are also exploited for more functionalities. In addition, the demonstration of a single GaAs/AlGaAs nanowire photoconductive detector shows a promising future of miniaturization of terahertz-integrated circuits [25].

Antenna design

Contact geometries on the substrate act as an electromagnetic antenna, which determine to a large extent the coupling between generated photocurrent in the active zone and emitted electromagnetic waves in free space. The most commonly used simple contact geometries include dipole antenna, bow-tie antenna and strip-line antenna. Spiral, logarithmic periodic antennas, and other non-resonant antennas are frequently

employed for broadband emission. Over the last two decades, the influence of typical antenna structures (dipole and bow-tie antenna) on the performance of PCA have been largely studied [26], [27]. Recently, special designs with multi-contacts have been proposed, allowing the detection of different components of the terahertz electric field, making polarization-resolved TDS possible [28]. In the following part, the studies using new antenna geometries to improve poor conversion efficiency are reviewed. These investigations address mainly two issues during the generation: (i) photocarrier screening effect and (ii) low absorption coefficient of the surface layer on the semiconductor substrate.

Since the generated terahertz field depends on the given bias field, a more intense terahertz pulse can be achieved by increasing the breakdown value of the bias field. Large area photoconductive antenna (LAPCA) is one of the most successful concepts to decrease the screening effect, in which the radiated terahertz field is linearly proportional to the applied bias field [29]–[31], [37]. In 2010, a 5 µm-spacing-electrode microstructured large-area photoconductor was demonstrated to generate high terahertz electric field in the frequency range of 0.2 - 4 THz up to 36 kV/cm (in vacuum electric field) [32]. The optical-to-terahertz conversion efficiency was up to 2 x 10^{-3}. Four years later, 20 THz broadband generation was realized by using a semi-insulating GaAs interdigitated photoconductive antenna, which combined the advantages of large aperture for optical excitation (avoid the need for silicon lenses) and small electrode gaps (3 µm, 20V peak-to-peak) [30].

The plasmonic structure is another key to improve the conversion efficiency by concentrating incident laser pump photons within nanoscale distance from the contact electrodes. As the collection time of the majority carriers between plasmonic electrodes is reduced to a sub-picosecond scale, the quantum efficiency of a PCA is enhanced. Compared to conventional PCAs, designs based on plasmonic structures have achieved improved performances [33], [34]. Studies performed in 2012 have demonstrated that nanostructures serving as plasmonic nano-antennas help to increase the coupling coefficient of the substrate [35]. In 2014, Yang *et al.* have proposed a 3D plasmonic electrode structure (shown in Figure I.3) to overcome the efficiency limitation related to the photo-absorption depth [36]. In 2015, high-power terahertz generation using a large-area plasmonic photoconductive emitter was demonstrated [37]. At the same year, Park *et al*. have reported the importance of bias field distribution in power enhancement via plasmonic nano-electrodes. Based on this research result, they have proposed a nano-electrode large-aperture PCA [38]. In 2018, 5-fold improvement in the generated signal around 1 THz was obtained by optimizing the size of silver nano-antenna array compared to PCA without nanostructure [39]. More details about the mentioned PCA designs and their experimental parameters are given in Table 1 and Figure I.3. Apart from a great of effort focused on the material properties and contact geometries, antireflection coating [40] as well as layered structure [41], [42] have been studied to improve the laser absorption coefficient, hence offering better PCA performances.

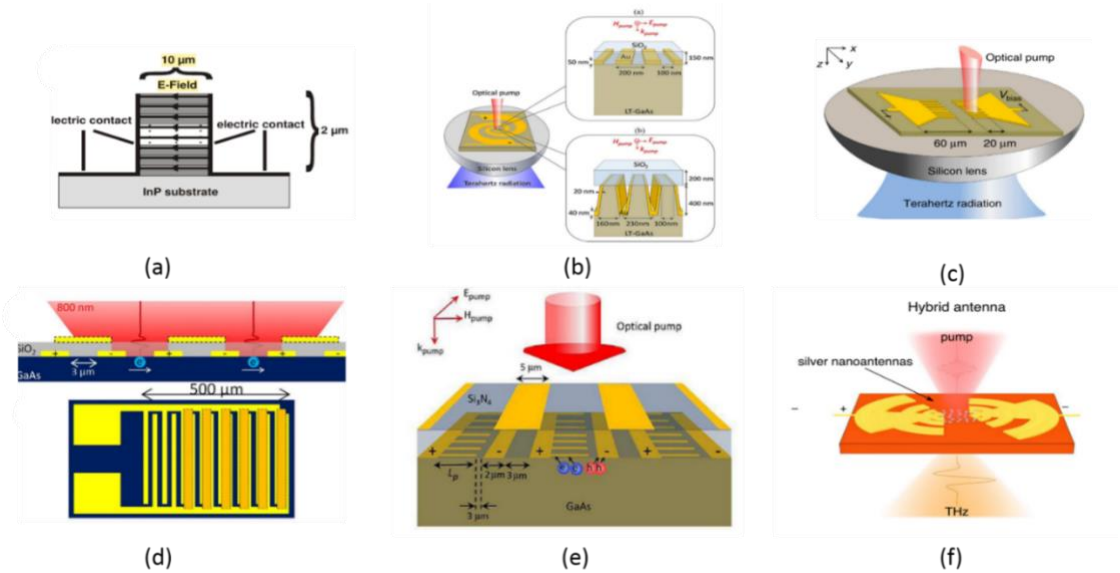

Figure I.3: Novel antenna designs proposed to improve PCA performance. (a) Mesa-structured InGaAs/InAsAl PA layer, from [43]. (b) LT-GaAs logarithmic spiral antenna with 3D plasmonic contact electrode [36]. (c) Bowtie antenna incorporating with plasmonic contact electrodes [33]. (d) Large area interdigitated PCA antenna allowing a broadband terahertz wave generation [30]. (e) High–Power large-area PC emitter exploiting plasmonic contact electrodes [37]. (f) Ag-nanoantenna coupled PCA, from [39].

TABLE 1. NOVEL DESIGNS OF PHOTOCONDUCTIVE ANTENNAS

PCA	Mesa-structured InGaAs/InAlAs layers [43]	Plasmonic nanocontact electrodes [33]	3D plasmonic Contact Electrodes [36]	Large area interdigitated PCA [30]	Interdigitated ZnSe large aperture PCA [31]	Optimized Plasmonic nanostructured PCA [39]
Year	2010	2013	2014	2014	2016	2018
Role	emitter & detector implemented in one terahertz system	emitter/detector characterization separately	emitter	emitter	emitter	emitter
Material	100 periods of InGaAs/InAlAs	LT-GaAs	LT-GaAs	SI-GaAs	ZnSe	SI-GaAs QD substrate
Laser beam	1550 nm	800 nm	800 nm	800 nm	400 nm	800 nm
Pulse width	100 fs	200 fs	200 fs	15 fs (~35fs)	60 fs	120 fs
Repetition rate	100 MHz	78 MHz		4 MHz	10 Hz	80 MHz
Optical excitation power	varied within the measurement (up to 60 mW)	varied within the measurement (5-25 mW)	5 µm spot, Varied (up to 5.6 mW)	varied within the measurement 2-3&	20 mJ	30 µm spot, 50 mW pump power
Bias voltage	varied (up to 14 V)	10-80V	varied (up to 60 V)	20 V		12 V
Contact structure	10 µm gap; 25 µm spacing strip line antenna	20 µm length plasmonic electrode contact (separation 100 nm); bowtie antenna	15*15 µm² 3D plasmonic contact electrodes embedded inside LT-GaAs substrate; logarithmic spiral antenna	3 µm width, 3 µm spacing; interdigitated antenna (500 µm length in total)	interdigitated PCA (12.2 cm² aperture area)	log-periodic terahertz PCA coupled to Ag nanoantenna array 8 µm gap, overall 1.8 mm diameter
Performances	27.5 folds improvement in amplitude compared to the system using non-mesa antenna; frequencies extending to 4 THz	As emitter, 250 µW average output power compared to 12 µW conventional PC emitter and frequency components up to 1.5 THz. 30 times higher detection sensitivities.	0.1-2 THz. High optical-to-terahertz conversion efficiency of 7.5 % at 1.4 mW optical pump (105 µW with a bias voltage 60 V).	Bandwidth up to 20 THz with peak electric field exceeding 1 kV/cm maximum peak at 1.5 THz. No Si lens needed.	8.3 ± 0.2 µJ generated energy of terahertz pulse, peak electric field 331±4kV/cm at frequency 0.28 THz.	Substantial enhancement around 1 THz.

Apart from PCA and optical rectification, difference-frequency generation (DFG) and stimulated polariton scattering (SPS) methods associated with laser excitation are also exploited as terahertz sources. The former type of source generates monochromatic signals by converting two optical frequencies into a terahertz frequency in a non-linear material. And the latter type of source taking advantage of parametric polariton scattering of laser light involves both second and third order non-linear in a polar crystal such as $LiNbO_3$ and GaP. They can provide a wide tunability and an excellent spectral purity [17]. Compared to DFG, the terahertz parametric oscillation (TPO) source exhibits similar performances in a simpler configuration, making it more attractive in practical applications. Besides, based on the Photo-Dember effect, a terahertz source generating radial polarization has been proposed [44].

Different types of terahertz sources have been reviewed, including thermal sources, vacuum electron devices, solid-state sources, terahertz lasers and optical-pumped sources. Their relevant generation principles were described. In particular, photoconductive antennas were more detailed with continuously improved designs. Depending on the nature of the source, different types of sources display their respective advantages and performance limitations. Figure I.4 is provided to give an overall view of terahertz sources in terms of output power and frequency, which can help one to select a suitable source for a specific application. As mentioned previously, tunable photo-mixers are also of great interest in practical use due to their compact size and output power. Depending on the available devices in my work, the state-of-the-art focuses on the photoconductive antennas.

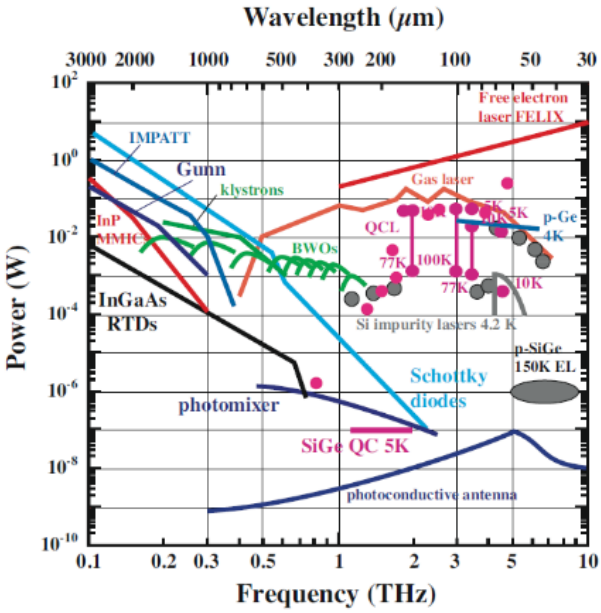

Figure I.4: Logarithmic plot of the emitted power of different terahertz technologies sources as a function of frequency and wavelength.

I.2.2. Terahertz detectors

Depending on working principles, terahertz detection techniques can be classified into three types: direct detection, heterodyne detection and optoelectronic detection. As optoelectronic detection techniques, photoconductive antennas and non-linear crystals (electro-optical sampling) can be deployed for detection via the inverse generation principle. Both of them belong to coherent detection methods, providing information on the amplitude and phase.

Before introducing other detectors, the notion of Noise Equivalent Power (NEP, in $W/Hz^{1/2}$) should be given. It is defined as the input power level at which the signal-to-noise ratio (SNR) over 1-Hz bandwidth is unity. As a critical figure of merit, NEP allows to compare the performances of different types of detectors in terms of the sensitivity and noise level [45]. The smaller the value of NEP is, the higher the sensitivity of the detector is. In addition to NEP, the response time and bandwidth should also be taken into consideration with regards to the intended application.

Direct Detection

Detectors exploiting direct detection consist of thermal detectors and some electronic devices developed from the microwave frequency band. Since the output signal of this type of detector is proportional to the square of the incident field, they are also called square-law devices. The most commonly used thermal devices include bolometers, pyroelectric detectors and Golay cells. They convert the electromagnetic field energy of terahertz waves into a measurable electric signal. More precisely, pyroelectric detectors measure the current linked to the change of dielectric material properties induced by thermal effect. Noise Equivalent Power (NEP) of a pyroelectric detector can be up to 500 $pW/Hz^{1/2}$ in a broad frequency band from terahertz to infrared. Golay cells measure the change of gas volume caused by the absorption of terahertz waves. Bolometers perform measurements through a resistance thermometer, which is thermally attached to an absorbing material. While certain bolometers can work at room temperature (NEP in order of 10^{-10} $W/Hz^{1/2}$), the most sensitive bolometers are liquid helium-cooled (NEP of 10^{-18} $W/Hz^{1/2}$) [46]. There is a trade-off between the operating temperature and the sensitivity. In spite of the slow response of a thermal detector, their large band detection capacity and high sensitivity make them attractive for the most research works. If the integration of a detector in a system is wanted, cryogenic setup may be problematic. In this way, electronic devices operating at room-temperature such as small-area Schottky diodes (used as antenna-coupled) and field-effect transistors (FET) shown more advantage. Based on plasma wave oscillation, the resonance absorption frequency of a FET is determined by the gate voltage related to channel dimensions [10]. Thus, as technology advances, FET can offer a wider detection frequency range. NEP of a FET under zero-bias source-drain conditions can reach the order of 10^{-11} ~10^{-12} $W/Hz^{1/2}$ while NEP of zero-bias Schottky barrier diode (SBD) can reach the order of 10^{-10} ~10^{-11} $W/Hz^{1/2}$ [11]. Since direct detection techniques measure the power of terahertz radiations, no phase information can be assessed.

Heterodyne detection

Heterodyne detection is another method providing phase information. With the help of a non-linear rectifying mixer device such as Schottky barrier diode (SBD), a hot-electron bolometer (HEB) mixer or superconductor-insulator-superconductor (SIS) tunnel junction mixer, the intermediate frequency (IF) can be obtained by multiplying the input signal and a closed spaced reference signal from a local oscillator. Finally, both amplitude and phase information of the input signal can be achieved. This kind of detection offers an extremely wide dynamic range and high signal-to-noise ratio while maintaining high-speed data acquisition, stable magnitude and phase measurements, room temperature measurement [47].

This is only a brief account of commonly used single detectors, a great deal of effort has been made to develop terahertz imagers with multi pixels. More information can be found in the thesis of J.-B. Perraud [48]. Figure I.5 depicts the progress of terahertz detectors over recent years, which gives a

comparison in terms of sensitivity between different types of detectors, including Micro-bolometer, CMOS based detectors, Schottky barrier diodes, pyroelectric detectors and Golay cells.

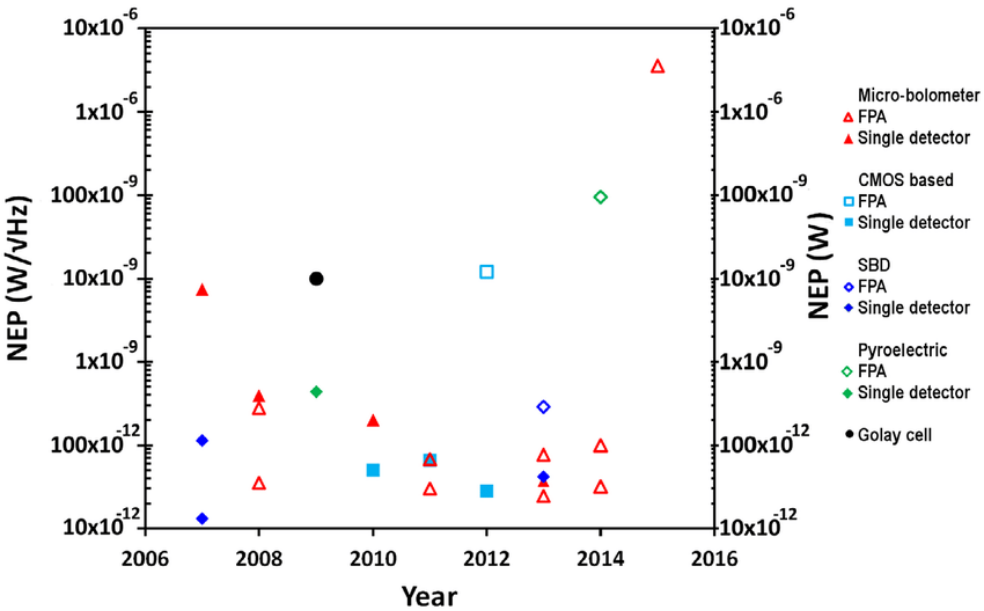

Figure I.5: Progress of terahertz detectors over recent years. It includes single detectors and the same technology-based focal-plane arrays (FPAs).

I.2.3. Terahertz measurement systems

All terahertz measurement systems consist of three types of components: a source to generate terahertz radiations, a detector to receive signals, and passive devices to control the propagation behaviors of the terahertz beam. Similar to the terahertz sources and detectors, passive terahertz components, such as quasi-optics, waveguides [49], filters [50], absorbers [51] and antennas, benefit from both well-developed technologies in microwaves and infrared frequency bands. In particular, quasi-optical components including lenses, parabolic mirrors are the most frequently used components in a terahertz measurement system. They are deployed to manipulate a terahertz beam (propagation direction and beam width) in free space. By collimating terahertz radiations out of an emitter, the losses related to the divergence in free space can, to a large extent, be reduced. In addition, a focused beam with a reduced size permits to obtain a better resolution for imaging applications.

A terahertz measurement system can be established either in transmission mode or in reflection geometry. Typically, transmission system configuration is preferred due to its simplicity. As shown in Figure I.6 (a), a terahertz emitter and detector are placed on each side of a sample. After being focused by lenses or parabolic mirrors, the terahertz beam with a reduced size passes through the sample. The transmitted signal is then collected and detected by the detector. This classical measurement setup is suitable for most applications. However, depending on the properties of sample and measurement conditions in a practical application, reflection configuration remains compulsory. The coating inspection for automobile is a good example, which is impossible to perform a transmission measurement due to the metal substrate. In fact, absorptive, thick samples or objects on a metallic substrate can easily exceed the limits of the measurement capacity of the system in transmission geometry. In these cases, a reflection configuration is more convenient. Since the sizes of terahertz emitter and detector cannot be ignored for device arrangements in a reflection configuration, a small

incident angle reflection setup (depicted in Figure I.6 (b)) is commonly applied to avoid the congestion issue of terahertz devices. Compared to a transmission geometry, the propagation paths of the terahertz beam in reflection mode are more complicated and optical alignment has a significant influence on the system performances. Otherwise, an alternate option is to implement a normal incidence reflection measurement (illustrated in Figure I.6 (c)) with a beam splitter or couple, which allows retrieving the reflected signal from the emitted beam.

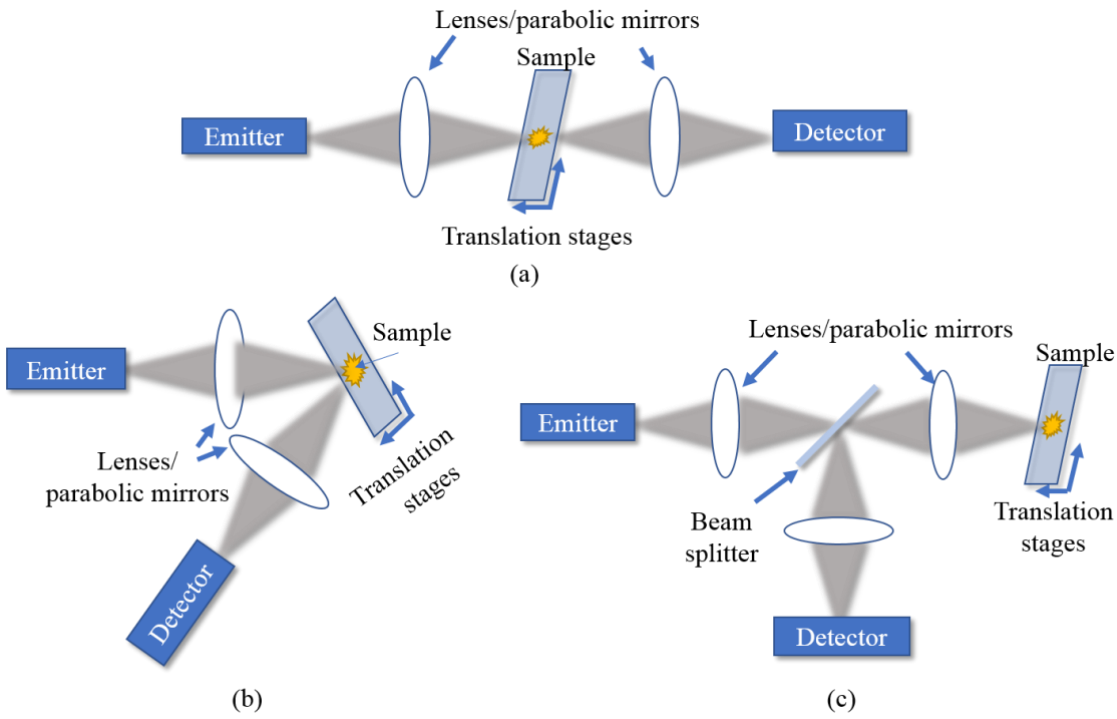

Figure I.6: Terahertz measurement systems (a) in transmission mode, (b) and (c) in reflection geometries. To avoid the space congestion issue between the emitter and detector, measurements in reflection mode can be performed with a small incident angle (b) or a normal incidence with a beam splitter or coupler to separate the incident and reflected signals (c).

Based on the above-mentioned configurations, a terahertz measurement system in pulse mode or CW/FMCW mode [52]–[54] can be established by choosing a suitable source and detector. Figure I.7 depicts a Time Domain Spectroscopy (TDS) system in transmission, which is composed of a near-infrared femtosecond pulsed source, a coherent detector and dedicated quasi-optics. By means of lenses or parabolic mirrors, a broadband pulse signal is focused and directed towards a sample. After that, terahertz radiations interact with the sample, the transmitted time signal is recorded for further analysis in the frequency domain. Since both amplitude and phase information can be achieved from recorded signals, the complex refractive index of the sample, that governs propagation within the object, can be obtained [55]. Specific characteristics in the spectrum enable the analysis or identification of materials. In addition to terahertz spectroscopy, terahertz imaging can also be performed with a TDS system setup. Instead of measuring at a single point, a raster scan in the targeted area is performed. The time signal at each point forms one pixel, and recorded signals over the entire area constitute a pixelated map containing sample information. Depending on the objective of the application, suitable parameters are selected to construct images with the desired information.

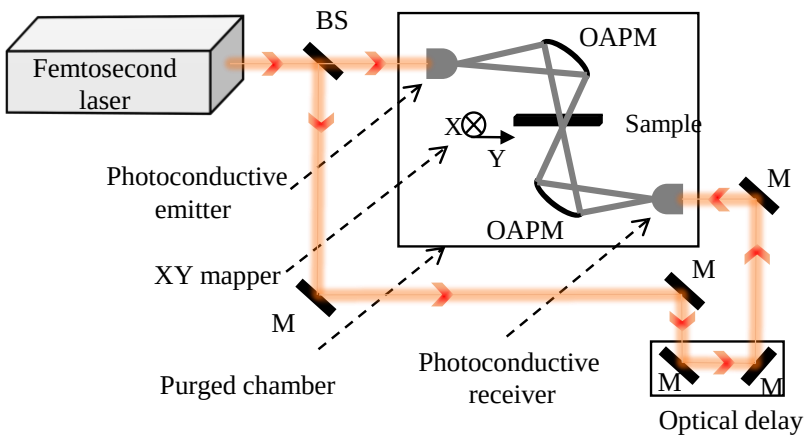

Figure I.7: Typical THz-TDS transmission setup. (OAPM: off-axis parabolic mirror, BS: beam splitter, M: mirror.) A femtosecond laser is used to excite and gate photoconductive antennas to generate and to detect terahertz waves. OAPM is employed to focus the terahertz beam on the sample.

I.2.4. Developments of optical-pumped pulsed transceivers

The importance of a reflection-mode system setup in a practical application has been emphasized in the review about the development of terahertz system configurations. However, two distinct devices, namely a source and detector, may impose space constraint between themselves. A beam splitter or a coupler is required to separate the incident beam and the reflected one. Over the last two decades, terahertz transceivers have attracted increasing attention with their compact size and excellent performances. A terahertz transceiver is defined as the device which integrates an emitter and receiver for signal generation and detection. The use of them allows simplifying the system setup in reflection geometry by removing the beam splitter. Two different types of terahertz waveguides are involved in this present work: pulsed ones and CW/FMCW ones. While the advance of the optical-pumped transceivers is given in the following part, the working principle of FMCW transceiver units are explained in Chapter II.3.1.

Although the concept of terahertz transceiver in pulse mode exploiting photoconductive antenna has been proposed [56] since 2000, it remains a poorly-studied research topic. Their broad frequency band is advantageous for a THz-TDS measurement. Studies concerning terahertz PCA transceivers can be divided into three types: single-PCA transceiver, double-PCA transceiver, and integrated transceiver module. While the two former types of transceivers have only one chip, the latter type integrates two distinct modules to form one device.

A single-PCA transceiver was firstly proposed by Tani *et al.* in 2000 [56], in which a PCA was used to transmit as well as to receive terahertz signals. Since the emitted terahertz beam was modulated by a chopper at a specific frequency, the photocurrent induced by reflected terahertz waves could be extracted from the photocurrents associated with the DC field during the generation process. Several years later, this PCA transceiver was implemented in a reflection system configuration for tomography measurement [57]. However, the background noise related to DC bias voltage resulted in a low signal-to-noise ratio. In 2003, a compact fiber-coupled single-PCA terahertz transceiver head was reported [58]. Compared to a free-space THz-TDS system, this transceiver head allowed a flexible operation thanks to the fiber-coupler PCA design [59]. SNR was as well improved to 40 dB at 300 GHz with a reduced optical beam power. In 2014, another single-PCA transceiver head based on the modulation of

optical pulses was introduced [60]. This transceiver head system operated at the telecom band (at 1.5 μm). Instead of mechanical chopping, optical pulses for generation and detection were modulated at different rates. It moved a step closer to achieve the goal of a compact and flexible terahertz measurement system.

To circumvent the noise issue occurring in a single PCA transceiver, Tani *et al.* proposed a transceiver with two spatially separated PCAs on the same chip in 2002 [61]. This terahertz transceiver achieved an SNR around 200 with a spectral peak located at around 100 GHz. In 2015, a Korean research team introduced an optical fiber-coupled double-PCA terahertz transceiver, which was aimed for *in-situ* biomedical measurement. The bandwidth of detected reflections from the metal was up to 2 THz, and an SNR of 1000:1 was achieved [62]. Although it is possible to introduce this optical fiber-coupled PCA transceiver inside the body, the danger related to the bias voltage (9 V) in the body cannot be ignored. Consequently, it was eventually unsuitable for in-vivo diagnosis. In 2016, a double-PCA terahertz transceiver with better performance (4.5 THz bandwidth and 70 dB dynamic range) was reported by Globisch *et al.* [63]. It was based on mesa-structures of beryllium-doped InGaAs/InAlAs multilayers PCA technology [43], [24], implying a lower cost for fiber laser source (well-developed fiber laser in the telecom band). The optical coupling between two PCAs and two individual polarization-maintaining fibers was realized by polymer waveguides on the chip. Therefore, the use of this fiber-coupled transceiver is no longer limited by the position of the laser source, providing more conveniences in practical use.

Meanwhile, the development of conventional PCA modules contributes to the advances of the transceiver. In 2009, a miniaturized optical fiber-coupled terahertz endoscope system with a front view of 8 x 6 mm² was reported, which consists of two distinct photoconductive generator and detector modules [64]. Less interferences between the emitter and detector are induced while taking advantage of the great performances of two separate modules. However, it should be pointed out that despite the reduced volume, the distance of 4 mm between the emitter and detector cannot be ignored when the size or the feature of the sample is comparable. It means that the resolution of a transceiver is limited for imaging applications. Table 2 below provides a comprehensive view of all aforementioned transceivers, includes their operation conditions, the shortcomings as well as the advantages. Since no beam splitter is required to separate the terahertz beams, transceivers can largely simplify the reflection-mode configuration. While a single-PCA transceiver has an easy optical coupling, a double-PCA transceiver can to a large extent mitigate the noise issue. While transceivers composed of two individual modules benefit the excellent performances of separate emitter and receiver, their resolution is limited by their proper size.

TABLE 2. OPTICAL-PUMPED TRANSCEIVERS

Transceiver Principle	One photoconductive antenna acting as both emitter and receiver			Two integrated individual module	Double PCA on the same substrate		
Year	2000	2008	2014	2009	2002	2015	2016
Modulation	Terahertz beam at 453 Hz		Optical pulses at different rates	Bias voltage at 500 Hz	Laser beam at 130 Hz	Terahertz beam	No lock-in detection was used.
PCA	LT-GaAs	LT-GaAs	LT-InGaAs/InAlAs heterostructre bowtie PCA	High resistivity GaAs & LT-GaAs	LT-GaAs dipole PCA x2	LT-GaAs dipole PCA x2	Be-doped **InGaAs/InAlAs** mesa-PCA x2
Laser beam	800 nm	800 nm	1550 nm	800 nm	800 nm	800 nm	1550 nm
Optical coupling	Free space	Fiber-coupled	Fiber-coupled	Fiber-coupled	Free space	Fiber-coupled	Fiber-coupled
Pulse width	120 fs		100 fs	70 fs	100 fs	90 fs	100 fs
Repetition rate	86 MHz		100 MHz	83 MHz	76 MHz	73 MHz	100 MHz
Optical power	20 mW	0.6 mW	25 mW	12 mW(emitter) 6.8 mW(receiver)	10 mW (E) 7 mW (R)	12 mW (E) 10 mW (R)	20 mW each respectively
Bias voltage	9 V	20 V		90 V	9 V	9 V	35 V
Size of housing/module		26 x 27 x96 mm housing		Cross section (2x4 mm)x6 mm	26 mm in diameter	5 mm in diameter	25 mm in diameter
2 PCA separation	\			3 mm, 20 °	500 µm	250 µm	45 µm
Performance **Frequency** **Bandwidth** **SNR**	SNR~200	SNR ~40 dB at 300 GHz	BW of 500 GHz with an SNR ~ 40 dB within a distance 18*2 cm.	Face to face: 6.2 nA peak to peak amplitude of Terahertz signal, bandwidth up to 2 THz	Spectral peak at frequency 100 GHz SNR~200with a round-trip path 45 cm	Frequency reaches up to 2 THz with an SNR ~1000. (Reflection from metal)	Bandwidth of 4.5 THz with a peak dynamic range larger than 70 dB
Advantage	Simplifying system set up, especially for reflection mode						

&	✓ Simple optical coupling • Limited bandwidth and dynamic rang due to the noise induced by bias voltage and laser beam			✓ Simple concept	✓ Reducing the noise in detected signal induced by the bias voltage of emitter and laser beams thanks to the spatial separation of two PCAs • Resonance & unwanted crosstalk between two PCAs		
		✓ Allowing for a flexible operation				Allowing for a flexible operation	
Shortcoming		✓ Reduced the need of laser power thanks to the improved optical coupling efficiency	✓ No require external chopping, more compact	× High bias voltage prevents the use in vivo	× Large background noise when the pump beam is chopped Alignment	✓ Better SNR, smaller size	Fiber laser in Telecom band frequency Fast data acquisition No lock-in detection was used
Refs.	[56]	[65]	[60]	[64]	[61]	[62]	[63]

I.3. Terahertz waveguides

The development of terahertz devices and system configurations have been briefly presented previously. In particular, terahertz transceivers (optical-pumped type) was reviewed owing to their potential to the simplify the system setup in reflection mode. To prompt the progress of the terahertz science and applications, it is also crucial to develop low-cost terahertz waveguides with high performances. In this part, an overall account of the advances in terahertz waveguides and reported applications is provided. The state-of-the-art about waveguides is divided into two parts: metal waveguides and dielectric waveguides. In addition to the working principles of different types of waveguides, their respective performances (advantages and disadvantages) are discussed. Considering the eventual use of waveguides in the present work, planar waveguides are not reviewed thoroughly here. Nevertheless, their potential and importance in an integrated circuit is worthy of attention.

As shown in Figure I.8, current terahertz waveguides are either scaled-down versions of metallic waveguides or upscaled versions of optical fibers [66]. While the structure of a waveguide can be adapted to the wanted operating frequency band, the host material loss of a terahertz waveguide remains problematic. Indeed, the material absorption of waves in dielectrics and ohmic loss in metals are not negligible in the terahertz band, which limits performances of terahertz waveguides. It should be pointed out that a long-distance transmission of terahertz waves through a waveguide in an analogous manner to the transmission via an optical fiber, is not yet realizable. The current studies and works are focused on the utilization of terahertz waveguides for sensing and imaging applications.

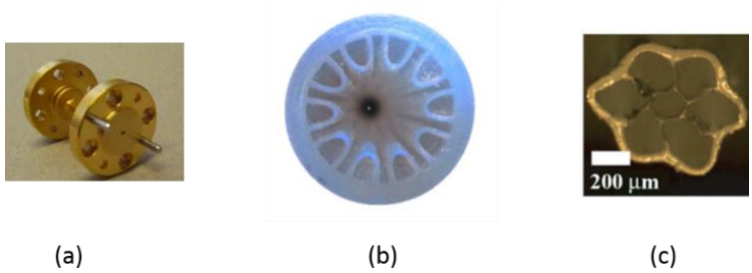

Figure I.8: Photographs of different types of terahertz waveguides. (a) Metallic rigid rectangular waveguide (WR-3 band). (b) 3D printed dielectric waveguide. (c) Dielectric porous waveguide.

I.3.1. Metallic terahertz waveguides

The review on metallic waveguides is separated into three parts: rigid metallic waveguides, metal wires, and finally other waveguides that do not fit in the previous categories. The reported studies that exploit metallic waveguides for sensing purposes are revised, with a particular focus on the coupling issues occurred in applications.

I.3.1.1. Rigid metallic waveguides

Rigid rectangular waveguides, belonging to metallic terahertz waveguides, are the most commonly used components in solid-state devices. By scaling down their sizes, rectangular waveguides can operate at frequencies above 1 THz. For example, a WR-1.0 waveguide with internal dimensions of 0.254*0.127 mm² has an operating frequency region from 750 GHz to 1100 GHz. They are commonly used as the output component in fast electronic devices, allowing the connection with the waveguide-based antenna or probe. The high-frequency on-wafer probe is a good example, in which a

rectangular waveguide is employed as a housing structure, connecting the vector network analyzer (VNA) extender and samples on a wafer. Rigid metallic waveguides have also been exploited for sensing purposes. Figure I.9 (a) shows a millimeter reflectometry system aimed for skin burns diagnosis which consists of a vector network analyzer (VNA) and an opened-end rectangular waveguide probe [67]. With the help of a scanning platform, the feasibility of millimeter-wave imaging at V-band frequency was demonstrated. In 2012, a K-band (18-27 GHz) FMCW radar sensor aimed for position detection of a piston was demonstrated by exploiting a circle waveguide inserted in a hydraulic cylinder (illustrated in Figure I.9 (b)). By analyzing the reflections from the liquid surface in specific guided modes, the position of the piston with an accuracy better than 200 µm was achieved [68].

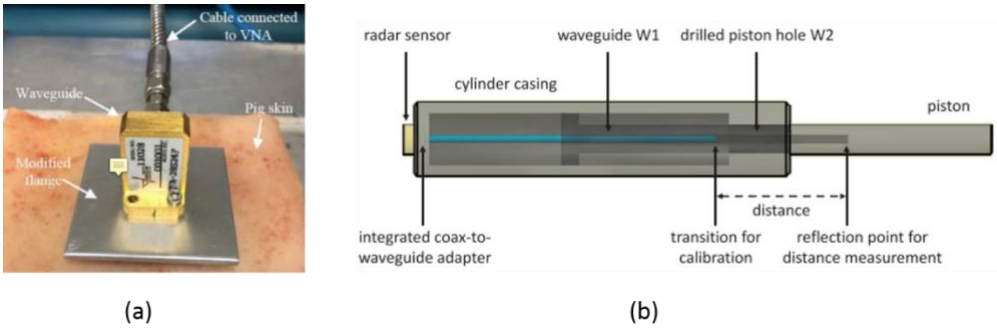

Figure I.9 : (a) Millimeter-wave reflectometry used for the investigation into skin burn injuries [67]. (b) FMCW radar in oil-filled waveguides for position detection [68].

Although millimeter/submillimeter hollow-core rigid waveguides benefit the sensing and imaging applications, their wider use in diverse systems is restricted. In fact, the operating frequency of a waveguide depends on its internal dimension. The micrometer-scale machining technique is required to manufacture high-frequency waveguides, resulting in two main issues: increasing fabrication cost and coupling difficulties. Besides, losses in metal due to the finite conductivity and skin depth (which is inversely proportional to the square root of the frequency and it may cause more Joule losses) become more significant at high frequencies. Although their enclosed structure can prevent from perturbations arising from the outside, there are few flexibilities to adapt to different applications during the measurement.

I.3.1.2. Metal wires

Metal wire, another type of metallic waveguide, was firstly studied by G. Goubau [69]. Due to the finite conductivity of the metal, guided waves are loosely confined around the wire's surface, they are also called Sommerfeld waves. Over the last fifteen years, many investigations into their frequency-dependent characteristics [70], guiding properties [71], [72] and radiation patterns [73] in the terahertz band have been conducted. It has been revealed that metal wires exhibit low-dispersion, which makes them a good option for broadband signal transmission (*e.g.*, a pulse signal transmission in a TDS system). Nevertheless, it has also been reported that most of the guided waves are weakly confined around the metal surface, and a majority of the guided power propagate in free space. The guided waves are prone to disturbances in the surrounding environment and a smaller curve depth may cause an important bending loss. To address this problem, dielectric coating [73] wires and double-wire waveguides [74], [75], were proposed to enhance the field confinement and to decrease the bending loss.

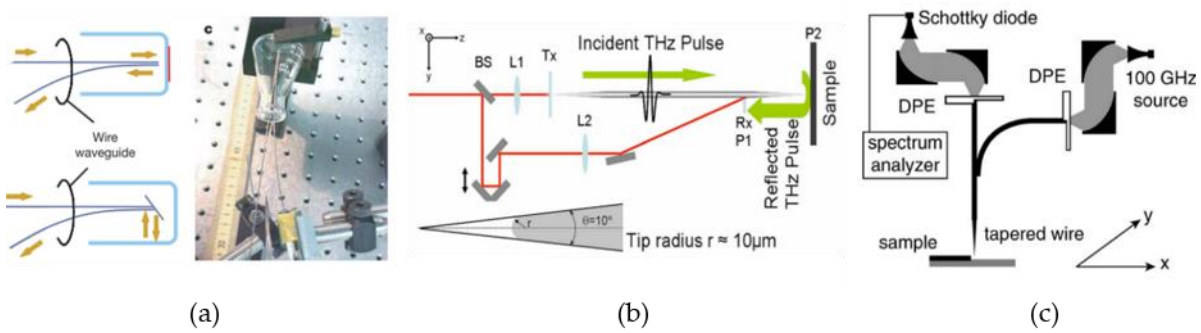

Figure I.10: (a) Terahertz endoscopy experiment setup using a metal wire [76]. (b)Near-field imaging setup using a tapered Sommerfeld wire [77]. (c) Continuous-wave near-field imaging setup using tapered wire as a probe [78].

In 2004, K. L. Wang and D. Mittleman successfully demonstrated the first proof-of-principle experiment of terahertz endoscopy using metal wire as waveguide [76]. As depicted in Figure I.10 (a), the incident pulse signal was first coupled into a wire and then reflected by the metal placed at the bottom of the container. The reflected signal was guided back to the detector through a second wire. After that, further work was carried out to investigate the guiding properties and different applications of metal wires. The tapered metal wire has drawn considerable attention due to its great confining capacity displayed at the tip. As illustrated in Figure I.10 (b) and (c), tapered wires were deployed as near field probes in conjunction with a pulse and continuous signal respectively. By exploiting the former setup in pulsed mode (shown in Figure I.10 (b)), two 20 µm width straight metal lines with a separation of 80 µm on a GaAs substrate were spatially resolved [77]. Using a CW signal of 100 GHz, the latter setup gave rise to a λ/33 subwavelength resolution [78].

Coupling issue

Possessing radial polarization, the Sommerfeld propagation mode is difficult to be excited efficiently by a linear terahertz source. Many studies have been performed to improve the coupling efficiency. They can be divided into two categories: (i) the one that uses supplementary components to improve the coupling efficiency with a linearly-polarized beam; (ii) the one providing a radially polarized incident beam.

Figure I.11 provides two experimental setups using the first method. As illustrated in Figure I.11 (a), Mittleman *et al.*[76] implemented two metallic perpendicular wires to couple linearly polarized beam into an aimed metal wire. Then in 2005, corrugated grooves on the metal wire, shown in Figure I.11 (b), were directly used to couple linearly polarized signals [79]. By varying the geometry and number of grooves, the waveform, the central frequency, and the linewidth of coupled surface waves were controlled. For a single continuous wave signal, a single discontinuities phase element (shown in Figure I.11 (c))was reported to be able to couple efficiently freely propagating waves into the wire with a coupling efficiency up to 23 % obtained at the frequencies of 100 GHz and 300 GHz [80].

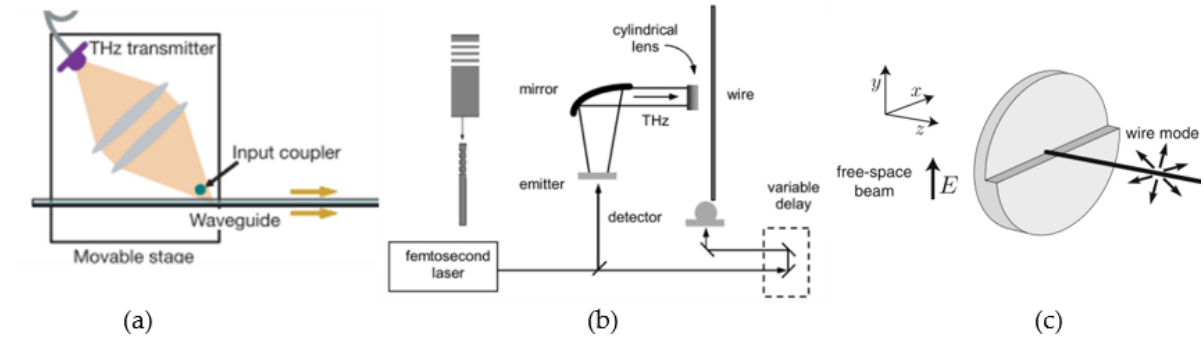

Figure I.11: (a) Dual-wire coupling configuration used in the proposed terahertz endoscope system setup [76]. (b) Experimental setup using milled grooves on a metal wire to couple incident radiation to a propagating surface wave [79]. (c) Differential phase element, used to improve the coupling efficiency between the linearly polarized beam and Sommerfeld waves on the metal [80].

Terahertz sources with radial polarization were proposed and tested as the second approach to dealing with the coupling issue. In the article of [81], instead of a dipole or striplines, radially symmetric contact geometry was deposited on the transmitter chip. The simulation results showed that compared to the dual-wire coupling method, the radially symmetric emitter antenna could improve the coupling efficiency from 0.4 % to 50% at a frequency of 100 GHz. Radially symmetric PCA design was also reported by D. Grischkowsky *et al.* [82]. In addition to radial PCA, a conical wire tip was placed 5 µm away from the transmitter chip (illustrated in Figure I.12 (a)) to optimize the terahertz coupling. The experimental setup based on a similar concept was depicted in Figure I.12 (b) [70]. After that, a tapered wire was frequently used to improve the coupling efficiency or to probe the sample in the near-field due to its enhanced field confinement in the vicinity [83], [84]. In addition to PCA, the optical rectification effect allows as well for the generation of the terahertz wave generation. Segmented non-linear crystals with three rotational symmetry (GaP (111) plate reported in [85]) and half wave-plate mode converter [86] were proposed to generate a broadband terahertz cylindrical vector beam polarized terahertz beam. The second method using a mode converter was demonstrated to achieve a total coupling efficiency of up to 16.8 %.

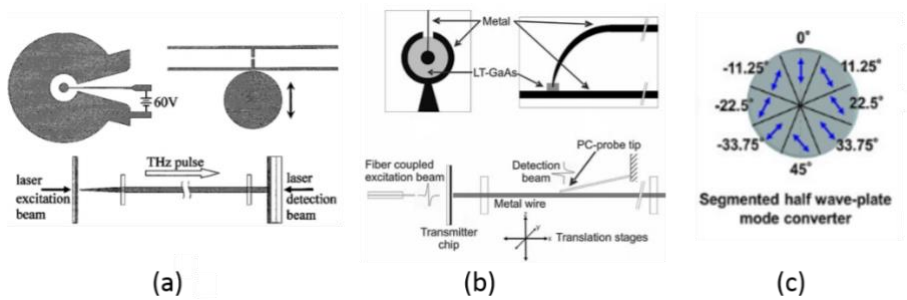

Figure I.12: Different methods to improve coupling efficiency. (a) Experimental setup including a metal wire as the waveguide, a transmitter with radial symmetric contact geometries, and a receiver [82]. (b) Experimental setup to forward a pulse signal along the metal wire, including a radical symmetric PCA transmitter and a PC-probe [70]. (c) Segmented half wave-plate (HWP) mode converter, consisting of eight pieces of HWP for controlling the spatial polarization mode of the incident laser beam [86].

In summary, a metal wire is an appealing choice for the transmission of a broadband signal thanks to its low-dispersion guiding property. Although the coupling efficiency is low due to the mismatch between the radial polarization of Sommerfeld mode and the conventional linearly polarized source, different methods have been proposed to address this issue. Depending on the selected source, metal wire can be used to forward a pulse signal and contribute to a high-resolution near-field measurement.

I.3.1.3. Other metallic waveguides

Apart from metal wires, parallel-plate waveguide (PPCW) exhibits alluring propagation properties for broadband signal transmission [87]–[89]. Since the fundamental mode in a PPCW is the quasi-TEM mode, there is no cut-off frequency. Moreover, the required polarization condition (perpendicular to the direction of two plates in PPCW) can be easily obtained by a conventional terahertz source. It allows a low-loss, low-dispersion propagation for a broadband signal. In order to improve its field confinement power, a tapered PPCW was proposed [90]. A spatial feature of 100 µm on a GaAs substrate was identified by using a tapered PPCW with a separation of 20 µm as a line-illumination probe for near-field inspection [91]. This study enlightened the potential of tapered PPCW in near field measurement. Nonetheless, the high-resolution power of PPCW exists only in one direction (normal to the plates), and the tapered air-gap structure is not easy to implement and hold, which make them impractical for applications outside of laboratory. Some other studies focused on the coaxial cable owing to its quasi-TEM mode [92]. However, higher modes can be easily excited by a linearly polarized pulse source. The signal distortion associated with multi-mode propagation complicates the interpretation of the transmitted signal, restricting its use in the terahertz domain.

Aside from these discrete wave-guided structures, planar transmission lines such as microstrip line, CPW (coplanar waveguide) [93] are largely used in the integrated circuits for high-frequency signal transmission. They have attracted considerable attention due to their essential role in high-speed integrated systems and devices [94]. Surface plasma polariton (SPP) propagation is another highly-concerned topic owing to its quasi-zero dispersion transmission capacity for broadband pulse signal and the excellent ability to confine the electric field. On the one hand, the coupling between a transmission line and a source can be carried out directly by a contact thanks to the loosely confined field around the transmission line and the substrate. On the other hand, guided waves are easily prone to the disturbances in the surrounding environment. Besides, the coupling efficiency out of a planar waveguide to interact with a sample remains problematic. Although a planar waveguide is not optimized for remote sensing applications, it shows excellent potentials for further developments of microstructure sensor and on-wafer measurement. If a full integration of a sensor system consisting of a transceiver and a waveguide is desired, the knowledge about planar waveguide is hence of paramount importance.

To sum up, previously-mentioned metallic waveguides possess their respective advantages and shortcomings. According to the used source, the polarization condition, difficulties of implementation and the dimension of the structure should be taken into consideration to select a suitable waveguide for wanted application.

I.3.2. Developments of dielectric waveguides

In addition to metallic waveguides, various dielectric waveguide designs are proposed and applied in the terahertz region. Most of the dielectric terahertz waveguide designs originate from the optical domain. Their structure can be solid-core, hollow-core, or porous-core. According to the guiding mechanisms, these waveguides can be classified into three types: total internal reflection waveguides, photonic microstructured waveguides and antiresonant reflection waveguides. In the following parts, the review about dielectric waveguides are separated into two main parts: (i) waveguide exploiting total internal reflection (TIR) or modified total internal reflection (MTIR), and (ii) hollow-core waveguides capitalizing on photonic bandgap or anti-resonant reflections. Not only their guiding properties but also

relevant sensing and imaging applications are reviewed to provide necessary reference information. That aims to help to select a suitable waveguide for the guided terahertz reflectometry system.

It is worth noting that although optical waveguide designs can be applied in the terahertz band, silica as the most frequently used material in the optical domain, possesses a significant material loss in the terahertz band. Compared to fused silica exhibiting an absorption coefficient of around 2 cm^{-1} [95], the absorption of PTFE (polytetrafluoroethylene, also called Teflon), and COC (cyclic olefin copolymer, also called as Zeonex /TOPAS) [96] are less than 0.9 cm^{-1} and 0.3 cm^{-1} at frequencies below 1 THz respectively [97]. Consequently, low-loss polymer materials such as HDPE (high-density polyethylene) [98], PTFE and COC are preferred for the fabrication of waveguide geometries.

I.3.2.1. (Modified) Total internal reflection waveguides

As the most classic design, a step-index optical fiber exploits total internal reflection occurring inside the high-index core as the guiding mechanism. If the normalized frequency (V number) is below 2.405 [99], a single-mode propagation can be obtained along a step-index waveguide. The concept of total internal reflection is then adapted in the terahertz region, giving rise to microwires, solid-core microstructured waveguides, and some porous-core waveguides.

Microwires

Dry air, regarded as the only terahertz ‘transparent’ material, has attracted full attention to achieve a low-loss terahertz waveguide. By increasing the guided power fraction in the air, less attenuation takes place in materials. In 2000, the propagation of a sub-ps pulse along sapphire fibers with a diameter of several hundreds of µm in HE_{11} mode [100] was firstly reported. In the same year, a plastic ribbon waveguide with a thickness of 120-150 µm [101] (in TM_{01} mode) was displayed. In 2006, a PE fiber with a core diameter of 200 µm was demonstrated with a propagation loss of less than 0.01 cm^{-1} at the frequency of 300 GHz [102]. Each of these three aforementioned waveguides has a subwavelength dimension, and most of their guided electric field is in the surrounding air, which contributes to the decrease of the absorption during the propagation. The waveguide exhibiting similar features is named as microwire. The subwavelength dimension of the waveguide gives rise to great flexibility, showing significant advantages in practical applications. For instance, a 180-µm-diameter PE wire was implemented in a transmission scan system as an imaging probe [103] so that the displacement of the sample is no longer required during the scan. In 2009, a terahertz fiber-scanning near-field microscopy, compatible with an optical microscope, was reported [104], in which a 240-µm-diameter PE fiber was utilized to send generated signals from the source to the bull’s eye structure. The property of being highly sensitive to the surrounding conditions can also be exploited for sensing purposes. The liquid detection by using a 300-µm-core-diameter PS wire was a good demonstration [105]. Nevertheless, microwires display some disadvantages due to their extended electric field. They are more prone to the perturbations such as bends, discontinuities, or fluctuations occurring in the surrounding. Additionally, the handing equipment of waveguides without impacting the guided signal remains problematic. For a practical guiding of terahertz waves, suspend core subwavelength fibers were reported in 2011 [106], and 0.02 cm^{-1} propagation loss was achieved.

Solid-core microstructured waveguides

Solid-core waveguide exploits modified total internal reflection (MTIR) as a guiding mechanism. Indeed, thanks to microstructured cladding composed of air-holes, the effective index of

the cladding is lower than the index of solid-core, meeting the MTIR condition. In 2002, an HDPE solid-core microstructured waveguide was firstly demonstrated in the terahertz band [107]. This study indicates that the propagation loss of a solid-core microstructured waveguide is mainly impacted by the host material and field confinement in the structure which is related to the index contrast between core and index (effective index). By using a lower refractive index material Teflon ($n_{Teflon} < n_{HDPE}$), the absorption loss of the microstructured waveguide has been reduced to 0.12 cm^{-1} for 0.1-1.3 THz [108]. In 2011, a microstructured waveguide using COC as the host material was reported to achieve a low absorption (< 0.1 cm^{-1} around 300 GHz) while keeping good field confinement [96]. Both analytical field models and numerical simulations [109],[110] were deployed to investigate the propagation characteristics of such type of microstructured waveguide, providing valuable information for waveguide's design with a deeper understanding of propagation modes. Apart from microwires and solid-core microstructured waveguides, there is another type of subwavelength waveguide taking advantage of total internal reflection: low-index discontinuity terahertz waveguides [111], which can provide high confinement at the low-index discontinuity area. In summary, by taking advantage of different cladding structures, solid-core microstructured waveguides can achieve better field confinement inside the core, decreasing the influence from the outside of the waveguide.

Porous-core air-clad waveguides

Although solid-core microstructured waveguides provide better confinement inside the core than microwires, their propagation loss is still highly impacted by the host material. With the intention of reducing the propagation loss whilst keeping field confinement inside the core, relevant studies focus on microstructured waveguides with a porous-core. The porosity of a waveguide is defined as the ratio of air holes' surface to the core area, dictated by the distribution of subwavelength holes. By increasing the porosity of the core of waveguide, the absorption loss in the core can be lessened. In 2008, Hassani *et al.* proposed a low-loss porous terahertz waveguide containing multiple subwavelength air holes within a hexagonal array, revealing that the propagation loss can be reduced to 1/10 ~ 1/20 of bulk loss by an important porosity in the core [112]. In addition to circular air holes [113], rectangular and slotted-shaped air holes in a porous-core were also investigated by Atakaramians *et al.* [114], demonstrating that the effective material loss and group velocity of a porous-core waveguide are independent of the shape of the holes. Besides, this study indicated that a birefringence can be obtained by introducing asymmetrical air-holes structure. In 2009, spider-web and rectangular waveguides with a porosity of 57 % and 67 % respectively were fabricated by means of extrusion and drawing techniques[115]. The propagation losses of the rectangular-web waveguide were demonstrated to be less than 0.08 cm^{-1} in the frequency range from 0.2 to 0.35 THz [116] and birefringence of 0.012 at 0.65 THz was achieved. Dupuis *et al.* reported two PE porous-core subwavelength waveguides using two different techniques: stack-and-draw and subtraction technique. The latter methods need a sacrificial material (PMMA in the article), which is dissolved after the drawing process. The lowest loss of the reported subwavelength waveguide (a porosity of 40 % and a diameter 380 um) was 0.01 cm^{-1} at around 0.3 THz [117].

These proposed porous-core air-clad waveguides have a subwavelength/wavelength diameter (varying from 200 to 700 μm, depending on the proposed design). Compared to microwires, the propagation losses associated with material absorption are significantly reduced by increasing the guided power fraction in the air holes. However, few experimental investigations were conducted to study the field distribution and guided-mode across the waveguide and current fabrication techniques cannot guarantee the manufacturing quality.

Porous-core microstructured waveguides

Since 2011, dielectric waveguides with a porous-core and microstructured cladding has attracted increasing attention in order to develop a low-loss, broadband, flatted dispersion, single-mode waveguide. For instance, a porous-core honeycomb cladding waveguide was designed [118]and fabricated [119] by Nielsen.K and H.Bao. Thanks to the increased effective index of the core, the bandgap formed by the honeycomb cladding resulted in a broad bandgap. By employing drilling and drawing techniques, a flexible TOPAS waveguide with an outer diameter of 3.65 mm was fabricated. It was demonstrated that this waveguide exhibited low losses <1.5 dB/cm at the fundamental band of 0.75-1.05 THz (1dB/ cm in a 0.78-1.02 THz). Based on the same concept, the possibility to use honeycomb and Kagome lattice air holes for a broadband bandgap waveguide design was studied via a semi-analytical approach [120].

Over the last five years, more novel waveguide designs, aimed for a low-loss flattened-dispersion single-mode transmission, have been reported in the terahertz band, including the ones in the core-cladding structures of hexa-hexa [121], octa-octa [122], rotated hexa-hexa [123], hexa-ring [124], and hexa-Kagome [125]. Since a high birefringence of a waveguide holds particular interest for polarization-sensitive biological applications, substantial attention has been focused on the asymmetric core structure to achieve a high birefringence. For example, a waveguide design with a trip-holes unit in the core and hexagonal cladding structure [126] was reported to exhibit a birefringence at a level of 10^{-2}. Amongst all the relevant studies, the research team guided by M. Islam and D. Abotte makes continuous effort to explore the novel designs for the performance improvement, including the proposed hybrid core in 2017 [127] (rotated circular air-holes in an hexagonal arrangement and four supplementary air-holes to form a rectangular core structure), elliptical-shaped air holes core in the modified hexagonal arrangement in 2018 [128]. Their potential for sensing applications was demonstrated for alcohol detection by using the analysis based on numerical simulation [129]. They have also proposed slotted-shaped cladding with different core structures composed of rectangular holes [130] (for low dispersion) and elliptical holes [131] (for flattened dispersion and high birefringence). In particular, a hollow-core version of the slotted air-holes microstructured waveguide was demonstrated to enable a high sensitivity sensing application [132].

With the aim of reducing further the propagation loss, porous-core with subwavelength air holes have been considered, including air-clad and microstructured cladding waveguide. They have been demonstrated as an efficient solution to decrease the propagation loss and dispersion, to broaden the frequency band. Special porous-core designs exhibiting a high birefringence were as well reported. Their polarization-maintaining capacity is of great interest for biomedical applications. While field confinement is enhanced compared to the subwavelength waveguide, large dimensions of cladding (generally several cladding layers) make them inflexible.

Fabrication technique difficulties

It is notable that while a large number of novel designs of waveguide have been proposed, the investigations are limited via analytical methods or 3D full-wave simulation due to the lack of suitable efficient fabrication techniques for microstructured terahertz waveguides. Most of the used fabrication techniques for terahertz waveguides originates from the optical domain. They can be separated into two steps: the preparation of a preform and drawing. A preform of the waveguide can be carried out by the techniques, such as extrusion, molding, drilling or stack. Once the perform is realized with scaled-up

dimensions, it passes the next step of drilling with optimized manufacturing parameters, including drilling velocity and air/vacuum pressure. To decrease the propagation loss related to the material absorption, low-loss materials such as PTFE, COC are recommended as hold materials for terahertz waveguides, which is not compatible with the well-developed glass-based fabrication techniques used in the optical domain. In addition to the scaled-up size of terahertz waveguides, the complex structure with high air-filling, thin-wall capillaries features impose more difficulties on the fabrication process. The existing fabrication techniques cannot meet all the requirements for the high-quality production of terahertz waveguides. More efforts are needed in the domain to improve and to optimize the fabrication techniques. Within such a context, the 3D printing technique has attracted increasing attention in the terahertz domain, more details and discussion are given in Chapter II.5.

Conclusion

The main features of solid-core and porous-core with air-clad or microstructured cladding waveguides have been reviewed in this part. In regard to the microwires, their widespread field in free space causes the difficulties in holding the structure without disturbing the propagation mode. While solid-core microstructured waveguides exhibit better field confinement in the core, their propagation loss is strongly dependent on the absorption of host material. To achieve a better trade-off between the propagation loss and the field confinement, porous-core waveguides (both air-clad and microstructured one) have been proposed and tested. However, the existing fabrication techniques are not optimized for complex structure. The availability of terahertz waveguides with novel design is limited in certain laboratories and their quality cannot be guaranteed. To conclude, these dielectric waveguides provide different advantages, such as the propagation loss, the flexibility or the filed confinement. Depending on the targeted application and ued devices, each of them may provide different benefits.

I.3.2.2. Hollow-core waveguides

The major difficulty for terahertz waveguiding is the lack of low-loss materials. Since the most transparent medium for terahertz waves is dry air, hollow-core waveguides with various cladding structures have been studied to provide acceptable solutions by confining waves inside the air-core region. Compared to solid-core and porous-core waveguides, hollow-core waveguides inherently exhibit less loss related to the bulk material. The concept used in the optical domain, such as photonic crystal fiber (PCF), Kagome lattice, Bragg structures and anti-resonant reflecting structure, has been adapted in the terahertz band. Besides, different hybrid claddings were proposed to further lessen the loss during the propagation[133]–[135]. For instance, the absorption coefficient of a dual cylindrical metallic grating-cladding polymer hollow waveguide was reduced to 0.62 dB/m in 2010 [136]. In the following part, hollow-core waveguides based on the photonic bandgap and anti-resonant reflection are described subsequently.

Photonic bandgap waveguides

One part of hollow-core waveguides exploits the bandgap formed by the periodic cladding structure as the guiding mechanism. According to the crystal structure of the cladding, they can be divided into three types: one-dimension PCF, also called as omnidirectional waveguide or Bragg waveguide [137]–[139], two-dimension PCF [140] (composed of triangles air-holes in a hexagonal or octagonal arrangement) and three-dimension PCF (not yet applied in the terahertz domain). The waves cannot propagate in the cladding structure at frequencies lying in the bandgap. Instead, they are

restrained inside the air-core for waveguiding. By controlling the parameters of the periodic structure, the bandgap of the cladding, *i.e.*, the transmission window of the PCF, can be established in the desired frequency regions. Depending on the air-core mode, either a tightly confined mode or surface state of core mode can be obtained. The former mode is desired to achieve a low-loss, low-dispersion transmission. Nevertheless, this type of waveguide possesses a relatively narrow bandgap due to the guiding nature of photonic bandgap waveguides. At the border of the transmission window, the signal distortion becomes more significant owing to the dispersion, making them less attractive for broadband transmission. Similar to other microstructured waveguides, the lack of efficient fabrication techniques limits the development of terahertz photonic bandgap waveguides.

Anti-resonant waveguides

The anti-resonance effect has been proposed to guide the light since the *1980s* [141]. In the optical domain, this type of waveguide is called anti-resonant reflecting optical waveguides (ARROW). During the developments of integrated optics, the ones with rectangular cross-section were investigated [142]. Due to the simplicity, ARROWs with a simple capillary structure began to drawn attention in the visible frequency band [143], [144]. In 2008, ARROW-like mode was firstly reported in a study of an air-core microstructure fiber in the terahertz region [145]. One year later, a commercially available Teflon air pipe was first demonstrated as a low-loss anti-resonant terahertz waveguide [146], and an attenuation constant as low as 0.008 cm^{-1} was obtained. Given the simple structure (easily-fabricated) and low-loss guiding, more studies have been conducted to investigate its propagation properties and to explore its potential for diverse application. The working principle of the thin-wall hollow-core waveguide is described below.

Anti-resonant waveguides with negative curvatures is also one of the anti-resonant waveguide family. By controlling the structure parameters, *e.g.*, the form, size and number of negative-curvature, the wavenumber mismatch condition can be established so that the coupling between the core mode and cladding modes is prohibited. Compared to anti-resonant waveguides with a capillary structure, negative-curvature waveguides provide more possibilities to improve the propagation performances of a waveguide by manipulating the structure of the negative curvatures. More discussion is given in Chapter II.5 together with the 3D printing technique.

Thin-wall antiresonant waveguide

In 2010, Lai, C. *et al.* provided a more detailed study about the propagation properties of a thin-wall anti-resonant pipe waveguide, including the defined transmission bands and different modes, which were verified by the experimental results [147]. In 2011, a plastic and silica thin-wall plastic with a thinner wall were characterized over the frequency band from 0.3 THz to 2 THz [148], the anti-resonant effect was then corroborated by the corresponding transmission dips. Based on the same principles of ARROWs, a thin-wall hollow-core waveguide can transmit terahertz waves by taking advantage of the anti-resonant effect. As shown in Figure I.13, a thin-wall dielectric waveguide consists of two materials, a low-index core (n_1) and a high-index cladding layer (n_2) with a thickness of d. For the core-mode propagation, the high-index cladding acts as a Fabry-Pérot etalon. Depending on the properties of the cladding (material n_2 and thickness d), a high transmission through the cladding in the transverse direction can be obtained at specific frequencies which is due to the constructive interference of waves through two interfaces of the cladding at its resonant frequencies. Consequently, most of the emitted power leaks out from the waveguide at resonant frequencies, and core mode doesn't exist.

Otherwise, the majority of the transmitted power is reflected back in the core, giving rise to the confined air-mode at non-resonant frequencies.

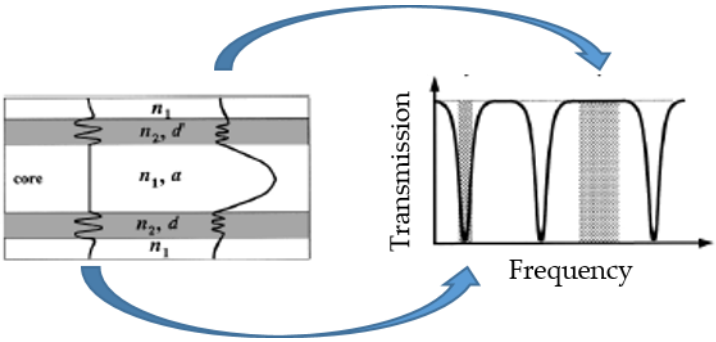

Figure I.13: Schematic diagram of a thin-wall waveguide exploiting the anti-resonant reflections as the guiding mechanism. At non-resonant frequencies, most of the incident power propagate inside the low-index core, resulting in a high transmission band. The resonant frequencies of the cladding correspond to the dips displayed in the transmission spectrum.

In regard to a dielectric hollow-core thin-wall waveguide, the low-index core is composed of the air (*i.e.*, n_1= 1). The characteristic frequencies of the cladding can be expressed as [149][148],

$$f_m = \frac{mc}{2d\sqrt{n_2^2 - 1}} \quad (5)$$

where c is the speed of the light in vacuum, m is an integer, d and n_2 are the thickness and refractive index of the cladding respectively. The resonant frequencies can be identified in the transmission spectrum of the waveguide as the repeated high-loss dips (seen in Figure I.13). Several transmission bands are determined by resonant frequencies. This spectral feature (repeated transmission dips) helps to recognize anti-resonant waveguides, confirming the guiding mechanism.

This kind of waveguide has been applied for powder and liquid-vapor sensing applications [150]. In 2011, B. You *et al.* has used the terahertz endoscope consisting of a pipe waveguide to identify molecular concentration and measure the surface of the object [151]. Several years later, the same concept was used to monitor a chemical reaction [152]. In 2019, thin-wall COC pipe waveguides with a wall thickness of 33-58.6 µm were reported, in which a minimum loss of 0.1 dB/cm is obtained for 1.05 THz [153]. It should be noticed that although the core diameter has no impact on the resonant frequencies, it plays an important role in determining the propagation modes and corresponding propagation loss.

To sum up, dielectric hollow-core waveguides are aimed for low-loss transmission by confining the guided power into the air core. In comparison to the hollow-core bandgap waveguides, the structure of the anti-resonant waveguide is much simpler. They can be easily fabricated with a low cost using different materials. The transmission bands can be determined by controlling the thickness of the cladding. A thin cladding can give rise to a wide bandwidth, beneficial for a broadband signal transmission. Since the diameter of an anti-resonant waveguide doesn't impact the resonant frequencies of the cladding, the size of the waveguide can be adjusted for a better coupling or the optimization of desired guided modes. Although hollow-core microstructured waveguides exhibit better field confinement in the core thanks to the periodic cladding, the fabrication techniques developed in the optical domain are not optimized for the theses waveguides made of polymers with high-air filling, complex cladding structure. Indeed, due to the lack of suitable fabrication techniques, most of the

investigations into the novel porous-core and hollow-core waveguide designs is limited to the simulation results.

I.3.3. Conclusion

A brief overview of terahertz waveguides, including metallic waveguides and dielectric waveguides, has been provided. While waveguides such as metal wires, coax cables, PPCW show great low-dispersion propagation properties, the hollow-core dielectric waveguide displays low-loss propagation and the microstructured waveguide possesses better field confinement. On the other hand, the main difficulty in using a metallic waveguide is its poor coupling efficiency and small structural dimension while the deployment of a dielectric waveguide is limited by their availability and holding issue without disturbing the guided signal. Their working principles, propagation losses, dimension of structure, coupling issue, fabrication techniques and corresponding applications have been reviewed thoroughly, offering valuable information to select a suitable waveguide to implement a terahertz wave-guided system later.

By taking account of all the parameters, thin-wall hollow-core waveguides have attracted attention in this present work due to their advantages over the other waveguides for the implementation of a terahertz measurement system with a transceiver. Their simple structure can be easily fabricated with a low-cost and their transmission properties can be controlled via the thickness and property of the cladding to match the selected source. Besides, the size of the air-core of a thin-wall hollow-core waveguide may facilitate the coupling task. In Chapter II.4, more details are given to justify the choice of the waveguides for a terahertz wave-guiding reflectometry system.

I.4. Terahertz applications

Two main terahertz techniques, namely terahertz spectroscopy [154] and terahertz imaging [155], [156], are deployed in diverse domains for different applications. Compared to the radiofrequency (RF) signal, terahertz radiations possess a much higher frequency band covering from 100 GHz to 10 THz. Thanks to the broad bandwidth, the exploitation of terahertz radiations in wireless communication allows an extremely high-rate data exchange (> 100Gb/s), which helps to meet the increasing need for high-speed signal transmission in the communication field [157], [158], [159]. Considering the absorption of water vapor molecules in the air, freely propagating terahertz waves can only transmit over a short distance. Based on this property, a concept of a secure indoor large capacity network communication was proposed [160]. Besides, the studies in this domain have prompted the development of ultra-fast electronic devices. More and more attention has been brought in this domain, offering a promising future of terahertz communication link.

With respect to low-loss non-polarized dielectrics such as cotton and carton, terahertz waves exhibit penetrating capacity. Besides, terahertz waves are non-ionizing sources, they pose no health risk for the people exposed to radiation. By taking these properties into consideration, terahertz waves have drawn considerable attention for public security applications [161], [6], [162]. As shown in Figure I.14 (c), terahertz radiations are deployed for parcel threats inspection, which allows to check the content of a package without opening it. Besides, terahertz technology also has been brought in industries as a complementary non-destructive testing technique for quality control, for example, in the wood industry, in the food package chain [163], [164], [165], and in the aeronautic industry (multilayer painting measurement shown in Figure I.14 (d)) [166], [167]. TeraCota sensor [168], a commercial system

developed by the company Teraview Ltd., exploits terahertz waves to examine the coating quality for automobile components. Moreover, painting restoration and art conservation (shown in Figure I.14 (b)) can benefit from the valuable information provided by terahertz technology [54] [169], [170].

As terahertz radiations excite the rotational or vibrational modes of molecules, they can be used to identify specific materials by their spectral features [154]. In particular, the possibilities to take advantage of terahertz waves to recognize explosives and illicit drugs [171], [172] have been investigated, showing therefore great interest to public security applications. Since terahertz waves are also sensitive to the intramolecular interaction, they are alluring for the pharmaceutical industry [173]. Attracted by the specific properties of terahertz waves, a large number of investigations have been conducted in the biomedical domain [174]. The potential of terahertz technology in clinical diagnosis, especially regarding tooth and skin diseases [175][176] have been demonstrated**.** The cancer diagnosis is another hot research topic in which terahertz radiations are expected to be able to distinguish between normal tissues and tumors. One of the final aims is to provide a supplementary tool to enhance the detection accuracy of tumor margin during cancer surgery [177]. More effort is being brought into the investigations in this research area [178], [179], [180].

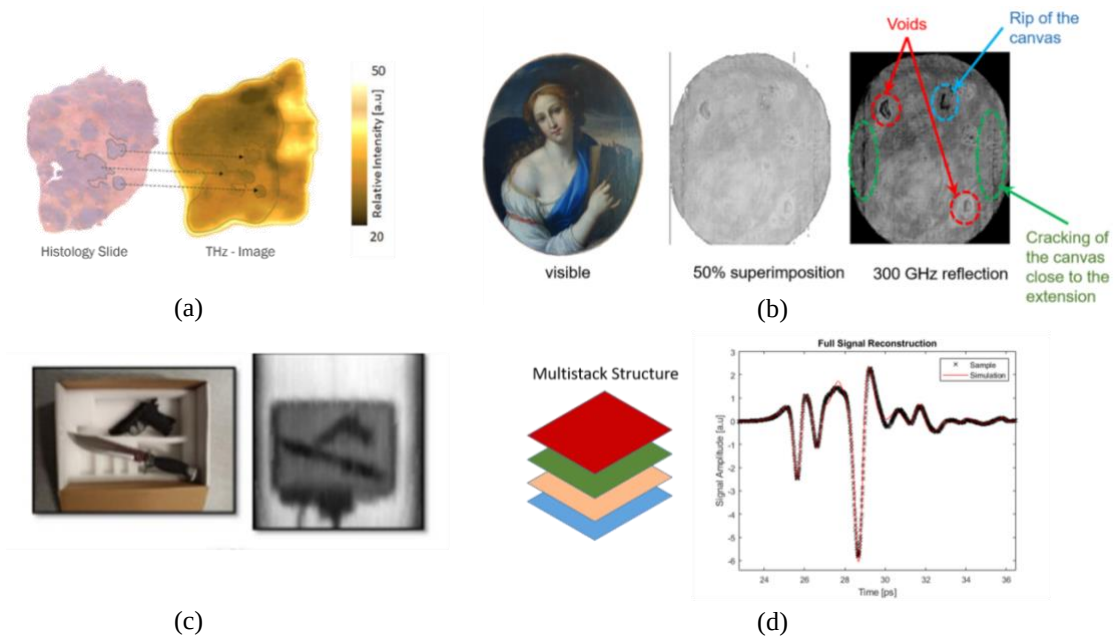

Figure I.14: Applications of terahertz technology. (a) Histology image and terahertz image of breast cancer tissue [177]. (b) Optical and terahertz images of an oil painting, the latter providing information for the art reconstruction (from [54]). (c) Image of weapons concealed in a box obtained in the terahertz band, benefiting the security inspection applications (from [6]). (d) Both simulation and experimental time responses of a terahertz pulse reflected from a multilayer structure, allowing for the material analysis (from [166]).

In addition to the development of terahertz sources and detectors, different configurations of terahertz measurement systems have been also reviewed. Apart from the studies in the wireless telecommunication field, terahertz techniques including terahertz spectroscopy and terahertz imaging have been applied in diverse domains for probing and sensing purposes. They are used as a non-destructive testing technique for quality control in industries. Besides, considerable attention has been drawn to terahertz radiations for the public security application and the biomedical application. Numerous studies have demonstrated the potential and advantages of terahertz radiations [46]. A promising future for terahertz technology can be anticipated, which will be further encouraged and pushed forward by the advance of technology.

I.5. Conclusion

While many domains have benefited from the existing terahertz technology, it is notable that the use of a terahertz system is still limited in practical use outside from the laboratory due to the size of the system and their requirements for a sample and measurement conditions. From a practical point of view, a compact terahertz measurement system in reflection mode rather than in transmission geometry is more advantageous. Indeed, a reflection-mode system demands few prerequisites on a sample, it can be used to measure a thick, absorptive sample with a metallic substrate. While a broader application scope makes systems in reflection-mode more attractive, the complex configuration hinders its development.

To address this issue, a terahertz transceiver together with a waveguide, has been investigated as an effective solution, during this present work, to construct a compact reflection system. Based on the review of the development of terahertz technology, three different transceivers and two waveguides are selected. Their performances are detailed in the following chapter.

Chapter II.

Terahertz wave-guided reflectometry qualification

II.1. INTRODUCTION **38**

II.2. DOUBLE-PCA FREE-LENS TRANSCEIVER PROBE **38**

II.2.1. Design of a double-PCA lens-free transceiver 39

II.2.1.1. 3D full-wave electromagnetic simulation 41

II.2.1.2. Experimental setup 46

II.2.1.3. Time-domain waveform characterization 48

II.2.2. Imaging capacity of double-PCA lens-free transceiver 51

II.2.2.1. Experimental setup 51

II.2.2.2. Image of vertical bars in group 1 54

II.2.2.3. Image of horizontal bars in group 1 60

II.2.3. Conclusion 61

II.3. TERAHERTZ FMCW RADAR TRANSCEIVER UNITS **61**

II.3.1. FMCW radar working principle 62

II.3.2. SynView FMCW radar module 63

II.3.3. Silicon radar chip 66

II.3.4. Conclusion 68

II.4. THIN-WALL HOLLOW-CORE WAVEGUIDES **68**

II.4.1. Fused silica hollow-core waveguide 70

II.4.2. Plastic thin-wall waveguide 73

II.5. 3D PRINTED NEGATIVE-CURVATURE WAVEGUIDE **75**

II.5.1. State-of-the-art of negative curvature waveguides 75

II.5.2. 3D printed fabrication techniques 77

II.5.3. 3D printed negative curvature waveguide 78

II.6. CONCLUSION **81**

II.1. Introduction

The advance of terahertz technology has been briefly reviewed, displaying the potential of terahertz systems in different domains. With the aim of extending the application scope of terahertz system, the present work focuses on the development toward a compact and practical reflection system by taking advantage of terahertz transceivers and waveguides. Indeed, a terahertz transceiver can replace two distinct devices source and detector, avoiding the space congested issues between them. Depending on the structure of a transceiver, optical components such as beam splitter is no more required to separate the incident beam and reflected signal, simplifying the system's configuration. Meanwhile, the guiding capacity of a waveguide allows it to transmit an emitted signal to the targeted position on the sample without any spatial requirements related to the opto-mechanical supports and working distance of optics. Since the structure of a waveguide indicates directly the propagation path, difficulties in alignment are also reduced in comparison to a conventional system using quasi-optical method.

Prior to the implementation of a terahertz wave-guiding reflectometry system, transceivers and waveguides with adapted performances should be selected and characterized separately. Three transceiver units operating in pulse mode and in FMCW mode (the latter two), namely double-PCA lens-free transceiver, 100 GHz SynView transceiver head and 122 GHz Silicon Radar transceiver chip, has been selected. Their working principles and performances are introduced in this chapter. In particular, being a novel design, the performance of double-PCA transceiver is few-reported in the literature. Consequently, one part of the present work is focused on the assessment of the imaging capacity of this pulsed transceiver probe.

The preliminary studies conducted in Chapter I.3 reveal that hollow-core anti-resonant waveguides are considered as a suitable candidate to construct a terahertz wave-guided terahertz reflectometry system with the aforementioned transceiver units. Two waveguides with different dimension have been selected. Their guiding capacity is verified by the transmission spectrum using THz-TDS system and the corresponding results are presented. As an innovate fabrication method, the additive manufacturing (3D printing) technique is introduced at the end, allowing a fast cost-efficient waveguide development chain.

II.2. Double-PCA free-lens transceiver probe

A terahertz transceiver allows simplifying the system setup in reflection geometry by replacing two distinct devices with one component. There is one common feature in the reviewed optical-pumped transceivers in Chapter I.2.4: a silicon lens attached on the backside of the substrate. This silicon lens contributes to an efficient emission of terahertz waves from the substrate into free space. More precisely, intrinsic properties of such a silicon lens allow to reduce the waves trapped in the high refractive index semiconductor layer (n = 3.5 for GaAs) by collecting and focusing generated terahertz waves. It gives rise to an emitted beam with a comparable size to the diameter of the lens.

Apart from large-aperture PCA, it exists a few PCA designs without lens. For instance, terahertz radiation directly into the air with no influence of the substrate was reported by using an integrated terahertz TEM horn antenna in 2007 [181]. Besides, a photoconductive free-space linear tapered slot antenna transmitter proposed in 2016 [182], which has applied a planar transmission line to radiate out waves efficiently into free space. Protemics GmbH company has developed different PCA microprobes

without silicon lens [41], [183] for near-field measurements. The long slim cantilever of microprobe gives them direct access to the vicinity of a sample for a low invasive near-field measurement. Under the same philosophy, a double-PCA transceiver probe was developed. Instead of a silicon lens, directional antennas on the transceiver are deployed to radiate out generated signals into free space and to detect the reflections. This double-PCA lens-free transceiver with a miniaturized dimension allows a direct coupling to a waveguide, which is beneficial for the reduction of the complexity of the entire system. No additional optical component is required to control the beam propagation behaviors between the transceiver and sample (no more lens or parabolic mirrors). Therefore, this double-PCA lens-free transceiver probe is selected to construct a terahertz wave-guided terahertz system in pulse mode.

II.2.1. Design of a double-PCA lens-free transceiver

This selected terahertz transceiver probe (shown in Figure II.1 (a) and (b)) was designed and fabricated by Protemics GmbH company. As illustrated in Figure II.1 (c), two identical directional PCAs with a separation of around 700 µm are deposited on a 1.3 µm thick LT-GaAs layer at the tip of a flexible 180 µm thick PET cantilever. Similar to a conventional THz-TDS, one PCA of transceiver under a bias voltage and laser excitation acts as an emitter to generate and radiate out terahertz waves into free space. Meanwhile, the other PCA acts as a receiver to measure reflected signals. The propagation process of terahertz waves can be described as three steps: (i) emission; (ii) interaction with a sample; (iii) detection.

Instead of using a PCA design in combination with a silicon lens, Yagi antennas are selected to enable the propagation direction of the emitted beam. Yagi antenna was first proposed by Yagi and Uda in 1926 [184]. It consists of three main parts, driven element (or called feed), reflector, and directors. Being the crucial component, a driven element could be a half-wave/full-wavelength or folded dipole antenna. A straight wire or rode is usually placed behind the driven element, acting as a reflector. Several shorter rods/wires act as directors in front of the driven element, indicating the main radiation direction of the antenna. Up to date, Yagi-Uda antennas have been widely used for various applications covering a broad frequency range due to its significant directivity. Television reception is the most well-known application of Yagi antennas (shown in Figure II.2 (a)). In addition, this antenna design has also been adapted in the frequency bands of radio frequency (RF) [185], [186], [187] and optical frequency region [188] (shown in Figure II.2 (b) and (c)). Since these antennas at high frequencies are usually fabricated on a planar surface, they are also named planar quasi-Yagi antennas.

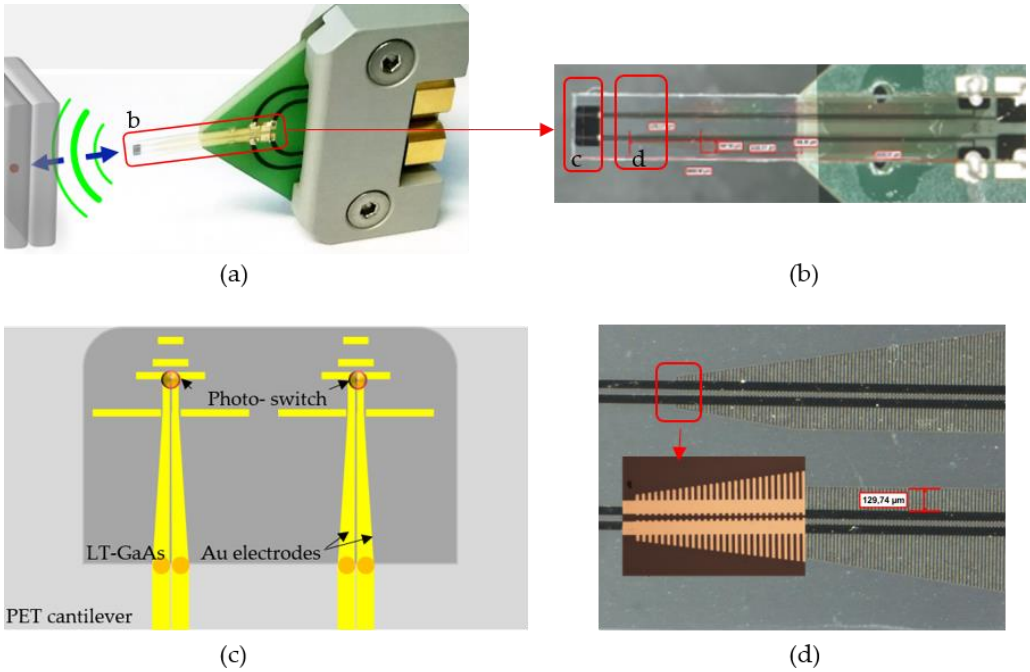

Figure II.1: (a) Photograph of double-PCA lens-free transceiver probe. (b) Close-up view of the slim PET cantilever of the transceiver, including an LT-GaAs layer and fed lines. (c) Schematic diagram of the double-PCA design on the apex of the transceiver probe. (d) Photograph of the feed lines on the PET cantilever. To suppress the internal reflections from the probe base, a special "wave-trap" design composed of different perpendicular lines along the feed lines are added.

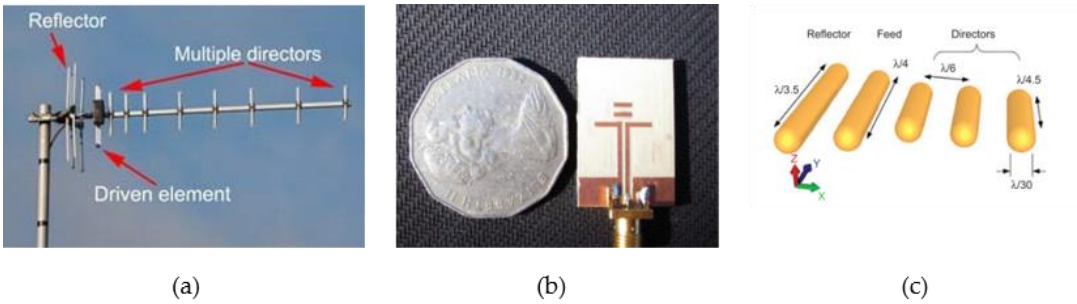

Figure II.2: (a) Yagi-Uda antenna for television reception. (b) Photograph of an X-band prototype planar Yagi antenna. (c) Optical Yagi antenna.

In addition to these three main components (directors, driver and reflector), feeding structure is also an indispensable element for a planar antenna to feed the dipole driver. Microstrip line feed with a microstrip-coplanar stripline (MS-CPS) transition [189], coplanar waveguide (CPW) feed with a coplanar waveguide-coplanar stripline (CPW-CPS) transition [190], or a microstrip line feed has been proposed and tested in the RF band. These feeding structures allow easy integration in wireless communication systems and broadband operation. Nevertheless, since they use the ground plane as a reflector, it is difficult to obtain a radiation pattern as good as a conventional Yagi antenna. Moreover, a PCA with ground plane design is impractical to construct. Simpler structures with CPS-fed line [191] [185] have been proposed to enable a broadband emission with more flexibility of reflector position. This CPS-fed line design is then applied in the double-PAC lens-free transceiver by Protemics GmbH. They are used to supply DC bias voltage and photocurrent measurement.

Nevertheless, the presence of CPS-fed lines leads to the current leakage from the antenna, *i.e.*, one part of the generated current can flow into the bias line, and then the CPS-fed line becomes one part of the antenna. As a result, terahertz waves can propagate towards the probe base along the CPS-fed line. This undesired propagation decreases the radiation efficiency of the antenna. Moreover, internal reflections from the probe base can propagate back to probe tip and then mix with signals reflected by the sample. To address this issue, a special design, "wave-trap" was added along the bias lines on the PET cantilever by Protemics GmbH. As shown in Figure II.1 (d), "Wave-trap" consists of numerous perpendicular short lines with different lengths attached along the bias lines. It contributes to the suppression of the internal reflections from the probe base. The fluctuations caused by the undesired propagation can be largely limited. To evaluate the performances of this transceiver in terms of frequency composition, optimal working distance and imaging capacity, both numerical methods and experiments were performed.

II.2.1.1. 3D full-wave electromagnetic simulation

CST Studio Suite is a high-performance three-dimension electromagnetic simulator, which exploits different calculation methods, such as finite element method (FEM), finite integration technique (FIT), and transmission line matrix method (TLM). It helps to design, to analyze, and to optimizer electromagnetic components and systems by simulating the propagation progress of electromagnetic waves. Among all provided solvers (such as frequency domain solver, eigenmode solver or integral equation solver), the time-domain solver can perform broadband simulations in a single run by taking advantage of the finite integration technique. This technique was first introduced by T. Weiland in 1977 [192]. It is a spatial discretization scheme to numerically solve electromagnetic field problems by using Maxwell's equations in integral form. Since the resulting equations of the discretized fields are suitable for computation calculations, FIT has been enhanced continuously and deployed in several electromagnetic simulators. Compared to other simulation techniques, FIT is more advantageous with respect to the models exhibiting complex geometries and arbitrary material distribution. Being computing- and memory-efficient algorithms, FIT is suitable for transient field analysis with a wide frequency band. This powerful multi-purpose 3D full-wave time-domain solver helps to predict the performances of the transceiver probe efficiently, including the operating frequency band and radiation patterns at different frequencies. Moreover, in regard to the constructed guided terahertz reflectometry system, this solver can offer valuable information both in the time domain and frequency domain, allowing to compare with experimental results.

Therefore, the simulation analysis method using the time-domain solver in CST is frequently deployed to predict and to provide a deeper understanding of the propagation behaviors of waves inside the system through the present work. The whole simulation process consists of several steps: modeling, setting up simulation parameters, launching the simulation and extracting desired results for analysis. In CST, a 3D model can be created easily with given dimensions. In addition to the materials provided in the built-in library, new materials can be established by entering corresponding electrical, thermal and mechanical properties. To perform the FIT, the first step is to impose the restriction of the electromagnetic field problem, *i.e.*, to delineate the boundary conditions of the simulation environment. Then the determined computational domain should be decomposed into a local finite number of simplicial cells such as hexagonal meshes for calculations. While the stability and conservation properties of the discrete fields can be always ensured by FIT, the mesh properties of the model, to a large extent, determine the resolution of the simulation. It is important de check for mesh number to

obtain correct simulation results. Once the energy contained in the model or the arranged time is reached, the simulation will be stopped and all required field properties are saved.

Operating frequency band of a planar quasi-Yagi antenna

To evaluate the transceiver performances and to investigate field properties of terahertz radiations, a simplified model of double-PCA lens-free transceiver was created with actual dimensions. As depicted in Figure II.3 (a), the simplified model consists of two planar quasi-Yagi antennas connected to CPS-fed lines, an LT-GaAs layer and a PET cantilever. All materials used in the simulation, including metals and dielectrics, were loss-free and no absorption in the air was considered. In order to calculate far-field radiation patterns at different frequencies, a Gaussian pulse signal with a full width at half maximal (FWHM) of 1.137 ps (frequencies up to 700 GHz) was used as the broadband excitation signal. Two discrete ports were placed at the center of the dipole drivers for signal excitation and signal detection (port 1 et 3 respectively, marked by red nodes). Additionally, two waveguide ports (port 2 and port 4) were added at the end of CPS-fed lines to absorb waves that propagate towards the direction of the probe base. They avoid the perturbations related to the reflections from the border of the model. The boundary conditions were set as “Open add” for free space simulation. By default, the unit of the signal’s amplitude is $\sqrt{W}$, which corresponds to $\sqrt{\frac{V^2}{\Omega}}$. It refers to the voltage value normalized with respect to the root of the input impedance $\frac{V}{\sqrt{\Omega}}$.

The operating frequency band of the double-PCA transceiver depends not only on the radiation properties of antennas but also on propagation paths. In the first place, the bandwidth of a planar Yagi-antenna acting as an emitter was investigated. Here, the bandwidth of an antenna refers to a frequency range in which a given return loss can be maintained. S_{11} denotes the proportion of rejected energy as a ratio against waves that arrive at the antenna input port, indicating the quality of the impedance match between the antenna and excitation. Hence, it can be used to assess the return loss. Based on the selected criterion that return loss should be less than -9 dB (S_{11}< -9 dB), a bandwidth of 540 GHz (90-630 GHz) was identified. In addition to S_{11}, the radiation efficiency of the emitter, which is defined as the ratio of the total power radiated by an antenna to the net power accepted by the antenna from the connected transmitter, is also given in Figure II.3 (b), which has a substantial impact on the antenna’s performances. By taking these two factors into account, the total efficiency was obtained, shown in Figure II.3 (c). The total efficiency of the emitter is higher than 0.4 over the frequency region from 365 GHz to 645 GHz. The frequency components out of this frequency band cannot be radiated into free space efficiently. This large bandwidth of 280 GHz (365-645 GHz) enables the functionality of transceiver in pulse mode.

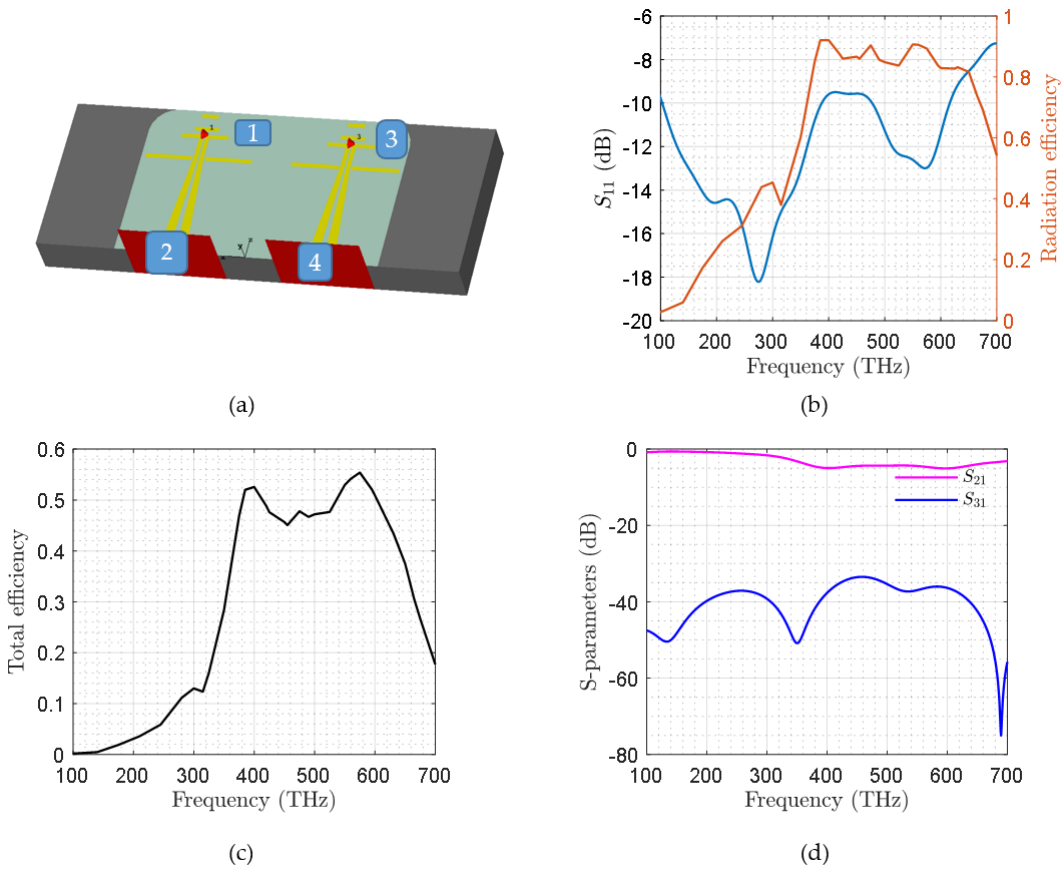

Figure II.3: (a) Simplified model of double-PCA transceiver probe. Discrete ports 1 and 3 are used to excite the antenna and to detect signals. Two waveguide ports (port 2 and 4) are placed at the end of CPS-fed lines to absorb the waves propagating towards the probe base. (b) S_{11} and radiation efficiency of the emitter antenna as a function of frequency. (c) Total efficiency of the emitter as a function of frequency. (d) S_{21} and S_{31} curves. While S_{21} indicates the cross-talking signal between two PCAs, S_{31} represents the crosstalk signal between two antennas.

S_{21} and S_{31} have also been evaluated, shown in Figure II.3 (d). While S_{21} represents waves propagating along the CPS-fed line towards the direction of probe-based, S_{31} depicts the power fraction arriving at the detector (port 2) from the emitter (port 1). The considerable value of S_{21} proves the existence of the unwanted leaked waves along the CPS-fed line and the necessity of "Wave-trap" design for suppression of internal reflections in the real design. The non-zero value of S_{31} implies that there is a direct transmission between two PCAs. It can be explained by the side lobe of the radiation pattern of the antenna, which will be given in the following part. It should be pointed out that although this direct transmission signal can announce the generation of terahertz pulse, it is not the generated or emitted signal.

Radiation diagram of a planar quasi-Yagi antenna

Since the double-PCA transceiver probe is lens-free, radiation properties of PCAs, especially their directivity, plays a critical role in enabling reflection-mode measurements. While experimental verifications are challenging to perform, 3D full-wave simulation can calculate far-field radiation patterns to reveal the directional dependence of emitted waves from the antenna. A radiation diagram can be plotted by different parameters. The two most widely used parameters are the directivity and gain. While the directivity refers to the ratio of the power density in one direction between the antenna radiates and an ideal isotropic radiator emits, the gain performance considers both directivity and the

total electrical efficiency of the antenna [193]. Since the gain value combines both total efficiency and directivity, it was selected to plot all radiation patterns presented below.

Generally, the main lobe of a conventional Yagi antenna points to the axis of directors, *i.e.*, most of the input signal is radiated into free space in front of itself. However, due to the high-index LT-GaAs layer and PET substrate, the effective dielectric constant of the whole structure increases. The main lobe of the emitter is supposed to be titled, slightly towards the high-index substrate, which is consistent with the obtained 3D plot of radiation pattern shown in Figure II.4 (a). This plot of radiation pattern at a frequency of 400 GHz gives an intuitive and direct view of the propagation directions of radiations emitted by the model. In order to observe clearly this slope angle, a polar diagram based on the antenna's gain in the xy-plane ($\theta = 90$ °) is depicted in Figure II.4 (b), where the main lobe lies in the direction of $\phi = 27$ ° instead of $\phi = 0$ ° (corresponding to the director axis). In the xz-plane ($\phi = 0$ °, shown in Figure II.4 (c)), apart from gains points to the front direction, a significant side lobe can be seen at an angle of around $\theta = 180$ °. It implies that a considerable power fraction is radiated to the right side of the emitter, *i.e.*, to the direction of the other PCA on the same substrate. That can explain the origin of S_{31} mentioned previously, which is the crosstalk signal between two PCAs. Since this direct transmission can be carried out either in the air or through the substrate, the crosstalk signal is not the exact same as emitted waves in free space. It is important to notice the difference between them, which means the detected crosstalk signal and the real emitted signal may have different frequency compositions.

Considering that a PCA generates a broadband signal, radiation patterns at different frequencies covering from 300 GHz to 700 GHz were calculated. Figure II.4 (d) and (e) display 3D plots of far-field radiation patterns of the double-PCA transceiver model at frequencies of 475, 550 GHz respectively. To facilitate the comparison, their gain in the xy-plane are plotted in the same polar diagrams (shown in Figure II.4 (f)). It can be seen that as the frequency increases, there is less power fraction radiated into free space in front. Instead, more power fraction is radiated in the down direction (down side of the substrate). The main lobe of the radiation pattern is more oriented towards the bottom of the transceiver.

As mentioned before, the propagation path of emitted waves has an important influence on the performances of the transceiver. To enable the functionality of the transceiver, not only the emitter is required to radiate a pulse signal efficiently, the reflected waves from sample should be able to be detected by the other PCA on the substrate. Once emitted waves arrive at the interface of a sample, one part of signal power will be reflected. Compared to radiations that arrive with a large incident angle, the power fraction arriving with a small/ normal incident angle has more chance to be detected by the other PCA on the transceiver. Although there may be more losses at high frequencies due to the propagation paths (inefficient detection), a normal reflection configuration with a large frequency band can still be guaranteed by this transceiver probe.

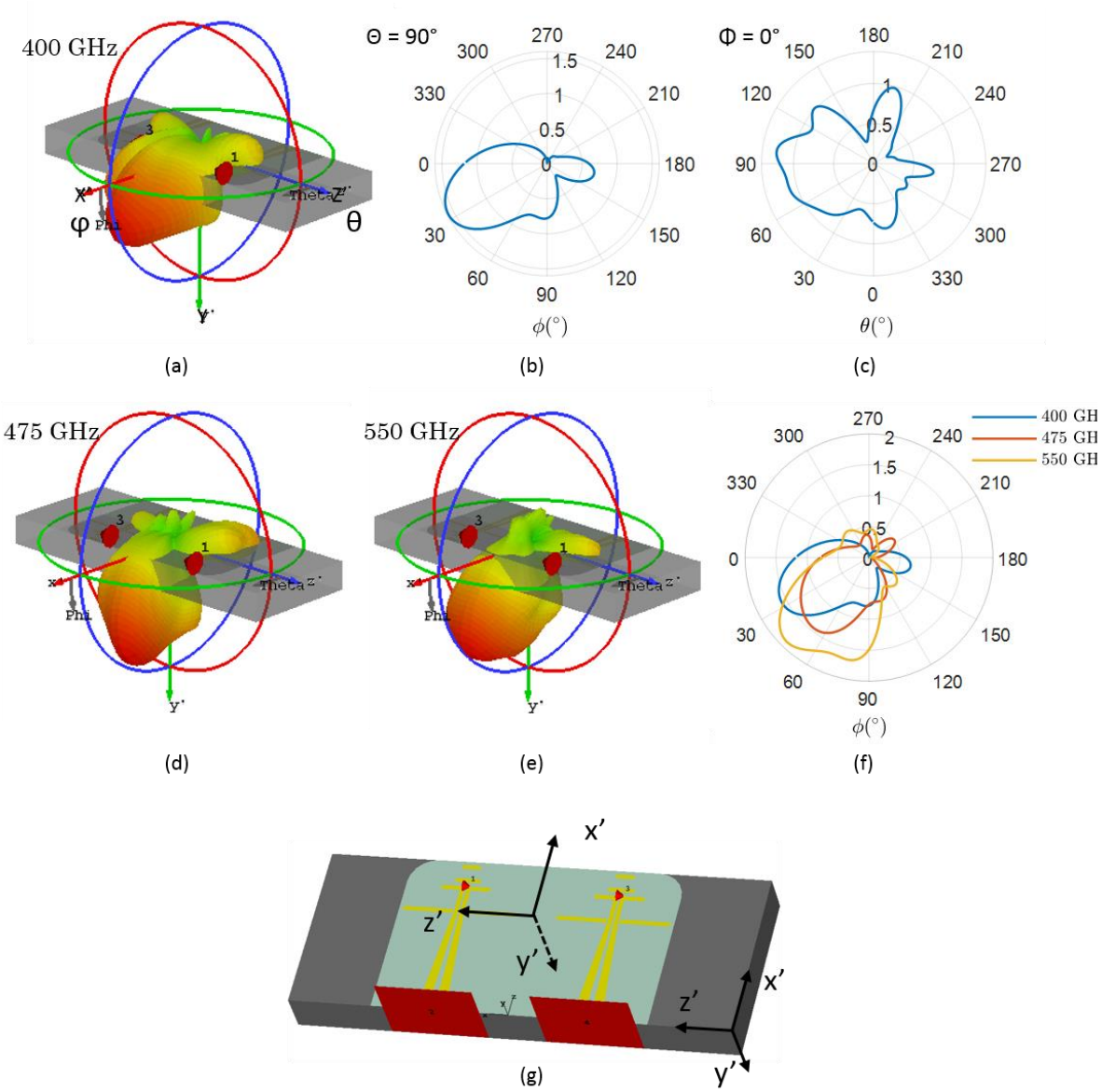

Figure II.4: (a) 3D plot of radiation pattern (based on gain) of the emitter of the transceiver at a frequency of 400 GHz. (b) Polar diagram based on the gain value of emitter of the transceiver in the xy-plane with θ = 90 °. The main lobe points to the direction of θ = 27 ° and its angular width (3dB) is 85 °. (c) Polar diagram based on the gain value of emitter of the transceiver in the xz-plane with ϕ = 0 ° The main lobe points to the direction of ϕ = 96 ° and its angular width (3dB) is 127.5 °. (d) and (e) 3D plots of radiation pattern at frequencies of 475 GHz and 550 GHz respectively. (f) Polar diagram of radiation patterns of the transceiver at θ = 90 ° at different frequencies . The main lobes at different frequencies (400/475/550 GHz) point to the direction of θ = 27/41/16 ° and their angular width (3dB) are 85/70.9/50.9 ° respectively. (g) Transceiver model in CST.

Apart from S parameters and far-field radiation patterns, electric field distribution in the near field was also simulated by means of time-domain solver in CST. As illuminated in Figure II.5 (a), a 2 mm long air block was added in front of the transceiver mode, allowing to observe the propagation process of emitted waves in free space. While the propagation of the waves can be observed in the time domain, it is easier to display field distributions with RMS values, which is time-independent. As shown in Figure II.5 (b) to (d), electric field distributions of emitted waves at the frequency of 400 GHz are plotted on the three different planes. It can be observed in the cut yz-plane that most emitted terahertz waves are radiated into free space in the front direction, slightly towards the substrate, which is in accordance with the previously obtained radiation pattern. Meanwhile, the direct power transmission

from the emitter to the receiver can be observed in the xz-plane (Figure II.5 (d)). Additionally, waves propagate along the CPS-fed line due to current leakage can also be clearly observed, expressed as a strong electric field along the bias line. The electric field distribution in the xy-plane depends on the distance to the transceiver. In the vicinity of the transceiver probe (Figure II.5 (d)), the strongest electric field can be found in front of the emitter while more radiations propagate below the substrate than above the substrate. As the distance increases, the field distribution changes due to the beam divergence. This simulation result provides an intuitive view of the propagation process of emitted waves from the transceiver, helping to understand the working principle of the transceiver in reflection-mode. In conclusion, quasi-normal reflection measurement can be guaranteed by this lens-free transceiver probe thanks to the directivity of planar quasi-Yagi antennas.

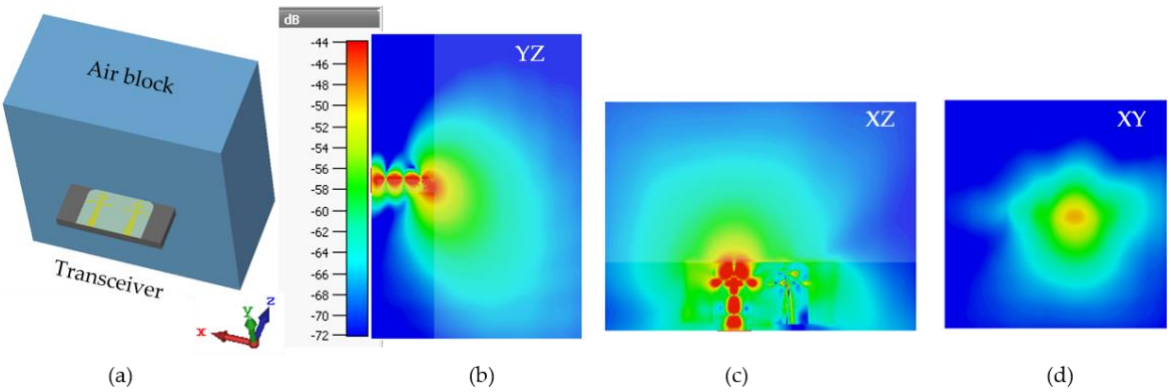

Figure II.5: (a) Simulation model consisting of a simplified transceiver probe and an air block (blue one) of 4*4*2 mm. (b), (c) and (d) Electric field distribution in the yz-plane, xz-plane and xy-plane respectively.

II.2.1.2. Experimental setup

By means of 3D full-wave simulations, the operating frequency band and radiation patterns of PCAs of transceiver have been investigated. Following these simulation results, characterization experiments were performed to validate the simulation results. The entire system setup can be divided into three subsystems, a subsystem on the optical table (shown in Figure II.6 (a)), a subsystem fixed on a vertical breadboard and a horizontal platform as sample's support (shown in Figure II.6 (b)). A schematic diagram of the constructed TDS experimental setup composed of this transceiver and a waveguide is presented in Chapter III.2.1, providing a more straightforward explication about the experimental setup. As shown in the photographs, most of the optical and mechanical components such as laser source, mirrors, beam splitters and chopper were placed on the optical table. An 800 nm wavelength laser beam generated by a Ti:sapphire mode-locked source was divided into two in-phase beams, namely pump and probe. They were sent into the vertical subsystem via mirrors. Since the direct output power of the laser source was too strong (an average power around 2.8W) for PCAs, neutral density filters (ND) were used to reduce laser power to a suitable level (around 4 mW). To optimize the performances of the double-PCA transceiver, not only the power of the optical excitation but also the size of the laser spot should be adjusted. According to the specifications given by the Protemics, the optimal size of the laser beam should be around 30-50 µm. Before exciting the active zone on PCAs, two laser beams must be resized by lenses. Considering the space constraint nearby transceiver, two lenses with a focal distance of 50 mm /75 mm were selected to be implemented on the vertical breadboard to achieve a 30 µm diameter laser spot.

Being an optical-pumped device, once the optical paths composed of mirrors and lens are fixed, the position of the transceiver probe is determined. The horizontal platform in the setup was equipped with multi-directional translation stages, allowing the movements in x, y and z directions. Consequently, it is preferred to move the sample by changing the position of the platform instead of the transceiver for a raster scan.

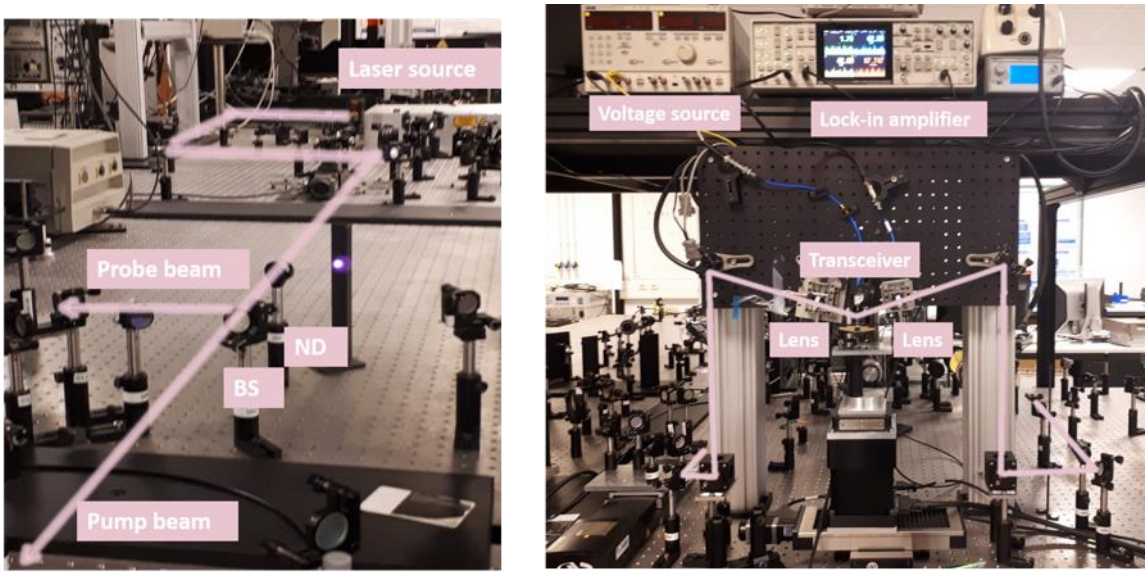

(a) (b)

Figure II.6: Photographs of the whole system setup. (a) A laser source and optical components (mirrors, BS:beam splitter, ND: neutral density filter) are placed on the optical table to send the pump beam and probe beams to the transceiver. (b) Apart from all the aforementioned components, the system can be divided into two parts. The first subsystem system is fixed on a vertical breadboard, consisting of a double-PCA transceiver and required optical components such as mirrors and lens to excite the transceiver. The second part is a horizontal platform equipped with three-dimension linear translation stages, acting as the sample support.

As illustrated in Figure II.7, there are two approaches to illuminating photoconductive switches located on the substrate: (a) from the front side with antenna pattern or (b) from the two sides separately. Although the camera vision of antenna patterns can facilitate the laser alignment work, it is challenging to irradiate both PCAs from the front side due to the limited space for lenses' supports around the transceiver. Besides, it is difficult to carry out two normal incidences to PCAs through the lenses due to the large volume of the support and the small distance between two PCAs on the substrate. A non-zero incident angle may lead to the direction change of laser beams after passing through lenses, resulting in more complicated alignment work and inefficient laser excitation. Therefore, this configuration was not selected in the first place. The second method is to excite PCAs from both sides of the substrate. It is not evident to illuminate a PCA from the backside without the antenna pattern to indicate the active zone. However, since the PET cantilever is transparent and the LT-GaAs layer is very thin (1.3 µm), camera vision at the front side can help to identify the position of laser spot irradiated on the other side. In addition, photocurrent generated by laser beam gives as well an indication of laser location on the substrate. Hence, laser excitation can be achieved from the two sides of the transceiver and no space constraint is imposed due to lenses' support.

To measure the reflected signal, a mechanical chopper and a lock-in amplifier are also included in the system. They are used to modulate the pump laser beam and perform lock-in detection, which allows measuring a weak signal drown in much stronger noises. A linear translation stage with two

mirrors forms a delay line, providing a linear motion range by ± 75 mm (150 mm), corresponding to a detectable 450 picosecond time span. By changing the position of the delay line, the difference in length between the two optical paths varies, giving rise to time delay. Consequently, the time signal's reconstruction can be realized by photoconductive sampling.

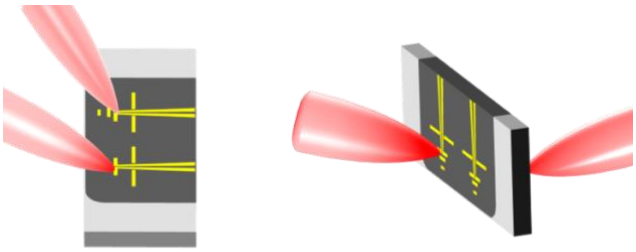

(a) (b)

Figure II.7: Two different configurations for two laser beam excitation. (a) Both laser beams excite the PCAs from the front side of the probe. (b) Laser beams excite two PCAs from both sides of the transceiver probe.

II.2.1.3. Time-domain waveform characterization

A close-view of the core part of the experimental setup is shown in Figure II.8 (a). In addition to the transceiver probe and relevant optics, a horizontal platform acting as a sample's support was placed below the transceiver. As depicted in Figure II.8 (b), a metallic sheet was selected as the sample. Acting as a perfect mirror, a metallic sheet reflects the maximum terahertz waves back to the detector of the transceiver.

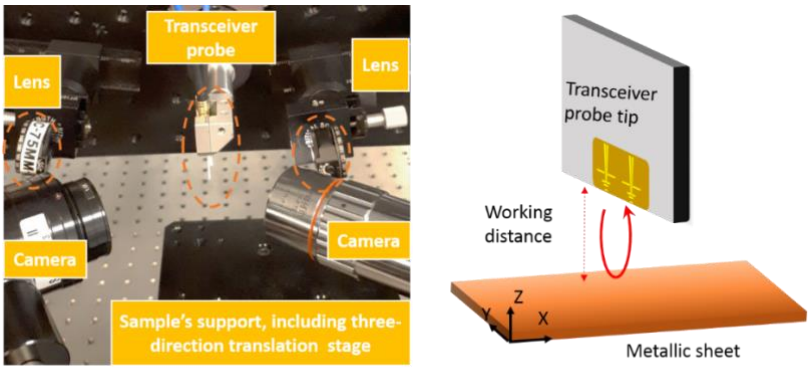

(a) (b)

Figure II.8: (a) Photograph of the experimental setup, including transceiver probe, lenses, sample's support and two cameras. (b) Schematic diagram of the experimental setup. A metallic sheet was used as the sample. During the measurements, the distance between the transceiver tip and the metallic sheet varied.

The first measurement was performed with a small distance d (roughly estimation value was 1.5 mm). The recorded time signal is shown in Figure II.9 (a), which can be separated into two parts: main pulses at the beginning (Figure II.9 (b)) and reflections from the metal surface (Figure II.9 (c)). Previous simulation results have brought into light the origin of the first main pulse waveform, which originates from the crosstalk signal between two PCAs through the substrate and the air. It can be obtained without any sample, indicating the generation of terahertz waves by the emitter. It should be pointed out that this signal does not carry any information about the sample. In order to focus on the reflections from the sample, this crosstalk signal was then removed from the originally detected signal. By using the FFT function, spectra of the crosstalk signal between the two PCAs and reflected signals from the metallic sheet were obtained. As depicted in Figure II.9 (d), the noise level during the measurements was around -90 dB, which means the signal weaker than this value cannot be

distinguished. The crosstalk signal covered a wider frequency band up to 800 GHz with 30 dB dynamics. Considering the antenna's properties obtained by simulation, the high attenuation at frequencies above 800 GHz is associated with loss due to the input impedance mismatch of the antenna. In comparison to the crosstalk signal, the bandwidth of reflected signals is much narrower, mainly lying in the frequency band from 400 to 600 GHz. This result is consistent with the operating frequency band deduced from simulation analysis.

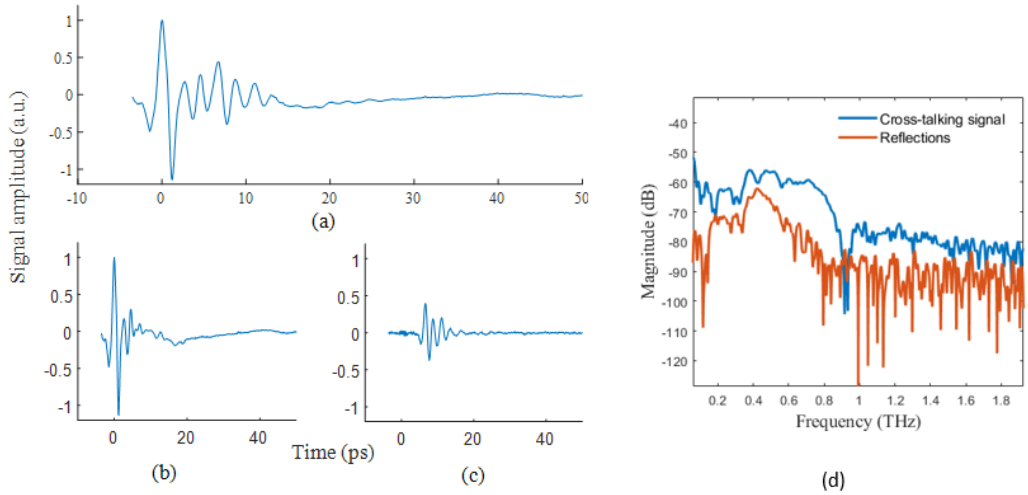

Figure II.9: (a) Recorded signal by the transceiver probe. The distance between the probe tip and the metallic sheet was around 2 mm. (b) Crosstalk signal between two PCAs on the transceiver. (c) Reflections from the sample. It was obtained by removing crosstalk between two PCAs from the detected signal. (d) Spectra of the cross-talk signal and pure reflected signal from the perfect mirror.

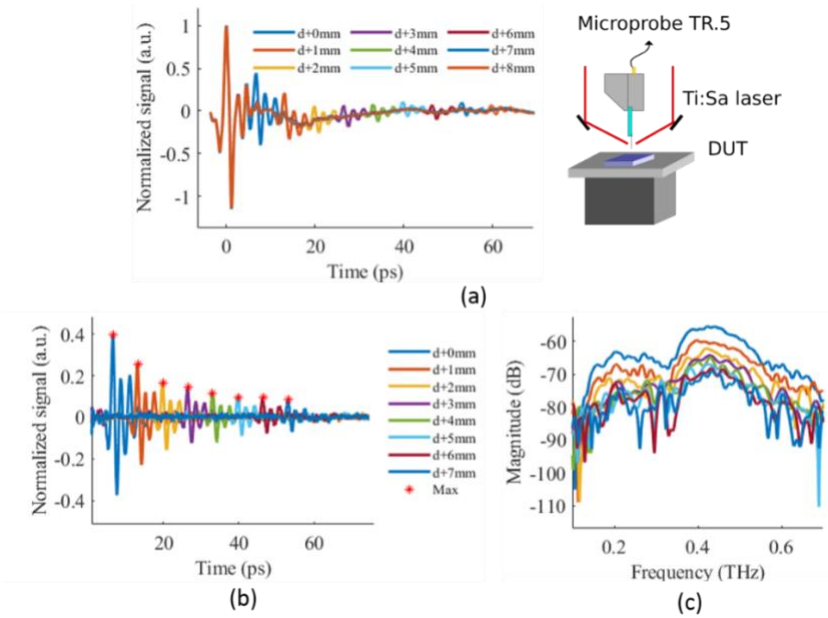

Figure II.10: (a) Nine recorded waveforms. A metallic sheet was placed right below the probe tip with a varied distance (distance step =1 mm). Here, d represents a small distance between the probe tip and metallic sheet, less than 1.5 mm. (b) Reflected signals from the metallic sheet. They were obtained by removing the crosstalk signal. (c) Spectra of reflected signals.

More measurements were performed by moving farther the metallic sheet with a step of 1 mm. Nine waveforms of detected signals are shown in Figure II.10 (a). All of them can be separated into two parts, overlapped crosstalk signal and reflections from the metal surface. The crosstalk signal was

removed from initially detected signals, giving rise to in Figure II.10 (b). As the distance increases, the reflected power decreases due to the beam divergence in free space and absorption in water vapor. Since there is no significant dispersion during the propagation in the air, the waveform of reflected signals remains similar. They have a similar frequency composition, in which most of the energy is preserved in the frequency band ranging from over 400 GHz to 600 GHz (shown in Figure II.10 (c)). In addition, it can be observed that the time-of-flight of reflections depends on the distance between the transceiver and the sample, allowing to estimate the properties of the propagation medium and the surface state of the sample.

These experimental results validate the previous analysis by means of simulation, demonstrating that a double-PCA lens-free transceiver can enable measurements in reflection-mode in a large frequency band roughly from 400 GHz to 600 GHz. Additionally, this series of experiments reveal that the signal-to-noise ratio (SNR) of the measurements can be enhanced by decreasing the distance between the transceiver and sample. Therefore, a new series of experiments with shorter working distances were performed using the same setup and corresponding waveforms of time signal were recorded.

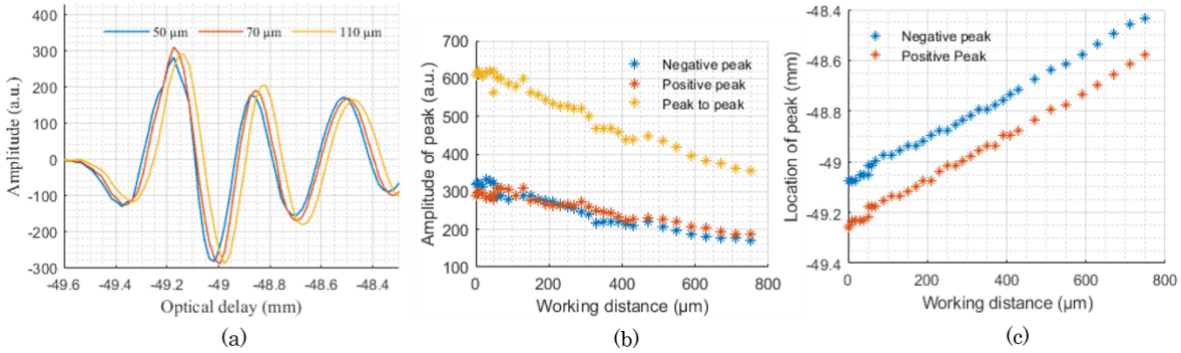

Figure II.11: (a) Three waveforms of reflected signals obtained with a working distance of 50 µm, 70 µm and 110 µm. It should be noted that even with 0 µm working distance, there is a minimum distance d between the probe tip and sample to prevent the mechanical damage to the transceiver probe. (b) Absolute value of the amplitude of peaks as a function of the distance between transceiver probe and sample. The positive peak is the first maximal peak lying around the optical delay of -49.2 mm. The negative peak is the minimum peak lying around the optical delay of -49 mm. (c) Locations of peaks as a function of the distance between transceiver probe and sample. Here, optical delay in mm represents the peak location in the time domain.

Measurements were performed with a distance range of over 750 µm by rising the horizontal platform on which the sample was positioned. Considering the fragility of the transceiver probe, a small distance between the transceiver tip and metal plate was respected (estimated distance < 50 µm), no closer measurements were performed. The closest position was taken as a basic point for distance calculation, *i.e.*, the distance in that position was regarded as 0 µm. As previously, reflections from the metallic sheet were obtained by subtracting the crosstalk signal from originally detected signals. Time –domain waveform detected by the transceiver probe from the metallic sheet in three different distances are shown in Figure II.11 (a), where time shifts and changes in amplitude can be observed.

In order to find out the relation between the waveform and working distance, the peaks analysis method was applied. Both the location and amplitude of peaks were plotted as a function of working distance. Regarding amplitudes of peaks, they enhance as the sample moved closer (shown in Figure II.11 (b)), implying a higher SNR is obtained by moving closer the metal. Figure II.11 (c) depicts the relation between the location of peaks of reflections and the working distance, which can be estimated

to follow a linear dependence. Having a closer look at the results obtained in the vicinity of the probe (distance less than 50 μm), one may observe that some irregular points appear in both figures. The amplitude and the time-of-flight of reflections vary slightly with the working distance. In fact, when the working distance is less than one wavelength (*e.g.*, 500 GHz corresponding to 600 μm), the sample is placed in the near field (or the transition field) of the antenna. The radiation pattern of the antenna is impacted by the presence of the sample. Additionally, the separation between the two PCAs must be considered in a near-field measurement, which further complicates the response of the transceiver to a sample.

To sum up, after having explored the working principles of the transceiver by 3D full-wave simulations, the responses (time-domain waveform) of the transceiver to a plate metal surface were characterized by experiments. It reveals that the waveform recorded by the transceiver is composed of the crosstalk signal between two PCAs and reflections from a sample. As predicted by the simulation, the efficient operating frequency band of the transceiver covers the 365 GHz-645 GHz window (roughly 400-600 GHz). By decreasing the working distance between the transceiver and sample, a greater power fraction reflected by a sample can be detected so that the operating frequency band may be extended. Nevertheless, it is worth noting that although the SNR of a measurement can be enhanced by decreasing the working distance, the sophisticated propagation behaviors of radiations in the near field make it difficult to extract the information about sample from the detected signal by the transceiver. This issue is discussed in the following part from imaging application.

II.2.2. Imaging capacity of double-PCA lens-free transceiver

It is known that after emitted terahertz radiations arrive at the interface of a sample, one part of the signal is reflected and detected by the receiver on the transceiver. This part of the waveform contains information about sample properties and the propagation path. An image of an object can be obtained by performing a raster scan with the transceiver probe. As was pointed out in the foregoing, the shorter the working distance is, the stronger the reflected signal becomes. Nevertheless, the presence of a sample in the near field may influence the response of the transceiver.

The investigation into the resolution power of the transceiver probe in the near field is reported in the following part. Both experimental and simulation results are provided to highlight and to explain the imaging limitations of the transceiver. Different methods can be applied to characterize and validate the lateral resolution of an imaging system, such as line spread function (LSF), edge response, and contrast transfer function (CTF). In this part, the contrast transfer function which can be obtained by using a test chart is studied. Based on the scan results, the discussion focused on the impacts of a sample (geometry and configuration) on the time response of the transceiver is given.

II.2.2.1. Experimental setup

A 1951 USAF resolution test chart is widely used to evaluate the resolution of an optical imaging system, in which chrome-covered patterns are deposited on the clear glass substrate to form black-white patterns. As shown in Figure II.12 (a), it consists of 9 groups, and each group is composed of 6 elements. Every element includes three vertical metal-covered bars and three horizontal metal-covered bars, which allow verifying resolution power in two different directions. Since metallic materials are considered as a perfect mirror for terahertz waves and a glass substrate reflect back less

power fraction, a 1951 USAF chart can be as well applied to assess the imaging capacity of the terahertz system.

Prior to the definition of the resolution power of the transceiver probe, several notions should be introduced. A contrast transfer function is a commonly used method for the characterization of an imaging system. It permits to obtain the modulation transfer function (MFT) curves as a function of spatial resolution by applying the binary black-white bar pattern. It reveals how much of the object's contrast is captured in the image as a function of spatial frequency. MFT has a range from 0 to 1, and it tends to decrease with the increasing spatial frequency due to the diffraction limit. In the experiments, contrast can be used as MTF to plot the curves. The contrast between the metal covered line (bright area) and clear substrate (dark area) can be calculated as follows:

$$\text{Contrast} = \frac{A_{max} - A_{min}}{A_{max} + A_{min}} \tag{6}$$

where A_{max} represents the magnitude of the signal reflected by the metal-covered line, A_{min} represents the magnitude of the signal reflected by the glass substrate. The table, shown in Figure II.12 (b), gives the corresponding spatial frequencies and line widths for all elements in group 1. The spatial frequency can be as well calculated as follows:

$$\text{Resolution (lp/mm)} = 2^{\left(\text{group}+\left(\frac{\text{element}-1}{6}\right)\right)} \tag{7}$$

The lp (line pair) corresponds to one black and one white line. Here, a contrast of 0.4 is applied as the criterion to determine if the element is spatially resolved. Once the smallest distinguishable element in the test chart is fixed, the corresponding spatial frequency is the spectral spatial resolution of the transceiver. Yet, it should be underlined that the definition of the contrast value for which are considered resolved spatially distant elements remains subjective.

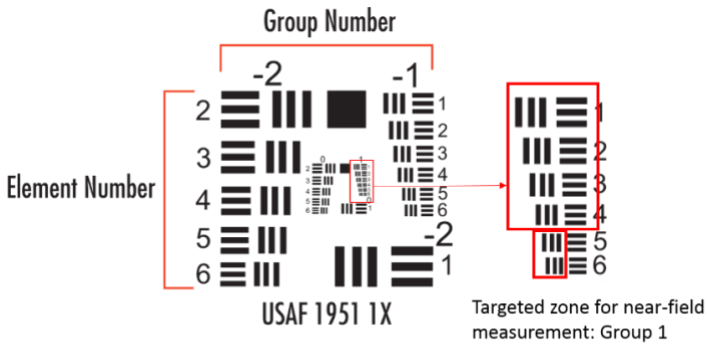

(a)

Group1 Element	Number of Line Pairs / mm	Width of 1 line in µm
1	2.00	250.00
2	2.24	222.72
3	2.52	198.43
4	2.83	176.78
5	3.17	157.49
6	3.56	140.31

(b)

Figure II.12: (a) 1951 USAF resolution test chart, in which group 1 was scanned. (b) Table of spatial resolution indicated by each element in group 1.

The same setup was deployed to perform a raster scan. While the transceiver probe was fixed in the vertical subsystem with other optical components, a 1951 USAF test chart was placed on the horizontal platform equipped with three direction linear translation stages to perform a raster scan. By adjusting the height of the platform, the distance between the probe tip and test chart was set around 110 µm (plus a minimum distance mentioned before). No active height control was applied during scans. Element patterns in group 1 of a 1951 USAF resolution test chart were scanned to evaluate the resolution performance of the transceiver. These elements have a width varying from 250 µm to 140.31 µm. They can provide a standardized series of logarithmic steps in the spatial frequency range from 2 to 3.56 line

pairs per millimeter (lp/mm). To optimize the time cost, two scans were performed separately. As marked by red rectangles in Figure II.12 (a), the first scan zone covered both horizontal and vertical elements from 1 to 4 while the second raster scan was performed in the area including only the vertical lines of element 5 and 6. It should be noted that vertical bars in group 1 were parallel to the transceiver cantilever (axis of two PCAs).

In the first raster scan, the translation step in x and y directions were both 50 µm. At each point, the time signal with a duration of 5.87 ps (corresponding 0.88 mm optical delay) was recorded. Eventually, 570240 points constituted a pixelated data map covering the zone of 4.4*7.2 mm² (88*144 pixels). In the second raster scan, the translation step in x and y directions was reduced to 20 µm instead of 50 µm and a shorter time signal of 3.33 ps (corresponding 0.5 mm optical distance) was recorded at each point. 437500 points constituted the second pixelated data map covering the zone of 2.5 *2.8 mm² (125*140 pixels). After removing the cross-talking signal from the recorded time signals, reflected signals from the 1951 USAF test chart were transformed in the frequency domain via Fast Fourier transform (FFT) analysis. It was realized with 257 points with zeros padding sampling method. While the previous studies have demonstrated that a double-PCA lens-free transceiver can operate efficiently in the frequency range of roughly from 400 GHz to 600 GHz, higher or lower frequency components which possess a small power fraction can still be emitted and detected by the transceiver, especially for the measurements in the near-field. For that reason, images based on magnitude were obtained over frequencies from 300 GHz to 800 GHz with a frequency resolution of 14.6 GHz.

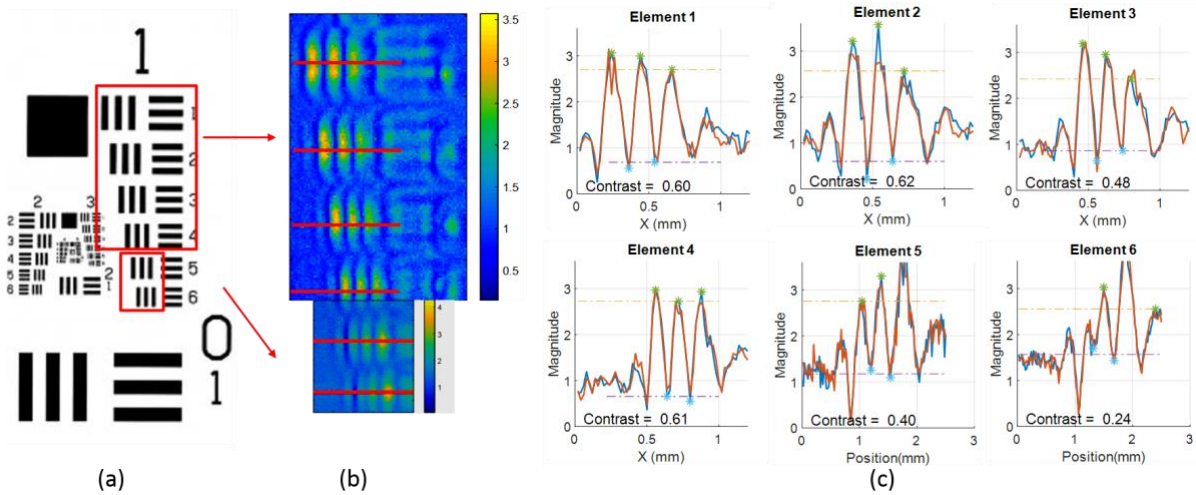

Figure II.13: (a) Image of a1951 USAF resolution test chart, in which two scan zones in group 1 are marked by red rectangles. (b) Reconstructed images of scanned zones at a frequency of 791 GHz. (c) Line profiles of different elements in group1, corresponding to the red line noted in the (b).

It is known that the resolution of an imaging system depends, to a large extent, on the frequency of emitted waves. As the frequency increases, the resolution capacity of emitted waves enhances. Therefore, two images of the scanned zones at a frequency of 791 GHz are shown in Figure II.13 (b) to provide the best imaging resolution of the transceiver. Limited by SNR, no frequency components above 800 GHz can be used to extract the sample information. Distinct differences of resolution power in two directions can be observed: while vertical bars are distinguishable, horizontal lines cannot be spatially resolved. Therefore, investigations into the imaging capacity of the transceiver are separated into two parts: resolution power demonstrated by vertical bars and defaults with horizontal bars. In order to deepen the understanding of artifacts caused by the transceiver, 3D full-wave simulations were

as well performed to study the propagation behaviors of waves between the transceiver and the sample, which are present in the next part.

II.2.2.2. Image of vertical bars in group 1

Since vertical bars in group 1 are parallel to the slim cantilever of the transceiver, it facilitates the detection of reflected signals for the detector of the transceiver which is positioned on the same substrate with the emitter. The resolution power of the transceiver in this direction is first given and investigations focused on the causes of artifacts that appear in the previously obtained image are then presented.

Imaging resolution at different frequencies

Based on the magnitude of reflected signals at the frequency of 791 GHz, line profiles of vertical bars in group 1 were extracted, shown in Figure II.13 (c). Accordingly, the corresponding contrasts of elements in group 1 were calculated: 0.60/ 0.62/ 0.48/ 0.61/ 0.40/ 0.24 respectively. Using the criterion that contrast between the substrate and metal elements should be higher than 0.4, the resolution of the transceiver is 3.17 lp/mm at a frequency of 791 GHz with a working distance of 110 µm. Using the same method, line profiles and corresponding contrasts of vertical bars in element 1 to element 6 were deduced. Figure II.14 depicts the contrast curves as a function of spatial frequency at four different frequencies of 300 GHz, 500 GHz, 700 GHz and 791 GHz respectively. It can be observed that the minimum distinguishable bars were limited to element 2 (width of 222.72 µm) at frequencies of 300 and 500 GHz. Vertical lines in elements 4 can be spatially resolved at the frequency of 700 GHz while the contrast of element 5 is higher than 0.4 at the frequencies of 791 GHz. This result is consistent with the previous analysis: as the frequency increases, resolution of the transceiver probe for imaging applications enhances. It should be noted that although better contrast can be obtained at higher frequencies, the noise during the measurement has a more significant effect on the quality of the image due to their weak SNR. There is a trade-off between the noise level in the obtained image and the lateral resolution.

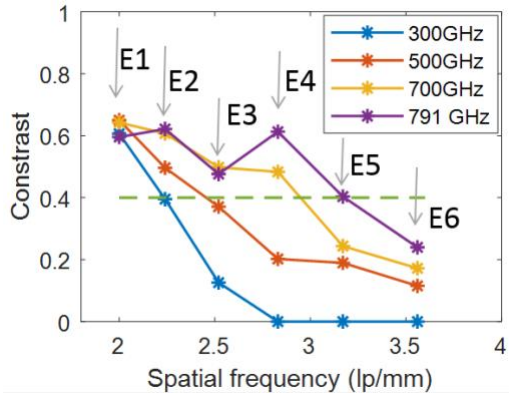

Figure II.14: Contrast versus spatial frequency at frequencies of 300 GHz, 500 GHz, 700 GHz and 790 GHz respectively. E1 to E6 represent the element 1 to 6 in group 1 of the test chart.

To conclude, the resolution of this transceiver probe in the x-direction (evaluated by the vertical bars) can reach up to 2.24 lp/mm at the frequency of 791 GHz. It can differentiate vertical bars with the smallest width of 157.49 µm, which is close to the limitation induced by the diffraction effect of conventional imaging systems, *i.e.*, resolution in the order of λ/2 (379/2 µm).

Artifact in the x-direction

In addition to the imaging resolution of the transceiver probe in the x-direction, some interesting phenomena can be observed in the obtained images. As shown in Figure II.13 (c), the center of three vertical bars have different amplitudes at the frequency of 791 GHz. While elements 1 to 4 have the weakest amplitude of reflection from the bars at the right side, the bars of elements 5 and 6 have the weakest amplitude in the bar on the left side. The possible tilted surface of the sample cannot solely explain the unusual phenomenon. In fact, according to radiation patterns of the PCA on the substrate introduced in Chapter II.2.1.1, the directivity and beamwidth of the antenna are expected to change with the frequency. As the frequency increases, more power fractions are radiated towards the substrate (down direction) instead of the front side of the transceiver. Besides, the electric field distribution in the proximity of the transceiver displayed in Figure II.5 (d) has revealed that the form of the emitted beam is irregular due to the high-index substrate, express as more power fractions radiated towards the substrate. By considering all the mentioned factors, the different amplitudes of the three bars in an element can be explained. Since the main lobe of the PCA on the transceiver at the frequency of 791 GHz is tilted towards the substrate, a non-negligible power portion arrives on the right side of the sample, *i.e.*, the next bar of the targeted one. Since there is more empty area without any metallic pattern at the right side of the third bar for elements 1 and 4, the third bars possess less power portion than the two others. In regard to element 5 and 6, bar sizes and separation between the vertical and horizontal pattern is much small. Hence, the horizontals bars are suggested to contribute to the higher amplitude of the right bars in elements 5 and 6.

The above analysis is based on the radiation properties of the emitter of the transceiver, in which no propagation path or detection efficiency related to the other PCA is considered. By means of 3D full-wave simulation, the response of the transceiver to a sample were directly investigated. A simplified double-PCA transceiver probe model was used in the following simulation. The CPS-fed lines were removed to decrease the calculation number. Similarly to previous cases, two discrete ports were inserted at the center of the dipole driver for signal excitation and detection. All materials used in the simulation were loss-free, no absorption in the air or in the substrate was considered. Prior to the simulation with a metallic sheet, the transceiver model was simulated alone with “Open Add” boundaries conditions to obtain a default crosstalk signal between two PCAs, which was consistently removed from the detected signals, giving rise to reflections from the sample.

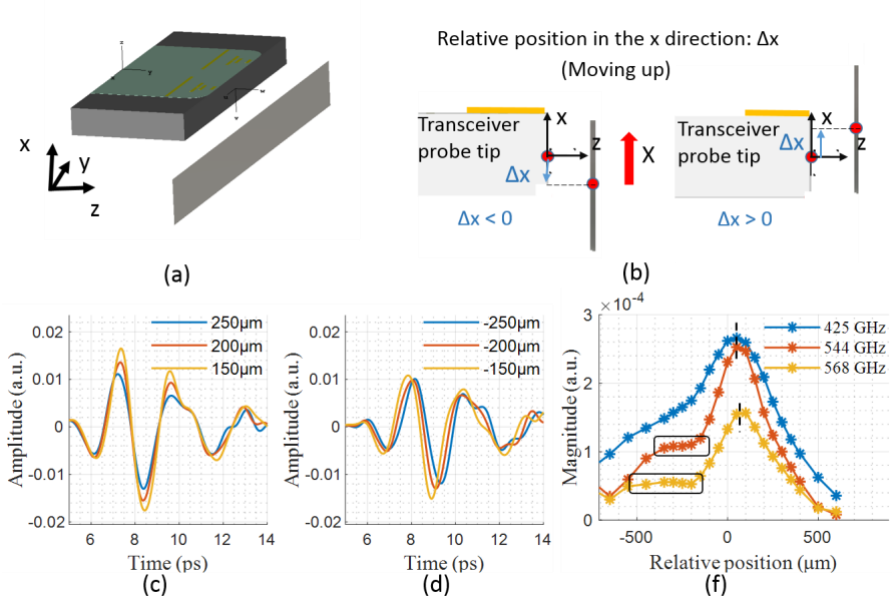

Figure II.15: (a) Simulation model in CST, including a simplified transceiver model (2*0.77*0.18 mm3) and a 0.3*3 mm² metallic sheet in front. (b) Side view of the model in the xz-plane, illustrating the metallic sheet moving up with respect to the transceiver. The relative distance between the transceiver and the metal plate can be calculated based on their center position. Left: the relative distance between two objects is negative. Right: the relative distance in the x-direction is positive. (c) and (d) show the time responses when the relative distance between them is positive and negative respectively. (f) Line profiles obtained at different frequencies, corresponding to 425 GHz, 544 GHz, and 568 GHz.

In order to verify the previous analysis, the transceiver probe was simulated together with a slim metallic sheet moving in the x-direction, shown in Figure II.15 (a). A slim metallic sheet with a surface of 0.3*3 mm² is placed in front of the transceiver tip. To achieve the same configuration in the experiment, this sheet is placed parallel to the double-PCAs axis (parallel to the y-axis). The relative distance between the transceiver and sample is calculated based on the center position of the sample with respect to the transceiver, *i.e.*, the origin point is at the center of the substrate. Figure II.15 (b) illustrates the movement process of the metallic bar in the x-direction during the ascent in simulations, where the relative distance changes from negative ($\Delta x < 0$) to positive ($\Delta x > 0$). Detected signals by the other PCA were recorded after each movement.

Figure II.15 (c) gives the detected reflections by the transceiver when the metallic bar is higher than the transceiver (Δx = 150/200/250 µm respectively). As the bar rises, the amplitude of peaks decreases and no significant time shift can be observed, implying that more power fraction can be reflected and detected by the transceiver efficiently when the sample is placed right in front of the transceiver. On the other hand, as the metallic bar moves down ($\Delta x<0$), there is less change in amplitude while there is a significant time delay compared to the previous results, shown in Figure II.15 (d) with Δx = -150/-200/-250 µm respectively. According to the radiation patterns of the emitter, a considerable power portion is radiated to the front-down direction with a wide angle width. Consequently, the decrease of the reflected power fraction is less prominent during the descent of the transceiver. Since the detected reflection power from the metallic bar below the transceiver must propagate through the substrate (LT-GaAs and PET cantilever), a longer time-of-flight is required due to the high-index substrate compared to the air.

Line profiles of the metallic sheet in the x-direction were obtained based on the magnitude of different frequency components by using the FFT analysis. Figure II.15 (f) gives line profiles at three

frequencies of 425 GHz, 544 GHz and 568 GHz respectively. While the highest magnitude is achieved at the relative position of 90 µm, the asymmetrical line profile that depends on the moving direction can be observed. In particular, when the sample moves far away from the transceiver probe towards the down direction, signal attenuates quickly at first and then the diminution of power reaches a stable value within Δx varying from -200 to -400 µm at high frequencies (marked by the black rectangle in Figure II.15 (f)). After this stable platform phase, the signal continues to attenuate with distance. Considering that the thickness of the PET substrate is 180µm, this result reveals that the front side in the proximity of the antennas is the most sensitive area of the transceiver during the measurement. The asymmetrical property and stable phase occurring at the backside of the transceiver is on account of the tilted emission beam, which is in accordance with the previous analysis.

Thanks to this simulation, it corroborates that the response of the transceiver to a sample depends unsymmetrically on its relative position with respect to the transceiver (up-down side of the transceiver). In regard to the experimental three-bars pattern scan, while the time response of the transceiver depends to a great extent on the bar right in front of it, the close surrounding of the targeted area also has a strong impact on the response of the transceiver. The detected signal is the superposition of the reflection from the bar right in front of it and the ones from the pattern nearby. More precisely, as frequency increases, the objects at the backside of the substrate (right side in the experiments) of the transceiver have an increasing influence, which can explain the uneven amplitude of three bars on the images obtained at different frequencies.

Artifacts in the y-direction (active area in front of the double antenna)

Figure II.16 (a) shows a reconstructed image of elements 1 to 4 based on the averaging magnitude over the frequency range from 400 GHz to 600 GHz. The line profiles of verticals bars of elements 1 and 2 in the y-direction at two different frequencies are plotted in Figure II.16 (b) and (c) respectively. Typically, when the beam size is comparable with a sample, the highest reflection amplitude is obtained at the center of the sample. However, it is noticeable that there is a dip at the center of the bars in element 1, and the highest amplitudes are achieved aside (shown in Figure II.16 (b)). In order to ascertain the reason behind this unexpected phenomenon, two simulations were performed with a metallic bar standing as a sample.

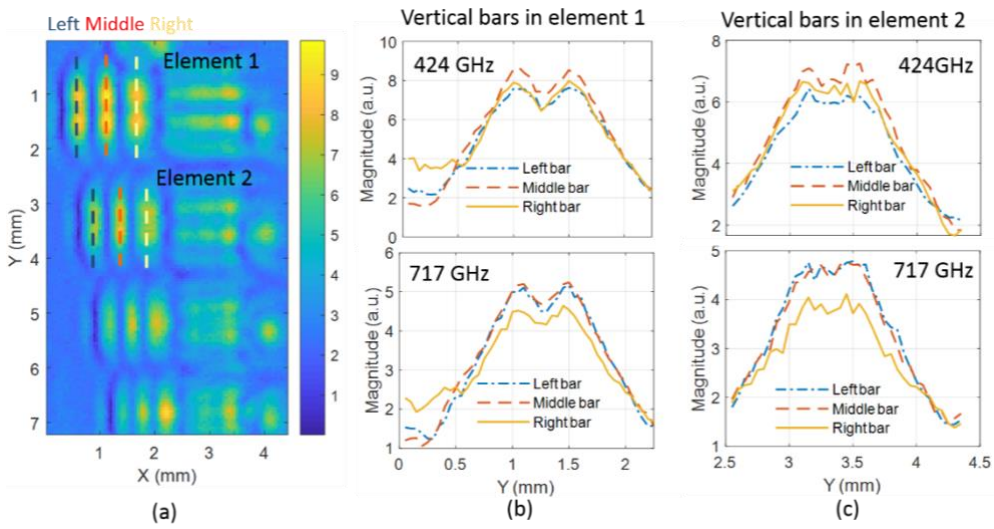

Figure II.16: (a) Reconstituted image in the frequency domain. (b) Line profile of vertical bars in element 1 in the y-direction. Top: profile obtained at a frequency of 424 GHz. Top figure: profile obtained at a frequency of 424 GHz. Bottom figure: profile obtained at a frequency of 717 GHz. (c) Line profile of vertical bars in element 2 in the y-direction. Top: at a frequency of 424 GHz. Bottom: at a frequency of 717 GHz.

As shown in Figure II.17 (a), a slim metallic sheet with a width of 300 µm is placed right in front of the transceiver probe. While the center of the metallic sheet is aligned with the transceiver, the length of the sheet *l* varies from 2750 to 100 µm. Figure II.17 (b) depicts the reflections detected by the transceiver when the length *l* is equal to 1200, 1000, 800 µm, respectively. Unexpectedly, as the length decreases, the detected power enhances. Additionally, it is worth noting that the change in amplitude mainly takes place in the second peak and time delays of the third peak can be observed. While the length of the metallic bar continues to decreases (shown in Figure II.17 (c)), the reflected power decreases. By using FFT analysis, the magnitude of reflected signals as a function of the sheet length at frequencies of 377 GHz, 425 GHz and 544 GHz are given in Figure II.17 (d). When the metallic sheet is longer than 2 mm, the response of the transceiver to the sample remains the same. In the case of $l <$ 800 µm, the reflected power is proportional to the length of the bar. When *l* is between 800 µm and 2 mm, the relation between the bar's length and reflected power becomes more complicated. To understand this result, it should be kept in mind that since the distance to the sample is less than one wavelength (in the near or transition-field), the separation of 700 µm between two PCAs can no longer be ignored. The transceiver cannot be considered as one component but rather as an entity made of several components.

When the metallic sheet is small, most of the emitted power passes through the sample and radiate into free space. As it becomes larger, more emitted power fraction is reflected back. Meanwhile, this metallic bar can guide high-frequency components as transmission lines due to its small dimension. Instead of being reflected, one part of power propagates along this metallic sheet, which can explain why detected reflections decrease as the length continues to increase. The maximum power fraction is obtained with *l of* around 800 µm owing to the fact that the reflections occurring at the end of the sheet are in front of the detector, allowing for efficient detection of reflections. To include, the strongest reflections can be obtained when a metallic sheet is placed in front the transceiver and it has a comparable size to the separation between two PCAs due to the wave propagation along the sample's surface.

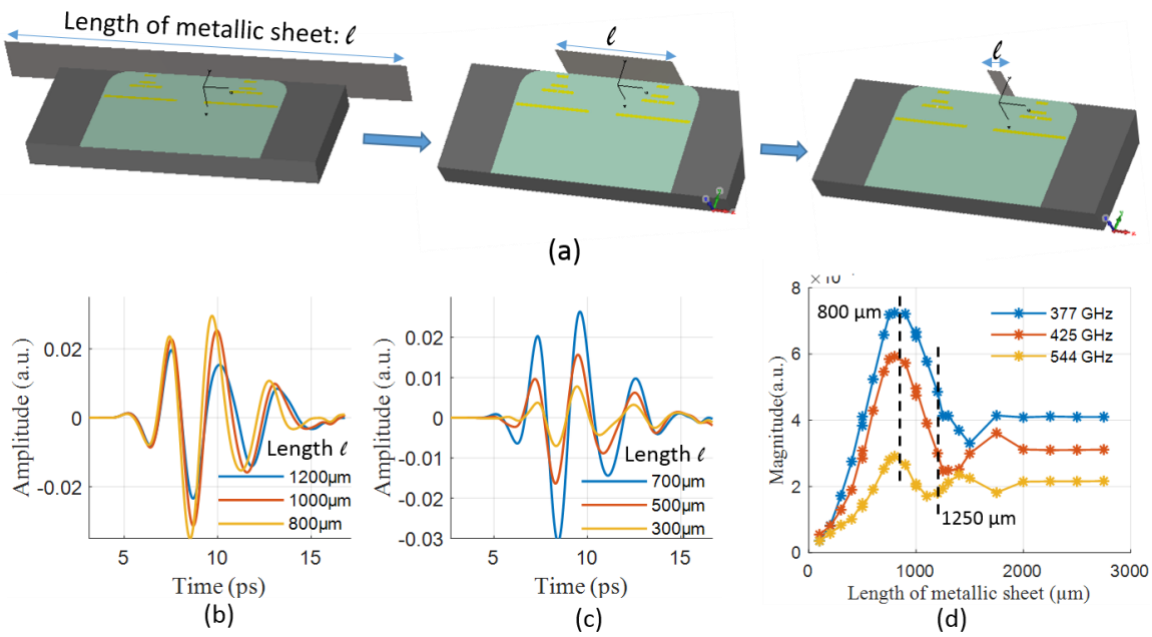

Figure II.17: (a) Simulation model in CST, including a simplified transceiver model and a metallic sheet with a varying length from 2750 µm to 100 µm. (b) Waveforms of reflected signals from the metal sheet with a length of 1200/100/800 µm. (c) Waveforms of reflected signals from the metal sheet with a length of 700/500/300 µm. (d) Magnitude of reflected signal as a function of sheet length at frequencies of 377 GHz, 425 GHz, and 544 GHz, respectively.

To clarify the origin of the dip at the center of the vertical bar shown in Figure II.16 (b), another simulation was performed to simulate a scan of a vertical bar in the y-direction. As shown in Figure II.18 (a), a metallic sheet of 0.3 *1 mm² move towards the right side during the simulation and the relative position of the metallic sheet (Δy) is calculated based on the distance from its center position with respect to the transceiver (illustrated in Figure II.18 (b)). Reflected signals obtained with relative distances of ± 200 µm (shown in Figure II.18 (c)) and of ± 400 µm (Figure II.18 (d)), have the exact same waveforms. It reveals that the time response of the transceiver as a function of the metallic sheet's position in the y-direction is symmetric with respect to the center. It is also demonstrated by the line profiles of the sheet shown in Figure II.18 (e), which was obtained from the magnitude of the frequency components by using FFT. Apart from the symmetrical property, a dip of magnitude can be observed at the center of the curves and the maximum value is achieved at both sides, which are similar to the experimental results.

It has been revealed that the strongest reflected signal can be achieved with an around 800 µm long metallic bar because reflected power from the sample can be more efficiently reflected. In this simulation, the length of the metallic sheet is 1000 µm. Since the response of the transceiver with respect to the position of the metallic sheet (Δy) is symmetric, only one side movement needs to be studied. Therefore, to achieve the maximum detected power, the sample should be moved 200 µm to one side. In this way, one end of the metallic sheet is in front of a PCA, resulting in better detection of reflections.

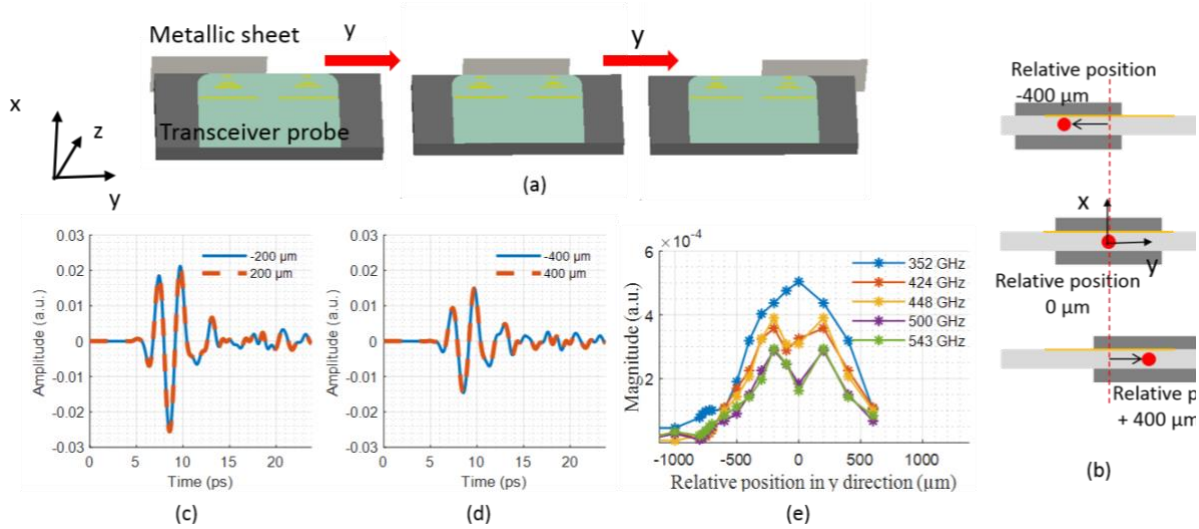

Figure II.18: (a) Simulation model in CST, including a simplified transceiver probe and a metallic sheet mowing in the y-direction. (b) View of the model in the xy-plane during the movement of the metallic sheet. The relative distance Δy in the y-direction between the metallic sheet and the transceiver probe tip is calculated with reference to the center of the transceiver probe. (c) and (d) Time responses of the transceiver when the metallic sheet is in different relative positions (Δy = ± 200, ±400 µm respectively). (e) Line profiles obtained at different frequencies varying from 352 GHz to 543 GHz.

Conclusion

The imaging resolution of the transceiver in the x-direction (perpendicular to the vertical bars) can reach up to 3.17 lp/mm at a frequency of 791 GHz with a working distance around 110 µm, which means that vertical bars with a width of 175.49 µm can be distinguished (contrast > 0.4). By means of 3D full-wave simulations, it has been revealed that the surrounding of the targeted object, especially the zone that receives radiations from the backside of the transceiver, contributes as well to the detected signal by the transceiver. This fact can serve to explain the uneven amplitude of the three bars in the same element. Besides, it is demonstrated that the distance between the two PCAs cannot be ignored during the near field measurement and the strongest reflected signal can be detected when the sample has a size comparable to the separation between two PCAs, around 700 - 800 µm.

II.2.2.3. Image of horizontal bars in group 1

As depicted in Figure II.19 (a), while vertical bars in group 1 can be distinguished by selecting a suitable frequency component, the image of horizontal bars remained ambiguous. Although four zones of element patterns (element 1 to 4) can be recognized, three horizontal bars inside the element pattern cannot be differentiated. Instead of three high-amplitude peaks reflected by metal-covered bars, two high peaks at the center and two small peaks can be observed in the line profiles shown in Figure II.19 (b).

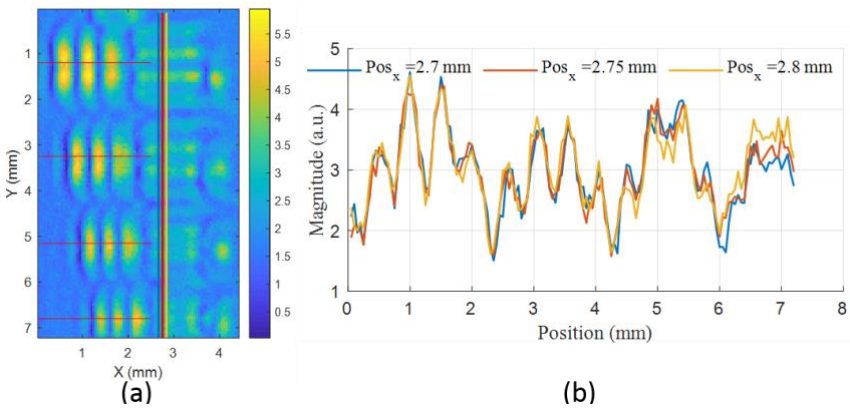

Figure II.19: (a) Image of element 1 to 4 in group 1 of 1951 USAF test resolution chart obtained at a frequency of 659 GHz (b) Line profiles corresponding to marked color lines in the left.

To understand this unresolved image result, it is important to realize that the width of horizontal bars in group 1 varies from 250 µm to 176 µm, smaller than the wavelength of emitted waves (300 GHz to 800 GHz, corresponding to 1 mm to 375 µm). When emitted waves arrive at the interface with horizontal bars, diffraction may take place and one part of the waves travels through and one part of power is reflected. Most importantly, since the area in front of the transceiver between two PCAs is composed of two different materials (glass substrate and metal-covered bars), the complex geometry and material composition make it more difficult to predict or to interpreted the response of the transceiver. To sum up, this transceiver probe has limited imaging resolution in the y-direction (parallel to the two-PCAs axis). The object with subwavelength-dimension feature or smaller than the separation of the PCAs cannot be spatially resolved. If a high-quality image with high resolution in both directions is required, two raster scan should be performed to provide correct information about vertical and horizontal features.

II.2.3. Conclusion

In addition to the development on PCA transceivers in the literature, the properties and the imaging performances of a double-PCA lens-free transceiver are studied in this section by taking advantage of 3D full-wave simulations and experiments. It is verified that the transceiver operates efficiently in the frequency band from 400 GHz to 600 GHz. Its bandwidth can be further extended by decreasing the working distance, reaching up to 300 - 800 GHz. In regard to the imaging capabilities, a resolution of 3.17 lp/mm was obtained at a frequency of 791 GHz in the direction perpendicular to the two-PCAs axis. However, the imaging resolution is limited in the other direction due to the unique double-PCA design. In fact, the choice of the waveguide is partly determined by the properties of the transceiver such as its emission pattern, frequency band. These preliminary studies provide valuable information to select a suitable waveguide to construct a guided terahertz reflectometry system in pulse mode.

II.3. Terahertz FMCW radar transceiver units

Apart from optical-pumped transceivers, there are many transceivers developed in the RF and microwave bands. As a commonly used concept, transceiver modules have a wide application scope in the electronic systems, such as in radars or sensors. As the operating frequency of electronic devices increases, more and more terahertz transceivers are available in the market, they can be divided into

two categories: transceiver in CW modes or in FMCW mode. These transceivers are usually realized by the integration of two individual detector and emitter modules into one device. This part provides more information about FMCW radars, including their architectures, working principles. In particular, two specific radar transceiver units are introduced with details: (i) III-V based 100 GHz SynView unit and (ii) 122 GHz Si-based radar chip.

II.3.1. FMCW radar working principle

The continuous scaling of Si-based on-chip transistors and the investigations into III-V technologies (such as InP-based transistors) push up the operating frequency of electronic devices towards the terahertz regime. On this basis, high-speed electronic devices with low power consumption, high switch speed and better compactness have been developed in the terahertz frequency region. Being cost-effective systems supported by continuously improved fabrication techniques, solid-state terahertz devices play an important role in academic researches and industrial applications. Compared to a conventional continuous-wave (CW) system combined with reconstruction approaches such as Shape from focus [156] and Computed tomography [155], a terahertz Frequency-Modulated Continuous-Wave (FMCW) radar unit can natively provide supplementary phase information for result analysis and to simplify 3D reconstruction process. In particular, exploiting an FMCW system in conjunction with a simple quasi-optical method (using lenses or parabolic mirror) allows in-depth measurements for quality control or defect detection. It combines the high sensitivity possessed by FMCW signal with the penetration capabilities of terahertz waves. Based on those benefits, wideband FMCW Radars have found suitable applications in the automobile, aerospace industry [194], [53] and art-painting diagnosis [54] amongst others for their non-destructive testing capabilities.

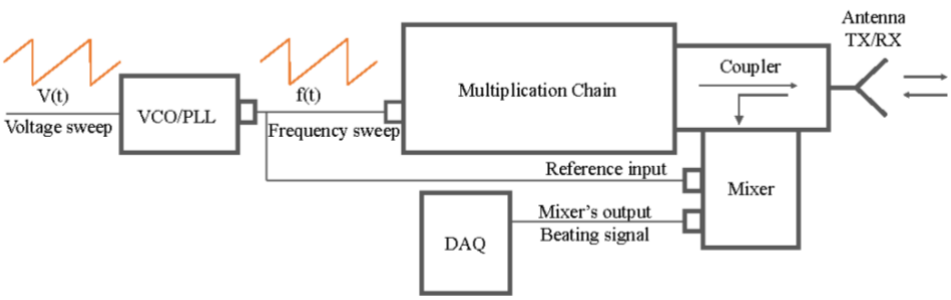

Figure II.20: Simplified architecture of a monostatic FMCW radar transceiver.

The typical implementation of a mono-static radar transceiver (including both transmitter and receiver modules) is given in Figure II.20, in which a linear FMCW reference signal is generated at low frequency by a Voltage Control Oscillator (VCO) or a Phase Locked Loop (PLL) oscillator. This reference signal is then fed into the frequency multiplication chain for signal up-conversion to reach the desired operating frequency band. A 3-ports coupler leads this probing signal towards the emission antenna while redirecting the reflected signal towards the mixing unit for down-conversion. Based on well-developed Si-based IC technologies and advanced packaging techniques, similar bi-static architectures with a full integration are also practicable. Consequently, the partition between the emitting chain and the receiving unit is required, resulting in a complexification of the system.

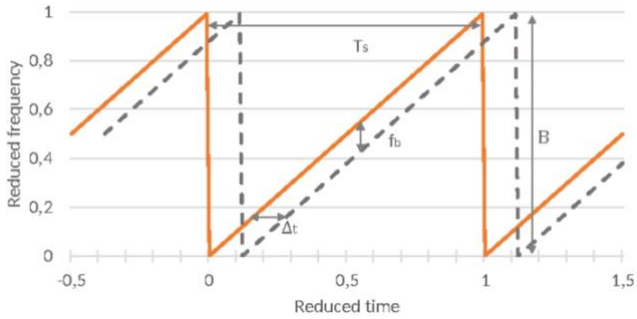

Figure II.21: Working principle of distance detection using frequency modulation continuous wave radar signal. While the solid line represents the reference radar signal, the dashed line denotes the reflected signal from the sample.

As depicted in Figure II.21, the reflected signal (dash line) from the target is delayed by Δt with respect to the reference signal (solid line) and thus gives rise to a beating signal at a frequency of f_b. This beating signal contains amplitude and phase information, depending on the distance to the sample d and the chirp slope, *i.e.*, the rate of change of frequency $\frac{B}{T_s}$. Their relation is given in Equation (8) below:

$$f_b = \frac{B}{T_s}\,\Delta t \tag{8}$$

where B denotes the sweep frequency bandwidth and T_s represents the period of a sweep cycle. The distance d to the object can be derived from f_b and FMCW radar setup parameters, expressed in Equation (9). It implies that the longitudinal resolution is limited by the bandwidth of radar signal B.

$$d = \frac{\Delta t}{2}\,\frac{c_o}{n} = \frac{c_o}{n}.\frac{f_b\,\frac{T_s}{B}}{2} \tag{9}$$

where n is the optical refractive index of the propagation media and c_o is the speed of light in vacuum.

When multiple targets are involved, the contribution of each object on the received signal is expressed as a distance-related beating frequency f_b. By means of simple data processing, FMCW technique enables remoteness sensing possibilities and in-depth measurement. This auxiliary feature is meaningful for the analysis of multilayer materials in industries. In particular, the phase information provided by FMCW radar signal is extremely valuable to differentiate the contributions of the sample from the reflections induced along the waveguide in a guided reflectometry system. Compared to the same configuration exploiting CW sources, FMCW radar signal allows localizing the targeted zone and giving rise to an enhanced dynamic range. That is the primary motivation for applying terahertz FMCW radar units rather than CW sources to construct a guided reflectometry setup.

II.3.2. SynView FMCW radar module

Recently, III-V based transistors have attracted increasing attention due to their advantages in terms of electron mobility, thermal conductivity and operating voltages. Their maximum frequencies can easily exceed 1 THz, which makes it possible to realize highly integrated, powerful complex transmitter and receiver at higher terahertz frequencies. Thanks to the Schottky diodes implementation, 2 THz [195] frequency multiplication chains are achievable. Despite all mentioned advantages, III/V-based integrated MMIC [196] displays high-frequency implementation limitations. To address this issue,

hybrid integration is proposed as a solution for high-end applications. A high-frequency device can be established through fine-tuning of a succession of components in discrete waveguide blocks [194], [197].

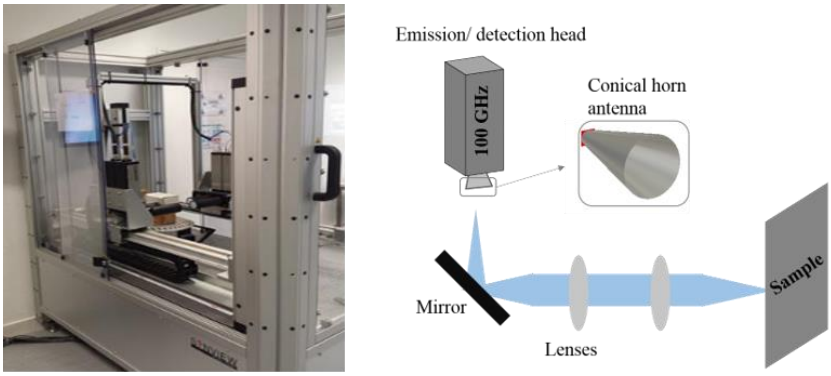

(a) (b)

Figure II.22: (a) Photograph of SynView system setup. (b) Schematic diagram of Synwiew radar system in reflection configuration with 100 GHz head. The closeup view illustrates the conical horn antenna used as Tx and Rx in the 100 GHz transceiver head.

III-V based radars have been demonstrated at 300 GHz and 600 GHz for different application cases, and solutions up to 850 GHz are developed by SynView GmbH. Figure II.22 (a) shows a SynView system composed of 4 radar heads, 3D motion control translation stages for radar units and relevant mechanical supports. The equipped radar heads are a pair of SynView Scan 100 heads (frequency range of 75-110 GHz) and a pair of SynView Scan 300 heads (frequency range of 230-320 GHz) respectively. While two heads (transceiver and receiver respectively) should be implemented in transmission mode setup for signal emission and detection, only one transceiver head is required in reflection configuration. Figure II.22 (b) illustrates the experimental setup in reflection geometry using the quasi-optical method. By focusing the radar signal beam with HDPE lenses, this FMCW system can be used for sensing and imaging purposes. During the measurements, a sample is fixed at the focal plane of the lens and selected heads move simultaneously to acquire data. Being an efficient imaging device, SynView system allows for measurements at two frequency bands in both transmission and reflection configuration simultaneously.

Emission pattern of conical horn antenna

A 100 GHz SynView FMCW transceiver head provides 50 dB measurement dynamics. A conical horn antenna acts as a Tx (transmission) and Rx (reception) antenna to ensure the functionality of this transceiver head in a mono-static block-integrated architecture. Single antenna configuration simplifies the coupling process between a transceiver unit and a waveguide, therefore this mono-static architecture transceiver is selected to construct a guided terahertz FMCW reflectometry system. Prior to constructing a guided reflectometry system, the radiation pattern of the horn antenna was investigated to provide essential information for the selection of a suitable waveguide. Based on the measured dimensions (shown in Figure II.23), a conical horn antenna model was created in CST. To simplify the calculation, the components before the horn antenna was not included in the simulation model. Instead, the circular input facet of the conical horn antenna was selected as a waveguide port for signal excitation covering the frequency band from 88 GHz to 110 GHz. Once the excitation signal is fed into the horn antenna, most of the energy is radiated efficiently into free space as a narrow beam thanks to the gradual impedance change in horn antenna. Figure II.24(a) depicts a 3D plot radiation pattern of the antenna at

a frequency of 100 GHz. A maximum directivity of 20 dBi is obtained in the direction of the antenna. While an angular width of 14.4 ° is obtained in the xz-plane (shown in Figure II.24(b)), a larger angular width of 24.1° is achieved in the yz-plane (shown in Figure II.24(c)). A satisfactory directivity and beam size in the far field is reached, ensuring the measurements using an optical method with lenses.

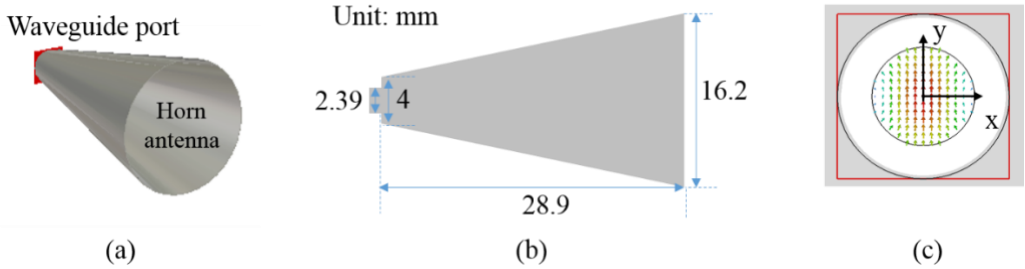

Figure II.23: (a) Simulation model of the conical horn antenna integrated in the 100 GHz synView radar head and its dimensions (b). (c) shows the excitation mode by the waveguide mode through a circular waveguide interface. (TE mode).

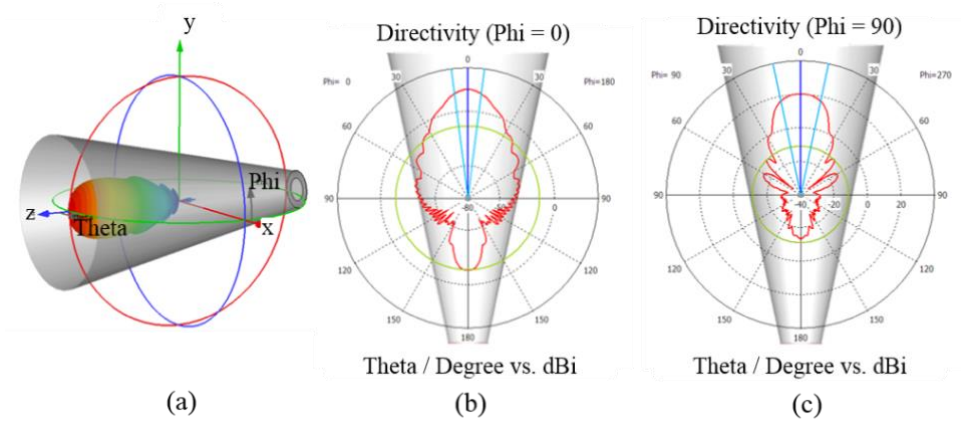

Figure II.24: Directivity-based radiation pattern of the conical horn antenna at a frequency of 100 GHz. It includes (a) a 3D plot, (b) a 2D polar diagram in the xz-plane at ϕ= 0°, and (c) a polar diagram in the yz-plane at ϕ= 90°.

Electric field distribution inside the horn antenna

The emission pattern indicating the direction in which the emitted waves radiate, only validates in the far field. Considering the dimensions of this horn antenna (outer diameter =16.2 mm), it is of interest to insert a waveguide inside the antenna to achieve a higher coupled power. Therefore, the electric field properties inside the antenna were as well simulated. Figure II.25 (a) and (b) provide the electric-field energy density in the yz-plane, xz-plane and xy planes at a frequency of 100 GHz. It can be observed that waves are radiated out of the horn antenna in a narrow beam. Instead of a symmetric Gaussian beam, the electric field of the emitted beam is more tightly confined in the y-direction than in the x-direction. It is noted that the electric field is more tightly confined at the center in the area of from z = 10 mm to z = 15 mm (Figure II.25 (a)). The E-energy density at the cross-section of z = 10 mm and z = 25 mm are provided in Figure II.25 (b) I and beam profiles in x and y direction are given in (c-d). Compared to the beam profile at z = 25 mm, the maximum E-field energy density at z = 10 mm is 2.5 times stronger and the Full Widths at Half Maximum (FWHM) of the radiated beam is smaller (4 mm/ 6 mm in comparison to 8 mm/5 mm in the x/y direction respectively. Depending on the selected

waveguide, an optimized insertion position may be achieved, which will be discussed in Chapter III. to construct a guided FMCW radar reflectometry system.

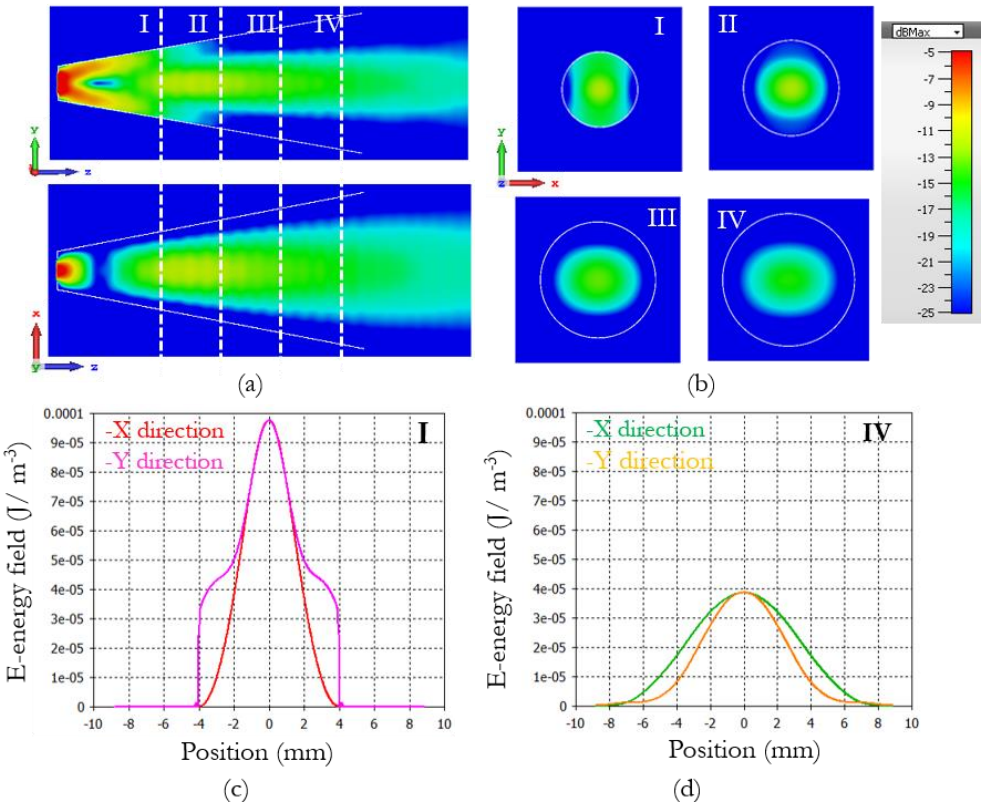

Figure II.25: Electric field energy density distribution inside the horn antenna at a frequency of 100 GHz (nearfield distribution). (a) E-energy density on the yz-plane and xz-plane. (b) E-energy density in the xy-plane at the position of z = 10, 15, 20 and 25 mm. (c) and (d) Beam profiles in x and y directions at the position of z = 10 (Position II) and 25 mm(Position IV) respectively. While FWHM at z = 10 mm is around 4 mm in both directions, 8 mm width in the x-direction and 5mm width in the y-direction are obtained in the xy-plane of z = 25 mm.

II.3.3. Silicon radar chip

By continuously scaling down the dimension of the Si-based transistors, the overall performances of electronic devices such as the operating frequency, the integration level is consistently enhanced. While the fabrication techniques of Si-based transistors are being improved, the production cost of the Si-based device is continuously lowering. Thanks to the high integration level, low-cost and versatility, Si-based FMCW radar transceivers are drawing attention in industrial fields. As an example, various radar designs for automotive applications [198] have been developed in the 77 GHz band instead of 24 GHz band with bi-static architectures. It should be noted that although the scaling helps to obtain higher density and efficiency in the IC system, the maximum oscillation frequency of Si-based transistor does not scale up simultaneously. The low speed of silicon MOSFET and bipolar transistor begins to limit the IC's development in the terahertz region above 300 GHz.

While III-V technologies offer possibilities to develop high frequency, high power, low noise devices, the great strength of Si-based technologies lies in its high integration level, large yield at low cost. A 120 GHz radar transceiver based on SiGe technology [199], [200] is developed by Silicon-Radar GmbH. Apart from the 245 GHz radar unit under development [201], this transceiver is the only

commercially available Si-based radar unit above 100 GHz. This radar unit is characterized by miniaturization, high measurement resolution, and low-cost. As shown in Figure II.26 (a), the radar front end is realized in a QFN package with a size of 8x8 mm. Operating in FMCW mode, this transceiver chip can offer a full tuning frequency range up to 7 GHz (119-126 GHz). Different from the aforementioned SynView FMCW radar system, its main field of application is in a short range radar system for distance and speed detection. By using dielectric lenses, depicted in Figure II.26 (b), the detection range can be increased to 10 meters and beyond 100 meters. Moreover, this optical method allows to conduct an investigation of a material surfaces, to perform a measurement of layer thicknesses and other properties of the measurement objects. Figure II.26 (c) shows a compact subsystem composed of a 122 GHz transceiver and an adapted objective fabricated by 3D-printed technique, which are developed by Laser & Terahertz team in the IMS laboratory for low-cost imaging purpose.

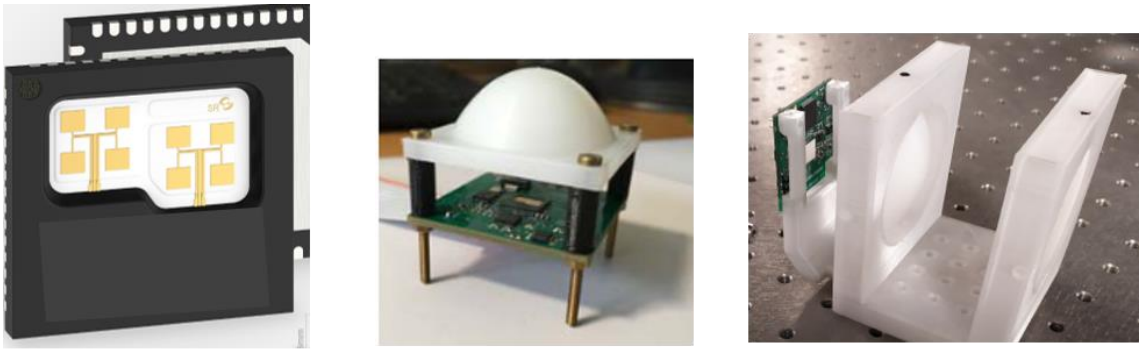

(a) (b) (c)

Figure II.26: (a) Photography of a 122 GHz radar transceiver chip. (b) Photograph of a 122 GHz radar transceiver in conjunction with the HDPE lens, proposed by Silicon Radar GmbH. (c) Photograph of a 122 GHz radar transceiver chip with an adapted objective composed of two 3D printed lens, proposed by the research team in IMS laboratory.

Radiation pattern of planar patch antennas

Being low-cost, low-profile, easily fabricated antennas, patch antennas have been widely deployed in different frequency regions for diverse applications. The widespread use of mobile phones is a good example. This planar antenna design has also been applied in the 122 GHz FMCW radar transceiver chip to ensure the apparition of the transmitting and receiving units in a small dimension. Prior to integrating this FMCW radar into a guided reflectometry system, the radiation pattern of planar antennas on the transceiver unit is investigated.

As shown in Figure II.26(a), two 2x2 patch array antennas are on the surface of the transceiver chip (which are then covered by a ceramic layer as protection), acting as Tx and Rx antennas respectively. They are coupled to the integrated circuit to enable the functionality of the radar transceiver. Figure II.27 (a) displays the simulation model of the transceiver chip created in reference to the actual dimensions of patch antennas. Two waveguide ports were connected to the feed lines to excite and detect signals. The excitation signal covered the frequency band from 110 GHz to 130 GHz. All the boundary conditions were set as “Open add” and no material loss was considered in this simulation. Figure II.27 (b) shows the scattering parameters S_{11} of the Tx antenna, representing return loss caused by the impedance mismatch at the input of the antenna. It can be seen that a minimum return loss (corresponding to the smallest S_{11} of -25 dB) is obtained at a frequency of 125 GHz. Determined by radiation efficiency and impedance mismatch loss, the total efficiency of the Tx antenna is higher

than 58% in the full tuning frequency band (119 -126 GHz), ensuring the wide-band operation of the transceiver in FMCW mode. In comparison to lower frequencies, high-frequency components around 125 GHz are more efficiently radiated into free space by the antenna.

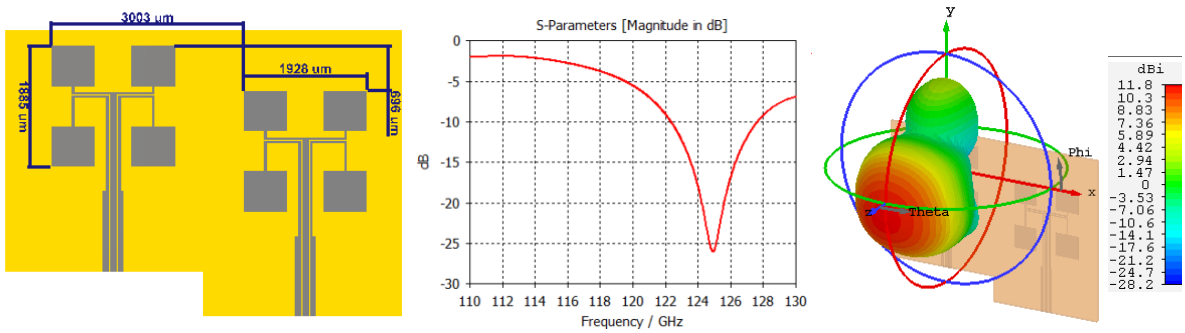

(a) (b) (c)

Figure II.27: (a) Schematic of 2x2 patch antennas acting as Tx and Rx on the radar transceiver front-end. (b) S-parameter S_{11} of patch antenna Tx as a function of frequency. (c) 3D emission pattern of Tx antenna at the frequency of 122 GHz. The maximum directivity is 11.4 dBi, while the angular width in the xz-plane and yz-plane is 48.4 and 46.7° respectively.

Figure II.27 (c) provides a directivity-based 3D plot of the radiation pattern of the Tx antenna operating at the frequency of 122 GHz. A maximum directivity of 11.4 dBi together with an angular width of 47° and 48° on the xz-plane and yz-plane respectively is achieved, corresponding to a typical response of such patch array antennas design.

II.3.4. Conclusion

In addition to the basic principle of FMCW radars, the structure and radiation pattern of a III-V technology based 100 GHz SynView transceiver head and a SiGe-based 122 GHz transceiver chip were studied respectively. Their respective geometries and performances impose requirements on the choice of the waveguide. The knowledge about transceivers allows to achieve a better understanding of propagation behaviors of waves in a guided reflectometry system.

II.4. Thin-wall hollow-core waveguides

A variety of waveguides based on RF waveguide and optical fiber designs has been developed in the terahertz band, offering more choices for diverse application. While metal wires, PPCWs, coax cables possess low dispersion for a broadband transmission, dielectric microwires exhibit low-loss propagation and flexibility. In regard to microstructured PCF waveguides, a better trade-off between the propagation loss and field confinement can be achieved. Considering the ultimate goal of this work is to construct a terahertz wave-guided reflectometry system with a transceiver unit (one of three options mentioned before), the properties of transceivers must be taken into consideration to select a suitable waveguide. The selected waveguide must match with the operating frequency band of the transceiver to support signal transmission from the transceiver towards a sample. Since the propagation behaviors of waves inside the system is controlled by a waveguide, its guiding modes with specific field distribution and propagation loss are worthy of attention, thus determining the performance limitations of the whole system. In particular, a great field confinement capacity allows a small beam, which is beneficial for high-resolution imaging probe. To enable the dynamic range of the measurement using the guided reflectometry system, a low-loss waveguide is wanted. To address the coupling issues, a

waveguide possessing a field distribution similar to the emission pattern of the transceiver seems to be a good choice.

Regarding the double-PCA lens-free transceiver, it operates efficiently in the frequency band of 400 GHz to 600 GHz, requiring a wideband transmission band. Considering the 700 μm separation between two PCAs of transceiver tip, the propagation area along a waveguide should be larger than this value to ensure the coupling between the emitter-waveguide and the receiver-waveguide simultaneously. With respect to 122 GHz silicon FMCW radar (119 GHz -126 GHz), a waveguide with a propagation area larger than 3 mm separation between two patch array antennas is preferred. Otherwise, supplementary devices such as beam splitter should be added in the system setup, leading to an unwanted complexity of the system configuration.

Although metal wires, coax cables can support a wideband transmission with low dispersion, radial polarization condition required to achieve efficient coupling cannot be meet by the double-PCA transceiver. A rectangular waveguide in WR-1.9 band (400 GHz to 600 GHz) is adapted to the frequency band of the double-PCA transceiver. Yet, its small cross-section of 0.483*0.241 mm² cannot ensure the coupling between two PCAs of transceiver and the waveguide at the same time. While PPCW can provide a low-dispersion transmission with linear polarization, the implementation of two parallel plates with small gap is not easy. Despite their respective advantages, previously-mentioned metallic waveguides are unsuitable choices for selected transceiver units due to unsuited dimensions, mismatched polarization condition and difficulties of implementation. Fortunately, a variety of dielectric waveguides based on optical fiber design has been developed in the terahertz band, offering more choices as a communication channel between the transceiver and sample. Given the difficulties in holding and the subwavelength size, dielectric microwires are less attractive for the selected transceivers. While a solid-core waveguide exploiting modified total internal reflections can provide a large transmission band, its propagation loss is strongly dependent on the material absorption of the core material. Due to the lack of the low-loss terahertz materials, this type of waveguide is not the best choice for a terahertz wave-guided reflectometry system. A porous-core waveguide (both air-clad and microstructured one) seems to be a suitable option with lowered propagation losses. Nevertheless, its availability is limited in certain laboratories and the existing fabrication techniques are not optimized for complex microstructure. The quality of the waveguide cannot be guaranteed. Although these dielectric waveguides show advantages in terms of the propagation loss, flexibility or the filed confinement, they are not suitable/available to build up a terahertz wave-guided reflectometry system.

After taking account of the availability, propagation properties and implementation difficulties, the hollow-core thin-wall waveguide is considered as the best candidate for a terahertz wave-guided reflectometry system. With a single “ring” structure, a hollow-core thin-wall waveguide can guide the waves in the air core with low losses by exploiting anti-resonant reflections at non-resonant frequencies of the cladding. A thin cladding can provide wide transmission bands, benefiting the transmission of the pulse signal emitted by the double-PCA lens-free transceiver (frequency band covering from 400 GHz to 600 GHz). The previous studies have revealed that while the diameter of the waveguide has no impact on the transmission band, it alters the propagation loss of the fundamental mode of the waveguide. To obtain a low-loss propagation, a larger diameter is wanted. In view of the distance between two PCAs of the transceiver (~700 μm), a diameter larger than this separation is required to facilitate the coupling process. In the case of the 122 GHz radar with the separation of around 3 mm, a waveguide with a larger diameter is demanded.

The advantages of the anti-resonant waveguide have been highlighted to justify the choice of the selected waveguide. On this basis, two hollow-core thin-wall dielectric waveguides with different dimensions and cladding materials were selected as a suitable candidate to integrate into the guided terahertz reflectometry system with the aforementioned transceiver units: a 3 mm diameter silica thin-wall waveguide and a 6 mm diameter plastic thin-wall waveguide. Their transmission properties are verified through a THz-TDS measurement, and corresponding results are presented in the following part. Standing as an innovative fabrication process, the additive manufacturing (3D printing) technique, that allows fast cost-efficient waveguide development chain, is presented at the end of this chapter.

II.4.1. Fused silica hollow-core waveguide

In view of the foregoing, a silica hollow-core thin-wall waveguide with a diameter of 3 mm and a cladding thickness of 130 µm (shown in Figure II.28 (a)) was selected to work with the terahertz double-PCA transceiver. A time-domain spectroscopic measurement was performed with a slice of fused silica to assess its material properties. The obtained result is shown in Figure II.28 (b), including the refractive index and extinction coefficient as a function of the frequency. It can be seen that the material loss increases with frequencies in the terahertz band. For the frequencies below 2 THz, the refractive index of the used silica is around 1.935, and the corresponding absorption coefficient is in the order of several cm^{-1}. The extracted results are consistent with the value (1.95±0.05) given in the literature [148]. The mean value of the refractive index (n = 1.935) was used to calculate the resonant frequencies. Based on Equation (5), the transmission dips, *i.e.*, the resonant frequencies of the silica cladding, are anticipated at frequencies of around 0.70 THz, 1.39 THz, 2.09 THz and 2.78 THz.

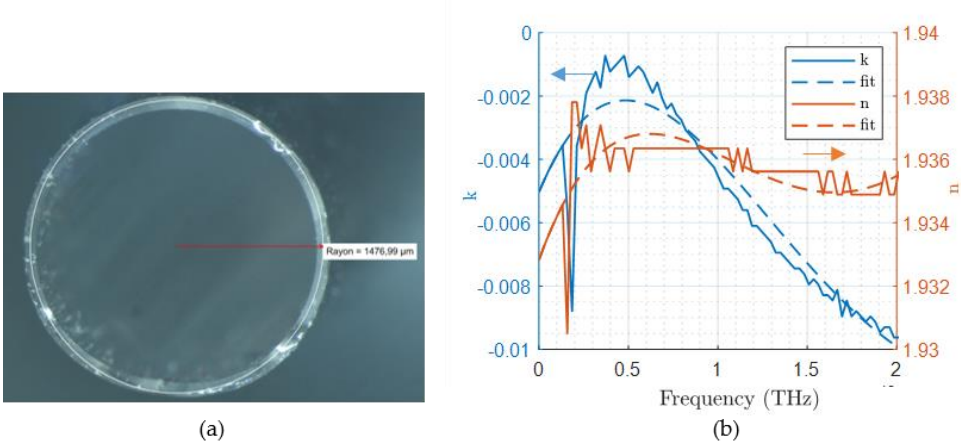

Figure II.28: (a) Microscope photograph of the silica hollow-core thin-wall waveguide. (b) Extracted material properties of the fused silica as a function of the frequency.

Transmission characterization results

In order to verify the propagation properties of this thin-wall anti-resonant waveguide, measurements in transmission configuration were performed with a commercial fiber-coupled THz-TDS system (Teraview Terapulse 4000) with an effective frequency band ranging from 0.1 to 3 THz. Since the beam size out of the PCA emitter is around tens of millimeters, a polyethylene lens was added before the waveguide to focus the THz beam, providing a preferential excitation for core modes. A diaphragm was added at the beginning of the propagation path to filter out the unguided power fraction in free space. The transmitted signal was detected and recorded by the PCA receiver on the other side. It should be pointed out that the cut-back method was not performed due to the cleaving difficulties on

a thin-wall silica waveguide. Instead, two waveguides with different lengths (201 and 301 mm respectively) were characterized in transmission configuration.

Figure II.29 (a) and (b) display the transmitted signals through two waveguides and their corresponding spectra respectively. The distortion and the broadening of the transmitted signals shows the dispersive propagation properties of the waveguide. By extending the time window, signals in higher-order modes with a considerable time delay of around 50 ps can be observed (not shown in the figure), which mainly lies in the frequency region around 200 GHz. As depicted in Figure II.29 (b), the dips in the spectrum of the transmitted signals (marked by the black dot-dash lines) correspond appropriately to the calculated resonant frequencies, confirming the waveguide's guiding mechanism. Between the resonant frequencies of the cladding, several low-loss transmission bands appear around the frequencies of 500 GHz, 1.2 THz and 1.71 THz. The first transmission band is roughly from 400 GHz to 600 GHz, matching the main operating frequency band of the transceiver.

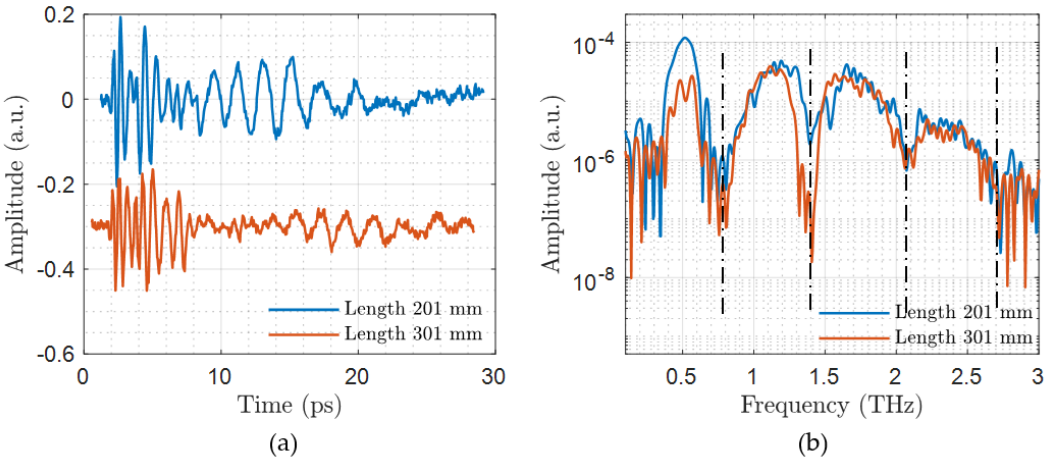

Figure II.29: Transmitted signals (a) and corresponding spectra (b) through silica hollow-core pipe waveguides with different lengths. Blue curves: silica waveguide with a length of 201 mm. Red curves: silica waveguide with a length of 301 mm.

In regard to the propagation loss, no significant attenuation is observed between two measurements for frequency higher than 1 THz, indicating the low-loss propagation properties of the waveguide. However, an important attenuation coefficient of 0.33 cm^{-1} at the frequency of 500 GHz can be deduced from the two measurements, which is higher than previously reported results in the order of 10^{-2} cm^{-1}[149],[148]. Compared to the waveguides possessing a diameter of 5/7/9 mm diameter in [146], silica thin-wall waveguide has a much smaller diameter (3 mm) and the higher material absorption, resulting in more significant propagation loss in air-core mode. Limited by the SNR of the TDS system, a much longer waveguide is required to estimate the absorption coefficient at high frequencies. It should be pointed out that although careful attention was paid to maintain the same coupling condition, small differences may exist, giving rise to the higher transmitted power through the longer waveguide.

In addition to the transmission band and propagation losses, the field distribution along the waveguide is as well of interest. By varying the aperture of the diaphragm across the waveguide, the leaked field outside of the waveguide was studied. When the diaphragm across the waveguide is closed, transmission spectral dips related to the resonant frequencies remain clear, indicating that most of the guided waves propagate in the air core. As the aperture of the diaphragm increases, more power lying in the lower part of the spectrum (from 300 GHz to 600 GHz) is transmitted, while few changes of high-

frequency components occur. It reveals that waves at lower frequencies are less tightly confined, and one part of guided waves exceeds the cladding structure.

Reflection characterization results

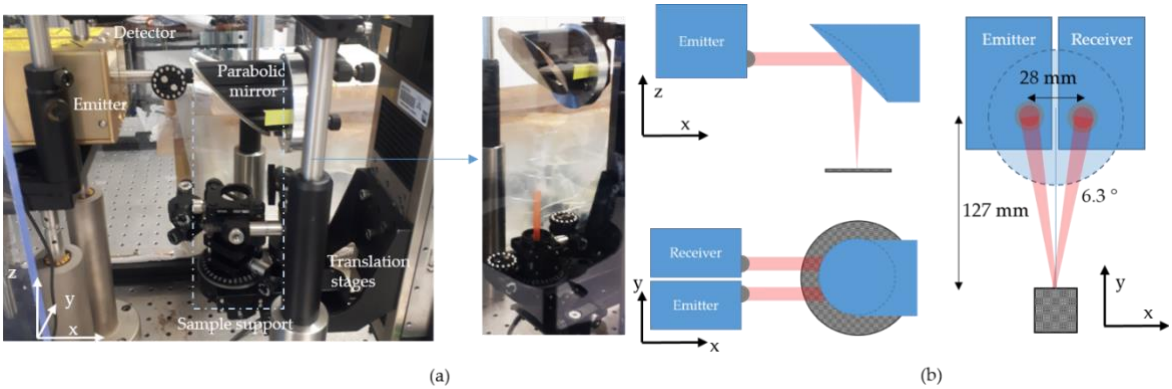

Figure II.30: (a) Photographs of experimental setup in reflection, without sample (left) and with a plastic hollow-core waveguide (right). (b) Simplified schematic diagrams of the experimental setup.

The aforementioned measurement results in transmission mode demonstrate that this silica waveguide has a large carrying bandwidth from 400 GHz up to 600 GHz, matching the operating frequency band of the transceiver. Since the final usage of this thin-wall silica waveguide is in reflection geometry, a measurement in reflection-mode with a short waveguide was as well performed. As shown in Figure II.30, a parabolic mirror were used to focus the emitted beams before entering the waveguide and to collect the reflected signal to the receiver. The entrance of the waveguide was placed at the focus plane of the parabolic mirrors and a metal plate is positioned at the end of the waveguide to obtain the maximum reflection.

The spectrum of the reflected signal is shown in Figure II.31, in which resonant frequencies of the cladding can be identified appropriately. Since the waveguide under test is much shorter than the ones in transmission mode, less propagation loss gives rise to a higher detected power. In particular, the power fraction lying in the first transmission band around 500 GHz is significantly less than the ones in the frequency band around 1THz. Depending on the wavelength, frequency components obtain different beam width after passing through the parabolic mirrors, *i.e.*, the excitation condition varies as frequencies. The larger beamwidth at lower frequencies leads to a poor coupling efficiency between the emitted waves and the waveguide. These phenomena emphasize the importance of an optimized coupling condition.

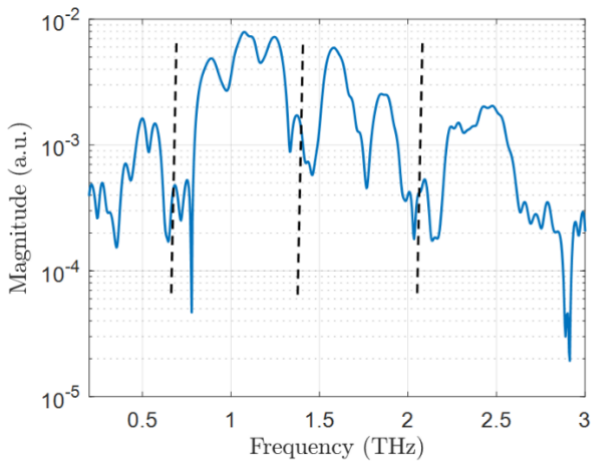

Figure II.31: Spectrum of the reflected signals via a silica hollow-core waveguide.

II.4.2. Plastic thin-wall waveguide

The same method was applied to access the propagation properties of a plastic hollow-core waveguide: the assessment of the material properties, prediction about the resonant frequencies of the cladding, and verifications of transmission dips by THz-TDS measurements. As shown in Figure II.32 (a), the selected plastic pipe waveguide has a diameter of 6 mm and a cladding thickness of 158 µm. A time domain spectroscopy was performed with a small piece of the cladding to assess the material properties. The extracted refractive index and extinction coefficient as a function of the frequency are shown in Figure II.32(b). The absorption coefficient is < 0.8 cm^{-1} at frequencies below 2THz and the value of 1.49 was taken as the refractive index of the plastic to calculate the resonant frequencies. By applying Equation (5), the transmission dips were anticipated at frequencies of around 0.86 THz, 1.72 THz and 2.58 THz. The same experimental setups were used to characterize this plastic waveguide, both in transmission (54 cm long) and in reflection modes (8 cm long). The detected time signals and corresponding spectra in two configurations are given in Figure II.32 (c-f). The dips of the transmission and reflection spectra are identified in the vicinity of the calculated resonant frequencies, confirming the anti-resonant guiding mechanism. The slight shift of the resonant frequencies may be associated with the inhomogeneity of the cladding caused by the fabrication. While the same spectral features can be identified in two experiments, it is remarkable that the waveform of the detected signal in transmission (Figure II.32 (c)) is different from the one obtained in reflection mode (Figure II.32 (e)), which may be related to the different excitation condition and propagation length. It is worth noting that since the entrance of this waveguide is much larger, the beam size as a function of the frequency does not play an important role during the coupling process. The reflected power fraction in the transmission band around 500 GHz is comparable to the one lying around 1 THz in the reflection geometry, unlike the previous case with a small entrance silica waveguide.

Considering the diameter of the plastic hollow-core thin-wall waveguide (6 mm), the propagation area in the air core can enable the direct coupling between the transceiver and the waveguide, both photoconductive transceiver and the FMCW radar units. The resonant frequencies of the plastic waveguides around 0.86 THz also provide a transmission band large enough for the pulsed signal emitted by a double-PCA transceiver. It should be noticed that although the used THz-TDS measurement system operates in the frequency region from 100 GHz to 3 THz, the measurement at the lower part of the spectrum (around 100 GHz) is not precise and it cannot be taken as reference. A transmission measurement with a 30 cm long plastic waveguide was performed by means of a vector

network analyzer (VNA) in the frequency band from the 75 GHz to 105 GHz. Two horn antennas were added to the output of the VNA for signal emission and detection. The waveguide was inserted inside the antennas for better coupling. The result shows that the attenuation is less than 4 dB after 30 cm propagation at the frequency around 100 GHz. The attenuation increases as the frequency decreases.

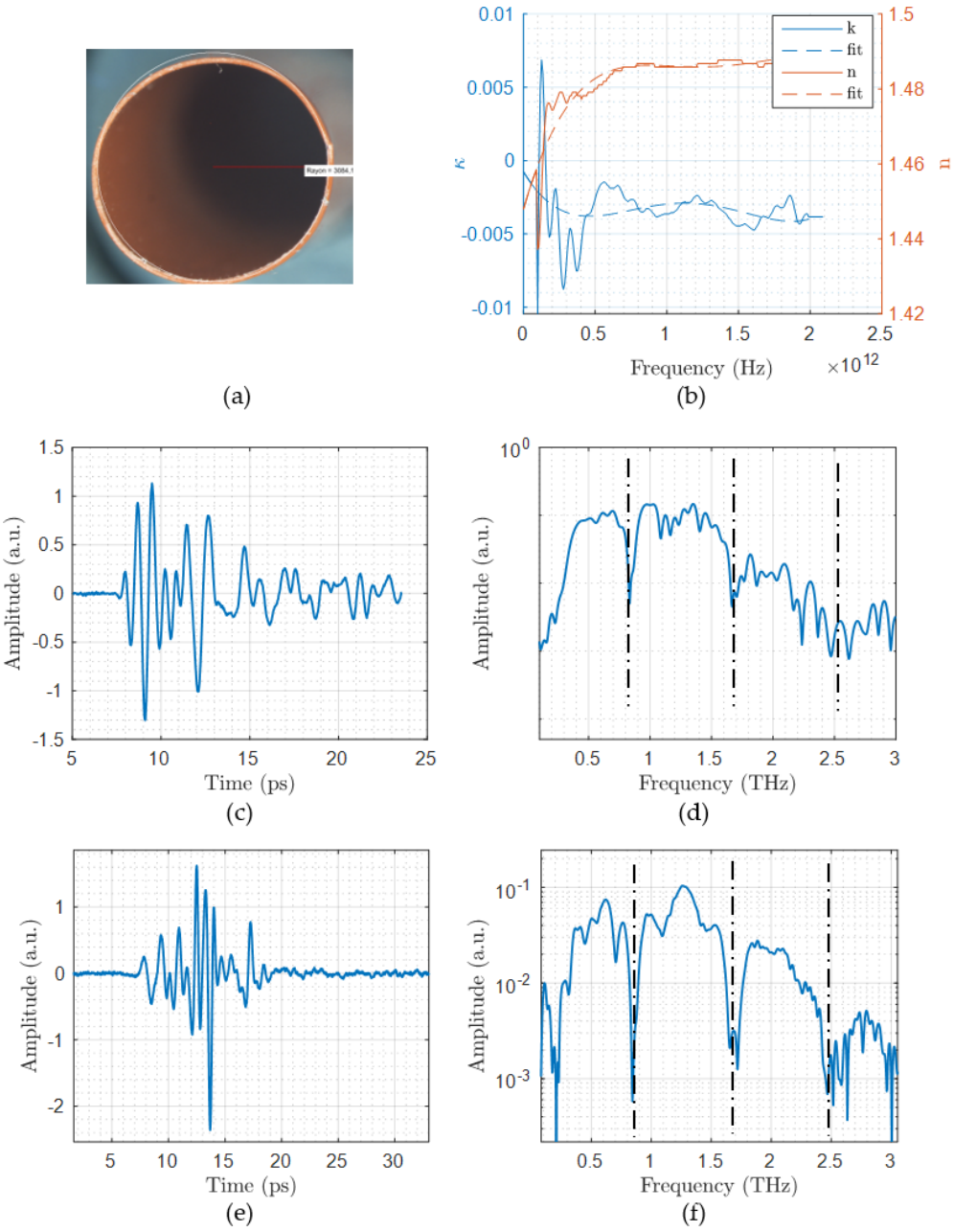

Figure II.32: (a) Microscope photograph of the hollow-core thin-wall waveguide. (b) Extracted material properties (refractive index and extinction coefficient) of the plastic as a function of the frequency. (c) Transmitted signals through a 54 cm-long-waveguide and (d) its corresponding transmission spectrum. (e) Reflected signals through an 8 cm-long-waveguide and (f) its corresponding spectrum.

II.5. 3D printed negative-curvature waveguide

In parallel to thin-wall pipe waveguides, negative curvature waveguides, firstly proposed in the optical domain (more details can be found in the review [202]), are also adapted in the terahertz region. This type of waveguide inhibits coupling between the core and cladding modes by the wavenumber mismatch conditions, consequently reducing the propagation loss of the fundamental mode.

II.5.1. State-of-the-art of negative curvature waveguides

Besides the study performed by Lu *et al.* in 2008[145], Vincetti L. conducted investigations into the propagation properties of a plastic hollow-core microstructured fiber by the numerical method in the following two years [203], [204], revealing that the transmission bands of the waveguide depend on the thickness of tubes. In 2013, a PMMA hollow-core waveguide composed of eight circular tube lattice was characterized [205] and a low loss of 0.16 dB/cm was demonstrated at the frequency of 0.828 THz. These microstructure waveguides (both designs and fabricated waveguides) are recognized as negative curvature waveguides instead of hollow-core photonic bandgap waveguide for two reasons. Firstly, dips of the transmission spectrum depend on the thickness of the tube lattice. Secondly, the periodic structure in the cladding has no influence on the propagation properties, which is distinct from the photonic bandgap waveguide.

The investigations conducted in the optical domain have revealed that the form, dimension, and the number of the tube lattices impact performances of a negative curvature waveguide, including the field confinement, transmission band, propagation losses, mode coupling, *etc.* Since the separation between the cladding tubes can eliminate additional resonances in the transmission bands, the nodes created by the contact of the tubes are suggested to avoid. Apart from twelve negative curvature waveguides [145] and the version with eight tubes [206], novel designs were proposed and tested in the terahertz region, including a waveguide with hypocycloid negative curvatures [207], the one with elliptical cladding [208] and nested negative curvatures waveguide [209]. In 2020, a novel design of hollow-core negative curvature with metal-wire inclusions is proposed to achieve a low-loss propagation with better confinement in the core [210]. An overall review of the negative curvature waveguides in the terahertz domain is given in Table 3, providing information about the proposed waveguide's structure and guiding performances.

TABLE 3. TERAHERTZ NEGATIVE CURVATURE WAVEGUIDES

Reference	Structure (Core-cladding) Hold material	Loss (cm-1), Targeted frequencies, Power fraction, Dispersion
2008, [145] Fabrication & Characterization 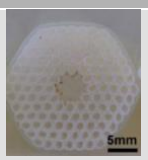	Teflon Air-core (d_{core} = 2.64, Λ = 5.5 mm) microstructure five-layer Cladding: hexagonal closet arrangement tube: Douter = 2.08, Dinner = 1.68, Λ = 2.08 mm	Loss of 0.002 cm-1 at 700 GHz
2009[203] and 2010 [204], Design & analysis. 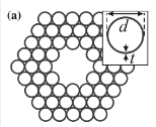	Teflon. Triangular lattice formed by a periodic arrangement of dielectric tubes of Teflon	Propagation loss four decades lower than bulk absorption.
2013 [205] Characterization 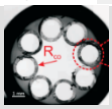	PMMA. Circular arrangement of dielectric tubes surrounded by a heat-shrink jacket. t = 252 um, Dtube = 1.99mm Dcore = 1.62*2 = 3.24 mm	Loss of 0.3 and 0.16 dB/cm for 0.375 THz and 0.828 THz respectively. Dispersion < 0.03 ps/nm km over a band of about 1.7 THz centered at 2.1 THz.
2015 [211]	Zonex. Eight circular tube lattice. t = 0.378 mm, Dtube = 2.4 mm Dcore = 3.84 mm	Loss of 0.01-0.05 dB/cm.
2018 [206] Fabrication & Characterization, 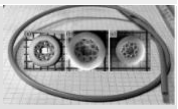	PP. Hollow-core fiber with a cladding of eight PP capillaries.	Loss of 7 dB/m at 2-2.2 THz. Dispersion < 1 ps/THz /cm.
2018 [209], Design and analysis 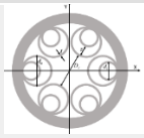	TOPAS. Anti-resonant node-free cladding tubes. DC = 3 mm, do = 2.6 mm; z = 1 mm t = 0.09 mm = 90 um .	Loss of 0.05dB/m at 1 THz. Wide dispersion flattened bandwidth of 0.6 THz.
2020[210] Design & Analysis 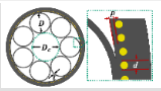	TOPAS, HC-ARRCF with metal inclusion.	Six-time lower loss compared to the tube lattice fiber at 700 GHz.

Compared to the thin-wall anti-resonant waveguides, negative curvature waveguides provide more design possibilities to optimize the propagation properties by modifying the cladding structures. Although their structure is much simpler than microstructured waveguides, the irregular forms (such as the semi-elliptical lattices) remain challenging for conventional fabrication techniques. On that account, more attention has been focused on 3D printing techniques.

II.5.2. 3D printed fabrication techniques

The conventional fabrication techniques developed in the optical domain face important challenges in the terahertz domain due to the change of the host material and the scaled-up high air-filling structure. Within such a context, the 3D printing technique has drawn increasing attention in the terahertz domain. In the *1980s*, the first 3D object was created via additive manufacturing layer by layer. According to the fabrication method, the additive manufacturing techniques can be divided into several categories: Fused Deposition Modeling (FDM), Stereolithography (SLA), Electron Beam Melting (EBM), Selective Laser Sintering (SLS), Polymer Jetting (Polyjet), and so on [212]. Different materials such as polymer, metal, biocompatible material, ceramic and organic compounds are available for these additive manufacturing processes. Various fields have benefited from these fabrication techniques, for instance, food, medical, pharmaceutical and mechanical domains [212]. In the microwaves and terahertz band, they have been deployed to fabricate metallic and dielectric waveguides [213], antennas [214], lens, couplers [215] and beam splitters [216] [217] over the last decade. The very first terahertz waveguide fabricated via a 3D printing technique was in 2011 [218].

Fused Deposition Modeling (FDM) technique extrudes the heated thermoplastic filaments (such as ABS, PC and PLA) through a nozzle and subsequently deposits materials on the building bed. As a result, the spatial resolution of this technique depends on the nozzle opening and the surface of the printed object commonly appears step defects. Overall, it is a cost-efficient technique for the application with a moderate resolution requirement. Stereolithography (SLA) process exploits a UV laser beam to scan the surface of a photo-resin tank to form each layer of the object. Being a high-precision technique, the platform is more costly. In the process of polymer jetting, a print head, in the first place, deposits thin layers of UV-curable construction tray, then UB lamps cure the deposited material. The spatial resolution of the Polyjet technique depends on the laser spot size. It is one of the most frequently used technique due to its cost-efficiency and good precision around 100 μm. These three techniques have been used to produce Bragg waveguides [219], [139], hollow-core PCFs [218], [220] and different negative curvature waveguides [207], [208], [221] . More examples are provided in Table 4, giving the details about the used materials, structures and corresponding guiding performances.

The precise reproduction of a designed structure requires great effort and time to optimize the facility's parameters. By taking advantage of 3D printing techniques, the fabrication process of a terahertz waveguide with a complex structure becomes faster and more cost-efficient, allowing to verify and to improve the performances of various novel waveguide designs. Apart from the direct fabrication, a 3D printer can be used to make up the preform of a waveguide with a complex structure before the drawing process, which benefits as well waveguides with structural dimension smaller than the precision of the printer. The potential of 3D printing techniques in the terahertz domains is enormous.

TABLE 4. 3D PRINTED TERAHERTZ DIELECTRIC WAVEGUIDES

Reference	3D printing method and hold material	Structure (Core-cladding)	Loss (cm-1)	Model
2011 [218], Photonic Bandgap	Polyjet, UV-curable polymer (n = 2.75, tangent loss = 0.02 near 150 GHz).	Rcore = 4.2 mm tair-cyclinder = 400 um	0.3dB/cm at 105 GHz (80-220 GHz)	
2015 [207] Negative curvature	FDM ABS (n = 1.6), resolution aorun 400 um	Dtotal = 25 mm, e = 0.5 mm, Rcore = 4.2 mm	0.3dB/cm at 0.47 THz	
2016 [220] PCF waveguide		hollow-core with Kagome PCF structured cladding	0.02 cm-1 for 0.2-1.0 THz Advantages: mechanically spiced.	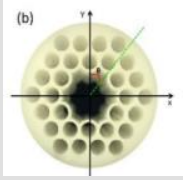
2017 [219] Bragg waveguide	SLA , UV –resin	both air and resin layer has a thickness of 512 um. Dcore = 4.5 mm (n = 1.63 at 0.3 THz, alpha = 2 cm-1)	0.65AT 0.35 THz	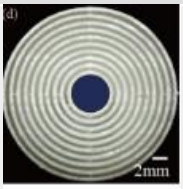
2018 [139] Bragg Waveguide	SLA, UV-resin n = 1.64 at 0.3 THz,	Dcore = 2*Rcore = 2*4.742 =9.484 mm	< 5dB/m = 0.05 dB /cm at 0.246-0.276 THz in HE11 mode	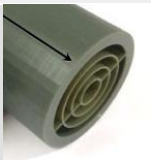
2018 [208] Negative curvatures	FDM printer, multiples of 0.6 mm . Polycarbonate PC (n = 1.6), absorption in the order of tens of dB/cm	Dcore = 6 mm/10/10 mm t= 0.6/0.6/1.2 mm elipse length = 3.6/5/5 mm	10 times lower than in the bulk material	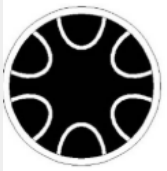
2019 [221] Anti-resonant	photosensitive resin n = 1.62 at 1 THz, tangent loss = 0.024	Pentagram THz hollow-core Rtotal = 10/10/8 mm, d (thickness)= 1/0.8/1 mm	/	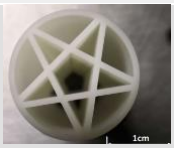

II.5.3. 3D printed negative curvature waveguide

Compared to hollow-core thin-wall waveguides, negative curvature waveguides offer more possibility to adjust the propagation properties (field confinement, propagation loss) by changing the structure of the negative cladding. With the help of 3D printing techniques, the potential of this type of waveguide with complex structures can be explored in a cost-efficient way. Based on this concept, a new geometry composed of half-elliptical capillaries was proposed by Prof. Cristiano Cordeiro in the terahertz regime. The numerical study and fabrication via 3D printing techniques were carried out by

Prof. Cristiano Cordeiro and Prof. Marcos A.R. Franco in 2018 [222], [223]. The experimental characterization was then performed by the author in the IMS laboratory and corresponding results are given in the following part.

The whole design process of waveguide consists of modeling, fabrication and characterization. Once the design of a waveguide is created, the fabrication process includes generally three phases: drawing in CAD software, converted to an STL file, and sent to the printer for producing. After that, the fabricated waveguide is characterized by the THz-TDS experiment to verify its propagation properties. The experimental results are compared to the ones obtained by simulation. The fabricated design is shown in Figure II.33 (a) and (b), in which the cladding is composed of six half-ellipse. The core is determined as the center area surrounding by these negative curvature structures, around 3.5 mm in diameter. The length of the waveguide is 11.6 cm. Limited by the available materials for SLA 3D printing technique, UV-resin has been used as the host material of the waveguide. The material properties are assessed by means of the THz-TDS measurement with a slice of bulk material with a thickness of 6 mm. The extracted refractive index and the absorption coefficient are shown in Figure II.33 (c). It can be observed that the refractive index is around 1.67.

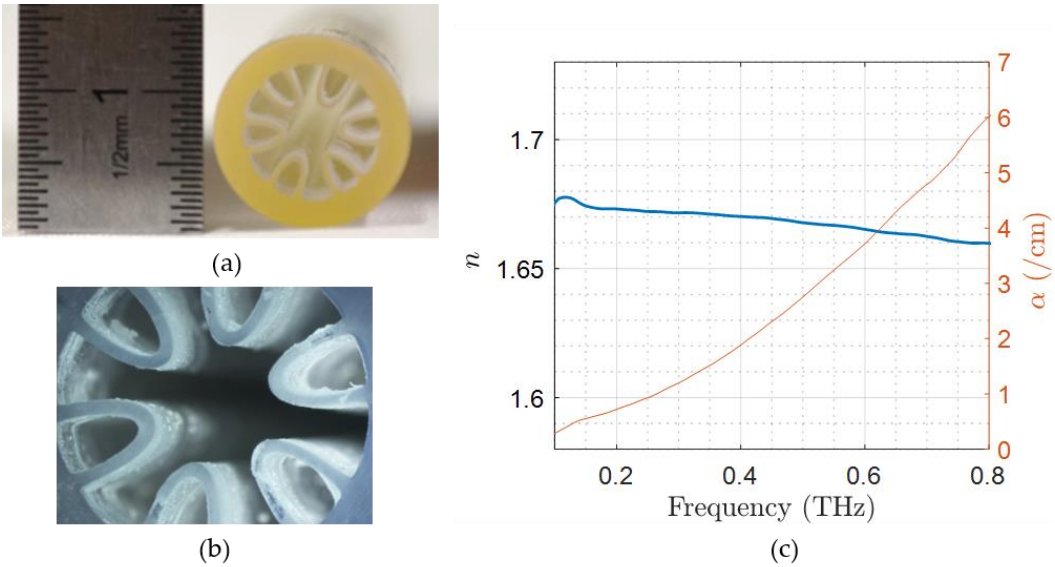

Figure II.33: (a) Photographs of 3D printed hollow-core waveguide with negative curvature. (b) Microscopy photo of the waveguide. (c) Material properties of the bulk material used for 3D printing.

Characterization results

As shown in Figure II.34 (a), the same experimental setup in transmission geometry was applied to characterize this 3D printed waveguide. Considering the size of the emitted beam, a PE lens was inserted before the entrance of the waveguide to excite the core mode efficiently. The transmitted signal and its corresponding spectrum are given in Figure II.34 (b) and (c). The prediction of the transmission band of the negative curvature waveguide was performed through the numerical method: Beam Propagation Method (BPM) implemented in the BeamPROP software from RSoft Design. Limited by the BPM software, the frequency-dependent refractive index of material is simplified to a fixed value. Based on the extracted results from the THz-TDS measurement, n = 1.67 and frequency-dependent absorption in material were used to evaluate the spectral transmission of the waveguide in the simulation. To compare the numerical results with the experimental ones, it is necessary to evaluate the spectral

transmission of THz fiber without the influence of the THz source. Therefore, the transmitted signal is normalized with respect to the reference signal (transmitted signal without the waveguide), shown in Figure II.34 (d).

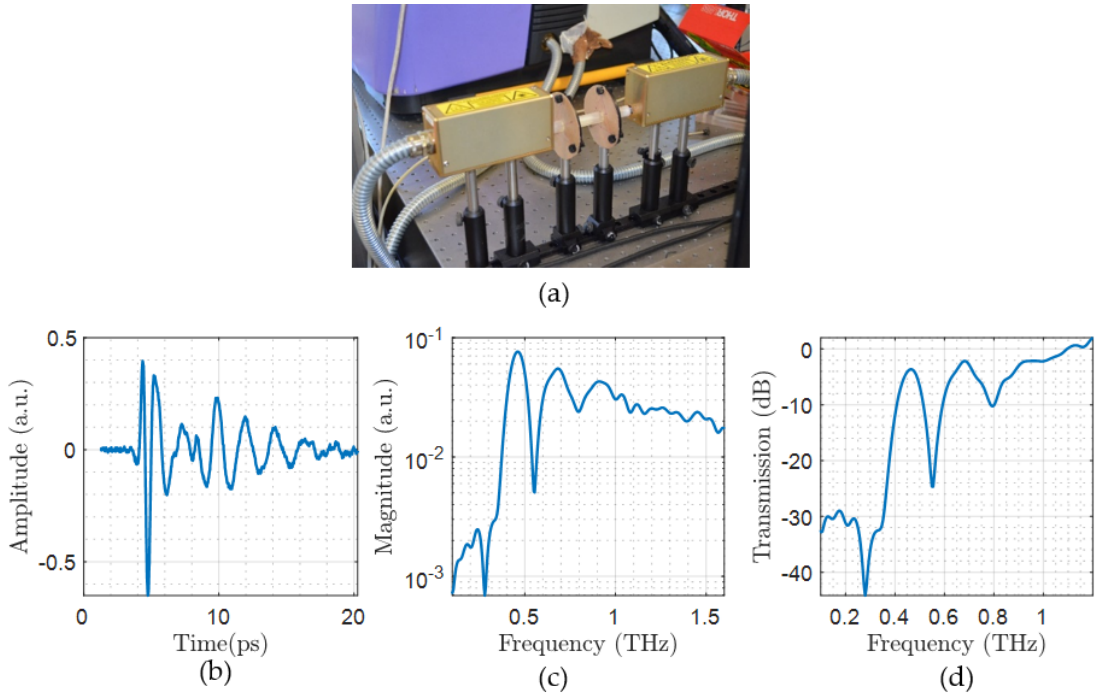

Figure II.34: (a) Photograph of the experimental setup. (b) Transmitted signal and (c) the corresponding spectrum. (d) The normalized transmittance as a function of the frequency.

The normalized transmission data and the simulated transmission based on the initially designed dimensions are given in Figure II.35 (a). Since the main dimensional parameter is the web thickness, it is important to verify the fabrication quality. Figure II.35 (c) shows the original waveguide design and the microscopy photo of the produced 3D printed waveguide. Instead of a web thickness of 400 µm, the printing process resulted in thicker webs varying from 440 to 540 µm. Considering the thickness change related to the precision of the fabrication technique (Polyjet), a new simulation was performed with increased web size (from 400 µm to 480 µm), giving rise to the result shown in Figure II.35 (b). A better match is obtained between the simulation results with a scaled factor of 1.2 and the experimental results, in which the transmission dips at frequencies of around 300 GHz, 550 GHz and 760 GHz correspond appropriately to the ones appeared in the experimental results. Concerning the transmission band, this 3D printed waveguide provides a transmission peak around the frequency of 450 GHz, then the transmission decreases rapidly. Since the relatively narrow band of the waveguide doesn't fully comply with the broadband requirement of the double-PCA transceiver probe, it was not selected as the communication channel between the transceiver and the sample. Although the 3D printed negative curvature waveguide is not suitable to work with the transmitted probe, it provides a cost-efficient, fast method to design, fabricate and validate the novel design of the waveguide. It can be expected that the resolution improvement and more material availability of 3D printing techniques will further contribute to the development of terahertz waveguide. Waveguides with better performances will be more applied in the terahertz system as an indispensable component.

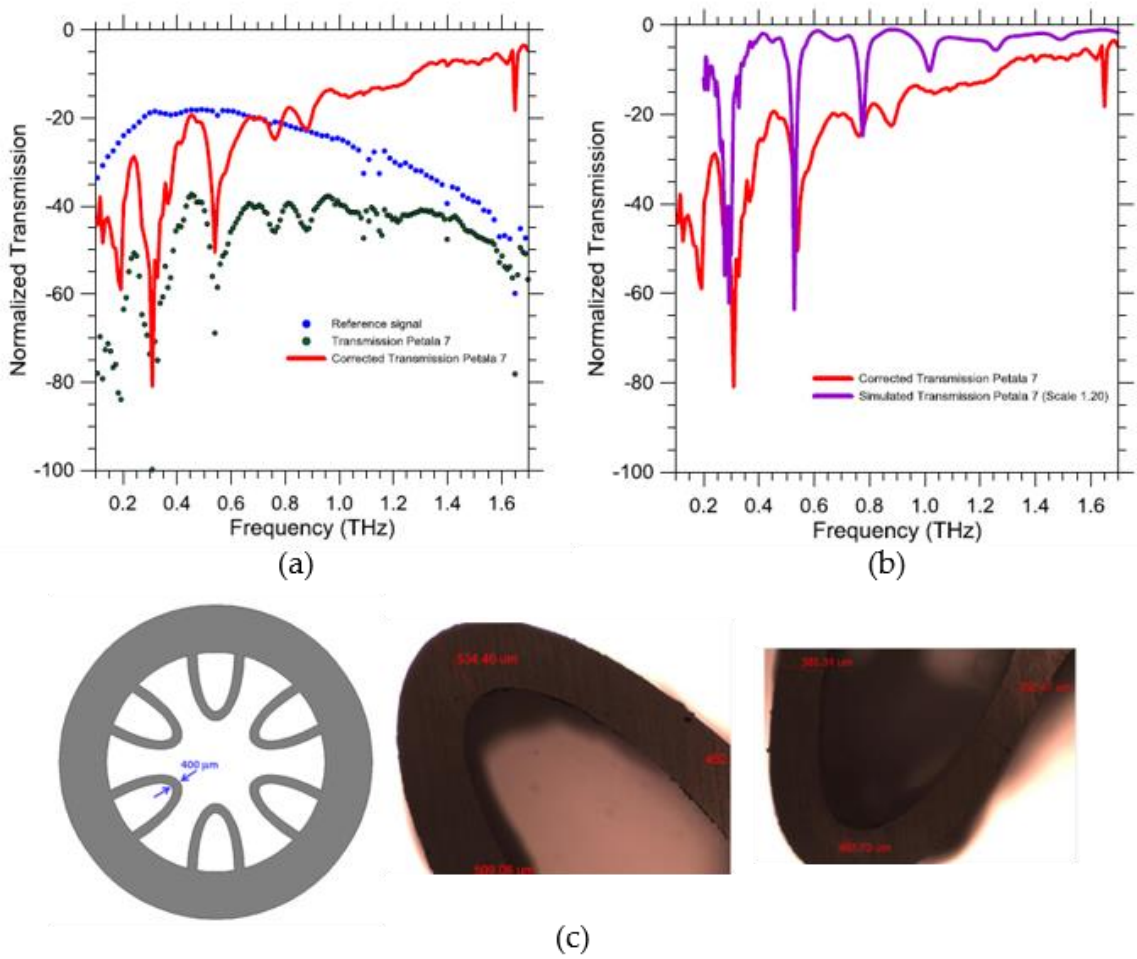

Figure II.35: (a) Normalized transmission spectrum obtained by the simulation and experiment with initial design dimensions. (b) Normalized transmission spectrum obtained by increasing the web size by a factor of 1.2. (c) Schematic of the waveguide design and the microscopy photos of two half-ellipse webs. It can be seen that the thickness of the web varies with the position.

By exploiting a 3D printing technique, a negative curvature waveguide with 6 half-ellipse capillaries was fabricated. Despite small dimensional error related to the precision of printing technique, the accordance between the simulation result and experimental results demonstrate the potential of the 3D printing techniques for terahertz waveguides. Being a new fabrication technique, it allows shortening the time spent and development cost of novel waveguide designs before achieving a performant fabrication process. While novel designs of terahertz waveguides aimed for broadband transmission, lower losses, bending losses are proposed, the fabrication of these waveguides can be ensured by 3D additive manufacturing techniques. Moreover, 3D printing technique can be used to manufacture the preform of a more complex waveguide (such as microstructured PCF waveguides), allowing to decrease the dimension of waveguide by drawing process. The future collaboration with ICMCB laboratory will permit to explore the potential of their waveguides.

II.6. Conclusion

Before the implementation of a terahertz wave-guided reflectometry system, three transceivers units (a double-PCA lens-free transceiver, an III-V technology-based FMCW module and a Si-based radar unit) and two hollow-core thin-wall waveguide have been investigated separately. The simulation and experimental results have revealed that the double-PCA transceiver can operate efficiently in the

frequency region from 400 GHz to 600 GHz. Depending on the working distance, the bandwidth of emitted signal can be further enlarged. While a resolution of 3.17 lp/mm was achieved at a frequency of 791 GHz in the direction perpendicular to the two-PCAs axis for imaging purposes, the imaging capacity of the transceiver is severely restricted by the distance between two PCAs. Besides, the structure and emission pattern of two FMCW radars have been introduced as the preliminary studies.

Based on the aforementioned information about transceivers, hollow-core thin-wall waveguides are suggested as a good choice for its easily-adjustable transmission bands with simple structure, low-loss propagation and low-cost availability. Two hollow-core waveguides with suitable dimensions were eventually selected and the measurements in transmission and reflection have demonstrated their guiding capacity for the frequency lying between 400 GHz and 600 GHz, which meets the operating band of the double-PCA transceiver. In regard to the two FMCW radars operating in the lower part of spectrum, the measurements performed by a vector network analyzer guarantee the guiding capacity of the hollow-core waveguide with a diameter of 6 mm. To address the fabrication difficulties encountered for terahertz waveguides, 3D printing techniques have also been mentioned. The fabrication and obtained consistent transmission bands of the negative curvature waveguide composed of six half-elliptical capillaries demonstrate the potential of 3D printing technique, providing a fast, cost-efficient development process for novel waveguide designs. After all these investigations, it’s time to build up terahertz wave-guiding reflectometry systems!

Chapter III.

Terahertz wave-guided reflectometry systems

III.1. INTRODUCTION **84**

III.2. TERAHERTZ WAVE-GUIDED REFLECTOMETRY SYSTEMS IN PULSE MODE ... **87**

III.2.1. Global experimental setup 87

III.2.2. TGR-P system I with a silica waveguide 88

III.2.2.1. Propagation behaviors analysis (simulation) 88

III.2.2.2. Characterization of detected time signal 94

III.2.2.3. Imaging application 95

III.2.3. TGR-P system II with a plastic waveguide 97

III.2.3.1. Propagation behaviors analysis (simulation) 97

III.2.3.2. Characterization of detected time signal 100

III.2.3.3. Liquid depth detection application 102

III.3. TERAHERTZ WAVE-GUIDED REFLECTOMETRY SYSTEM IN FMCW MODE ... **107**

III.3.1. TGR-FMCW system I using SynView transceiver unit 108

III.3.1.1. Propagation behaviors of radar signal (simulation) 109

III.3.1.2. Imaging application 113

III.3.1.3. Optical resolution improvement 114

III.3.1.4. Conclusion 117

III.3.2. TGR-FMCW system II using Silicon Radar transceiver chip 118

III.3.2.1. Propagation behaviors analysis 118

III.3.2.2. Imaging application 120

III.3.2.3. Resolution improvement via an HDPE lens 120

III.3.2.4. Resolution improvement via a Si bullet lens 122

III.4. CONCLUSION **126**

III.1. Introduction

From the point of view of applications, reflection geometry imposes less restriction on the form of the object and measurement conditions, it can enable measurements on a thick or metal-substrate material. A terahertz system in reflection mode exhibits broader applicability than the one in transmission modality, and it permits as well to study the surface properties without mixing the contributions from the bulk of the substrate [224]. However, the quasi-optical method used in a conventional terahertz sensing system limits developments towards a compact practical terahertz system configuration for the following reasons. Firstly, optical components such as lenses and parabolic mirrors require specific longitudinal operating distances and a minimum volume for implementation. Secondly, due to their optical nature, a large number of alignment work is demanded to obtain and to maintain the optimum system's performance. Thirdly, additional space along the propagation path should be kept to avoid the disturbance from the environment, which makes the conventional setup unsuitable for applications aiming to probe samples directly *in-situ* or in a narrow semi-enclosed environment. Sophisticated alignment requirements together with space-consuming configuration hinder the terahertz system from a wider application scope in practical use.

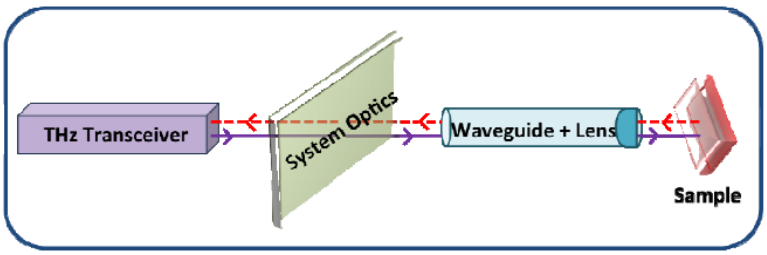

Figure III.1: Schematic diagram of a terahertz wave-guided reflectometry system demonstrated in the literature.

To overcome these issues, the use of a waveguide to guide the terahertz signal directly to the region of interest and to carry back the reflected signal has been proposed as one solution. Throughout the literature, guided reflectometry operations have been realized with different metallic waveguides, including metal wire [80], [78], [225], parallel-plate waveguide (PPWG) [91] and coax cable [226]. Their low dispersion property of quasi-TEM mode allows for a broadband signal transmission in the terahertz regime. Dielectric waveguides have also been tested as alternative components to develop terahertz wave-guided reflectometry systems. It has been demonstrated that dielectric waveguides can be applied to analyze the surface state of objects, or to determine the molecular concentration and for chemical reaction monitoring [152]. In particular, a considerable amount of effort has been focused on differentiating the cancerous and normal tissues [176], [227], [228] by using terahertz radiations in reflection mode. In 2014, a single–channel flexible waveguide-based terahertz endoscopic system was reported for future clinical application [229]. Figure III.1 depicts its system configuration, in which system optics should be added before the input of the waveguide. While a beam splitter is deployed to separate the incident beam and reflected signal due to the volume of the source and the detector, either a lens or a parabolic mirror is used to reduce the beam size to couple the terahertz signal into the waveguide efficiently. After adding all these devices to optimize the terahertz beam, the whole system becomes complicated and bulky. Table 5 provides a detailed summary of studies of terahertz wave-guided reflectometry systems, giving information about the experimental configuration and related applications. It is noticeable that most of the studies were conducted with continuous sources and detectors. Apart from the study [57], no terahertz wave-guided reflectometry has been yet investigated with a transceiver unit (in pulse or FMCW mode).

To further push up the development of a compact reflectometry system, the present work exploits the combination of a transceiver unit and a hollow-core thin-wall waveguide to construct a terahertz wave-guided reflectometry system. Thanks to the small separation between the emitter and receiver of the transceiver or their mono-static architecture, the separation of the beams is no longer necessary, simplifying the system configuration. The selected hollow-core thin-wall waveguides offer a low-loss propagation mode in their core, which allows as well the direct coupling between the transceiver unit and the waveguide. According to the selected transceiver unit, this chapter is divided into two main parts: (i) terahertz wave-guided reflectometry system in pulsed mode (TGR-P), and (ii) terahertz wave-guided reflectometry systems in FMCW mode (TGR-FMCW). In addition to their experimental setups and applications, studies about field properties inside the system related to their uncommon excitation condition such as coupling efficiency, propagation modes, imaging resolutions are presented.

TABLE 5. REVIEW OF GUIDED REFLECTOMETRY SYSTEMS

Waveguide & System	Metal wire	Tapered wire	Tapered PPCW	Dielectric Pipe Waveguide	Metal-coated dielectric waveguide
Material	Stainless steel	Stainless steel	2.5 cm * 5 cm (plate) 20 µm to the sample	Teflon 30 cm length	Silver-coated dielectric fiber, 45 cm length
Dimensions	D_{metal} = 0.9 mm	D_{metal}= 0.8 mm (D_{apex} = 50 µm)	Spacing from 2 mm to 20 µm	D_{out} = 8.5 mm t_{Teflon} = 1 mm	D_{inner} = 4 mm
Absorption coefficient α /Bending loss	α = 0.03 cm^{-1}	α = 0.2 dB/cm		Bending loss: below 10% within +/−5°; negligible within +/−1°	
Applications	Endoscopy (Guiding terahertz pulses inside containers or around corners)	Near-field imaging (λ/33 resolution)	Near-field imaging (Identifying 100µm feature on the substrate GaAs)	Refractive index detection and chemical reaction sensing	Endoscopy (Aimed for the diagnosis of colorectal cancer)
Terahertz devices	• Pulsed Fiber-coupler PCA transmitter and receiver	• CW 100 GHz electronic source; Schottky diode	• Pulsed Fiber-coupled PCA transmitter and receiver with a Al foil	• CW Gunn oscillator module generation at 0.4 THz around 100µW; Zero Schottky diode	• CW CO_2 pumped gas laser at 584 GHz around 33 mW; Liquid Helium cooled silicon bolometer
Terahertz passive component	• Second wire to serve as coupler • Y-splitter	• DPE to enhance the coupling efficient (theoretical 35 %) • Y-splitter	• Teflon lens to couple the terahertz beam into the tapered PPCW	• OAP mirrors to collimate and focus terahertz beam into the pipe • Waveguide + lens	• Short waveguide to obtain the Gaussian mode • Waveguide + lens
Shortcoming × **Advantage** ✓	× Low coupling efficient × Bend loss × radiation loss ✓ low loss ✓ negligible group velocity dispersion	× High resolution (λ/33resolution)	× High resolution × Only in one direction (perpendicular to two plates)	× Real-time measurement by reflectivity. × Flexible, moving the pipe to realize a scan SNR approaching 200;	SNR ~ 26 dB
Refs.	[76]	[78]	[91]	[152]	[230]

III.2. Terahertz wave-guided reflectometry systems in pulse mode

Thanks to the tiny size of the transceiver probe tip (0.18 mm thick and 2 mm wide), the communication between the transceiver and a waveguide with adapted size can be carried without supplemental optics (beam splitter). Two selected hollow-core dielectric waveguides are tested separately with this double-PCA lens-free transceiver to implement a terahertz wave-guided reflectometry system. After the waveform characterization, the constructed systems are applied for imaging and sensing applications. Propagation behaviors of waves inside the system, including the coupling issue, dynamic range, and lateral resolution are investigated via 3D full-wave simulation and experiments. The corresponding results are given in the following part.

III.2.1. Global experimental setup

Based on the previous studies, two dielectric hollow-core thin-wall waveguides have been selected to integrate into the terahertz wave-guided reflectometry system. They are a 3 mm diameter silica hollow-core thin-wall waveguide with a thickness of 130 µm, and a 6 mm diameter plastic waveguide with a thickness of 158 µm respectively. Their guiding mechanism has been confirmed by the repeated transmission dips in THz-TDS measurements. Most importantly, both two waveguides can provide an adapted transmission band covering from 400 GHz to 600 GHz, corresponding to the operating frequencies of the double-PCA lens-free transceiver. Regarding the propagation loss, air-core mode propagation can reduce the absorption in the host material of the waveguide. Since the distance around two photoconductive antennas on the transceiver probe is around 700 µm, which is smaller than the diameter of the two hollow-core waveguides (3mm and 6 mm respectively), the reflected beam can be directly detected by the receiver of the transceiver without the help of a beam splitter. Considering the beam size out of the transceiver in the proximity (beam size less than 2 mm at a distance of 1 mm at 475 GHz), no lens or parabolic mirror is used to enable the coupling between the transceiver and the waveguide.

Above all, two waveguides were implemented separately in association with the double-PCA transceiver to construct a terahertz wave-guided reflectometry system in pulse mode (TGR-P). The experimental setup of the TGR-P is shown in Figure III.2, in which the transceiver probe and hollow-core waveguide are fixed on the vertical breadboard. A sample is placed on the horizontal platform equipped with three-directional translation stages, which is close to the output of the waveguide. Once the waveguide is positioned with respect to the transceiver, it is fixed to keep the same excitation condition. Considering the fragility of the probe, a small distance is kept between the transceiver probe tip and waveguide entrance. This distance can also avoid the perturbation to the guided wave caused by the presence of the transceiver tip.

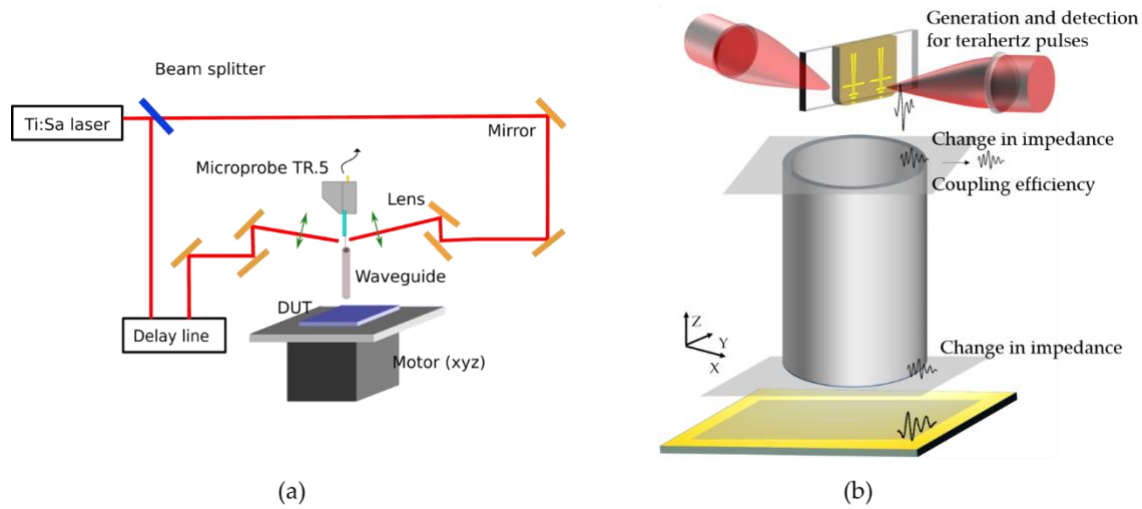

Figure III.2: (a) Schematic diagram of a guided terahertz pulse reflectometry system setup, including the double-PCA transceiver probe and dielectric hollow-core waveguide. (b) Schematic diagram of the propagation process from the transceiver to waveguide and then back to the transceiver.

Figure III.2 (b) depicts the propagation process of waves in a GTPR system. First, one of PCAs of transceiver, acting as emitter, radiates a pulse signal into free space. Due to the crosstalk between two antennas, the generated signal is recorded by the receiver antenna. When the emitted pulse signal arrives at the input of waveguide, the mismatch of impedance between the freely propagating waves and guided waves along the waveguide may give rise to reflections. The same reflections occur at the output of waveguide. Since the reflection coefficient is determined by the impedance difference between two propagation mediums, the air-core waveguides are supposed to have unimportant reflections. Depending on field distribution of arrived signals, various propagation modes may be excited and uncoupled power is radiated into free space as coupling loss. While higher propagation modes attenuate rapidly with distance, a stable propagation with low losses along the waveguide is expected after a certain distance. Once the guided signal propagates out of the waveguide, it encounters the sample and it is reflected back to the transceiver with information about the properties of the sample. Depending on the waveguide in use, the following part is separated into two parts: (i) the TGR-P system consisting of the transceiver and a silica waveguide, and (ii) the one composed of the transceiver in conjunction with a plastic waveguide.

III.2.2. TGR-P system I with a silica waveguide

The first TGR-P system was built up with the double-PCA transceiver and a 5.3 cm-long silica hollow-core waveguide. The coupling process between the transceiver and the waveguide was directly carried out in free space. The divergent emitted waves from the transceiver provide an atypical excitation condition, complicating the propagation behaviors of the coupled waves along the waveguide. Both numerical method and experiments have been performed to explore the performance limitations of the constructed system and their respective causes.

III.2.2.1. Propagation behaviors analysis (simulation)

By taking advantage of the time domain solver in CST Microwave Suit, the propagation behaviors of waves inside this TGR-P system in association with a silica waveguide were simulated. As shown in

Figure III.3 (a), the TGR-P system model was composed of a double-PCA transceiver probe, a 5.3 cm-long silica hollow-core waveguide and a metal plate placed at the end as a perfect mirror to maximize the reflected signal. Since foregoing studies have revealed that the transceiver probe is more efficient in the frequency band from 400 GHz to 600 GHz, a Gaussian pulse signal covering over the interested frequency region (300 GHz to 600 GHz) was applied as the excitation source signal. The material parameters of fused silica (cladding material) are extracted through THz-TDS measurements. In the simulation, the permittivity and dielectric loss $tan(\delta)$ of the silica was set as 3.74 and 0.0027 at the frequency of 450 GHz respectively. Since the transceiver tip and the input facet of the waveguide were very close in the experiment, a distance of 130 µm was kept between the two objects. Both the electric field and power flow were monitored during the simulation.

Pulse propagation in the time domain

The electric field distribution in the xz-plane at different propagation times are given in Figure III.3 (b). As can be observed, after the pulse signal is radiated into free space, one part of the emitted energy is coupled into the waveguide (at the time of 20 ps). After 140 ps, the separation of guided waves can be clearly observed: while some power fractions propagate in free space (both inside the air-core and outside the waveguide), another power fraction is confined inside the cladding with a significant time delay. This spatial segregation of waves in the time domain reveals the presence of two different kinds of propagation modes: air-core mode and cladding mode. The air-core mode propagation exploits the anti-resonant reflection as the guidance mechanism. Due to the loose confinement, one part of guided waves is leaked out of the waveguide, resulting in some propagation loss. The waves confined inside the silica wall are guided by the total internal reflection. Owing to the high refractive index of fused silica, waves in the cladding display a significant time delay with respect to the waves propagating in the air-core, explaining the separation of waves in the time domain.

Apart from the electric field distribution, the time signal detected by the receiver of the transceiver is as well given in Figure III.3 (c). After t = 8 ps, a pulse signal is fed to the Tx antenna for the emission. The direct communication between the two antennas is recorded in the time window from 10 ps to 50 ps (Zone I in Figure III.3 (c)), in which the reflected portion from the entrance of the hollow-core waveguide is also included. Considering the dimension and structure of the waveguide, no considerable reflection at the beginning was expected. The signal reflected from the metal lies in zone II in Figure III.3 (c), recorded in the period between t = 355 ps and 400 ps. The amplitude ratio between reflected signal (0.000842) and crosstalk signal (0.022) is equal to 3.8 %, allowing to compare with experimental results later. By taking account of the propagation time required in the cladding, it is logical that only waves in air-core mode are recorded in this limited time window. It takes around 350 ps for guided waves to be reflected and detected, which is very close to the free space propagation time (345 ps), implying a low effective index of the air-core propagation mode. As a result, a weak response of the TGR-P system in an open-end configuration is anticipated, contributing to the dynamic range of the whole system.

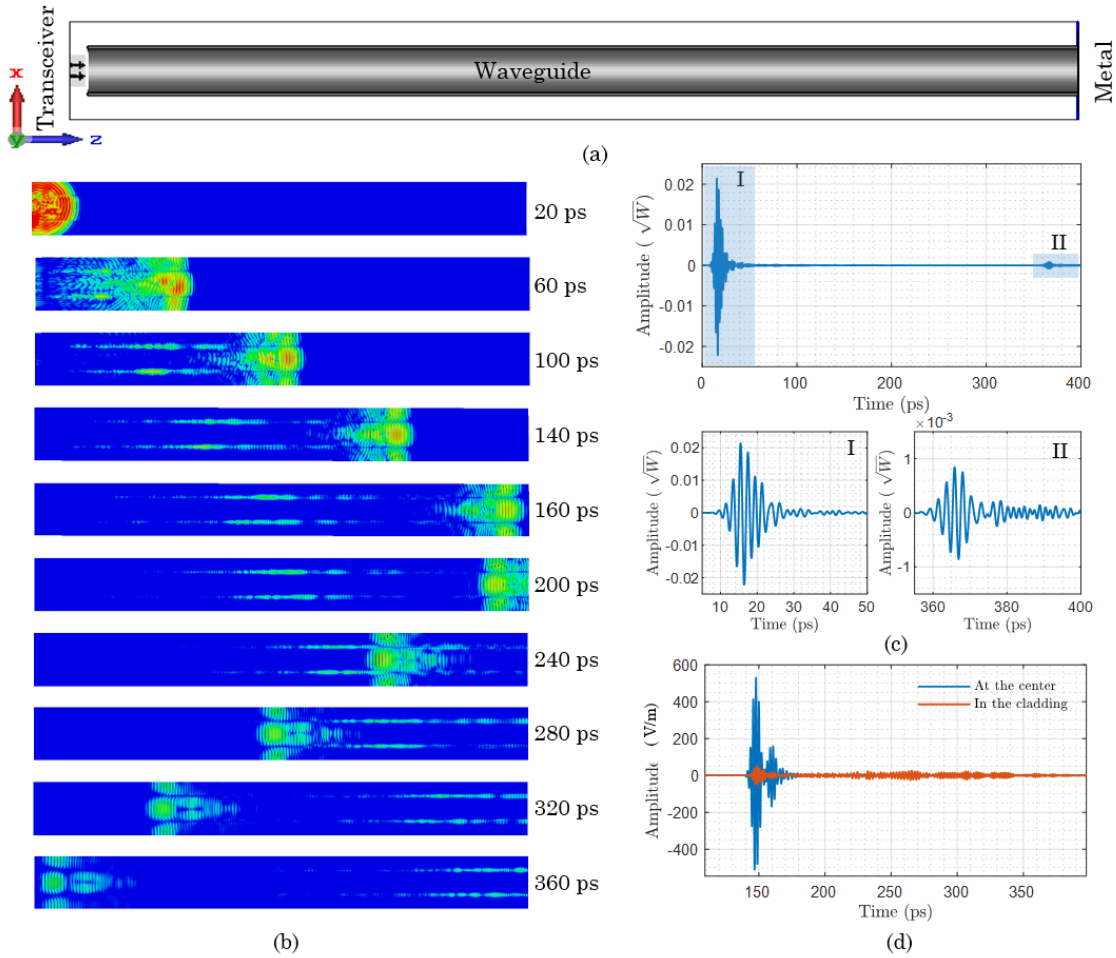

Figure III.3: Full simulation of the setup. (a) Scheme of the model including the transceiver, a 5 cm-long silica waveguide and a metal plate placed at the output. (b) E-field distribution (based on the absolute value) on the xz cross-section along the waveguide at different times. (c) Reflected signal detected by the Rx antenna on the transceiver. Two small figures below provide a close-up view on the waveform in the zone I and II. (d) X component of the electric field detected at the center of the core and in the cladding at the cutplane of z = 40 mm.

At last, the focus is given on the power distribution in two different propagation modes. Two electric field probes were placed at the center of the air-core and inside the cladding at the position of z = 4 cm respectively. Since the planar antennas are more sensitive to the components polarized in the x-direction, only X components of the electric field are displayed in Figure III.3 (d), where the blue curve represents the time signal detected at the center of the waveguide and red curve denotes the one detected in the cladding. At t = 150 ps, the X component of the electric field (blue curve) at the center displays two distinct waveforms with a short time delay, representing the incident and reflected signals guided in air-core mode respectively. A ten times weaker electric field is as well detected in the cladding at the time around 150 ps due to the weak confinement. After the time delay of around 100 ps, the second part of energy in cladding mode begins to appear. This result reveals that although two different kinds of propagating modes are both excited along the waveguide, more guided power propagates in air-core mode. The quantitative analysis of the power proportion in different modes will be given in the following part at a specific frequency.

To conclude, the simulated propagation of waves inside the TGR-P system in the time domain validates the guiding capacity of the silica hollow-core waveguide in air-core mode. It displays as well the presence of the cladding mode which is excited by an atypical coupling condition related to the emission pattern of the transceiver.

Propagation behaviors of waves at 450 GHz

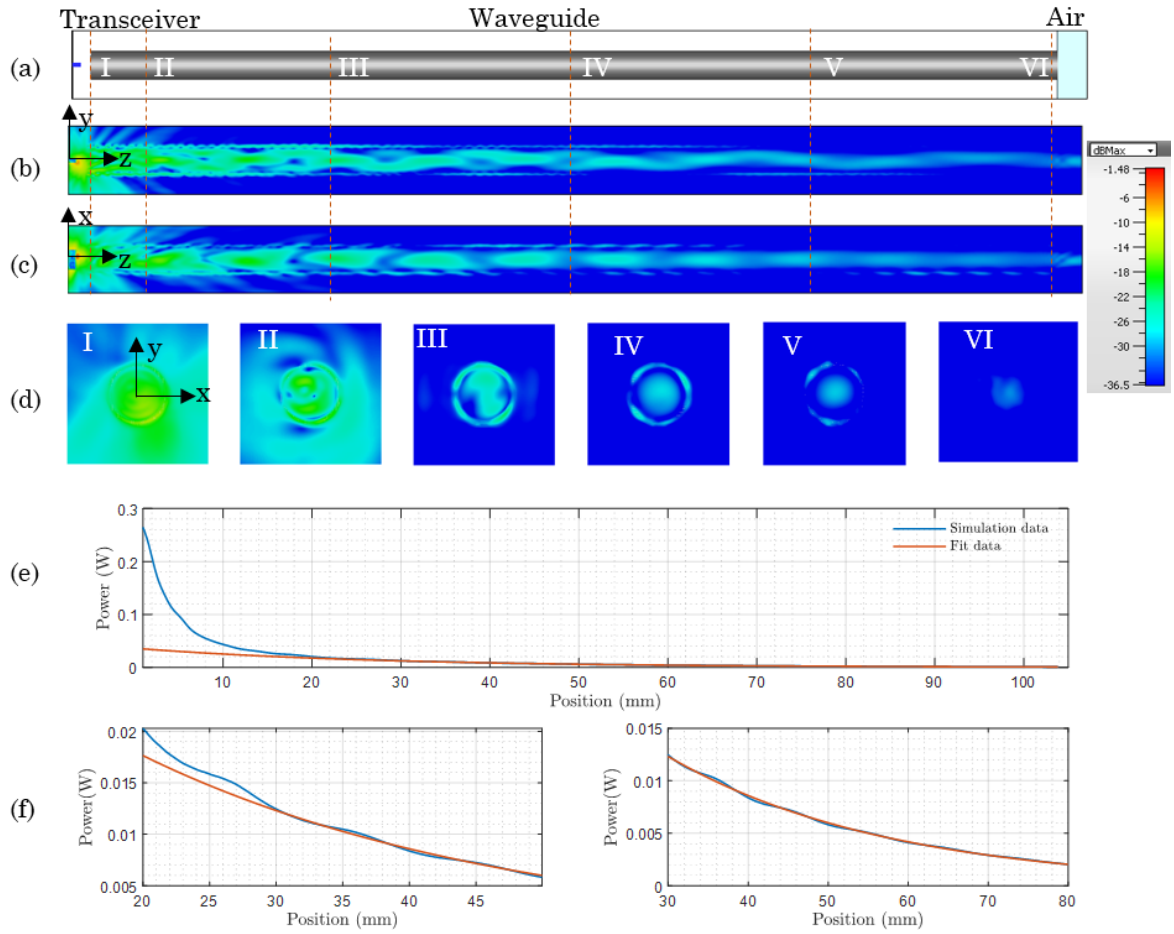

Figure III.4: 3D full-wave simulation results obtained at the frequency of 450 GHz. (a) Numerical model including a transceiver probe, a 10 cm long waveguide and an air-block. (b-d) Power flow distribution on different cutplanes. Position I to VI correspond to z = 2/5/25/50/75/102.5 mm respectively. In the position I, strong power density displays at the right-down side of cutplane, which is related to the emission pattern of the antenna on the transceiver. In position II, while part of the energy is radiated out of waveguide as coupling loss, part of the energy is coupled inside the waveguide. From the position III, guided power in mixed propagation modes along the waveguide can be observed. (e) Power passing through cross-section as a function of distance. Based on the simulation data, the attenuation coefficient of the waveguide is deduced (red curve with α = 0.0036 cm^{-1}). (f) Close-up in the zone of 20-50 mm and 30 to 80 mm.

Since the waveguide in the TGR-P system is employed in reflection geometry, the total guided propagation distance is two times of waveguide length. To facilitate the investigations task, the following study is exclusively focused on the propagation properties of waves along a 10 mm-long waveguide in transmission. As illustrated in Figure III.4 (a), a 10 cm long waveguide together with an air block is placed

after the transceiver probe. Figure III.4 (b-d) displays the power flow of the frequency component 450 GHz on the yz-, xz- and xy-plane respectively. The different colors indicate the maximum value (peak value) of Poynting vector of the electromagnetic field at every spatial point.

The whole power transmission process can be concluded into three steps: the emission of the pulse signal from the transceiver, the coupling into the waveguide, and the propagation along the waveguide in certain guided mode. As the first step, the generated pulse signal is emitted into free space by one PCA of transceiver. The total efficiency of the antenna is around 45% at the frequency of 450 GHz, *i.e.*, maximum power of 0.45 W can be radiated into free space with a 1W power excitation signal. Amongst emitted waves, only the waves arriving inside the waveguide (inside the core or cladding) have the possibilities to excite propagation modes along the waveguide, which is defined as the effective incident power here. Since the power directing outward of a surface can be derived from the surface integral of the Poynting vector and the propagation direction of waves along the waveguide points to the z-axis, the power P traversing a cross-section of the waveguide can be calculated based on the Z component of the power flow (Poynting vector $\boldsymbol{\mathcal{P}}$), expressed as:

$$P = \oiint_S \boldsymbol{\mathcal{P}} \cdot \boldsymbol{n}\, dS = \oiint_S \boldsymbol{\mathcal{P}}_{\mathbf{z}}\, dS \tag{10}$$

where $\boldsymbol{\mathcal{P}}$ represents the Poynting vector, $\boldsymbol{\mathcal{P}}_{\mathbf{z}}$ denotes the Z component of the Poynting vector and $\boldsymbol{n}$ is the normal vector of the surface. By applying Equation (10), an effective incident power of 0.26 W is achieved at the entrance of waveguide. Depending on the field distribution of the incident waves, certain propagation modes are excited along the waveguide and the other power is radiated into free space as coupling loss, which is expressed as radiations propagating outside the waveguide between the position I and II in Figure III.4 (b) and (c). After a certain distance propagation, the uncoupled power is radiated into free space and waves propagating in higher modes vanish due to significant loss. Consequently, only low-loss modes remain, and stable guided waves are formed along the waveguide and they continue to propagate with an attenuation coefficient determined by the propagation mode. Figure III.4 (b) and (c) show a continuous power flow inside the air-core after position III (z = 25 mm). Based on Equation (10), the power propagating along the waveguide is plotted as a function of the z position, shown as the blue curve in Figure III.4 (e). By analyzing the relation between the power and distance starting from z = 50 mm, an attenuation coefficient of $\alpha = 0.0036\ \mathrm{cm}^{-1}$ is deduced from the red fitting curve shown in Figure III.4 (e). In reality, the absorption of the waveguide should be slightly higher than this value due to the absorption of water vapor in the air.

Coupling issues and propagation loss

A close-up view is provided in Figure III.4 (f), in which two curves match well except for the results obtained with a distance less than 30 mm, which is associated with the coupling loss at the beginning. Hence, the power passing through the cross-section at z = 30 mm is regarded as the coupled power. Due to the complexity of the modes existing along the waveguide, the method of the power overlap integral between the incident beam and propagation modes was not applied. Instead, the coupling efficiency η is defined as the ratio of the coupled power (deduced from data fit shown in Figure III.4 (e)) to the initial

excited power (1W) in the present work, expressed as Equation (11). The coupling efficiency of 4 % ($\frac{0.04}{1} \approx$ 4 %) is then obtained.

$$\eta = \frac{P_{coupled}}{P_{excitation}} \tag{11}$$

It should be noted that here both the absorption coefficient and the coupling efficiency are calculated based on the power propagating along the waveguide, their values don't correspond to a specific propagation mode.

Multi-mode propagation

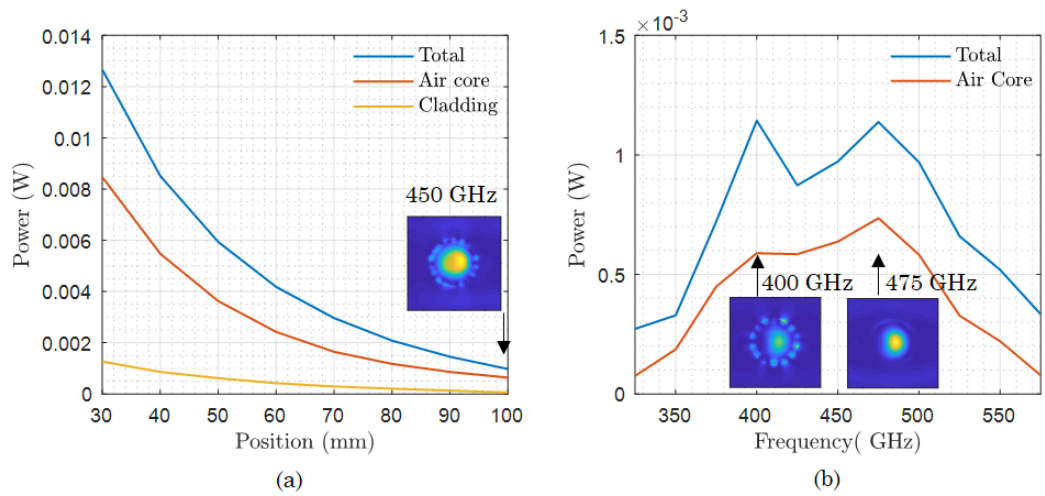

Figure III.5: (a) Power outgoing through cross-section as a function of position at a frequency of 450 GHz. Blue curve: power crossing over the whole cross-section. Red curve: power propagating through air core. Yellow curve: power transmitting in the cladding. The beam profile at the output of waveguide is as well provided in the figure, in which power passes through air core and cladding. (b) Remained power at the output of waveguide as a function of frequency. The blue curve represents the power passing through the whole cross-section and the red curve denotes the power crossing the air-core. Beam profile at frequencies of 400 GHz and 475 GHz are given.

Figure III.4 (d) illustrates the distribution of the power density in the xy-plane at the different positions, where most of the guided power is confined inside the core and the cladding after the position III, corroborating the previous simulation result in the time domain. It is of interest to assess the power proportion in these two different modes to estimate the efficiency of this optical-free coupling configuration. In accordance with the guiding mechanism, the locations of these waves are specific: while the cladding mode waves are confined in the silica layer, air-core mode waves propagate in the air around the waveguide (inside and outward). On this basis, transmitted power in different modes as a function of distance is given in Figure III.5 (a). It reveals that the waves propagating in the cladding doesn't occupy many shares of guided power, less than 10%. More than 60 % of the guided power propagate inside the air-core. From the field distribution on the xy-plane at the position of z = 100 mm, it can be seen that most of the guided field is confined inside the core.

Frequency composition

By combining the power flow results obtained at different frequencies, the transmitted power passing through the cross-section at the end of the 100 mm-long waveguide can be used to estimate the frequency composition of the detected signal by the transceiver in reflection modality with a 50 mm-long waveguide. It is notable that two curves as a function of the frequency are plotted in Figure III.5 (b). While the blue one represents the power over the whole cross-section and the red one denotes only the power traveling inside the core of the waveguide.

In reality, the power fraction guided in the cladding mode was not recorded during the experimental measurements due to the significant time delay between the air-core mode and cladding mode. In addition to the attenuation in material, the reflection occurring at the silica-air interface further reduced the power of the reflected signal from the sample, leading to a poor SNR. Consequently, this part of power is not useful and it should be included to evaluate the frequency composition of the time response of the system. Since one part of the electric field is loosely confined outside of the waveguide (shown in Figure III.3), this power fraction cannot be detected efficiently by the receiver of transceiver placed at the center of the waveguide due to the considerable distance. As a result, only the power confined inside the air core is detectable and valuable. The comparisons of two curves indicate that almost 60 % of the guided power is accessible to the transceiver and most of them lie in the frequency band varying from 400 GHz to 500 GHz. Besides, a peak power is anticipated obtained at the frequency of around 475 GHz.

To sum up, field properties in the time domain and frequency domain have been investigated through 3D full-wave simulation. Although both air-core mode and cladding mode propagation take place due to the atypical excitation condition, they are naturally separated by an important time delay. More importantly, the desired low-loss air-core mode takes the dominant roles in guided power, proving the feasibility of the concept of guided terahertz pulse reflectometry system.

III.2.2.2. Characterization of detected time signal

A guided terahertz pulse reflectometry system was built up based on the previously presented configuration, in which the coupling between the transceiver and the waveguide was carried out without any optics. Details about system setup have been given in Chapter III.2.1, shown in Figure III.2 (a). The detected time signal by the TGR-P system to a metal placed at the end of the waveguide was recorded, allowing to assess the performance of the system. Besides, a raster scan was also performed by applying this TGR-P system.

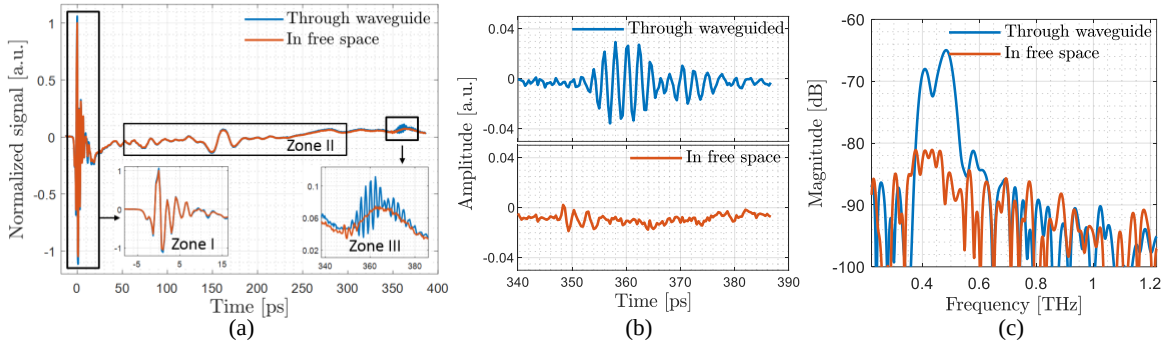

Figure III.6: (a) Detected signals by the terahertz transceiver. Blue curve: signal propagating through the waveguide. Red curve: signal propagating in free space. This signal can be divided into three zones. First, the zone I (t = [0-30] ps) corresponds to the crosstalk signal between the two photoconductive antennas on the transceiver. Then waveform in zone II (t=[30 -250] ps) corresponds to the reflection signal coming from probe-mount and imperfection of wave trapping design. Finally, the reflected signal from the sample at the end of the waveguide (blue curve) and a weak reflected signal by freely propagation (red curve) can be seen in zone III (after 340 ps). (b) Reflections from the metal propagating through a waveguide and in free space respectively. (c) Spectrum of reflection signals obtained at (b). Compared to the propagation in free space, more signal power is transmitted through waveguide owning to its guiding capacity.

The benefits of the wave-guiding lie in the fact that terahertz waves can reach the farther targeted site of inspection while minimizing energy dissipation in comparison to free space propagation. This aspect was verified by measuring the reflected signal from a metal plate situated 53 mm (the length of the used waveguide) from the terahertz transceiver. Results are reported in Figure III.6, including (a) originally detected signals, and (b) reflected signals from the sample after removing the direct transmission signal between two PCAs. According to the origin of the reflections, time signals can be divided into three zones. The zone I (t = [0-30] ps) and zone II (t=[30 -250] ps) correspond to the crosstalk signal between the two PCAs and internal reflections coming from probe-mount respectively. No information about the sample is carried. Zone III (after 340 ps) represents the reflected signal from the sample (metal) placed in the vicinity of the output of waveguide. The reflected signals (shown in Figure III.6 (b)) are hence compared between the free-space propagation (red curve) to that of the guided regime (blue curve), showing a small time delay of several picoseconds. Being close to the light velocity in free space, the propagation speed of the reflected signal confirms the air-core mode guidance of the waveguide. The amplitude ratio between the crosstalk signal and the reflected signal is around 0.038/1 = 3.8 %, which is in accordance with the estimation given by means of simulation (see in Page 89 of Section Pulse propagation in the time domain).

As expected, guided terahertz pulses exhibit a significantly higher amplitude than that of non-guided ones. The power fraction carried by reflected pulses propagating through the hollow-core waveguide is roughly 12 dB greater than that of those propagating in free space for frequencies spanning from 400 to 550 GHz (shown in Figure III.6.(c)). By taking account of the efficiency of the PCAs, the transmission band supported by the waveguide and their coupling efficiency, the frequency composition analysis that was carried out through 3D full-wave simulations (see Figure III.5 (b)) has anticipated a consistent result, in which the transmission peak at around 480 GHz also displayed. This accordance between the experimental and simulation results corroborates the correctness and precision of the simulation.

III.2.2.3. Imaging application

After demonstrating the pulse guiding capacity of the silica waveguide, the implemented TGR-P system was used for imaging application. As represented in Figure III.7 (a), a positive 1951 USAF resolution test target was placed below the output of waveguide. The scanned zones cover elements in group -1 and -2, which are marked with red rectangles. By moving the 1951 USAF test chart, a raster scan was performed to record the time signal at each point, giving rise to a pixelated data map. An image can be obtained both in the time or frequency domain by using different mathematical criteria [231]. For example, by integrating frequency components from 400 GHz to 500 GHz, two images have been extracted (Figure III.7 (b) and (c)).

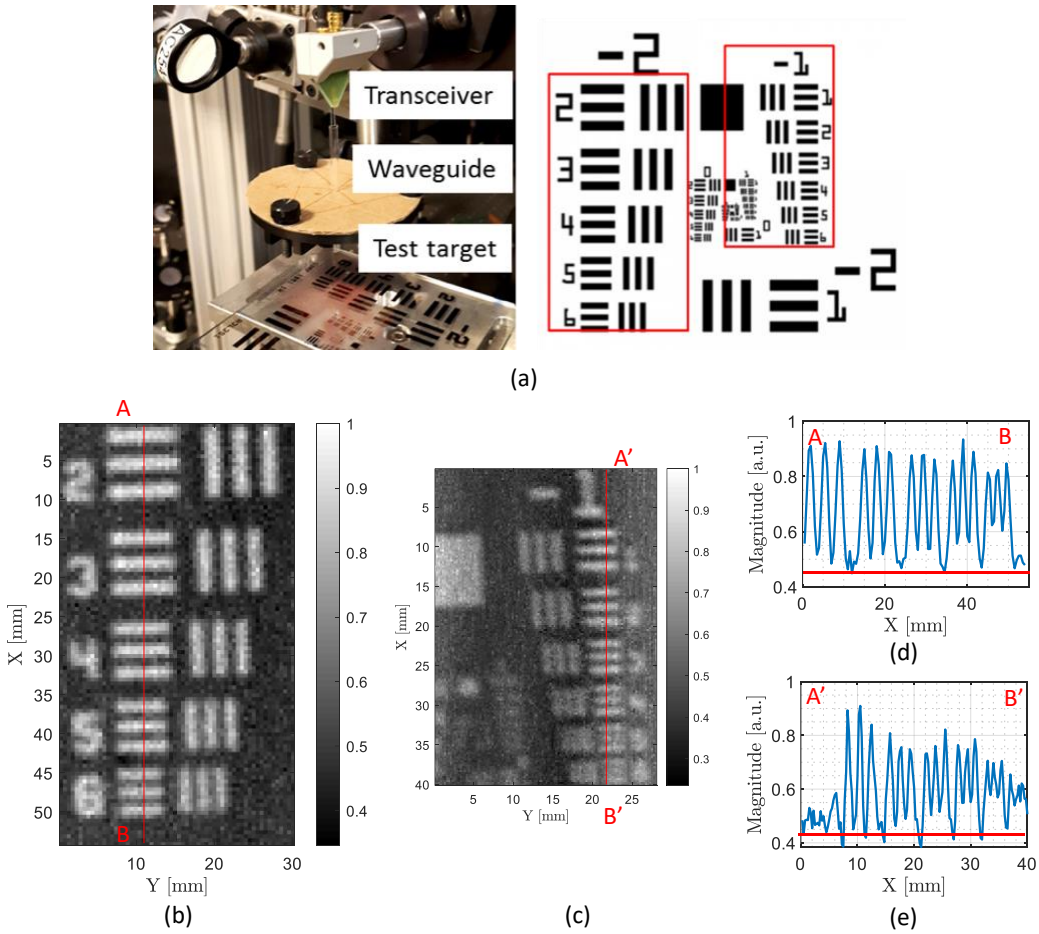

Figure III.7: (a) Left: Photograph of the experimental setup. The silica hollow-core waveguide is placed below the terahertz transceiver and a 1951 USAF test target as the sample is mounted on the multi-directional linear translation stages. Right: 1951 USAF resolution test target, in which the scanned areas are marked by the red rectangles. (b) and (c) Two images of the scanned areas (elements in group -1 and in group -2 respectively) are obtained from the trapezoidal integration over frequencies from 400 GHz and 500 GHz. (d) and (e) The line profiles of terahertz field magnitude along the solid line AB in group -2 and solid line A'B' in group -1.

Line profiles of terahertz magnitude along the solid line AB in group -2 and line A'B' in group -1 are additionally provided. The resolution is given in pairs of lines (a transparent and a reflective) per millimeter (pl/mm) or in the thickness of the corresponding line. When the contrast between bars and substrate is lower than 0.3 it is estimated that two stripes cannot be differentiated. Therefore, lines are still clearly distinguished until the element 4 in group -1. The width of the line is about 707 µm and the spatial

frequency is about 0.707 pl/mm. The imaging capacity of the constructed system is in the order of the wavelength.

To conclude, a terahertz wave-guiding reflectometry system in pulse mode has been demonstrated by combining a double-PCA lens-free transceiver with a silica hollow-core waveguide. The 3D full-wave simulation reveals that both cladding-mode and air-core mode are excited along the waveguide with the atypical excitation condition provided by the transceiver. In spite of it, only the waves propagating inside the air core contribute to the detected signals due to the small size and the position of the transceiver with respect to the waveguide. Thanks to the air-core propagation mode, the frequencies varying from 400 GHz and 500 GHz can be transmitted to the targeted area on the sample and then be reflected and detected. Its imaging capacity was then characterized by using a 1951 USAF test, giving rise to an imaging resolution around 0.707 pl/mm. It is worth noting that although the direct coupling was demonstrated feasible, only 5% (at 450 GHz) of the efficient incident power was coupled into the waveguide, which should be addressed if the performance improvement of the TGR-P system is wanted.

III.2.3. TGR-P system II with a plastic waveguide

In addition to a 3 mm silica hollow-core waveguide, a 6 mm diameter plastic waveguide was also selected to construct a TGR-P system. Although its guiding capacity exploiting the anti-resonant reflection has been demonstrated by THz-TDS measurements, the propagation behaviors of waves along the waveguide under the excitation condition provided by the transceiver remained unknown. To explore the feasibility of this system configuration and its application potential, the same approach (3D full-wave simulation in combination with experiments) has been applied. Relevant investigations are presented in the following part.

III.2.3.1. Propagation behaviors analysis (simulation)

As illustrated in Figure III.8 (a), the simulation model consisted of a simplified transceiver probe, a 10 cm-long plastic waveguide and an air block. During the transmission process, both electric field and power flow were both monitored. Figure III.8 (b-d) show the distribution of the power flow (Poynting vector) on different cutplanes at the frequency of 450 GHz.

Multi-mode propagation

Similar to the previous case, both air-core modes and cladding modes are excited along the waveguide, expressed as the spatially separated field confinement areas, in the air-core and inside the cladding (see Figure III.8 (d)). The segmentation of the guided power in the time domain related to the refractive index of the cladding also confirms the presence of two different kinds of propagation mode (not shown here). By surface integral of Poynting vector, the power propagating through the waveguide (total forward-propagating power, power propagating in the air-core and the one passing through the cladding respectively) was also deduced, depicted in Figure III.8 (e). The result indicates that only 0.22 W effective incident power arrives inside the entrance of waveguide. Due to the mode overlap mismatch between the transceiver emission pattern and guided modes, a considerable power fraction is radiated into free space as the coupling loss. This phenomenon can be seen in the area between the position I and II in Figure III.8 (b-d). After a propagation distance of 30 mm, 12 % of the effective incident power is coupled into the plastic

waveguide, which is higher than 5 % coupling efficiency obtained in the previous system incorporation with silica waveguide. After a 10 cm-long propagation, 0.005 W power is still confined in the air-core, 5 times higher than the results obtained with silica waveguide thanks to the improved coupling efficiency. Although the cladding mode is excited along the waveguide, their power portion amongst guided waves is reduced to 5% while the guided power portion in the core is higher than 58 %. In fact, waves propagating in cladding mode are of no interest in the experiment due to their low carried power portion with significant time delay, and the important distance to the detector of the transceiver. Further investigations focus on waves propagating in the air-core.

It is noticeable that the continuous power flow confined in the air-core obtained in the previous case (shown in Figure III.4) is not established here. Instead, power flow distribution on the xy-plane inside the waveguide varies with propagation distance. For instance, the power flow on the cutplanes of IV and V (z = 75 and 90 mm respectively) in Figure III.8 (d) display distinct differences: while the highest power intensity lies at the center of air-core with an FWHM of 1.7 mm at the xy-plane of z = 75 mm (IV), a ring-shaped power flow distribution can be observed inside the air-core on the cross-section of z = 90 mm (V). The geometry feature of the waveguide is suggested to be associated with this position-dependent field distribution. The applied plastic waveguide possesses a diameter of 6 mm, much larger than the dimension of the transceiver probe and transmitted wavelength. The emitted waves arrive at different positions inside the waveguide at different moments, exciting various propagation modes. The superposition of propagation modes may result in a strong/weak E-field at certain locations. Since the propagation direction changes after each reflection taking place at the interface of cladding, the final field distribution becomes position-dependent, expressed as the oscillation of power inside the core. It should be pointed out that although the power density at the center of waveguide varies sharply, the whole power guided by the waveguide remains stable.

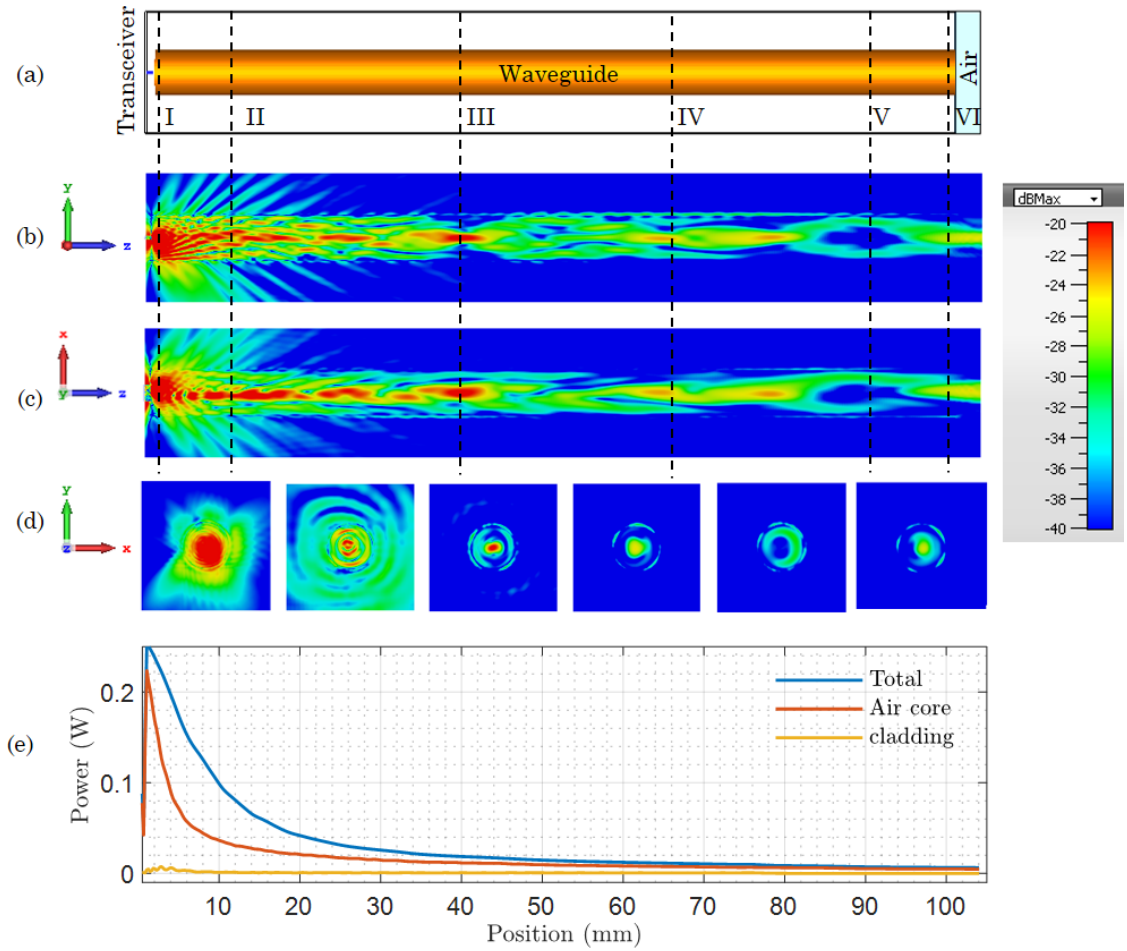

Figure III.8: Full-wave simulation result obtained at the frequency of 450 GHz. (a) Numerical model including a transceiver probe, a 10 cm long plastic waveguide and an air-block. (b-d) Power flow distribution on the cutplanes (V.A/m²). I to VI correspond to cutplanes of z = 2/10/40/75/90/100 mm respectively. (e) Power passing through cross-section as a function of distance. Blue curve: surface integral over the whole cross-section. Red curve: surface integral of the Poynting vector over the air-core section. Yellow curve: surface integral of the Poynting vector inside the cladding.

Frequency composition

Foregoing discussions reveal that the electric field distribution on the cross-section depends on the propagation distance at 450 GHz. As the pulse signal emitted by the transceiver probe is a broadband signal, it is of interest to study the frequency-dependent propagation properties. Considering the relative position between the waveguide and the transceiver, the signal propagating at the center area of the waveguide core can be detected efficiently by the transceiver. Figure III.9 provides the power passing through the central area (radius less than 1 mm, which is plotted as dash-dot lines) and the one cross all the air-core (plotted as the solid lines) as a function of the distance at two different frequencies of 450 and 550 GHz respectively. While the power inside the core decreases gradually and slowly (solid lines), the dependence of the power crossing the center area on the position is noticeable. While the guided power lies at the center of the air-core in the position of 70 mm for both frequency components of 450 GHz and 550 GHz, 450 GHz frequency component display a ring field distribution in the air core in the position of 90 mm. To conclude, the

frequency composition of the detectable signal (lying at the center of the core) at the end of the plastic waveguide varies with the propagation distance.

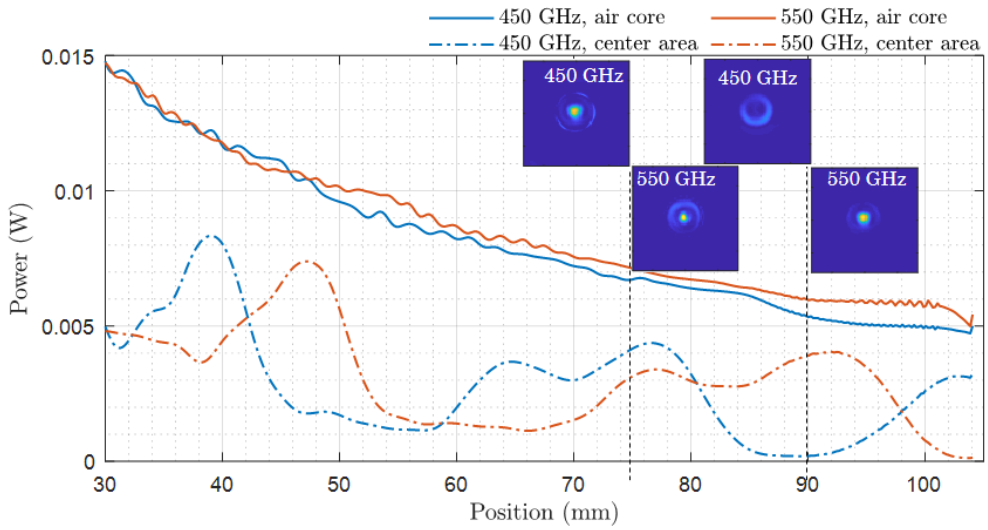

Figure III.9: Power passing through cross-section as a function of the propagation distance at the frequency of 450 GHz (blue curves) and 550 GHz (red curves). Solid curves represent the power crossing the whole cross-section while dash-dot curves denote the power passing through the center area of the waveguide's core (radius < 1 mm).

III.2.3.2. Characterization of detected time signal

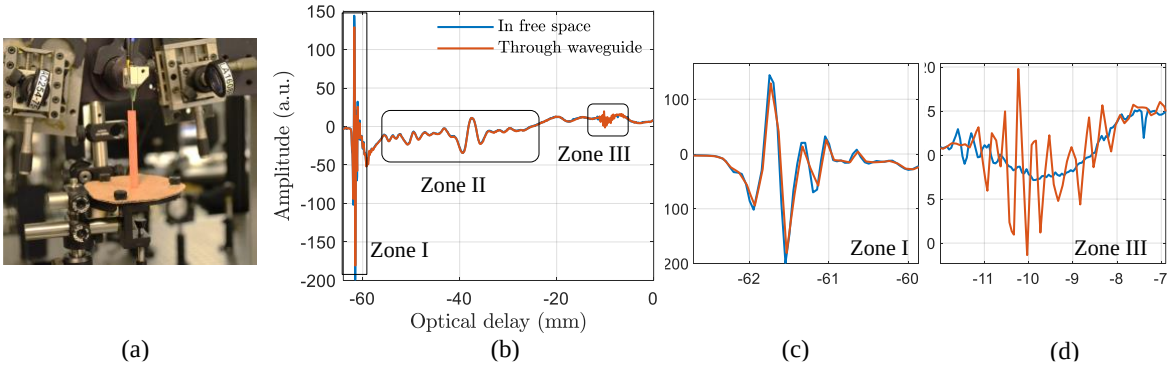

Figure III.10: (a) Photograph of experimental setup exploiting a plastic hollow-core waveguide as the single communication channel between the transceiver and sample. A metal plate acting as a perfect mirror is placed at the output of the waveguide to obtain the maximum reflected energy. (b) Time signals reflected by the metal, in the free space (blue curve) and though a plastic hollow-core waveguide (red curve). According to the origins of reflections, the waveform of time signal can be divided into three zones. The waveform in zone I corresponds to the crosstalk signal between two antennas and the one in zone II originates from the internal reflection from the probe-base. Signals reflected by the metal lie in zone III, a close-up view is given in (d), in which the amplitude of the signal passing through the waveguide is much stronger than that propagates in free space.

By taking advantage of the same experimental implementation as previously (depicted in Figure III.10 (a)), the time signal reflected from a metal sheet was characterized. While keeping the position of the metal plate, time signals were recorded in two different configurations, freely propagating signal (blue curve) and guided waves along the waveguide (red curve) respectively. As shown in Figure III.10 (b) and (c), the crosstalk signal between two PCAs can be observed in zone I, indicating the generation of a terahertz

pulse signal. Zone II contains significant low-frequency pulse signals induced by the internal reflections. In comparison to the reflections propagating in free space, the reflections passing through the waveguide display a considerable power enhancement lying in zone III shown in Figure III.10 (c). The distortion of pulses signal caused by modal dispersion and multi-mode propagation can also be observed.

Impact of length of plastic waveguides

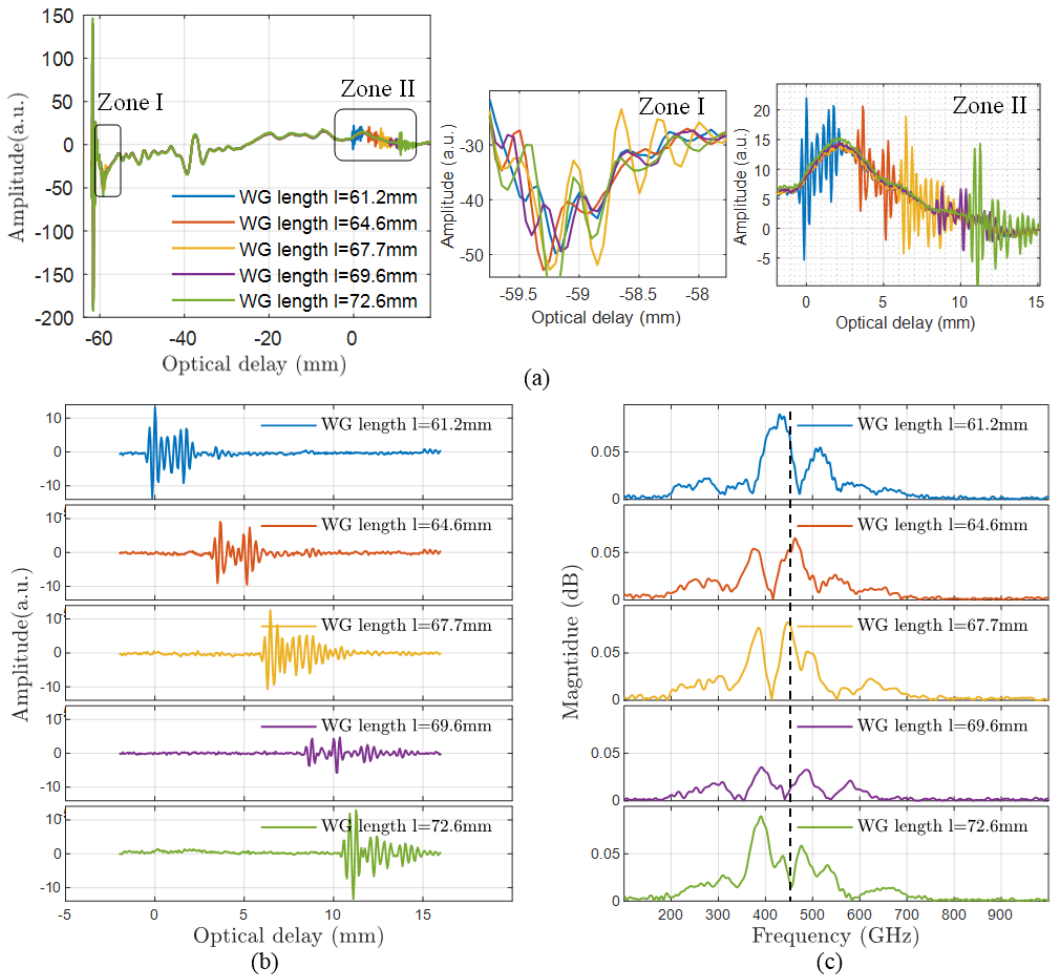

Figure III.11: (a) Reflected signals from metal placed at the output of plastic waveguide. In each measurement, the plastic hollow-core waveguide has a different length. While the crosstalk signals in different measurements are overlapped (zone I), reflections from the sample have different features (zone II). (b) Reflections from metal after removing the crosstalk signal induced by the probe itself. (c) Spectra of reflections shown in (b).

Based on the simulation results, it is anticipated that the time signal detected by constructed TGR-P system depends on the propagation distance, *i.e.*, the length of plastic waveguide. To verify this assumption, plastic hollow-core waveguides with different lengths varying from 61.2 to 72.6 mm were tested in association with the double-PCA transceiver probe. A metal plate was placed at the output of waveguide to maximize the reflected signal. The obtained waveforms of time signals are given in Figure III.11 (a) with two close-up views in zone I and II. By removing the crosstalk signal and internal reflections,

the reflections from the metal were obtained, shown in Figure III.11 (b). The corresponding spectrum is given in Figure III.11 (c). As shown in Figure III.11 (b), detected reflected signals via waveguides display significant time delay due to the different propagation lengths. In particular, they exhibit distinct waveforms, for instance, while the recorded waveform through a 64.6 mm-waveguide waveguide contains two pulse signals, the signal detected by the system through a 69.6 mm-long waveguide contains three distinct reflections. With respect to the frequency composition, clear dissimilarities can be observed between the spectra of reflected signals. While the frequency component of 450 GHz can be detected in the signal propagating through waveguides with a length of 64.6/67.7 mm, less power fraction at this frequency is contained in the detected reflections through the waveguides of 69.6/72.6 mm. These uncommon experimental results corroborate the assumption about distance-dependent field distribution developed on the basis of simulation analysis.

To sum up, experimental results are consistent with simulation presumption, demonstrating that the detected signal is extremely sensitive to the propagation distance. This distance-dependent propagation property preventing the TGR-P system from imaging applications. It is worth noting that despite multi-mode propagation and distance-dependent frequency composition, it is confirmed that the time delay is still in accordance with the propagation path length by taking the arrival time of the first peak as the reference.

III.2.3.3. Liquid depth detection application

Although the scope of application of this TGR-P system using a 6 mm diameter plastic hollow-core thin-wall waveguide is limited due to the distance-dependent field distribution, the time delay linked to the propagation path length opens the door to distance detection for this TGR-P system. Compared to a conventional terahertz system, the guiding capacity of the waveguide in a TGR-P system can facilitate the task to control the propagation properties of waves in the liquid. Consequently, the feasibility to perform a measurement in the liquid using the created TGR-P system was explored and relevant results are introduced in this part.

Working principle

As shown in Figure III.12 (a), a TGR-P system composed of a double-PCA transceiver and a plastic hollow-core waveguide was fixed on the vertical subsystem, and the liquid container in Teflon was placed on the horizontal platform. In order to maximizer the reflected signal, a metal plate was placed at the bottom of the container. Figure III.12 (b) illustrates two different measurement configurations, corresponding to the waveguide in an empty container and the waveguide inserted in a paraffin-filled container. The end of the waveguide is not in contact with the bottom of the container during the measurement.

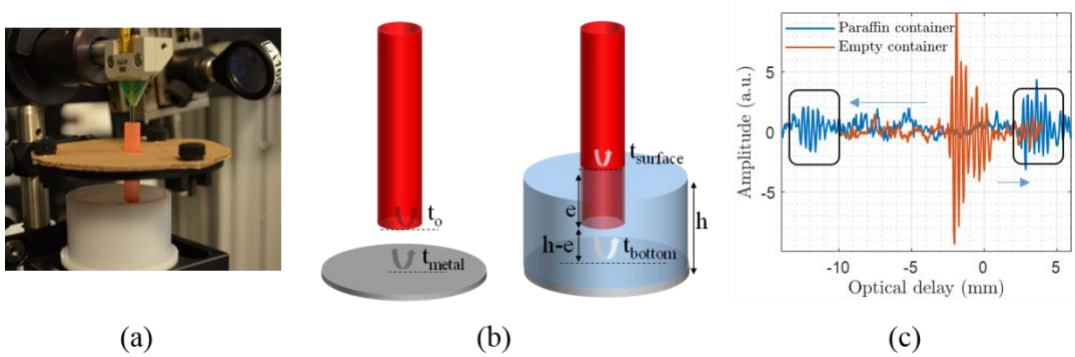

Figure III.12: (a) Photograph of the experimental setup. A metal plate is placed at the bottom of the container to maximize the reflected power. (b) Schematic diagram of two different measurement configurations. Left one represents the measurement performed without liquid, providing a time signal reference. Right one depicts the measurement in the liquid with a depth of *h*. (c) Time signals detected by the transceiver in two experimental conditions. Red curve: reference signal obtained with an empty container. Blue curve: Detected reflections from the liquid surface and the metal placed at the bottom.

In the case of an empty container, the guided signal after leaving out of the waveguide continues to propagate. When the freely propagating signal arrives at the bottom of the container, it will be reflected to the transceiver through the same waveguide. Apart from the reflection from metal at the bottom, no other significant reflection is expected at the output of the waveguide due to the modest mismatch in impedance between the guided waves and freely propagating waves. Once the liquid paraffin is poured into the container, the properties of the propagation media change. A significant portion of the incident power will be firstly reflected at the interface of air-paraffin, then another power fraction will be reflected by the metal plate placed at the bottom. Consequently, two distinct reflected signals with a time delay determined by the liquid depth are anticipated. The time signals recorded by the TGR-P system in two experimental conditions, depicted in Figure III.12 (c), confirm this assumption with two separate reflections. The second part of the reflected signal from the metal arrives later than the ones propagating in free space due to a slower propagation velocity in the liquid paraffin.

By taking the arrival time of reflections generated at the output of the waveguide in free space (t_0) as the reference (it cannot be observed clearly in the experiment), the arrival time of waves reflected from the liquid surface $t_{surface1}$ and $t_{surface2}$ can be expressed as Equation (12):

$$\begin{cases} t_{surface1} = t_0 - \Delta t_{os1} = t_o - \frac{2\times e_1}{v_g} \\ t_{surface2} = t_0 - \Delta t_{os2} = t_o - \frac{2\times e_2}{v_g} \end{cases} \Rightarrow \Delta t_{surface} = \frac{2\times \Delta e}{v_g} \quad \textbf{(12)}$$

where e_1 and e_2 denote the lengths of the waveguide submerged by the liquid in different measurements and the v_g represents the propagation velocity of waves along the waveguide. It is then deduced that the time shift of reflections from the liquid surface $(\Delta t_{surface})$depends on the change of the liquid surface level and the propagation speed along the waveguide (Δe, v_g). Given that the time delay used in the system is composed of two mirrors and a linear translation stage, *i.e.*, $\Delta t = \frac{\Delta ODelay\times 2}{c}$, optical delay in millimeter can further simplify Equations (12) as below,

$$\Delta ODelay_{\ surface} = \frac{\Delta e \cdot c}{v_g} \tag{13}$$

where Δe represents the change of the liquid surface level, v_g and c denote the propagation velocity along the waveguide and in vacuum respectively. It implies that if the liquid surface level detection is wanted, the propagation velocity in different mediums must be known. Although the propagation velocities along the waveguide (either in free space or in the liquid) are difficult to obtain by analytical formula due to their complicated multi-mode propagation behaviors, 3D full-wave simulation in the time domain allows to estimate the propagation velocity by calculating the time shift between the excitation signal and the transmitted signal in a certain distance. As a result, the propagation velocity along the waveguide in the air is inferred from the simulation, around $2.8 \cdot 10^8$ m/s ($\frac{c}{v_g} \approx 1.07$).

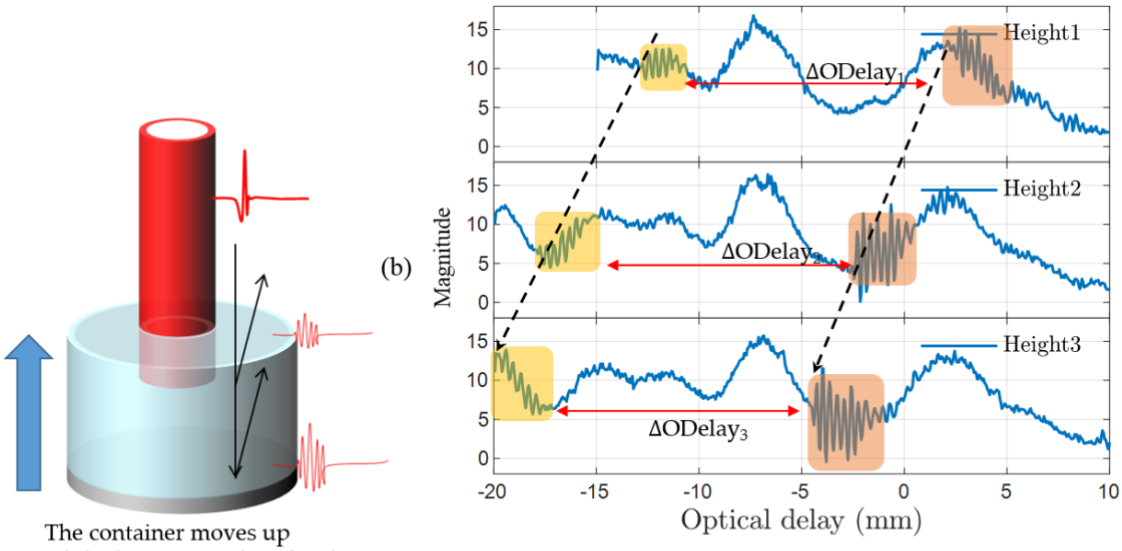

(c)

Unit : mm	Height 1: 15	Height 2: 20	Height 3: 22
$ODelay_{surface}$	-12.50	-17.40	-19.40
$ODelay_{bottom}$	2.70	-2.25	-4.25

Figure III.13: (a) Schematic diagram of the experimental setup. (b) Recorded time signals reflected by the liquid paraffin. While the quantity of paraffin in the container remains the same, the container is raised up twice during the experiment. (c) Arrival time (given as optical delay in mm) of the first peak in reflections from liquid surface and container bottom.

According to Equation (13), the propagation velocity along the hollow-core waveguide can also be assessed by monitoring the time shift of reflections from the liquid surface with controlled liquid surface levels. On this basis, an experiment in the liquid paraffin was performed to verify the propagation velocity in the different mediums. As shown in Figure III.13 (a), the TGR-P system is fixed while the liquid container is placed on a controlled movable platform. The quantity of liquid paraffin remains the same during the measurement and one part of the waveguide is submerged by the liquid. Three measurement results were obtained by raising the liquid container twice (5 mm and 2 mm respectively), given in Figure III.13(b). It can be seen that both reflections from the liquid surface (marked by yellow rectangles) and the

ones from the bottom of the container (marked by orange rectangles) arrive earlier due to the upward motion of the container.

By comparing the arrival time of the first peak of the reflections (Table shown in Figure III.13 (c)), the time shifts between the measurements were obtained ($\Delta ODelay = 4.9$ mm and 2 mm respectively). Based on Equation (13), it can be deduced that the propagation velocity is very close to the vacuum velocity of light ($\frac{c}{v_g} = \frac{\Delta ODelay_{\ surface}}{\Delta e} \approx 1$) , confirming the correctness of the simulation result. The approximate value ($v_g \approx c$) is then used in the following work.

Once the guided waves enter inside the liquid, the propagation path is divided into two parts: guided along the waveguide in the liquid and freely propagating in the liquid paraffin. Hence, the time delay between the reflections from the liquid surface and bottom of the container can be expressed as below,

$$t_{bottom} - t_{surface} = \frac{2 \cdot e}{v_{gl}} + \frac{2 \cdot (h - e)}{v_{liquid}} \tag{14}$$

where t_{bottom} represents the arrival time of reflections from the bottom of the container, h denotes the paraffin depth in the container, $h - e$ refers to the propagation length of waves freely propagating in the liquid, and v_{gl} and v_l represent the propagation speed of waves along the waveguide inside the liquid and the freely propagation velocity inside the liquid respectively. Since the refractive index of liquid paraffin is obtained ($n_{liquid} = 1.465$) through THz-TDS measurements [232], the propagation velocity in the liquid paraffin can be then calculated, *i.e.*, $v_{liquid} = \frac{c}{n_{liquid}} = 2 \cdot 10^8$ m/s. The propagation velocity along the waveguide in the liquid paraffin was inferred through 3D full-wave simulation ($v_{gl} = 1.887 \cdot 10^8$ m/s), which is very close to the value of v_{liquid} ($\frac{v_{liqud}}{v_{gl}} = 1.06$). Equation (14) can be transformed into Equation (15), expressed based on the optical delay values:

$$\begin{aligned} ODelay_{bottom} - ODelay_{surface} &= ODelay_{BS} \\ = \frac{e}{v_{gl}} \cdot c + \frac{(h-e)}{v_{liquid}} \cdot c &= \frac{h}{n_{liquid}} + \left(\frac{c}{v_{gl}} - \frac{c}{v_{liquid}}\right) \cdot e \end{aligned} \tag{15}$$

Since the difference between v_{liquid} and v_{gl} is small ($\frac{c}{v_{gl}} - \frac{c}{v_{liquid}} < 0.1$), Equation (15) can be further simplified as follows:

$$ODelay_{BS} = \frac{h}{n_{liquid}} \tag{16}$$

Measurement of the liquid depth

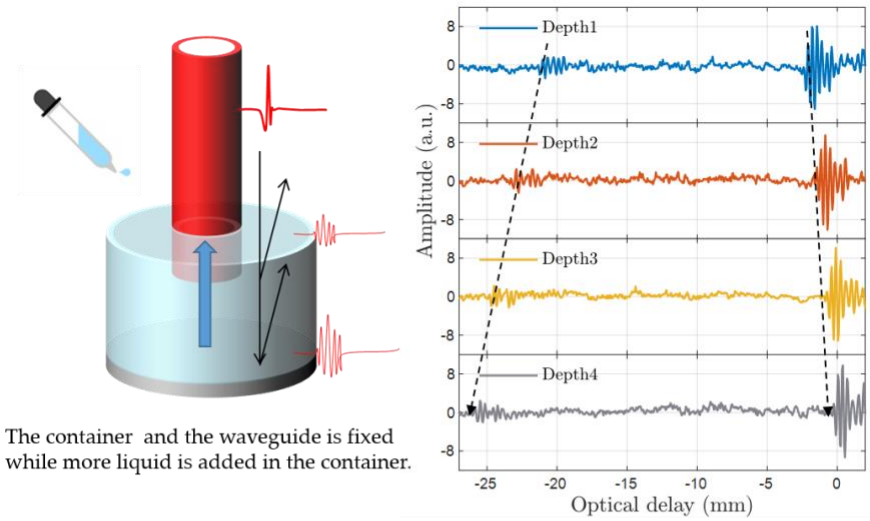

(a) (b)

Unit : mm	Depth1	Depth2	Depth3	Depth4
$ODelay_{surface}$	-21	-22.9	-24.5	-25.5
$ODelay_{bottom}$	-2.098	-1.147	-0.398	0.053
$\Delta ODelay_{SB}$	18.90	21.75	24.10	25.55
Depth:h	12.90	14.85	16.45	17.44
Δh	/	+1.95	+1.6	+0.99	/
Δe	/	+1.9	+1.6	+1	/

(c)

Figure III.14: (a) Experimental setup. While the liquid container is fixed, liquid paraffin is added after each measurement. (b) Recorded waveforms of time signal reflected by the liquid paraffin. (c) Arrival time (given as optical delay in mm) of the first peak in reflections from liquid surface and container bottom. Based on the time delay between two reflections, liquid depth and level change between measurements are given in the table.

New measurements were performed to verify the liquid depth detection capacity of the constructed guided reflectometry system. As shown in Figure III.14 (a), both TGR-P system and the container was fixed during the measurements while the liquid paraffin was added after each measurement. The recorded time signals and measured arrival time are shown in Figure III.14 (b) et (c). Due to the augmentation of liquid quantity, reflections from the liquid surface arrive earlier while the reflected signal from the bottom displays a more significant time delay due to the increment of the propagation path in the liquid. The approximation of the propagation velocity, *i.e.*, $v_g \approx c$, $v_{gl} \approx v_{liquid}$ were applied to calculate the liquid depth. Based on Equation (16), liquid depths of 12.90/14.85/16.45/17.44 mm were deduced. The depth difference between each measurement is in agreement with the one deduced from the arrival time of reflections from the surface level. Nevertheless, for a high-precision detection, the difference between the propagation velocity in diverse mediums ($\frac{c}{v_g} = 1.07$, $\frac{v_{liquid}}{v_{gl}} = 1.06$) must be taken into consideration. Additionally, it should be pointed out that the resolution of liquid depth detection is partly impacted by the dynamic range of this TGR-P system and its parameter set up, especially the step of the optical delay.

As a proof-of-concept, the aforementioned experiments for paraffin depth detection demonstrate the potential of the TGR-P probing system for diverse applications. By taking advantage of the time shift of reflections from the liquid surface, the change of the liquid surface level can be evaluated. If reflections from the surface and bottom are both recorded, the depth of liquid can be inferred. The use of a 6 mm diameter plastic hollow-core waveguide expands the scope of the application of the double-PCA transceiver to measurements in the liquid with a reduced damage risk. It is worth noting that if the liquid depth is set and known, the dielectric properties of the liquid can be inversely accessed by analyzing the time signals. At last, it should be pointed out that all analysis was based on the condition that the guided modes along the waveguide in the liquid can be maintained (anti-resonant reflection), which limits the liquid depth detection for the liquid with a lower refractive index than the plastic cladding ($n_{liquid} < n_{cladding}$).

III.3. Terahertz wave-guided reflectometry system in FMCW mode

Benefitting from the advances in semiconductor technologies, the performances of millimeter-waves devices are being improved continuously while their operating frequency has been pushed up in the terahertz band. Amongst these devices, FMCW radars in the terahertz band in combination with quasi-optical components have been widely used in different fields for imaging and sensing purposes. However, the implementation of optical components involves tedious alignment and imposes mechanical restrictions on the propagation path, limiting the development towards a compact, portable and easily-implementable terahertz measurement system for a larger scope of applications. To address this issue, an alternative solution is under investigation with the use of waveguide for signal transmission. Through the literature, this guided reflectometry concept has already been investigated with various CW sources and different waveguide specifications. For instance, the chemical process was monitored by a Teflon hollow-core waveguide in combination with a 400 GHz CW source [152] and a remote endoscopic system was displayed with a metal-coated waveguide and a 584 GHz CW source [230]. Compared to guided reflectometry measurement techniques using CW sources, where the detected signal is a superposition of all the contributions that are generated along the waveguide, the phase information provided by guided FMCW techniques unlocks depth sensing capabilities and allows for a differentiation of those contributions. In other words, FMCW radars can distinguish different origins of the contributions along the waveguide, ensuring a drastic improvement of the signal-to-noise ratio by detecting only the signal localizing at the targeted sensing area without taking account of other parasitic signals. Although a waveguide was used to forward a signal in the previously mentioned studies [152], [230], the complexity induced by the optical coupling system (beam splitter, lenses, parabolic mirror placed before the input of the waveguide) limits the progress towards compact guided sensing units.

To deal with this problem, the same concept used in Chapter III.2 (TGR-P system) was applied to construct a terahertz wave-guided reflectometry system in FMCW mode (TGR-FMCW): the system configuration can be highly simplified by combining a compact FMCW transceiver with a dielectric thin-wall hollow-core waveguide. An optic-free transmission channel between the transceiver and the sample is then ensured with all the benefits of the FMCW radar sensing technique. Chapter II.3 has presented two available FMCW transceiver units, namely 100 GHz SynView head and a 122 GHz Silicon Radar transceiver chip. In order to ensure the coupling between the transceiver unit and waveguide (both forward-coupling and back-coupling), the propagation area in the waveguide must cover the front zone of Tx and

Rx. This requirement can be easily meet in the case of the 100 GHz SynView head due to its mono-static architecture. Nevertheless, the separation of 3 mm between two patch array antennas on the 122 GHz Silicon Radar chip imposes a minimum diameter requirement for the hollow-core waveguide. As a result, only the 6 mm-diameter plastic waveguides was tested as the optic-free communication channel between the sample and transceiver chip.

In the following part, two guided reflectometry configurations consisting of different compact FMCW radar units are introduced. Investigations into the propagation behaviors along the waveguide conducted by simulation together with system performance assessed by experiments are given. In particular, discussions with respect to the guiding modes, coupling issue, dynamic range, and imaging capacity are detailed. Additionally, the imaging capacity improvement induced by the integration of an extra termination hemispherical lens is presented.

III.3.1. TGR-FMCW system I using SynView transceiver unit

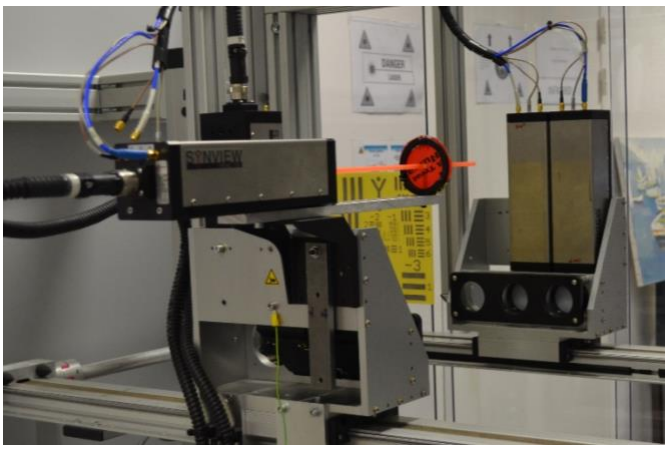

Figure III.15: Photograph of experimental setup by combining the SynView 100 GHz head with a hollow-core waveguide.

The first terahertz wave-guided reflectometry consists of a 100 GHz SynView transceiver head and a 30 cm-long thin-wall plastic waveguide. Since the horn antenna in 100 GHz transceiver head plays the roles of Tx and Rx antennas at the same time, a single communication-channel between the transceiver and sample can be directly ensured by a hollow-core dielectric waveguide. In regard to the coupling implementation, the dimension mismatch between the waveguide (6 mm diameter) and the horn antenna (16.2 mm diameter open mouth) must be taken into account. The field distribution inside the horn (illustrated in Figure II.25 in Chapter II.3.2) has revealed that the beamwidth out of the horn antenna is comparable to the outer diameter of the antenna. Besides, the result displayed that the electric field is better confined with a higher energy density at the center of the antenna at the position of z varying from 10 to 20 mm. For the aforesaid reasons, a hollow-core waveguide was directly inserted inside the horn antenna to maximize the forward-coupled power to implement the guided reflectometry system with the 100 GHz Synvview radar head (depicted in Figure III.15). As a simple optimization, the foam support acting as terahertz absorber was placed at the beginning of the waveguide to neutralize the unwanted parasitic reflections and fluctuations induced by the non-coupled echoes from optomechanical elements or the

presence of waveguide. Moreover, this inserted absorber helps to establish the symmetric positioning of the waveguide with respect to the input facet of the conical horn.

III.3.1.1. Propagation behaviors of radar signal (simulation)

As shown in Figure III.16 (a), the simulation model based on the 100 GHz SynView transceiver reflectometry unit was composed of a typical W-Band (WR-10) conical horn antenna, a 30 cm long plastic hollow-core waveguide and a 5 cm long air block. The circular input face of the conical horn antenna was selected as a waveguide port for signal excitation and detection. The waveguide was placed at 10 mm (Position I) after the interface of the horn antenna and circular waveguide (origin plane, z = 0). All the E-field results presented below were obtained at the frequency of 100 GHz. No material loss (neither in dielectric material nor in metal) was considered in those simulations.

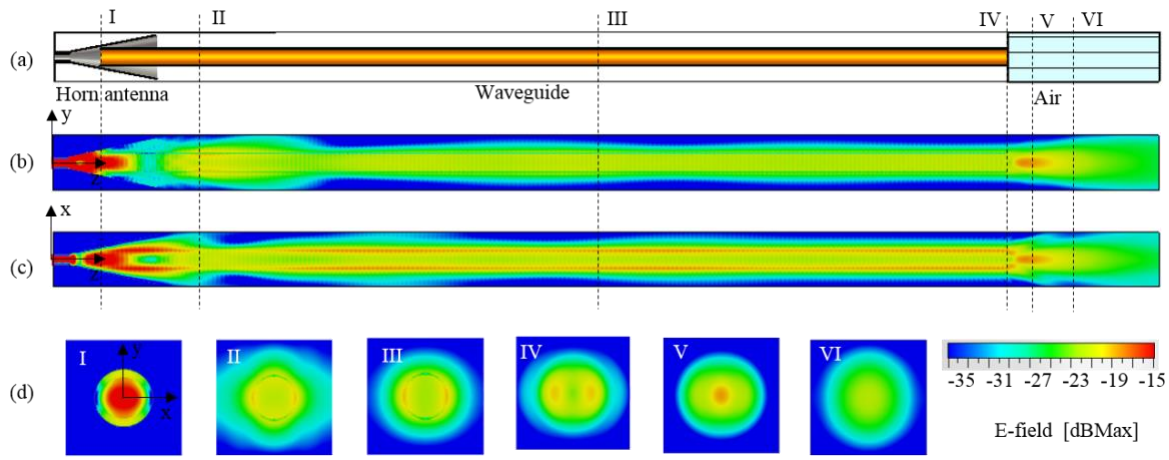

Figure III.16: (a) Simulation model of terahertz wave-guided reflectometry system consisting of a horn antenna and plastic pipe waveguide. (b) and (c) E-field distribution ($|\vec{E}|_{max}$) at frequency of 100 GHz on the cutplant of x = 0 and y = 0 respectively. (d) E-field on the xy-planes (18*18 mm²) at different positions of z = 10 mm (I, the entrance of waveguide), 40 mm (II), 180 mm (III), 310 mm (IV, the output of waveguide), 315 mm (V, 5 mm after the output), 330 mm (VI, 20 mm after the waveguide).

Propagation modes

Field distribution simulation results at the frequency of 100 GHz, displayed in Figure III.16 (b) and (c), provide substantial information concerning the propagation behaviors of guided waves in the system which are tightly related to the profile of the injection source. Over the first part of the propagation, a stabilization of the guided signal is noticeable. Once waves propagate out of the horn antenna, uncoupled waves radiate into free space and unfavorable modes attenuate rapidly with the distance. After 100 mm's propagation, a steady state is attained, expressed as the waves loosely confined along the waveguide. The stable guided waves corroborate the guidance capacity of the waveguide. Nevertheless, the field distribution along the waveguide in the xz-plane, shown in Figure III.16 (c), reveals that not only air-core modes but also cladding modes are excited under that specific excitation condition of the conical horn antenna, resulting in the significant field confinement in the vicinity of the cladding in the x-direction. In addition to the field distribution at specific frequencies, the propagation behaviors of waves simulated in the time domain were also examined (not shown here). Different from the cladding mode displayed in the silica

thin-wall (shown in Figure III.3), no power fraction can be observed in the cladding with considerable time delay related to the refractive index of the plastic. Moreover, the guided power in this mode exhibits a propagation speed close to the light velocity ($\approx 2.78 \cdot 10^8\ m/s$), and most of them is confined in the air close to the cladding. These propagation properties correspond to that of a dielectric microwire, which exploits modified total intern reflection as the guiding mechanism within a subwavelength dimension. Considering the thickness of the cladding (158 µm), the wavelength of radar signal (around 600 µm) and the field distribution along the waveguide, it is assumed that the part of the signal confined in the two extremities of the waveguide in the x-axis is guided in cladding mode with total internal reflection. Since most of the guided waves in cladding mode lie in the surrounding air, low-loss propagation enables the arrival of the guided waves at the end of the waveguide. While one part of guided power is reflected due to the change of resonant impedance, the other power fraction radiates into free space. More precisely, modest reflections from the waveguide-air interface are anticipated due to the effective index close to the air, ensuring a good system dynamic range.

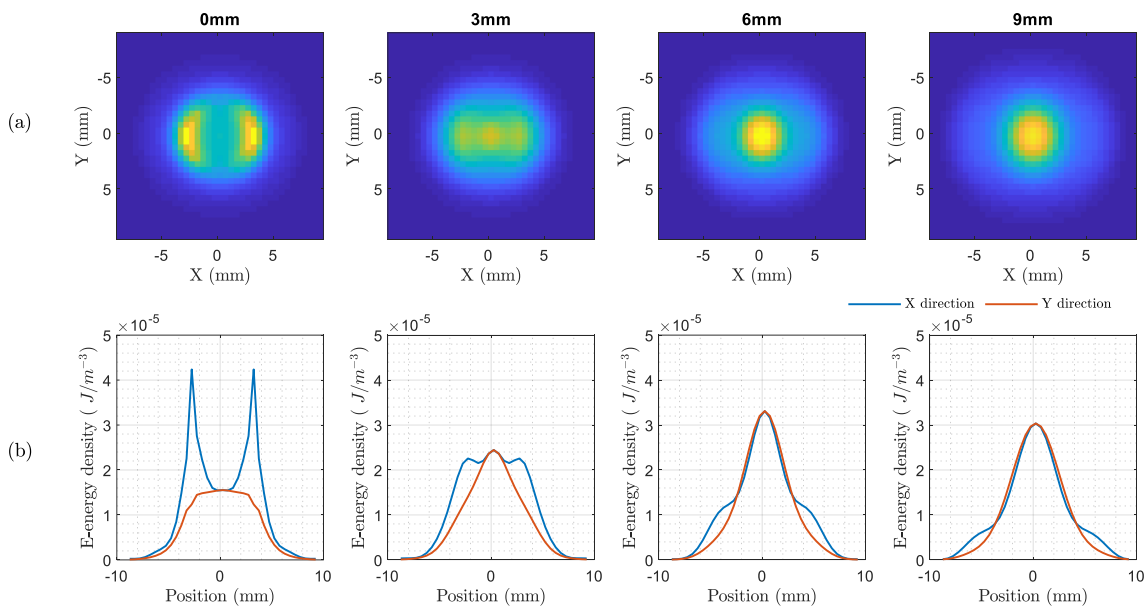

Figure III.17: Beam profile evolution in free space. (a) 2D beam profiles and (b) line profiles in the x- (blue curve) and y-direction (red curve) obtained at a distance of 0/3/6/9 mm from the output facet of the waveguide respectively.

It is worth noting that the cladding mode propagation contributes as well to the beam profile out of the waveguide in free space (depicted in Figure III.16 (c)). The cross-section views of the electric field in the vicinity of the output of the waveguide are given in Figure III.16 (d), in which Position IV to VI display the evolution of the beam profile in free space: two significant lobes of E-field confined in the vicinity of the cladding are transformed to one centered beam in a distance of several millimeters after the waveguide due to the beam spreading. The beam profiles radiating into free space as a function of the distance are also given in Figure III.17. The beam profile in the vicinity of the output of the waveguide exhibits two lobes (see Figure III.17 (a)), which may result in the unwanted artifacts (superposition of the two images) for imaging purposes. As waves continue to propagate in free space, the overlap of two lobes in free space leads to a significant peak at the center (see Figure III.17 (b) and (c)). While the highest power

can be obtained at the output of the waveguide, a Gaussian-like beam can be achieved at a working distance of > 5 mm, which can minimize the artifact caused by the irregular beam form. Without any imposed restriction, the output beam in free space continues to expand. It should be noticed that while the energy density increases at the center from Figure III.17 (b) to (c), the carried power begins to dissipate in the air.

Coupling efficiency

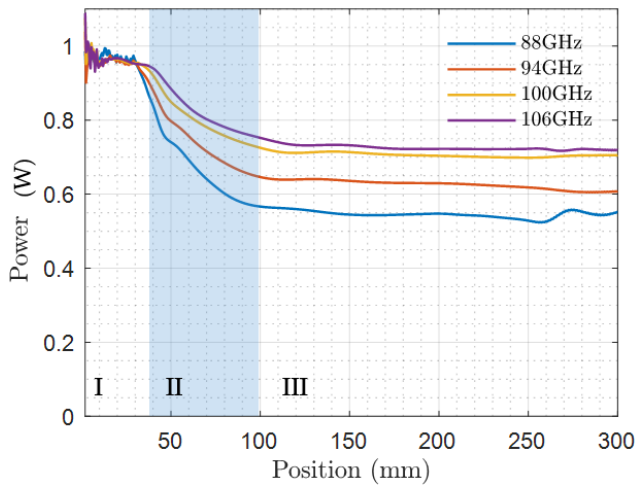

Figure III.18: Power propagating through the cross-section as a function of distance at the frequency of 88/94/100/106 GHz respectively.

The coupling was achieved directly by inserting the waveguide into the conical horn antenna of the radar unit with a proper position centering. Although the assessment of the coupling efficiency via experiment is difficult, 3D full-wave simulation can help to estimate the forward coupled power in the waveguide. Figure III.18 depicts the propagating power as a function of the distance (z_{max} = 300 mm) at different frequencies. The power featured over the first 30 mm (Phase I), corresponds to the excitation signal confined in the metallic horn antenna. The gradual decrease (Phase II) is induced by the radiation loss of non-coupled waves. The stable propagation then takes place along the waveguide (Phase III). Here, the forward-coupling efficiency is determined as a ratio of the coupled power and excited power. Therefore, the coupling efficiency at the frequency of 100 GHz can be directly inferred from the simulation, approximately 70%. Compared to lower frequencies, the components lying in the higher part of the spectrum display higher efficiency. The coupling efficiency varies from 52 % to 72% for frequencies spanning from 88 GHz to 106 GHz, demonstrating the efficiency of this simple optic-free coupling method.

Working distance and dynamics

The propagation behaviors of waves in free space after the waveguide is of interest to characterize the sensing and imaging capabilities of the entire system. Indeed, the propagation properties of radar signal leaving out of the waveguide determine the optimal sensing distance as well as the lateral resolution at the probing point. While the maximum sensing distance is related to the back-coupling efficiency between the sample and waveguide, the imaging capacity is established by the beam profile, the latter being especially important for imaging purposes. To investigate the back-coupling efficiency, a metal plate was added after the output facet of the waveguide at different distances and the energy remained in the simulation box was

monitored in the time domain. The relevant results are given in Figure III.19, displaying that the guided waves arrive at the end of the waveguide at the time of around 1300 ps and then encounter the perfect mirror. After 2500 ps, the reflected power is absorbed by the simulation box. Depending on the distance between the waveguide and the metal, the divergence of the beam occurring in free space results in the reduction of the reflected power fraction. As a result, the back-coupling efficiency between the sample and the waveguide is optimized in the vicinity of the waveguide's output (blue curve in Figure III.19 with distance = 0 mm).

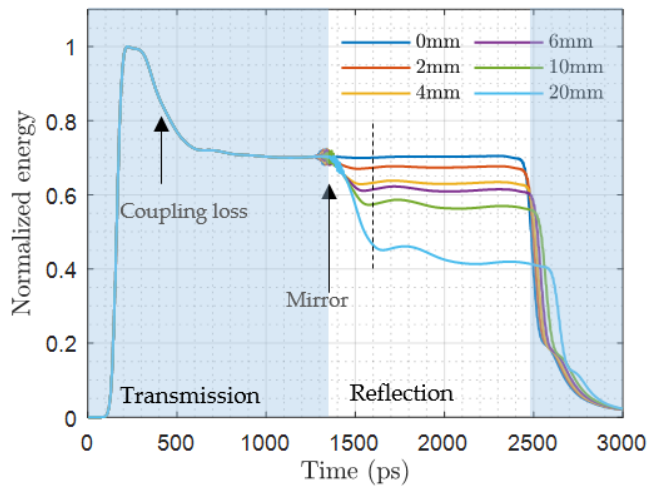

Figure III.19: Energy remained in the simulation box during the transmission and reflection under the condition that a perfect mirror (metal) is placed at the end of the waveguide with different distances. At the time of around 1300 ps, guided waves encounter the perfect mirror and then are reflected back through the waveguide. After 2500 ps, the reflected waves are detected and absorbed by the waveguide port.

For such reflectometry sensing tools, the measurement dynamic is one of the main performance indicators. A 100 GHz SynView FMCW Radar head itself offers a 50 dB dynamics when used in standard imaging configuration. Nevertheless, limitations induced by the implementations of the waveguide are expected. An unavoidable signal returns from the open probing end of the waveguide and the coupling loss are the main limiting factors for the dynamic range together with the imperfect waveguide-antenna coupling. A -28.5 dB amplitude reflection coefficient from this open-end back-reflection has been deduced from the conducted simulations. Similarly, using a perfect reflector at the end of the waveguide, a -0.5 dB return signal coefficient has been deducted from the reflected field amplitude in comparison with the input excitation, mainly impacted by the imperfect coupling from the horn antenna to the waveguide at the beginning, leading to a total dynamic range of 27 dB.

While the highest dynamic range can be achieved in the vicinity of the waveguide, the beam profile with two main amplitude lobes confined in the opposite sides of waveguide's cladding (depicted in Figure III.17, when distance = 0) may lead to ghost imaging artifacts. The simulated evolution of the beam profile in free space implies that a Gaussian-like beam with an FWHM of 4.5 mm can be obtained at a working distance of 6 mm thanks to the spreading of the two lobes (see Figure III.17), which may contribute to the quality improvement for imaging purpose. There is a trade-off between the dynamic range and lateral resolution power to determine an optimum working distance.

III.3.1.2. Imaging application

Resolution power of the TGR-FMCW system is extremely important for imaging applications, which is established by its beam profile. A test chart, shown in Figure III.20 (a), was used to evaluate the imaging capacity of the constructed guided reflectometry system. For comparative purposes, the far-field image obtained with the classical quasi-optical implementation of the 100 GHz SynView unit in the configuration of NA = 0.5 is as well displayed in Figure III.20 (b). Figure III.20 (c) shows the raster scan image obtained when the test chart was placed 1 mm far away from the output of the waveguide for a better back-coupling efficiency between the waveguide and sample.

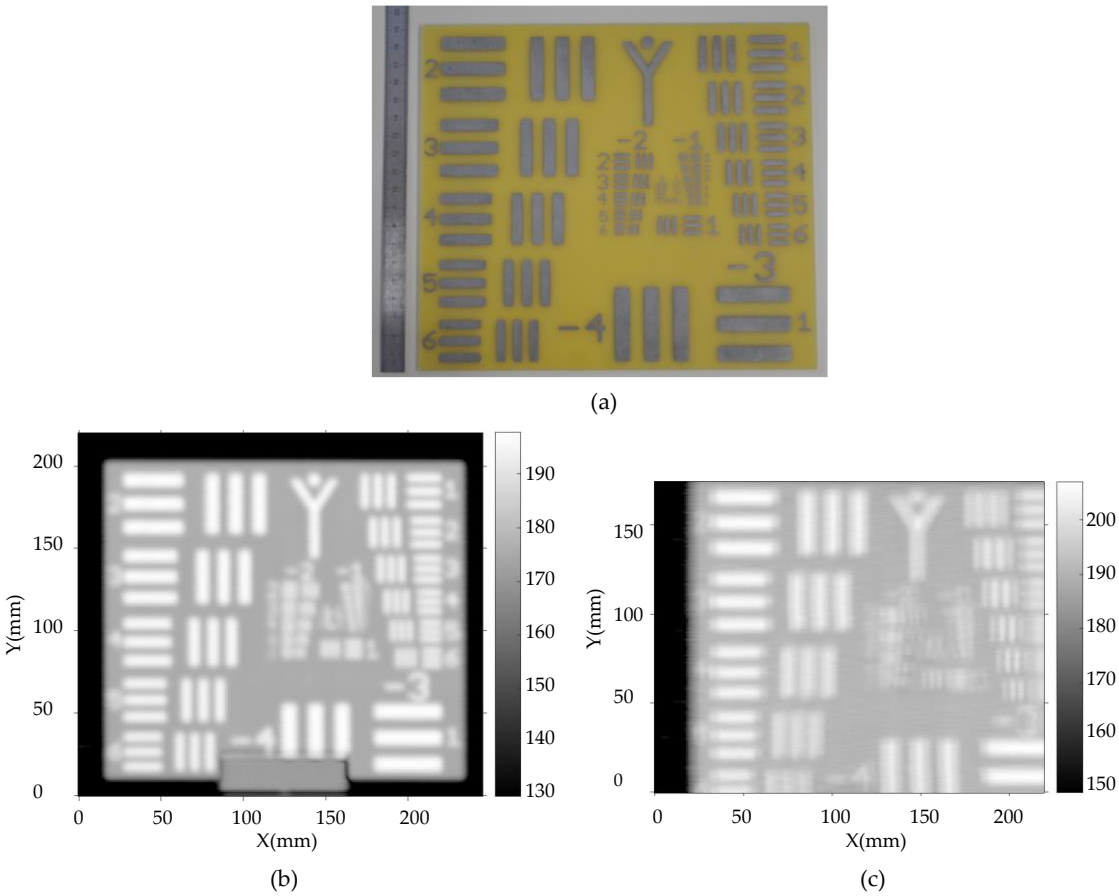

Figure III.20: (a) Photograph of a 1951 USAF test chart. (b) Raster scan acquired image using the regular far-field 100 GHz SynView unit at NA=0.5 (a 50 mm diameter dielectric lens with a focus distance of 50 mm was used to focuse the incident beam) for reference. (c) Raster scan acquired image using the guided 100 GHz Synwiew probing system in optic-free geometry at 1 mm imaging distance.

In comparison to the image obtained with the quasi-optical method, the constructed TGR system exhibits a similar resolution power: the vertical bars of element 6 of group -3 with a width of 2.2 mm, can be distinguished. However, the images of bars in group -3 are fuzzy, expressed as a duplication of the bars (shown in the left-top side of Figure III.20 (c)) in the x-direction. This obvious ghosting effect in a single direction validates the correctness of the simulation results, confirming that the cladding mode is excited along the waveguide and it contributes significantly to the guided waves. It has been discussed previously

that while the impact of the optical profile heterogeneity is noticeable in the proximity of the waveguide, a Gaussian-like beam can be achieved in a working distance of 6 mm due to the spreading of the two lobes. Although the experiment was not performed, it is estimated that while the ghosting effect will be avoided, the resolution power can reach up to 4.5 mm (FWHM of the beam) with a reduced dynamic.

III.3.1.3. Optical resolution improvement

Benefiting from the adapted dimensions of the waveguide, a satisfactory coupling efficiency from the transceiver to the waveguide (up to 70%) has been achieved via optic-free configuration. Nevertheless, significant power fraction confined in both sides of the cladding prevents the guided reflectometry system form high resolution required applications. To address the limitations of the imaging resolution linked to the waveguide's diameter while avoiding heavy configuration with optical components, an end-of-waveguide solid immersion lens has been selected as an adequate solution. Thanks to their specific geometries and materials, typically hemispherical, hypo or hyper-hemispherical or bullet dielectric lens designs, solid immersion lenses allow for high numerical aperture (NA) focusing for high-resolution imaging.

End-of-waveguide solid immersion lens

As illustrated in Figure III.21 (a), the improved system configuration added a 9 mm diameter hemispherical high-density polyethylene (HDPE), which was inserted at the output of the waveguide to focus the outgoing beam. Its relatively low refractive index induces a moderate unwanted signal return from the interfaces while contact-less sensing can still be ensured by the back working distance linked to its diameter. An air block was added at the end to observe the beam profile out of the lens. The energy density of the electric field (f = 100 GHz) on the yz-, xz- and xy-plane are given in Figure III.21 (b-d). It can be observed that waves propagating along the waveguide are focused by the HDPE, giving rise to a smaller beam size with intensified E-field at the center (see Figure III.21(d), obtained on the plane of z = 317 mm, 3 mm after the flat surface of the lens). This focused beam contributes to the enhancement of system performance in terms of resolution power for sensing and imaging applications.

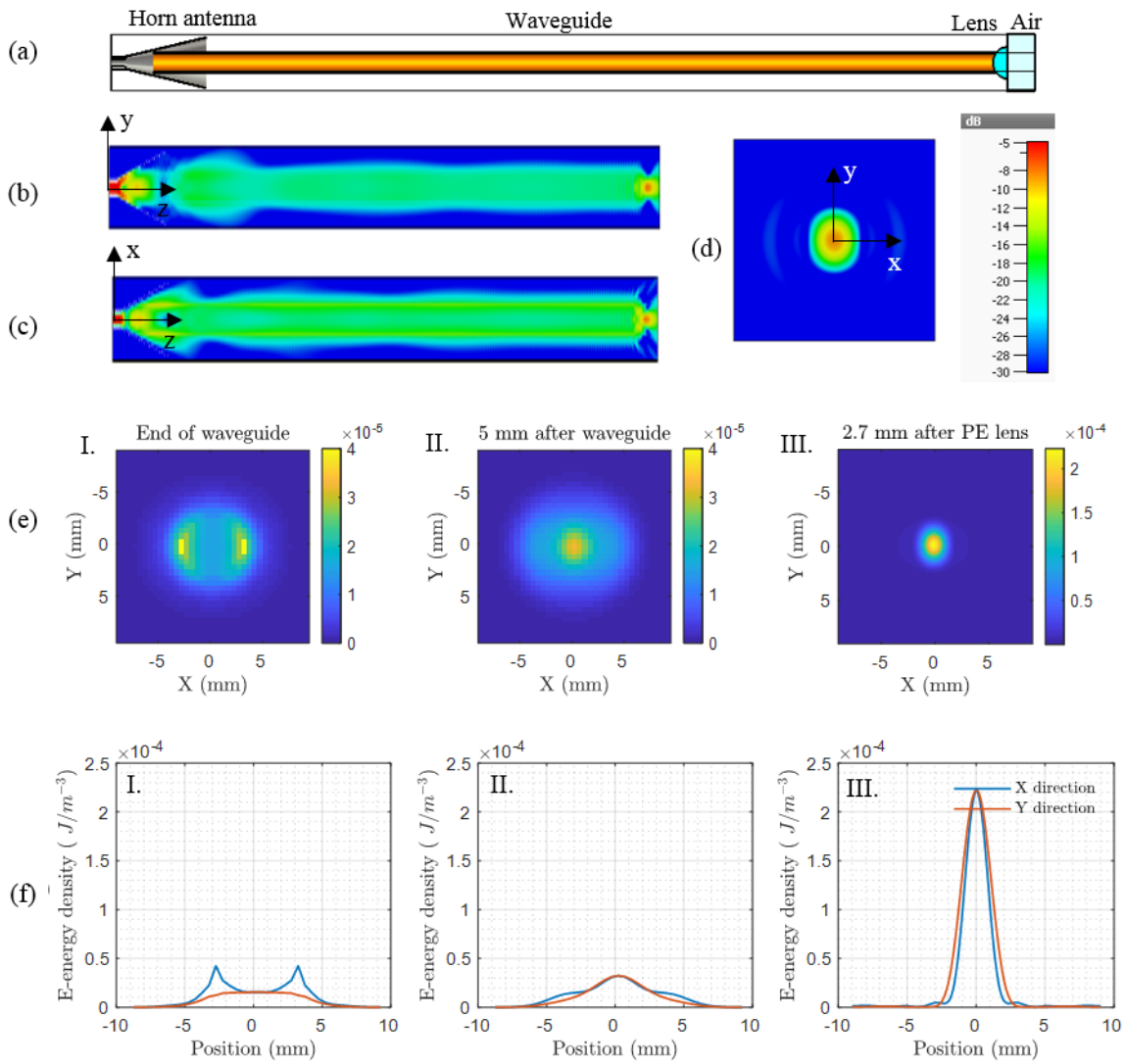

Figure III.21: Simulation results. (a) Schematic diagram of the terahertz wave-guided reflectometry system setup including a SynView 100 GHz head, a waveguide and a HDPE lens inserted in the output of the waveguide. (b) and (c) Electric field energy density distribution in the yz-and xz-plan respectively. (d) Beam profile in the xy-plane at a distance of 3 mm to the output of the waveguide. 2D beam profiles (e) and corresponding line profiles in the x and y directions (f) are given to highlight the improvement that is brought about by the solid immersion lens to the guided reflectometry systems. While I. and II. represent the beam profiles obtained in the original setup without the lens, (at the output, and at a distance of 5 mm after the output of the waveguide respectively), III. depicts the beam profile obtained in the position of 2.7 mm after the PE lens.

In order to offer a quantitative assessment of the efficiency of this optical method, the energy density distribution of the electric field out of the reflectometry system in two configurations (original setup and the ones with a lens) is given in Figure III.21 (e) and (f). Compared to the field distribution at the output of the waveguide (shown in Figure III.21 (e)-I and (f)-I), the beam obtained at a distance of 5 mm after the waveguide (shown in Figure III.21 (e)-II and (f)-II) and the one achieved at a distance of 2.7 mm after the lens (shown in Figure III.21 (e)-III and (f)-III) exhibit a Gaussian-like form, avoiding the unwanted artifacts for imaging purposes. In comparison to the results obtained with the original setup (I and II), the reshaped

beam out of the lens displays a reduced size with significantly enhanced energy density: the peak value of the E-field energy density at the center is 6.8 times higher (Figure III.21 (e)-III, 2.2 $\times 10^{-4} J/m^{-3}$) than the one obtained due to the beam spreading (Figure III.21 (e)-II 3.2 $\times 10^{-5} J/m^{-3}$). By exploiting the optical control capacity of the lens, the beam default related to cladding propagation modes can be significantly corrected. A smaller beamwidth in combination with higher E-field energy density validate the effectiveness of this solid immersion lens improvement method, promising a broader scope for high-resolution required imaging applications.

Working distance range

Figure III.22 (a) depicts the beam size (represented as FWHM in the x-and y-directions) and the maximum power density as a function of the distance after the lens. The results reveal that the smallest beamwidth with intensified power can be obtained in the position of around 2.7 mm, which is considered as the optimal working distance. If the distance from the object to the optimal working position is less than 1 mm, the increase of the beam size and the reduction of the power intensity are not significant, giving rise to a working distance range around several millimeters. In regard to a multi-layer sample, this beam property in conjunction with the phase information provided by FMCW radar allows for in-depth measurements. It is noticeable that the width in the x-and y-direction is slightly different due to the asymmetric field distribution along the waveguide prior to entering the lens.

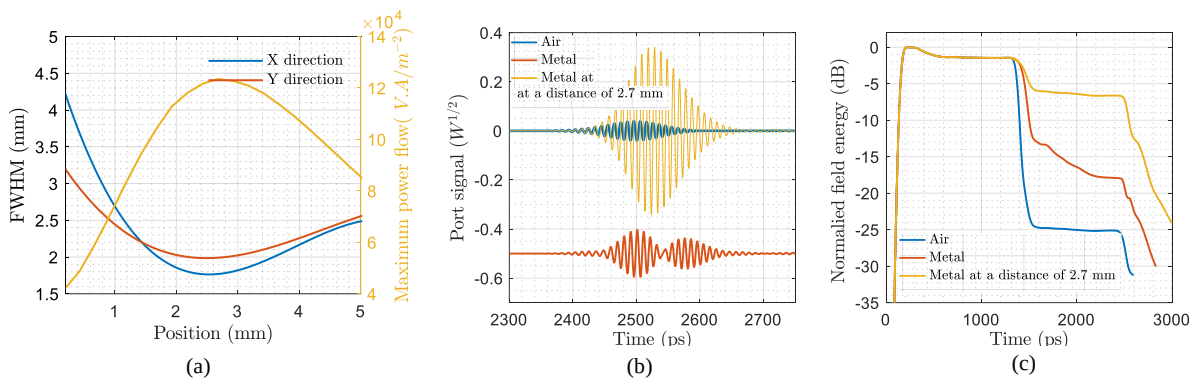

Figure III.22: Simulation results. (a) Beam size and power intensity as a function of distance after the PE lens. Bleu and red curve denote the FWHMs in the x- and y-directions respectively. The yellow curve represents the maximum power intensity as a function of distance. When d = 2.7 mm, the maximum power flow is obtained, corresponding to the focal plane of the lens. (b) Reflections detected by the conical horn antenna in different configurations. Blue curve: open-end configuration. Red curve: a metal is placed at the output of the lens. Yellow curve: a metal plate is placed at a distance of 2.7 mm after the lens. (c) Field energy contained in the simulation box as a function of time in different configurations.

The back-coupling efficiency between the sample and waveguide has also a significant impact on performances of the terahertz wave-guided reflectometry system. In addition to the open-end configuration, the responses of the improved TGR system (adding the lens) to a metal plate placed in different positions were simulated. The obtained waveform of the detected time signal together with the energy remained in the simulation environment are displayed in Figure III.22 (b) and (c) respectively. The reflected power fraction from the open-end air interface after inserting the lens is stronger (blue curves shown in Figure III.22 (c)) than the one obtained in the original lens-free system configuration (not shown here). The extra

gain of 3.5 dB (-25 dB rather than -28.5 dB) is associated with the supplementary reflection from the lens surface. Compared to the case that a metal plate is placed at the output facet of the HDPE (represented by red curves), the metal placed in the focal plane (yellow curves) can reflect more power fraction efficiently by providing a similar beam profile back to the lens and waveguide, giving rise to a higher back-coupling efficiency and a dynamic range of 18 dB (-7-(-25)dB). The red curves shown in Figure III.22 (b) displays two separate waveforms rather than a ring signal due to the change of the beam profile to the lens. It results in a poor back-coupling efficiency, expressed as the declining slope of the red curve shown in Figure III.22 (c). Consequently, the dynamic range of the system is reduced to 7 dB.

Experimental result

In order to corroborate the analysis based on simulation results and to validate this improvement method, the same test chart was placed at 3 mm after the lens to perform an imaging measurement with the constructed reflectometry system. Figure III.23 displays an obtained image of the test chart with a dynamic range of around 20 dB. Thanks to the solid immersion lens implementation, no more ghosting effect can be observed in the image. The bars of element 1 in group -2 with a width of 2 mm can be still distinguished, *i.e.*, the resolution power is limited to 0.25 lp/mm. This resolution power is comparable to the focused beam size predicted by the simulation. All the experimental results are consistent with previous simulation analysis.

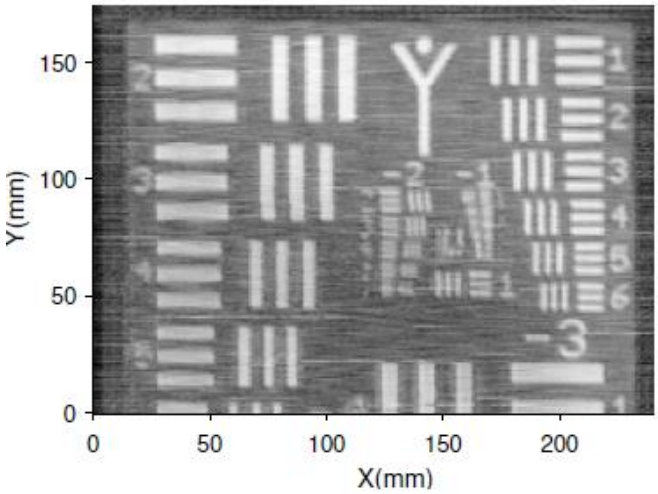

Figure III.23: Raster scan acquired image of a test chart using the guided terahertz FMCW radar reflectometry system with the help of an HDPE lens.

III.3.1.4. Conclusion

In this part, the terahertz guided reflectometry probing system concept was successfully demonstrated by taking advantage of a SynView 100GHz transceiver unit and a hollow-core waveguide. The single communication path between the FMCW radar unit and the sample was enabled by a hollow-core dielectric waveguide, and no dedicated quasi-optical elements were employed for coupling purposes. By means of experiments and simulations, the propagation properties of waves inside the TGR-FMCW system were investigated. The propagation modes, coupling issue, working distance and dynamics of the

systems were discussed. To improve the imaging capacity limited by the beam form out of the waveguide, the solid immersion lens implementation was proposed for beam reshaping, contributing to a resolution power up to 0.25 lp/mm. The bars with a width of 2 mm, which is smaller than the waveguide's diameter, can be clearly distinguished.

III.3.2. TGR-FMCW system II using Silicon Radar transceiver chip

Silicon radar chip, as a low-cost device with miniaturized size and satisfactory performances, meets well the requirements to develop a cost-effective, compact, and easily-implemented terahertz measurement system. Same research methodology as previously, *i.e.*, the combination of 3D full-wave simulation and experimental validation, was applied to explore the feasibility of constructing a low-cost terahertz wave-guided reflectometry probing system using the 120 GHz radar chip. In addition, the solid immersion lens implementation was applied to improve the imaging capacity of the system.

III.3.2.1. Propagation behaviors analysis

In the experimental setup, the hollow-core waveguide was placed in touch with the front side of the radar unit to avoid propagation loss in free space. The position of the plastic hollow-core waveguide was centered on the focal point between Tx antenna and Rx antenna (defined in the article [200] when the dielectric lens is applied to enhance the directivity of radar unit) to ensure the coupling of Tx-waveguide and waveguide-Rx at the same time. In consequence of the off-center position of the Tx antenna and its broad emission pattern, excitation conditions including E-field distribution and incident angle of the beam at the entrance of waveguide are distinctly different from the previous system setup with a horn antenna. More coupling losses were expected due to the mismatch of excitation condition and air-mode propagation modes. In the following part, the investigations via simulation into the field distribution, coupling, dynamic range and lateral resolution power of the original setup are presented. The image of a test chart using this guided reflectometry setup is provided.

Since structure features of the patch array antenna are much smaller than the hollow-core waveguide, the entire system model must be divided into a huge amount of meshes to maintain the correctness and precision of the simulation. However, limited by the calculation capacity of the computer, simulation with a complete model including antennas and waveguide are time-cost. To address this limitation, a near field source equivalent to the transceiver chip consisting of two patch antennas was deployed as the excitation source. Therefore, the final simulation model (shown in Figure III.24 (a)) included an equivalent near-field source of the 122 GHz transceiver chip and a 30 cm-long plastic hollow-core waveguide. The configuration implemented in the experiment was respected in the simulation where a 30 cm long waveguide was positioned very close to the equivalent source (distance less than 1 mm). Besides, a 5 cm long air block was added at the end to study the beam profile in free space. All below E-field results were obtained at a frequency of 122 GHz.

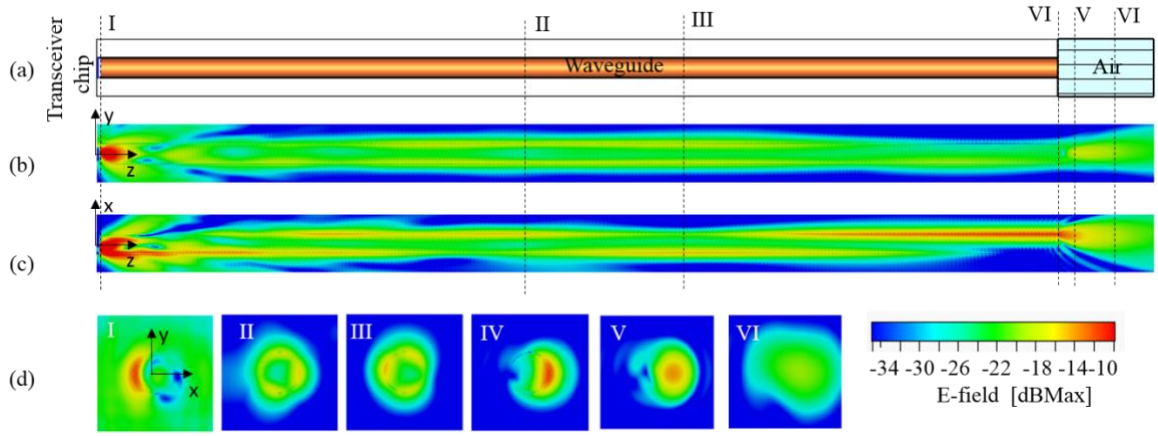

Figure III.24: (a) Simulation model of the TGR-FMCW system, consisting of a 122 GHz Silicon radar chip and a plastic waveguide. (b) and (c) E-field distribution on the yz-plane and xz-plane at a frequency of 122 GHz. (d) E-field distributions on the xy-plane at different z positions (xy-cutplane surface: 20*20 mm²). I to VI represent the cutplane of z =1/130/170/300/302/ 320 mm respectively.

Propagation mode

Compared to the 100 GHz SynView head, Silicon Radar transceiver chip displays a different front end architecture: two spatially-separated patch antennas with a much broader emission pattern. Significant modifications of the electric field distribution along the waveguide were expected and are depicted in Figure III.24 (b-d). Contrary to the symmetry field distribution in the x-direction obtained with the 100 GHz SynView head, obvious reflections on the waveguide's cladding can be observed through the oscillating behavior during the propagation. This can be explained by the decentering of the transmitter with respect to the waveguide, the excitation conditions not being symmetrical anymore. Moreover, the broad emission pattern of the antenna gives rise to different incident angles, which further complicates the excitation condition and leads to a sophisticated multi-mode propagation. Although it is difficult to recognize the overlapped propagation modes, the field distribution displays that on part of the power is guided along the waveguide. After the transmitted signal propagates out of the waveguide, and it begins to expand in free space (shown in Figure III.24(d), from IV to VI). According to simulation results, the electric field in the vicinity of the output waveguide with a small beam size can be exploited for imaging applications. However, the outgoing beam from the waveguide displays an irregular form (shown in Figure III.24 (d)-V).

Coupling efficiency and dynamics

Owing to the wide emission pattern of the patch antenna design, a considerable power fraction is radiated into free space rather than coupled into the waveguide. Figure III.25 phase I depicts this power loss while phase II indicates that the radar signal reaches guided power stabilization after a 50 mm propagation. As a direct consequence, the coupling efficiency is reduced to 20 % at the frequency of 122 GHz compared to the previously achieved 70 % with the former setup, induced by the near-isotropic emission profile of the patch antennas. In addition, it can be seen that the difference between guided power at different frequencies is less important. Aside from coupling efficiency, the dynamics of the constructed guided reflectometry system were deduced by comparing the remaining field energy in two different configurations, open-end and perfect mirror reflection respectively. The estimated full dynamic range

reaches up to 27.6 dB. Although the dynamic range of this reflectometry system are close to the one using SynView 100 GHz architecture, a much larger coupling loss is witnessed in the system using the 122 GHz integrated radar chip.

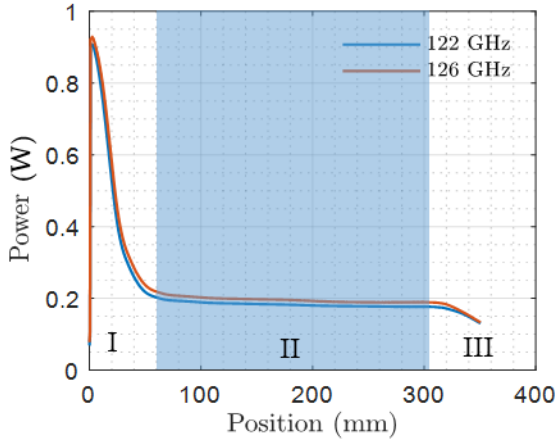

Figure III.25: Power passing through cross-section as a function of distance at two different frequencies (122 GHz and 126 GHz respectively). The couped power ratio is around 20% at the frequency of 122 GHz.

III.3.2.2. Imaging application

According to the simulation result, the proximity of output waveguide provides the highest dynamics. Hence, a test chart was placed at a distance of 1 mm to the waveguide for imaging purposes. Figure III.26 displays the obtained image of the test chart obtained using this guided reflectometry system setup. Limited by the beam size and irregular form, this image is fuzzy. While the bars of elements in group -4 can be distinguished, the shadow effect is displayed around the contour of the pattern. In fact, the atypical coupling-in geometry gives rise to an asymmetric field distribution at the output of the waveguide, where the highest electric field is confined at one side of the waveguide in the proximity of the cladding (Figure III.24 (d)-V). This irregular beam causes a noticeable shadowing effect on the image. In spite of it, the sample support on the backside can be seen in the center bottom part of the image, demonstrating the in-depth sensing capability of the system. Besides, sample support at the backside can be seen in the image, demonstrating the penetrating capacity of our system for in-depth measurement.

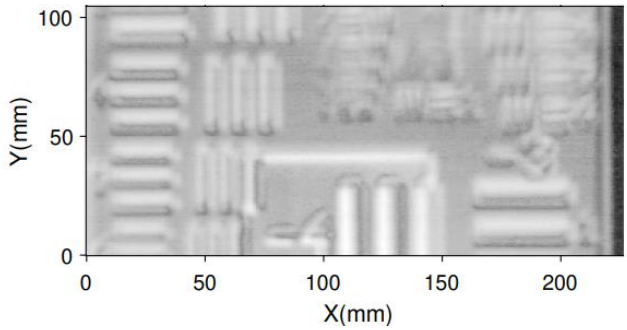

Figure III.26: Image of a test chart using terahertz wave-guided reflectometry system setup.

III.3.2.3. Resolution improvement via an HDPE lens

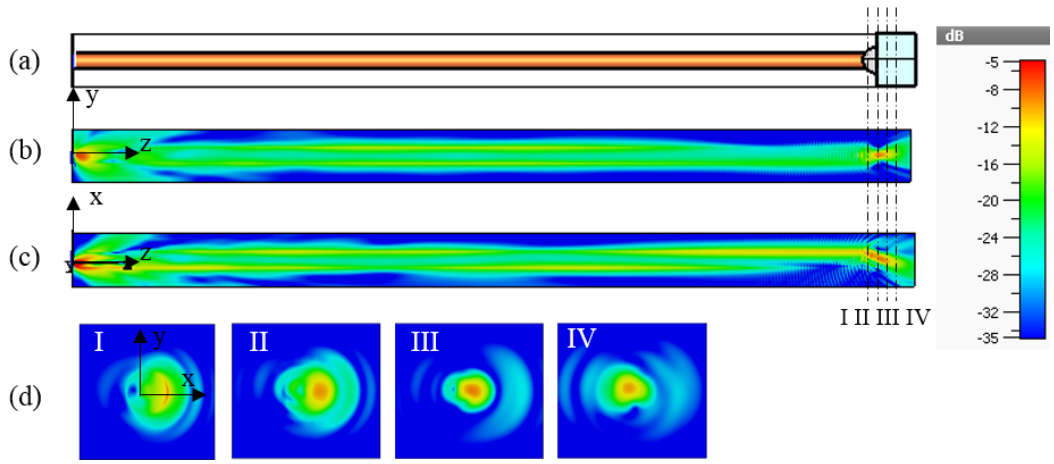

Figure III.27: E-energy density distribution on different cutplanes at a frequency of 122 GHz. (a) Simulation model including an equivalent field source of 122 GHz transceiver chip, a 30 cm long waveguide, a solid immersion HDPE lens and a 15 mm air block. (b) and (c) E-energy density on the yz-plane and xz-plane respectively. (d) E-energy density on the xy-planes (20*20 mm²) at the positions of z = 300 mm (Position I, in the vicinity of the output of the waveguide, inside the PE lens),304 (Position II, nearby the output of PE lens), 307 (Position III, after PE lens) and 310 mm (Position IV, after PE lens) respectively.

For the sake of imaging resolution improvement, a 9 mm diameter hemispherical HDPE termination lens was inserted to counteract the propagation beam divergence in free space and to obtain a better-resolved focus point. Prior to the experimental test, a model including an equivalent near-field source, a 30 cm-long waveguide, a lens and an air block (shown in Figure III.27 (a)) was simulated. The energy density distribution of the electric field at the frequency of 122 GHz are given in Figure III.27 (b-d).

Since the beam leaving out of the waveguide is not centered with respect to the optical axis of the lens, the propagation direction of the incident beam is changed by the HDPE lens and transmitted waves are focused on the optical center axis (depicted in Figure III.27 (c) and (d)-I to IV). Nevertheless, the focused beam displays an irregular form with a second beam lobe at one side (depicted in Figure III.27 (d)-II, III). From the point of view of imaging applications, this imperfect beam profile may deteriorate the lateral resolution and bring about unwanted artifacts.

Experimental result

The above experimental setup shown in Figure III.28 (a) was implemented to test the resolution power of the system, in which a test chart was placed at a distance of 3 mm after the PE lens. Two images, shown in Figure III.28 (c) and (d), were obtained by raster scans from the front and back sides of the test chart respectively, in which the elements in group -3 and -4 are distinguishable. The resolution power of the guided reflectometry reaches up to 0.353 lp/mm, corresponding to element 4 in group -2 with a width of 1.4 mm (at the center of the test chart), better than the resolution obtained with the TGR-FMCW system using a 100 GHz guided SynView unit (0.25 lp/mm, element 1 in group -2). Additionally, the presence of the sample support in Figure III.28 (c) and the bars in Figure III.28 (d) (the objects after the substrate) demonstrates that the penetrating capacities of FMCW radar within several millimeters have been kept, which is advantageous for multi-layer material analysis.

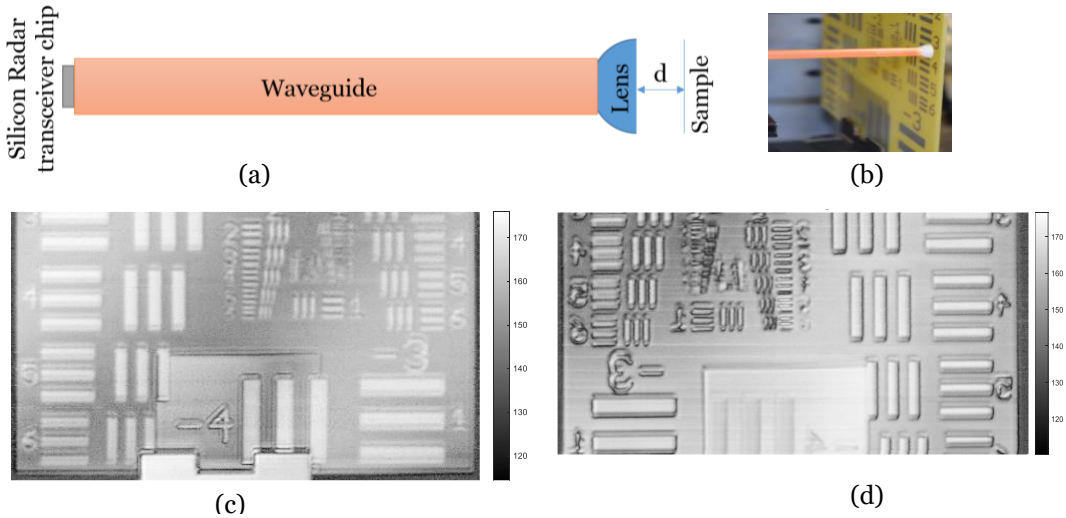

Figure III.28: (a) and (b) Schematic diagram and photograph of the experimental setup. The sample is placed at a distance of 3 mm after the HDPE lens. (c) Raster scan acquired image of the test target from the front face. (d) Raster scan acquired image of the test target from the backside.

Although the resolution power is enhanced with the help of the HDPE lens, some noticeable artifacts can be observed in the images. Different from the ghosting effect that appeared in the previous configuration, here the shadow around the contour of bars in the vertical direction (y-axis) is remarkable, for instance, shadow displaying in element 5 and 6 in group -4 situated at the left side in the image. According to the aforementioned simulation, the focused beam propagating out of lens displays an irregular form with a non-ignored side lobe in the x-direction (shown in the Figure III.27 (d)- position III and V) due to the misalignment between the incident beam and HDPE lens optical axis. Consequently, the shadow artifact in one direction, especially around the contour of an object is anticipated. To conclude, the enhanced resolution power of TGR-FMCW system validates the proposed optical improvement method using a HDPE lens. Nevertheless, quality defaults such as shadow artifacts are still noticeable in the obtained image, which are associated with the improper beam focusing with non-negligible side lobes.

III.3.2.4. Resolution improvement via a Si bullet lens

To further improve the imaging capacity of the TGR-FMCW system, a silicon bullet lens (10 mm diameter hemispherical lens in combination with a 1.46 mm long cylinder) was as well tested. The investigation into the propagation behaviors of waves in the system was firstly conducted via simulation. Figure III.29 (a-c) displays the energy density distribution of the electric field on the different cutplanes.

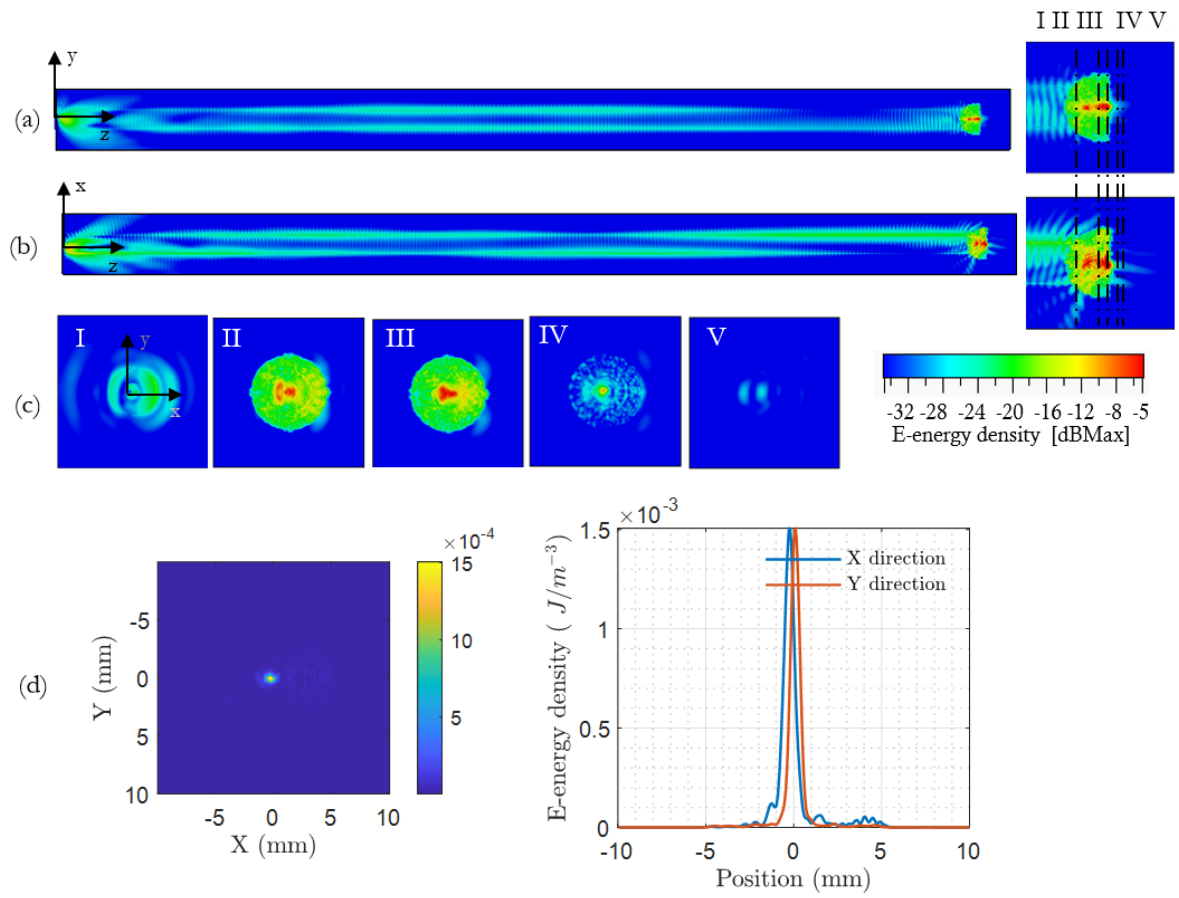

Figure III.29: (a-c) E-energy density distribution on different cutplanes (yz-plane, xz-plane and xy-palne respectively) at a frequency of 122 GHz in a reflectometry system in conjunction with a silicon bullet lens. I-V corresponds to the position of z = 300/ 305.5/ 306/307/308 mm respectively. The output facet of the silicon lens lies at the position of z = 306.55 mm. (d) 2D beam profile obtained on the xy-plane of z = 306.7 mm, (0.15 mm after bullet silicon) and the corresponding line profiles in the x-and y-direction. The FWHM in the x- and y-direction is 0.6 mm and 0.66 mm respectively.

As shown in Figure III.29 (c)-III, guided waves in the proximity of the waveguide's cladding is tightly focused at the center of the lens, along its optical axis with a high energy density. Figure III.29 (d) depicts the beam profile on the xy-plane at a distance of 150 µm after the output of the Si lens. Due to the misalignment between the incident beam and lens, the focused beam after the silicon lens is slightly shifted with respect to the center of the lens (0.4 mm) in the x-direction. In addition to the reduced beam size (0.6/0.66 mm), a maximum energy density of $1.5x10_{-3}$ J/m_{-3}, 31 times higher than the focused beam using the HDPE lens ($4.73x10_{-5}$ J/m_{-3}), is achieved. Regarding the imaging applications, the reshaped beam after the silicon lens allows for a much better lateral resolution power. Nonetheless, it can be observed that the highest energy density is achieved inside the lens. Once the beam leaves out of the lens, the energy dissipates rapidly.

Working distance and dynamics

Figure III.30 (a) illustrates the beam size (FMCW in two directions) and the maximum E-energy density curves as a function of the distance to the output facet of the silicon lens, allowing defining an

optimal working distance. It can be observed that while the beam size can be maintained in a short distance, the energy density decreases shapely with the distance. As a result, the working distance is limited to the area in the vicinity of the output of the silicon lens, *i.e.*, the sample should be placed as close as possible to the lens for the best imaging capacity. The penetrating capacity of this system is limited to the vicinity of the lens, making it unsuitable for in-depth measurements.

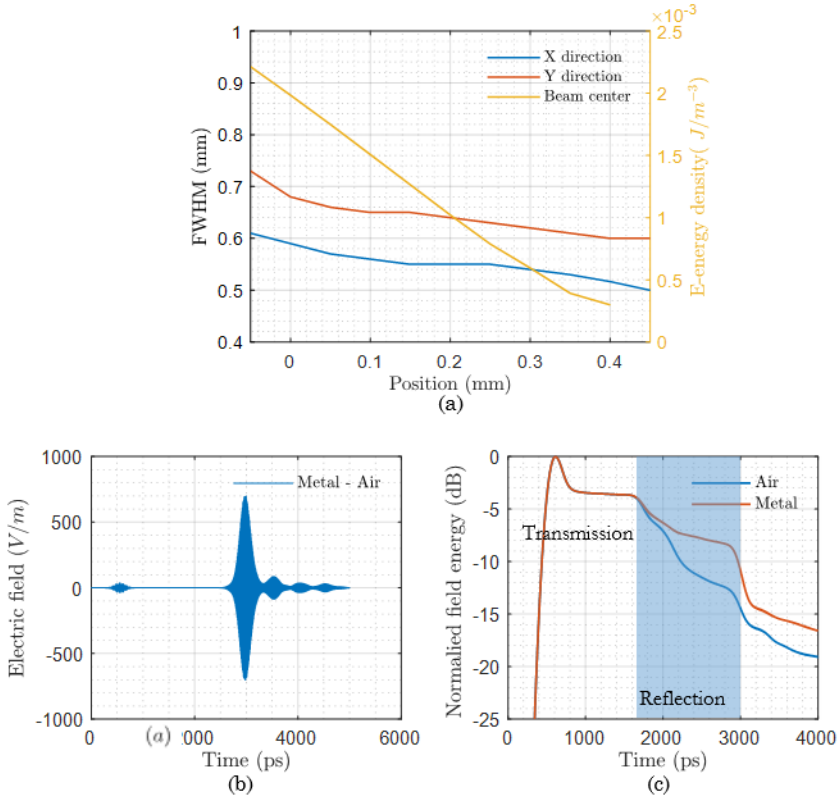

Figure III.30: (a) Analysis of beam profile after the silicon lens. Bleu and red curves represent the FWHM of the beam in the x- and y-direction as a function of distance. Yellow curve: the electric field energy density at the beam center as a function of distance. (d = 0 mm the focal plan with an FWHM of 0.6 mm and 0.66 mm are achieved in two directions.) (b) Difference of the electric field (Y component) detected by the probe in the receiver's position in two different configurations (reflected by the air and perfect mirror respectively). (c) E-field energy remained in the simulation box as a function of the time.

To assess the dynamic range of the TGR-FMCW system in combination with the silicon bullet lens, both open-end configuration (using an air block) and perfect mirror setup (a metal plate is placed at the output of the silicon lens) were simulated. Figure III.30 (b) shows the difference of the time-dependent electric field detected by a probe in the receiver's position in two different configurations. Multi-reflections from the end of the system can be observed, which are associated with the total internal reflections occurring inside the high-index silicon lens. The energy remained in the simulation box is also given in Figure III.30 (c), in which reflections from the output of the system occur at the time of around 1600 ps. Several factors contribute to the reduction of the energy during the reflection, including the loss caused by the total internal reflections inside the lens and the poor back-coupling efficiency between the sample and waveguide linked to the change of the field distribution. By comparing the remained power after the reflection in two cases

(from air interface and from the metal), a weak dynamic range of 4 dB is finally deduced from Figure III.30 (c).

Experimental result

According to the simulation result, the test chart was placed as close as possible to the silicon lens. Figure III.31 displays the experimental setup and the obtained image of the test chart. An excellent resolution up to 0.891 lp/mm is obtained, corresponding to element 6 in group -1with a width of 0.56 mm (the center of the test chart). It is consistent with the simulation result, in which the beam width is in the order of 0.6 mm. By taking account of the low dynamic range derived from simulation results, low-contrast between the flat metal surface on the bar and the dielectric substrate is anticipated. Indeed, after passing through the silicon lens, the propagation direction of the incident beam is changed. A non-zero incident angle means the reflected signal is more susceptible to the surface condition of the sample, which further impacts the back-coupling efficiency between the waveguide and sample and dynamic range of the system. That can explain the remarkable amplitude difference displayed at the contour of bars instead of whole metal bars' surface.

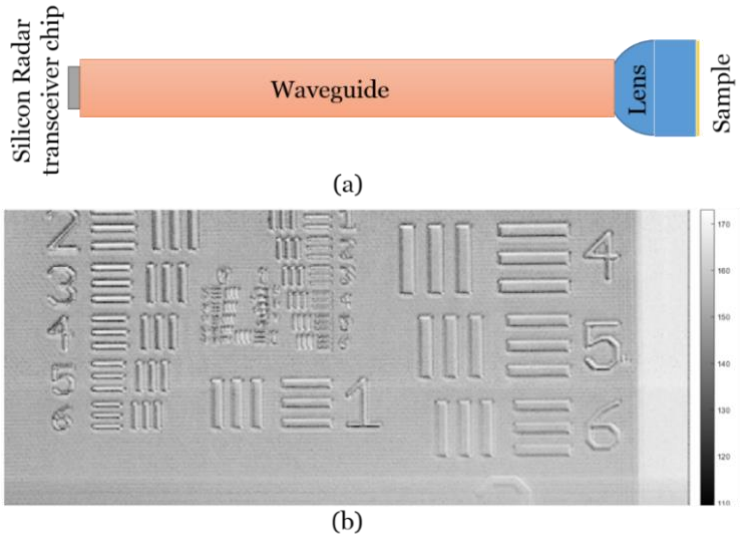

Figure III.31: (a) Experimental setup and (b) image of the test chart obtained using the reflectometry system in combination with a bullet silicon lens.

Performance improvements prompted by the solid immersion lens implementation have been validated in this part. Simulation results are in accordance with the experiments, giving a deep insight into the propagation behaviors of waves in the system. While the use of an HDPE lens keeps the penetrating capacities of TGR-FMCW for in-depth measurements with an acceptable dynamic range, a silicon bullet lens provides better resolution power. Depending on the application, a suitable lens should be implemented for performance improvement. Further optimization of lens design may bring a better trade-off between the lateral resolution and penetrating capacity. It is as well of great interest to investigate new waveguides possessing different propagation modes matching this transceiver chip.

III.4. Conclusion

After plenty of investigations based on simulations and experimental operations, easily-implementable, compact terahertz wave-guided reflectometry probing systems have been demonstrated by the transceiver units in combination with hollow-core thin-wall waveguides. Compared to a conventional terahertz measurement system requiring a sophisticated alignment process, all the aforementioned systems transmit straightly the signal to the targeted zone by a waveguide, simplifying the alignment process. Besides, no optic is used to carry out the coupling between the transceiver and waveguide, contributing to the compactness of the system.

By taking advantage of a double-PCA lens-free transceiver probe, the first terahertz wave-guided reflectometry system in pulse mode has been displayed. The 5.3 cm-long silica hollow-core waveguide is used as the remote probe to guide the signal covering the frequency band from 400 GHz to 550 GHz to the sample. A resolution power of 0.707 pl/mm has been demonstrated, which is comparable to the wavelength of the transmitted signal. Although the TGR-P system composed of the plastic waveguide is not suitable for imaging applications due to its complicated propagation modes, it has been applied for liquid depth detection to extend the scope of the application of the double-PCA transceiver. Compared to the direct use of the double-PCA transceiver, the TGR systems show more advantages for some specific measurement conditions, such as in a narrow semi-enclosed environment or in the liquid.

In addition to the TGR-P systems, FMCW transceiver units are also deployed to build up a terahertz wave-guided reflectometry system with a plastic hollow-core waveguide. Compared to CW sources, phase information provided by FMCW radars allows differentiating the contributions along the waveguide and then enhancing the measurement dynamic range. While a SynView 100 GHz head in monostatic architecture with a single horn antenna structure eases the task of establishing a single communication channel between the transmitter and sample, a SiGe-based 122 GHz transceiver chip appears attractive as a low-cost solution to construct a guided radar reflectometry measurement. Despite atypical excitation conditions, the optic-free implementation between the transceiver and the waveguide can ensure an adequate coupled power. The coupling efficiency between the FMCW transceiver units and waveguide is up to 70 % and 20 % for two TGR-FMCW systems. To address the limitation of the imaging capacity of these two systems, the solid immersion lens has been proposed to correct the irregular beam. Both HDPE hemispherical and silicon bullet lens have been tested at the output of waveguide for beam reshaping, contributing to the enhancement of imaging quality and resolution power. While the reformed system composed of the SynView 100 GHz head and an HDPE lens offers an imaging capacity around 0.25 lp/mm in a working distance around 3 mm, the other TGR-FMCW system consisting of the 122 GHz radar chip and silicon lens gives a resolution power up to 0.891 lp/mm in the vicinity of the lens. Depending on the application, the choice between the working distance range and lateral resolution power must be made to find out a suitable lens. Besides, simulation results reveals that although the resolution power can be enhanced by a lens, the use of a lens may decrease the dynamic range of the system.

It is worth mentioning that while the direct optic-free coupling is practical, atypical excitation conditions (divergent source, asymmetrical position) result in sophisticated propagation behaviors along the waveguide. The guided waves exhibit perplexing propagation properties, which is associated with multi-mode propagation. Thanks to 3D full-wave simulation, the guiding capacity of the waveguide is

corroborated and the field distribution inside the system are investigated, offering a deeper understanding of the constructed TGR systems. To further improve the performance of a TGR system, more effort should be brought into the terahertz waveguide's domain to achieve a deeper understanding of propagation properties of waveguides. This knowledge may allow to improve the excitation conditions of the incident beam while keeping the compactness of the system. Waveguides using new materials with different dimensions should also be considered. As millimeter, sub-millimeter technologies continue to develop, a more compact FMCW radar with higher power output is anticipated. The continuous advances of photoconductive devices will contribute to the improvement of the transceiver in pulse mode. Both of them promise more possibilities to construct a performant guided reflectometry system.

Chapter IV.

On-wafer reflectometry system: first tests

IV.1. DEVELOPMENT OF TMIC TECHNOLOGY 130
IV.1.1. On-wafer measurements 130
IV.1.1.1. RF probe development 131
IV.1.1.2. On-wafer measurement improvement 132
IV.1.2. Non-destructive fault isolation techniques 133
IV.1.2.1. Fault isolation techniques 134
IV.1.2.2. Electro-Optical Terahertz Pulse Reflectometry technique 136
IV.2. ATTEMPT TO AN ON-WAFER REFLECTOMETRY SYSTEM 137
IV.2.1. Experimental setup 138
IV.2.2. Reflected time signal I (Model 220) 141
IV.2.3. Reflected time signal II (Model 500) 142
IV.3. CONCLUSION 144

IV.1. Development of TMIC technology

Since the apparition of the integrated circuit around the early 1960s, the development of electronics has accelerated dramatically. Both active and passive components can be integrated into a single semiconductor chip to form an electronic circuit. The number of transistors contained for an equivalent IC volume continues to increase while the fabrication cost is being largely reduced. High switch speed and low power consummation contribute to improvements in electronic system performances. Over the last two decades, the scaling of the components and advanced packaging techniques have promoted the advance of monolithic microwave integrated circuit (MMIC) technology, benefiting the computing and communication application.

Thanks to the continued scaling of Si-based transistors on-chip and novel InP (Indium Phosphide)-based transistors technologies, the maximum frequencies of ICs can easily exceed 1 THz, which allows realizing highly integrated complex transmitter and receiver at terahertz frequencies. Terahertz monolithic integrated circuit (TMIC) technology with an operating frequency covering from 100 GHz to 10 THz is on its way. In 2016, a SiGe BiCMOS technology-based transmitter operating in a large frequency band from 341 to 386 GHz was reported. Compared to Si-based semiconductor technologies, InP (Indium Phosphide)-based transistors, both high electron-mobility transistor (HEMT) and heterojunction bipolar transistor (HBT), show advantages in terms of electron mobility, thermal conductivity and operating voltage. Being the leader of InP HEMT technology, Northrop Grumman corporation reported its first InP HEMT TMIC low noise amplifier operating at 670 GHz in 2011 [233]. A power amplifier at 650 GHz [234] together with a mixer and multipliers using the same process [235] were then demonstrated. In 2015, they reported the gain of an InP HEMP amplifier working at 850 GHz for the first time [236]. On the other hand, Teledyne Scientific Company is driving the state-of-art HBT technology. In 2011, a 250 nm InP HBT process with a maximum frequency of oscillation higher than 1 THz had been reported [237]. In 2016, the 130 nm HBT process along with a circuit demonstration at 670 GHz was displayed [238]. Up to date, a variety of integrated circuit blocks such as a fundamental oscillator, power amplifier, dynamic frequency divider [239] have been implemented based on their 250 nm or 130 nm InP HBT technologies. The heterogeneous integration between III-V and Si-based technologies is also proposed as an effective approach to obtain a better IC performance to take advantage of both well-developed Si-based technology and a higher operating frequency of III-V semiconductor [238], [240]. Smaller volume, higher integration, higher operating frequency, lower noise and higher power efficiency, all mentioned features promise a bright future for TMIC technology. More high-speed electronic devices will be developed for satellite communication, high-speed internet access or sensing applications.

IV.1.1. On-wafer measurements

While the advances in semiconductor technologies benefit the development of TMIC, their fabrication cost, especially one of InP-based, remains considerable due to high-level integration and low process yield. Before packing a TMIC in a suitable environment, on-wafer measurements is used to evaluate their performance at aimed frequencies via the extraction of resonants of components [241]. This quick assessment of performance is essential to validate and improve the design for sequent circuit fabrication iterations. On-wafer measurement is as well paramount for quality control in a mass production

environment [242]. Compared to the packaging-level characterization, on-wafer measurements can easily identify inherent design problems, helping to reduce the new product research and development cycle time and cost. Typically, a vector network analyzer (VNA) in conjunction with RF probes are deployed to measure S-parameters on wafer level. Calibration, as one necessary procedure during the measurement, allows setting the reference planes within the wafer past the probe contact pad. After the calibration, measurements can be directly applied to generate the model of the sample without further de-embedding [243].

IV.1.1.1. RF probe development

Being crucial for on-wafer measurements, RF probing technology makes amazing progress in meeting the increasing need at high frequencies in IC (MMIC & TMIC) domain [244]. Thanks to various novel technologies developed by several manufactures, the frequency capability of modern on-wafer probes has increased exponentially, from 4 GHz in the early 1980s up to 1.1 THz in 2014 [245]. Since Cascade Microtech was created, it has been playing an important role in on-wafer probe developments. Around the *1990s*, they have introduced two important probe designs contributing to the advances of microwave technology: waveguide input probe [246] and air coplanar probe [247]. Afterward, on-wafer probes provide two types of input connection to meet the needs in practical measurements: coaxial connector or waveguide. In particular, when frequencies exceed 110 GHz, waveguide-based frequency extenders have to be included in the measurement system, between the VNA and RF probe. While the first generation of probe tip was based on a microstrip line with a short wire tip through a probe substrate, nowadays the group-signal-group (GSG) probe tip has become a recommended standard contacts due to its precise line impedance. Depending on the transition to GSG probe-tip, RF probe technologies can be classified into several types, more details are given in Table 6. Being the latest technologies, T series probes developed by DMPI company are available in the frequency bands from 140 GHz to 1.1 THz [245], [248], [249], in which the micromachining Si wafer CPS probe tips are affixed to the probe body via mechanical clamping using SOI (silicon on insulator) technique.

TABLE 6. ON-WAFER PROBES FROM DIFFERENT COMPANIES

Company	Product series	Probe-tip	Transition
Cascade Microtech	ACP	Air-coplanar	Coax/Waveguide to micro coax to air-isolated CPW tip
GGB industries	Picoprobe	Micro-coax	Coax/Waveguide to micro coax to GSG tip (spring load ground)
Rosenberger-Cascade	|Z|-probe	MEMS	Direct transmission from coaxial to coplanar line
Cascade Microtech	Infinity	Thin-film microstrip	Direct transition from rectangular waveguide/ micro coax cable to a flexible polyamide microstrip line [250][251]
DMPI-Cascade	T	Si micromachined	Rectangular waveguide to silicon wafer CPW tip [252], [253] [254], [255]

Despite various choices of on-wafer probes operating at sub-millimeter wave frequency, their performances are not entirely satisfactory at frequencies above 300 GHz. The uncertainty of S-parameter measurements above 110 GHz at probe-level has been discussed over one decade. The results are prone to distortion due to spurious higher-propagation mode in the substrate generated by the discontinuities of the signal path at the probe tip. The crosstalk signal between the two probes or other devices on the same chip

may cause further parasite errors. In addition, the insertion loss and return loss of RF probes degrade as frequency increases. Most importantly, the physical contact between the probe and device under test (DUT) plays an important role in the measurement quality. Good physical contact can not only guarantee reliable and repeatable measurements [256], [257] but also ensure a long usage duration of the probe.

IV.1.1.2. On-wafer measurement improvement

To address the uncertainty issue at high frequencies, several approaches have been proposed and tested recently. The first kind of method exploits Z-travel control provided by the probe station [258] or strain sensors integrated inside the RF probe [259] [253] to maintain the same contact conditions. They can enhance the measurement repeatability as well as the probe lifetime. Aside from the solutions based on the waveguide-based RF probes, novel probe structures using quasi-optical methods are proposed. For instant, a broadband dielectric-based probe was demonstrated for on-wafer terahertz device characterization in 2018 [260]. Although the design is not yet consummated, dielectric probes show great advantages in terms of low loss, low-cost, polarization maintenance and minimized cross talk. In the following part, the novel configuration involved the non-contact probe and a quasi-optical directional coupler are presented.

Quasi-optical probe

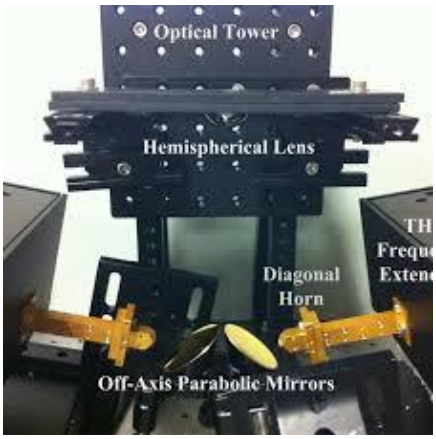

Figure IV.1: Photograph of the TeraProbe testbed.

While the dielectric-based probe still needs physical contact, a novel on-wafer non-contact probe [261], [262], [263], [264] has been developed by TeraProbes, Inc (See Figure IV.1). By taking advantage of parabolic mirrors and an extended hemispherical lens, the emitted waves are focused on the non-contact probes lying on the test device and then coupled into the sample through a transmission line. These non-contact probes are the planar antennas monolithically integrated on the chip, allowing an efficient reception/emission of high-frequency waves. Benefiting from a digital microscope with pattern recognition, the alignment of on-wafer antennas at the test ports can be performed automatically. The positioning repeatability errors can be then minimized [264] and the accuracy and repeatability of measurements can be enhanced. Since there is no physique contact between the probe and sample on-wafer, the use life of probe is largely extended and reliabilities issue caused by the probe landing such as electrical contact resistance and probe tip deflection variability can be largely avoided. Regarding the frequency bandwidth, the double-slot antennas integrated with DUT can operate for two frequency bands: WR2.2 and WR 1.5

bands, displaying the potential to simplify the measurement steps and reduces the probe cost for a wide frequency band measurement. Differential-mode noncontact measurement can also be performed by adding non-contact probes connected to the DUT. Nevertheless, to enable the use of non-contact probes, planar antennas must be directly fabricated on the substrate and an unobstructed access to the on-chip antenna between the VNA port and device under test is required, *i.e.*, the ground metallization at the bottom surface, especially directly under the on-chip antenna is unworkable.

To sum up, the use of optical components together with easily-fabricated planar antennas on-wafer allows a cost-efficient electromagnetic coupling of VNA port into a coplanar waveguide in DUT. It shows considerable advantages in terms of reliabilities, repeatability of measurements and life duration over conventional RF probes. Nevertheless, planar antennas must be considered specifically during the fabrication of the circuit or devices, imposing requirements on the device under test.

Quasi-optical VNA

Apart from the non-contact probe presented previously, most on-wafer measurements are performed with a RF probe and a VNA connected to waveguide-based high-frequency extender modules. Although ono-contact probe possesses a wide frequency band, the measurement range is limited by the bandwidth of the VNA extender, determined by the fundamental mode of the metallic waveguide. To address this issue, the concept of a terahertz quasi-optical vector network analyzer has been proposed. A directional coupler composed of dielectric lenses and beam splitter was proposed in 2017 [265]. In comparison to the metallic directional coupler, this coupler can be regarded as frequency-independent. Two years later, a terahertz quasi-optical system (directional coupler) in conjunction with non-contact probes at frequency band from 300 to 340 GHz were demonstrated for on-wafer measurements in one-port network reflectometer configuration [266]. Although the applied source and detector remain solid-state devices (a comb generator and VNA extenders) due to power consideration, all available devices are compatible with terahertz photonic sources and detectors. Indeed, photonics-based sources by means of photo-mixing can provide a broad tunable bandwidth with higher frequencies. Once the advances of photonic devices satisfy power requirements, a terahertz quasi-optical VNA system with an ultra-wide operation frequency band can be established.

IV.1.2. Non-destructive fault isolation techniques

Not only the advances in semiconductor technologies but also the rapid developments of the packaging techniques contribute to the progress of the high-speed electronic devices. To offer a background of the emergence of the terahertz fault isolation technique for 3D packaged devices, 3D integration techniques and technical challenges to face are introduced here. In fact, since the three-dimension (3D) integration allows achieving better performances (higher power, multi-functionality, better reliability) in a smaller volume for further miniaturization, this technique has attracted increasing attention in the IC industry. The 3D integration can be divided into three types: 3D IC packaging, 3D IC integration, and 3D Si integration. 3D memory stack is a typical application of 3D IC packaging, in which wire bonds and die attachments are applied to stack dies in the vertical direction. Package on package (PoP) is another mature technology allowing a high-volume production. The through silicon via (TSV) can connect directly the chips, or the chip and wafer in the vertical direction. It plays an essential role in the development of 3D

IC integration and 3D Si integration, allowing a single chip to contain several different active component layers, without bumps. It offers advantages in terms of power consumption, reliability, system size, weight, and electrical performance [267].

IV.1.2.1. Fault isolation techniques

While advanced packaging and 3D integration technology benefit high-density high-performance microelectronic devices, they also bring about considerable challenges related to product reliability, cost, and process integration. As an essential and indispensable step for product optimization in the development period and for quality control at the fabrication stage, failure analysis (FA) flows help to reduce costs and enable the device's reliability in the industry [268]. FA flows can be divided into two main steps: fault isolation and fault analysis. In order to find out the root cause of a failure, physical destructive sample preparation is necessary. Thanks to the great alignment and artifact-free finish capacity, the focused ion beam (FIB) technique is frequently used to cross-section the sample in a targeted zone. The techniques, such as energy-dispersive X-ray spectroscopy (EDX), X-ray photo-electron spectroscopy (XPS), are then used for material analysis [269]. In order to improve the efficiency of FA flows and to reduce the cost of the development, a fast non-destructive fault detection and localization technique is imperative prior to a time consuming, destructive sample preparation.

Many different fault isolation techniques have been proposed to localize the defect on chips or 2D packaged devices, such as Optical Beam-Induced Current (OBIC) technique for a semiconductor chip. However, the high miniaturization level, the complexity of the design and the diverse materials make it difficult to localize a default in a 3D package with the majority of the existing 2D FI techniques. As a consequence, new techniques, together with improved 2D methods, are being proposed to fulfill the need for defect localization in an advanced 3D package, hence improving the efficiency of FA flows. Different techniques exploiting ultrasound, magnetic field, X-ray, and lock-in thermography have demonstrated their capacity to work within a multi-layer structure over the last decade (more details are given in Table 7) with continuously improved performance. For example, scanning acoustic microscopy (SAM) remains a suitable analysis method to find out mechanical and thermomechanical issues in a 3D package, especially for cracking and for interface delamination [268], [270]. The new challenge is to reach a compromise between spatial and depth resolution capabilities.

TABLE 7. NON-DESTRUCTIVE FAULT ISOLATION TECHNIQUES FOR 3D PACKAGED DEVICES

Non-destructive FI techniques	LIT Lock-in thermography [271][272]	XCT X-ray computed tomography [273]	MFI Magnetic field imaging [274]–[276]	TDR Time domain reflectometry [277] [278]
Principle	Detecting and imaging of related hot spots generated by small amount of dissipated electrical power	Imaging based on X-ray in combination with computer tomography technology	Imaging based on sensitive detection of FA; the related local magnetic field caused by electrical leakage	Fault localization based on the reflected signal caused by the discontinuity of impedance
incorporation with the simulation of 3D packaged structure	The depth information is calculated using a quantitative phase shift analysis based on time delay between electrical simulation and thermal response	NO NEED	Direct information about spatial location of interconnect failure by visualization of electrical leakage paths	needed information including pulse group velocity as well as the architecture of device
Default type & Applicable device	Electrical defect in packaged devices, such as short, high resistance open, leakage and latch up. differentiate hot spots in the stacked dice of a 3D package [269]	Internal structure defect in 3D package, especially useful for dense interconnectors within a small volume	Electrical defect in packaged device and complex systems containing multi levels chips	Electrical defect, such as short or open within conducting line system
Lateral /depth resolution	below 5 µm Depth calculated by the time delay related to phase shift between the excitation signal and thermal response	/	about 3 µm, but limited by the minimal distance between magnetic sensor and the device. 3D image has been obtained.	Performance limited by the signal frequency (rise time)
Advantages / note	(direct thermal image and two phase lock-in amplification)	/	/	Difficulties : a fraction of power is reflected for every impedance change

IV.1.2.2. Electro-Optical Terahertz Pulse Reflectometry technique

Developed by Teraview Ltd., Electro-Optical Terahertz Pulse Reflectometry (EOTPR) system is declared as the world's fastest and most accurate fault isolation system with a pin measurement duration of less than 5 seconds and a distance-to-defect fault isolation accuracy up to less than 5 µm. Since the electro-optic (EO) technique was used in the initial setup, the system was named as EOTPR [226]. Nowadays, the EOTPR system utilizes PCAs to generate and detect pulse signals. Different versions of EOTPR systems are available, including EOTPR 3000, 4000, and 5000 [279]. The main difference lies in probe stations which may be manual, semi-auto, or fully automatic.

As shown in Figure IV.2 (a), laser beams from the TPI-core unit are sent to the transceiver module, which contains the two photoconductive devices linked by an umbilical. With the excitation of a femtosecond laser beam, PCA generates a short terahertz pulse signal (~1 ps). A semi-rigid coax line in association with an RF probe is used to deliver the terahertz pulse into the device under test (DUT) via BGA contact. Based on reflections caused by the discontinuities of impedance along the conducting line (including traces, via and other interconnectors), defaults in an IC package can be localized. Since the discontinuities of impedance may originate from electrical architecture's features or defects, a known good device (KGD) is needed to provide a reference signal.

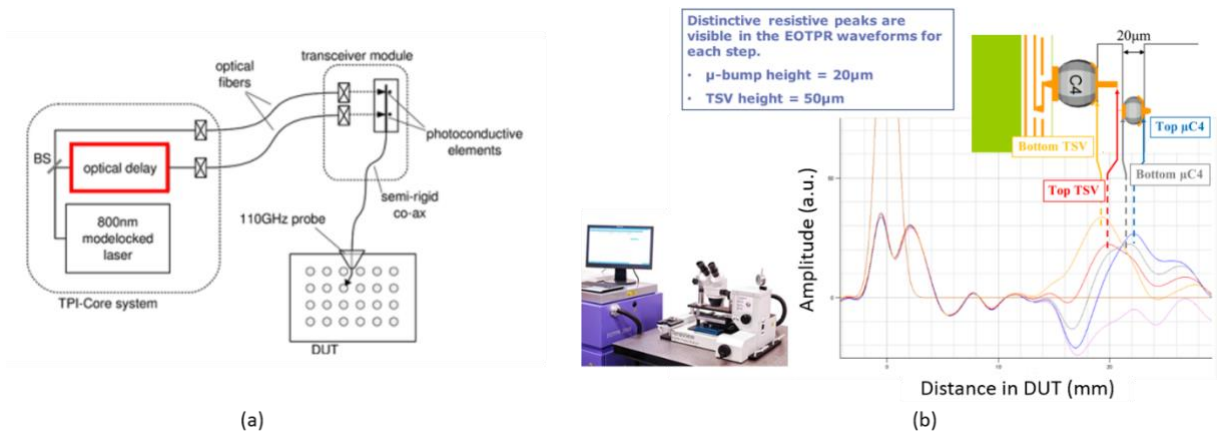

Figure IV.2 : (a) Schematic diagram of an EOTPR system developed by the Teraview Ltd. company. The terahertz pulses are coupled into the device under test (DUT) via a semi-rigid coaxial cable connected to a high-frequency probe. (b) References signals from different levels (from the top die to the substrate) of a packaging. At the left side, there is a photograph of EOTPR 2000 system.

To pre-define the suspected zone, the reference signals related to different architecture features in the package are imperative. For instance, the structure shown in Figure IV.2 (b) should have at least five reference signals [280]. The first reference signal should be measured with the whole component. Then top die should be removed to perform a new measurement. Subsequently, microbumps, circuit over TSV, and TSV should be removed respectively to re-measure a new reference signal. Finally, waveforms as a function of the position of defect are achieved. If there is an open circuit in a failed sample, then the defect can be localized easily by comparing its waveform with these reference signals. This example emphasizes the importance of the reference signal obtained by a KGD and complementary preparation. Without these prepared samples, the interpretation of EOTPR results is impossible.

If a KGD is not available, electromagnetic simulations should be carried out with all the necessary information about the materials and structure of the package to give a virtual known good device (VKGD) reference signal. By monitoring the propagation progress of signal during the simulation, the reflections arising from main architectural features in the device can be identified. Moreover, the simulation can also provide the group velocity of pulse in the package. As a consequence, not only the pro-localization of defect is achieved, but also the precise calculation of defect location using time-of-flight and group velocity can be performed. It has become an essential step to predict and interpreter the detected signals during the EOTPR workflow.

Compared to a conventional time-domain reflectometry (TDR) technique, an optical-pumped source can provide a high SNR short pulse signal with less jitter noise (< 30 fs). After passing through the coax cable and high-frequency probe, the rise time of the emitted terahertz signal is still less than 6 ps, much faster than the raise time obtained by a conventional TDR (~ 35 ps). Low jitter noise, together with high-frequency content, contribute to the enhanced accuracy of fault location. Depending on the system version, EOTPR has a penetration range that varies from 200 mm to 270 mm to meet the requirements for different samples. To sum up, an EOTPR system provides a quick, non-destructive and accurate fault isolation technique for IC package devices. The advances in 3D integration technology have given a promising future for this terahertz reflectometry system. Meanwhile, it is worth noting that despite various demonstrations of EOTPR techniques in diverse IC package devices, its working principles remain little-known. In regard to semi-rigid coax cable between the transceiver module and RF probe, no research results are given to explain the coupling issue between them and corresponding excited propagation modes. Further signal distortion resulted from modal dispersion and propagation loss is not mentioned in all investigated cases. While the PCA in the transceiver module can generate a pulse signal with a duration of less than 1 ps covering (frequencies up to several THz), an RF probe operating in a relatively low part of the spectrum (up to 110 GHz) is selected to deliver the pulse signal into the device. The questions about the choice of RF probe are then raised. Still, no detail about this issue is given. More studies focused on the propagation behaviors of pulse signal along the coax cable and RF probe are required to explain clearly the working principle behind this system.

IV.2. Attempt to an on-wafer reflectometry system

In addition to the rapid development of semiconductor technologies, advanced packaging techniques and 3D integration technologies benefit the progress of performant high-speed devices. The widespread use of electronic devices in the terahertz band can then be anticipated. Lying between the microwaves and the infrared frequency regions, terahertz radiations can take advantage of the methods applied in both domains.

To enable the reliability and repeatability of on-wafer measurements at high frequencies, non-contact probes composed of quasi-optical components and planar antenna are proposed to replace a waveguide-based high-frequency RF probe. Instead of a wave-guided coupler, a directional coupler consisting of optical components has been demonstrated with the aim of extending the operating frequency range. By exploiting PCA devices along with an RF probe, EOTPR technique with high resolution is developed on the basis of the TDR for fast non-destructive default detection in packaging level. All these

studies take advantage of both solid-state technology and optoelectronic technology to address the initial performance limitations. It is believed that the use of electronic components and photonic devices can further improve the overall performances of the terahertz measurement system. Indeed, the combination of the solid-state technologies and optical methods can, to a certain extent, compensate for their respective disadvantages to construct a more powerful measurement system.

Compared to the continuous-wave sources, a pulse signal has a wide bandwidth, allowing to achieve scattering parameters in an extra-wide band via a single measurement. The use of a pulse signal as an excitation signal can simplify the measurement process and reduce the time and cost. The main challenges to face are how to couple a pulse signal into a sample on-wafer and how to interpret the time signal with the presence of higher propagation modes. To address the coupling issue, the same approach applied in the EOTPR system is employed: using an RF probe to direct the electric field from a PCA transceiver to a sample. As the first attempt, the objective of the work is to explore the possibilities to couple a pulse signal into a sample on-wafer through an RF probe. On-wafer probes in the frequency band of 140-220 GHz and 330 GHz to 500 GHz were tested with a double-PCA transceiver separately to build up an on-wafer reflectometry setup.

IV.2.1. Experimental setup

Two on-wafer probes fabricated by GGB Industries INC were tested in association with the double-PCA transceiver: (Model 220 and Model 500 B respectively). As one of the main manufactures of RF probes, GGB Industries INC provides a series of high-performance microwave probes covering the frequency band from DC to 1.1 THz. The use of a microcoaxial cable as an intermediate transition between coax connector/waveguide input and CPW tip is their most distinctive feature, giving rise to better electrical characteristics (*i.e.*, low loss, low VSWR launch and broadband). Individual spring-loaded contacts of probe contribute to mechanical improvements for a reliable and repeatable measurement.

Picoprobe of GGB Industries ING

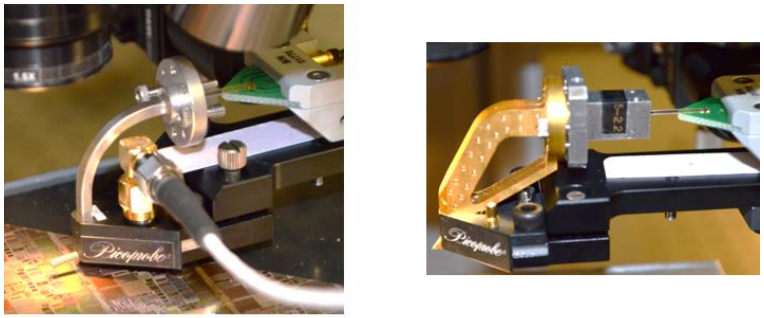

(a) (b)

Figure IV.3: Photographs of two available high-frequency probes. (a) Model 220. (b) Model 500 B in combination with waveguide transition. They are to couple a pulse signal, which is genrated by a double-PCA lens-free terahertz transceiver, into a sample on–wafer.

The RF probe of Model 220 with a WR-5 waveguide input is recommended for on-wafer measurement in the frequency region from 140 GHz to 220 GHz, determined by the cutoff frequencies of

the fundamental propagation mode of the waveguide (the lowest cutoff frequency of WR-5 is 115.74 GHz). When the frequency component is superior to 231.429 GHz, higher propagation modes can be excited, leading to unwanted multi-mode propagation. Considering the input size of the RF probe (WR-5, 1.2954 mm *0.6477 mm), the coupling between the transceiver and high-frequency probe can be carried out directly by simple alignment (depicted in Figure IV.3 (a)).

The RF probe of Model 500 B operates in a frequency band from 325 GHz -500 GHz with an input cross-section of 0.559 mm * 0.279 mm (WR-2.2), which is small than the distance between two PCAs. It results in a poor coupling between the transceiver and the high-frequency RF probe. To deal with this mismatch issue, a waveguide transition from WR-5 to WR-2.2 was added. It was connected to the high-frequency probe input by the flange (shown in Figure IV.3 (b)).

Testbed configuration

To enable a reliable measurement, a high-frequency probe station should be mounted on the air-isolated platform and equipped with a high-precision positioner. Since the optical-pumped sources prevented the possibility of using a commercial probe station (limited by the locations of laser source), the whole experimental setup was implemented on an optical table with different devices (shown in Figure IV.4 (a)). According to the key components (transceiver, high-frequency probe), this home-made on-wafer terahertz reflectometry system can be separated into three parts: a vertical subsystem composed of a transceiver probe and associated optical components, a horizontal subsystem including a high-frequency RF probe, probe positioner, and the sample support platform with three-dimension translation stages.

As explained previously, the coupling between the double-antenna transceiver and high-frequency probe (with or not waveguide transition) was directly implemented through the alignment in free space (see Figure IV.5 (a)). Considering the structure of the high-frequency probe, the double-PCA transceiver was placed horizontally, close to the waveguide input of the probe. In this case, the laser excitation from both sides of the probe tip became impractical, and two optical paths toward the same side of the transceiver probe possessing antenna patterns were constructed, shown in Figure IV.4 (b). In order to provide a clear view of the sample during the probe landing process, a vertical microscope system was installed at the left side of the vertical breadboard, right above the sample support (see in Figure IV.5 (e)). Consequently, two laser beams (pump and probe beam respectively) were arranged at one side of the microscope with different incident angles, shown in Figure IV.4 (b). Two lenses with different focal distances were used to avoid congested space issues. Additionally, a home-made microscope system was mounted on the optical table to offer a vision on the transceiver probe tip to check optical alignment.

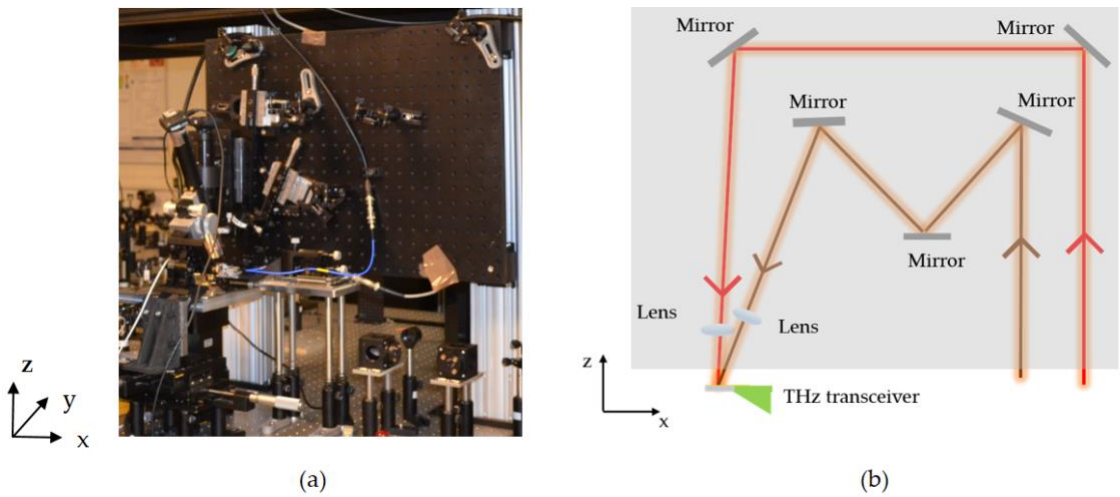

Figure IV.4: (a) Photograph of the experimental setup. (b) Optical paths on the vertical subsystem to excite the PCAs of the transceiver. Two laser paths correspond to pump and probe laser beams.

In general, both probe positioners and sample support are equipped with three-direction translation stages for position adjustment in a probe station. While translation stages on the sample support are aimed for wafer alignment to determine the measurement area, the high-resolution probe positioner is used to carry out pad-to-tip alignments. During the probe-landing process, once a probe tip and a sample both appear in the view of optical microscopy, the distance in the z-direction between them can be roughly estimated by observing the image while varying the working distance of the microscope. When both of them become clear in the view of the microscope, it implies that they are in touch. To enable a good and repeatable electrical contact, more force should be added to the probe tip to break through the passivation layer on-wafer. Nevertheless, it should avoid too much pressure on the tip, which may limit the probe performance and ultimately cause some probe's damage. It is worth noting that the position of the high-frequency RF probe in the present work is determined by the double-PCA transceiver unit. Once the optical paths of laser beams are established, the RF probe should not be moved anymore to keep the same coupling. Consequently, although both the sample's support platform and the probe positioner possess translation stages (shown in Figure IV.5 (c) and (d)), the contact between the RF probe and sample on-wafer was executed by controlling the sample support platform with a high-precision motorized z translation stage. Instead of lowering a RF probe, the landing process of the probe was accomplished by raising the sample's support attentively.

A wafer chuck with vacuum holes was added on the support platform of the sample to hold the wafer during the contact process (depicted in Figure IV.5 (c)). To realize a safe and high precision operation, a really-time optical visualization is imperative. Considering the dimension of the RF probe, the working distance of the camera must be long enough to avoid any possible contact. Besides, the resolution of the microscope should be adjustable to locate the sample on wafer quickly while providing a clear image of the probe tip during the landing process. As a result, a high-magnification zoom lens system in conjunction with a camera was implemented on the vertical platform, providing a clear machine vision on the wafer (depicted in Figure IV.5 (b) and (e)).

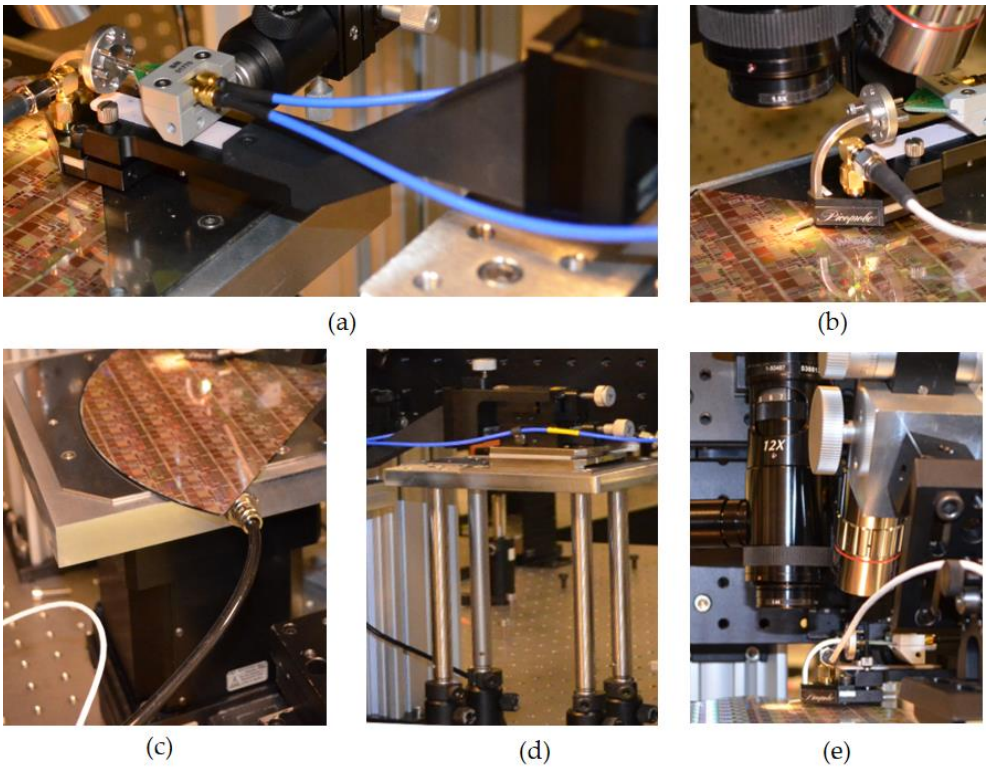

Figure IV.5: Photographs of the on-wafer reflectometry setup, displaying the details of different parts. As shown in (a) and (b), the transceiver probe is placed in the vicinity of the entrance of the high-frequency probe to achieve proper coupling. (c) Sample support equipped with 3D translation stages and a chuck with vacuum holes to hold the wafer during the measurement. (d) Manual probe positioner installed on an optical table. (e) Two microscope systems, providing machine visions for optical alignment and wafer alignment, respectively.

IV.2.2. Reflected time signal I (Model 220)

A 220 GHz on-wafer probe was tested in the first experiment. A calibration kit on-wafer was used as sample, including Open, Short, Thru, Line. As the first attempt, this measurement was aimed at observing the reflections detected by the double-PCA transceiver after passing through a 220 GHz RF probe and with different samples on-wafer. It may help to reveal the propagation behaviors of pulse signals inside the RF probe.

Time signals obtained with different samples on-wafer are given in Figure IV.6, in which distinct reflections can be observed in zone I and II. Compared to the crosstalk signal obtained in free space (shown in Figure II.9 (b)), noticeable waveform differences can be seen at the time of around 20 ps in zone I in Figure IV.6 (b). These reflections were anticipated by taking account of the small size of the waveguide input of the RF probe. Due to the bending of the rectangular waveguide WR-5, a small portion of power is continuously reflected, expressed as oscillations with weak amplitude in the time period from 30 ps to 120 ps. It should be recalled that the low-frequency peak lying at the time around 170 ps is induced by the internal reflections, which is linked to the design of the transceiver probe itself.

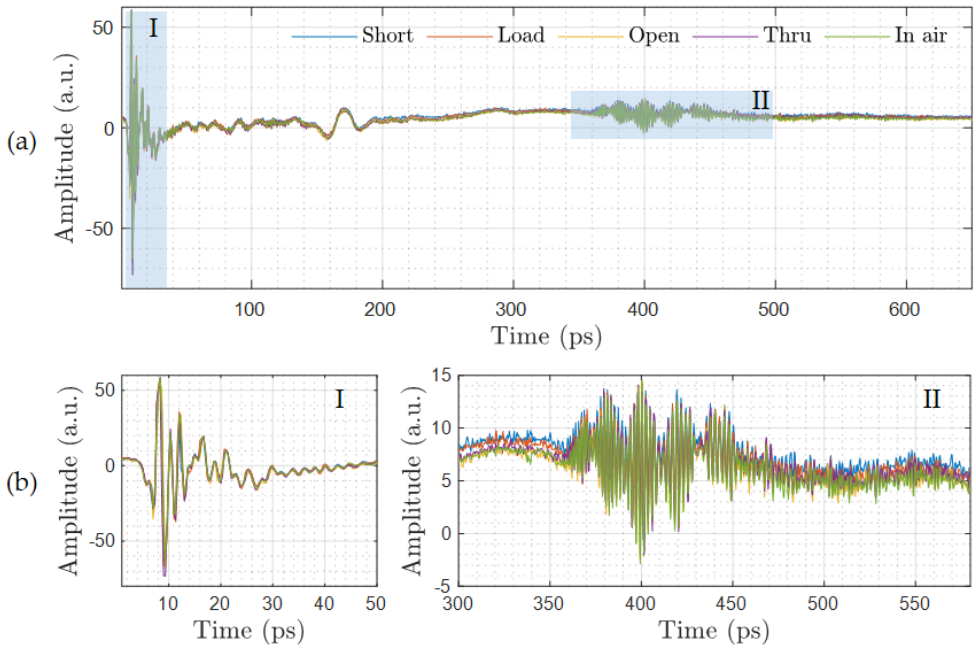

Figure IV.6: (a) Recorded waveforms of time signals reflected from samples on-wafer using the experimental setup with a 220 GHz high-frequency probe. In addition to the measurement in the air, other signals are recorded in the case that the high-frequency probe is in contact with the calibration kit, including short, load, open and Thru. (b) Close-up views of the waveform in zones I and II. It is known that zone (I) corresponds to the reflections induced at the entrance of the probe.

A significant ring signal with a duration of more than 150 ps (from 350 ps to 500 ps) is shown in zone II in Figure IV.6 (b). The considerable time delay between zone I and II demonstrates that one part of the emitted signal has successfully coupled into the high-frequency RF probe. Besides, the distortion of the reflected signal implies that considerable dispersion occurs during the propagation. In fact, while a WR-5 waveguide can support a single-mode propagation (TE_{01} mode) in the frequency band varying from 140 GHz to 220 GHz, higher modes can be excited for the frequencies exceeding this band. Considering that the used optical-pumped double-PCA transceiver emits a pulse signal covering the frequency roughly from 400 GHz to 600 GHz, multi-mode propagation is expected inside the RF probe. The superposition of higher modes with different group velocity and modal dispersion complicates the propagation behaviors of waves. Instead of a waveform similar to the excitation signal, a broadened ring signals with a long duration are observed. Since the short circuit on-wafer provides several hundreds of micrometers longer propagation distance than the measurement performed in the air (regarded as open-end as well) due to the transmission line between the contact pad and the short circuit, it was expected to observe a time shift in the order of several picoseconds between the recorded reflections. However, the broadened waveform and the measurement noise make it impossible to identify this time shift between measurements.

IV.2.3. Reflected time signal II (Model 500)

Due to the multimode propagation, it is extremely difficult to recognize the original reflections from samples on-wafer by using a 220 GHz RF probe. Since the RF probe with WR-2.2 waveguide input (Model 500) supports single-mode propagation in the frequency band from 330 GHz to 550 GHz, better frequency band match between the double-PCA transceiver and RF probe was expected to mitigate the

distortion issue. Consequently, this new RF on-wafer probe was tested in the second experiment by using the same testbed. A calibration kit with gold pads was selected to ensure the good electrical contact between the sample and the RF probe tip. Consider the small waveguide input of this 500 GHz probe (0.559 * 0.279 mm²), a waveguide transition of WR-5 to WR-2.2 was connected to the RF probe to provide a larger input surface, allowing to carry out directly a coupling from the transceiver to the on-wafer probe.

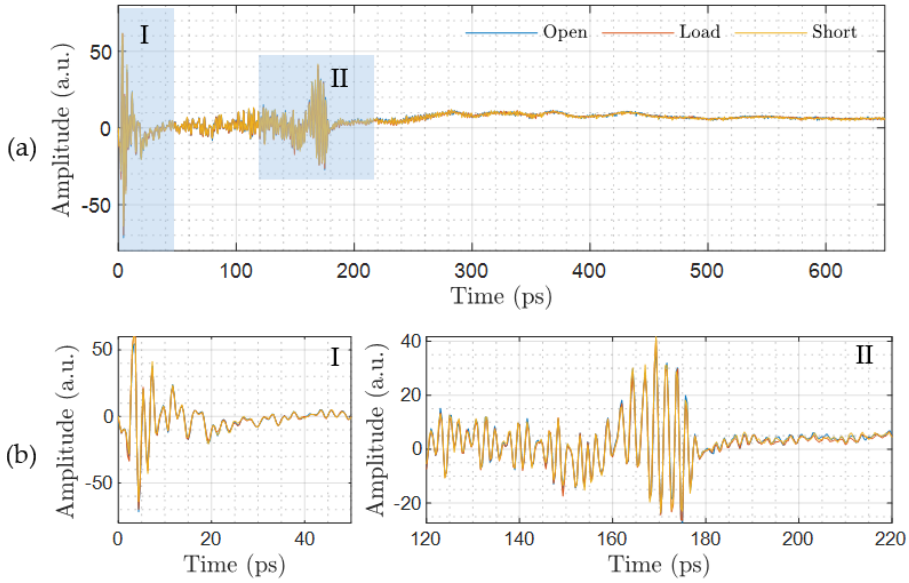

Figure IV.7: (a) Recorded waveforms of time signals reflected from the calibration kit using a 500 GHz high-frequency probe and a waveguide transition. In addition to the measurement in the air (open), other signals are recorded in the case that the high-frequency probe is in contact with the calibration kit, including short, load. (b) Close-up views of the waveform in zones I and II. The zones I and II correspond to the reflections from at the entrance of the probe and the end of transitions.

Figure IV.7 shows the obtained waveforms within a time window of 650 ps. One part of the emitted power is reflected at the entrance of the waveguide transition, displayed in zone I in Figure IV.7 (b). The progressive change of waveguide's dimension gives rise to a modest amount of reflections during the propagation (t varying from 20 to50 ps), then considerable reflections begin to appear at the time around 160 ps in zone II. After 180 ps, reflections with an extremely weak amplitude continue to be detected. Limited by the noise, it becomes difficult to recognize the waveform of the signal after 350 ps.

Based on the time-of-flight of the reflections in zone II (160 ps), an equivalent propagation distance in free space can be deduced, which is the order of 20 mm. This value is very close to the length of the waveguide transition, it is then supposed that most of the emitted waves are reflected at the end of the transition and little power couples into the 500 GHz RF on-wafer probe. There are two possible reasons that can explain the poor coupling between the transition and on-wafer probe. The first one refers to the mechanical issue: the connection between the transition and probe is not well established by the flange. Considering the micrometer dimension of the WR2-2, even a small misalignment between them can damage the propagation behaviors severely. The second possibility is related to the hasty change of the electromagnetic environment between the transition and the probe. Limited by time, further studies were not performed.

IV.3. Conclusion

The attempt to couple a broadband pulse into a sample on-wafer has been carried out by the implementation of a high-frequency on-wafer probe in association with an optical-pumped transceiver. With respect to the results obtained with the 220 GHz RF probe, the propagation distance has demonstrated the successful coupling from the transceiver into the RF probe. However, the severe distortion of the signal due to the multi-mode propagation and modal dispersion make it extremely difficult to interpret the reflected time signal. On the other hand, although 500 GHz Picoprobe has a suitable operation frequency band to operate with the double-PCA transceiver probe, the coupling issue becomes a stumbling block in the way toward a novel optical-pumped on-wafer reflectometry system.

Although further studies are not performed due to the limited time, several new configurations may be worth to be implemented to push up the investigation. Instead of a waveguide transition, a horn antenna adapted to the entrance of the RF probe with gradually changed impedance and a large open aperture may contribute to the coupling improvement between the double-PCA transceiver and the RF probe. Besides, the use of a horn antenna lifts the restrictions on the size of the transceiver, other optical-pumped transceiver devices with high power output and a larger bandwidth can also be applied to construct an on-wafer reflectometry system.

In addition to the coupling issues, the interpretation of the reflected signal is the other major difficulty. If the knowledge about the structure of the high-frequency probe is achieved, 3D full-wave simulation can be carried out to achieve a thorough understanding of the propagation behaviors of pulse signals inside an RF probe. It can as well contribute to the optimization of the RF probe and the whole system configuration. In particular, the investigation should be focused on the transition configuration inside the probe from the rectangular waveguide to the CPW probe-tip, which is supposed to impact significantly the waveform of the reflected signal. Only with full knowledge about the impact of transition between at the end of the RF on-wafer probe, a proper differentiation of reflections from the sample on-wafer is attainable. Besides, the entire environment of the chip including other devices in the vicinity of the sample on-wafer should be taken into consideration during the experiment and simulation to offer comprehensive understanding of the reflected signal. This calibration process step is mandatory to establish an applicable and practical on-wafer reflectometry system.

Apart from RF on-wafer probes, the development of near-field probes in the terahertz band is expected to benefit on-wafer measurements. For instance, if a CPW waveguide is properly integrated into an optoelectronic source/ detector as the output interface with a sample, it can be the solution to a quasi-optical wideband on-wafer reflectometry system. The potential of photonic devices for terahertz measurement systems is waiting to be explored.

Conclusion and perspectives

The present work aimed to construct a terahertz wave-guided reflectometry (TGR) system for a wider application scope in practical use, which can be used in certain circumstances under which, terahertz systems exploiting conventional optical methods may not be efficient. Remote TGR systems have been implemented by hollow-core waveguides in combination with different transceiver units, including TGR systems in pulse mode (TGR-P) and TGR system in FMCW mode (TGR-FMCW).

The focus of the work has first been given on terahertz transceivers amongst all existing sources and detectors, especially optical-pumped transceivers and FMCW ones, to address the space congestion issue between the source and the detector. Being a pulsed source, the used double-PCA lens-free transceiver can be directly employed for imaging over the frequency band roughly ranging from 400 GHz to 600 GHz. Its frequency band can be extended to 800 GHz by reducing the working distance. A resolution power higher than 3.17 lp/mm has been achieved at the frequency of 791 GHz in a near-field imaging application. Nevertheless, it is worth noting that the distance between two planar antennas on the transceiver results in differences in the resolution power in the two directions. In regard to FMCW radars, their phase information allows to differentiate the contributions induced by a sample from the ones generated along a waveguide, making them more advantageous than CW sources. Two FMCW radar units with different emission pattern have then been selected.

A thorough review of terahertz waveguides was conducted, providing valuable information about their corresponding propagation properties and possible difficulties occurring for different applications. After taking into account the propagation losses, the field confinement and the coupling difficulties, hollow-core thin-wall waveguides were selected as a suitable choice. Since the resonant frequencies of the cladding of two selected waveguides are multiple of 0.7 THz (3 mm diameter silica waveguide) and 0.86 THz (6 mm diameter plastic waveguide) respectively, both of them have been demonstrated to be able to transmit the pulse signal, emitted by the double-PCA transceiver.

Based on the selected transceivers, the TGR systems are divided into two types, the ones in pulse mode (TGR-P) and the systems in FMCW mode (TGR-FMCW). It is demonstrated that the TGR-P system composed of a double-PCA transceiver and a silica waveguide can operate efficiently in the frequency region from 400 GHz to 500 GHz, providing a lateral resolution up to 0.707 lp/mm. By means of 3D full simulation, the guided power along a silica waveguide is proved to propagate mainly in the air-core. While the other TGR-P system including a 6 mm diameter plastic waveguide as probe cannot be used for imaging application due to its complicated multi-mode propagation, its potential in liquid depth detection has been demonstrated by taking advantage of the waveform of pulse signals.

The same concept has been applied with FMCW radar units. Despite the atypical excitation conditions provided by two FMCW radars, one part of emitted waves is coupled into the waveguide in

specific guided modes. The unwanted ghosting and shadow effects induced by the irregular beam profile of the waveguide for imaging applications are then corrected by inserting a solid immersion lens at the end of the waveguide. While the TGR-FMCW systems composed of a HDPE lens and a 100 GHz Synview transceiver head provide a resolution power up to 0.25 lp/mm, the one consisting of a 122 GHz radar transceiver chip and a bullet silicon lens has achieved an imaging capacity of 0.891 lp/mm, much smaller than its corresponding wavelength. These studies reveal that depending on the application, either a longer working distance range or an enhanced lateral resolution can be obtained by selecting a suitable lens.

While the remote imaging and sensing abilities of TGR systems have been demonstrated, the irregular beam issues related to the complicated excited propagation modes along a waveguide remain to be addressed, especially for the plastic waveguide. Instead of an optimized focused beam with adapted size, a divergent beam provided by an emitter antenna in TGR systems (either the double-PCA transceiver or FMCW radars) has been used as excitation source. These atypical excitation conditions result in specific cladding mode propagation, even multi-mode propagation along the waveguide. Since the dimension of a waveguide have a considerable impact on the overall performances of the system, it is worth to find out an optimal diameter of the waveguide to improve the coupling efficiency and lateral resolution. To deal with the multi-mode propagation issues, the incident condition is suggested to be reformed so that the emitted power can be coupled properly into the waveguide with desired air-core mode. In these regards, the solid immersion lens integration at the beginning of the waveguide appears to be an interesting solution. By selecting a lens with suitable dimension and material, the incident beam can be focused by this integrated lens without supplementary opto-mechanic support, offering improved coupling efficiency, desired propagation mode and eventually a regular beam profile out of the system. Nevertheless, depending on the refractive index of lens, there will be a trade-off between the transmitted power and focused beam. More investigations are needed to be carried out to explore the efficiency of this suggestion.

From a long-term perspective, a full integration of a waveguide with a transceiver by a solid, reliable and space-saving connection is required to establish a performant compact, practical and widely applicable terahertz wave-guided reflectometry system. Before benefiting from a convenient TGR system, more efforts are needed to achieve progress in two fields, terahertz transceivers and waveguides. While a more compact high-power transceiver unit is wanted to ease restrictions on the choice of the integrated waveguide, other waveguides such as microstructured waveguides are expected to possess lower propagation losses and so that their confinement capacity can be used to maintain the beam shape before arriving onto the sample. In particular, the flexibility of a waveguide is extremely important to establish an endoscopic system for applications in the biomedical domain. More efforts should be brought out in this topic. Most importantly, the cross-section knowledge and cooperation of the two fields are required to contribute to the progress of the TGR systems.

After the construction of the TGR system, on-wafer measurements were targeted due to the increasing need in the TMIC industry. With the aim to capitalize on the wideband of the pulse signal, a double-PCA transceiver with two RF probes has been tested separately to implement an on-wafer

reflectometry system, which allows to simplify ultra-wide frequency band measurement process and decrease the corresponding cost. Despite the successful implementation of two on-wafer reflectometry systems, difficulties in analyzing reflected signals reveal two main predicaments: coupling issue and severe dispersion related to the high propagation modes. Although further studies are not performed due to the limited time, several new configurations including the horn corn in place of waveguide transition are worth to be implemented to push up the investigation. Moreover, the use of a horn antenna can lift the restrictions on the size of the transceiver, other optical-pumped transceiver devices with high power output and a larger bandwidth then can also be applied to construct an on-wafer reflectometry system. It is worth mentioning that the development of near-field probes in the terahertz band may benefit as well on-wafer measurements with adapted contact probe. A CPS-line waveguide integrated into a pulse source may be the solution to a quasi-optical wideband on-wafer reflectometry system. Last but not least, if the knowledge about the structure of the high-frequency probe is obtained, a thorough understanding of the propagation behaviors of pulse signals inside an RF probe can be achieved with the help of 3D full-wave simulation, contributing to the optimization of the RF probe and the whole system configuration.

To conclude, based on the detailed review of developments of transceivers and waveguides, suitable components are selected to demonstrate TGR systems in pulse mode and in FMCW mode in this manuscript. Both experiments and 3D full-wave simulations are used to evaluate system performances and to investigated the sophisticated propagation behaviors inside the system. The trends of the cooperation between the solid-state devices and optoelectronic ones in the terahertz band is mentioned in this work. Further advances of on-wafer measurements using optoelectronic sources is awaited. As the first thorough study about TGR systems, it is hoped that this work provides necessary information and gives an efficient method for researchers that aim to study this new system concept.

Bibliography

[1] S. S. Dhillon, M. S. Vitiello, E. H. Linfield, and E. Al, "The 2017 terahertz science and technology roadmap," *J. Phys. D. Appl. Phys.*, vol. 50, p. 43001, Feb. 2017.

[2] R. A. Lewis, "A review of terahertz sources," *J. Phys. D. Appl. Phys.*, vol. 47, no. 37, p. 374001, 2014.

[3] R. E. Miles and M. Naftaly, "Terahertz Sources," *Microw. Photonics Devices Appl.*, pp. 111–129, 2011.

[4] R. A. Friedel and A. G. Sharkey, "Comparison of glower and Globar sources for infra-red spectrometry," *Rev. Sci. Instrum.*, vol. 18, no. 12, p. 928, 1947.

[5] K. Charrada, G. Zissis, and M. Aubes, "Two-temperature, two-dimensional fluid modelling of mercury plasma in high-pressure lamps," *J. Phys. D. Appl. Phys.*, vol. 29, no. 9, pp. 2432–2438, 1996.

[6] J. B. Sleiman, "Terahertz Imaging and Spectroscopy: Application to Defense and Security," 2016.

[7] J. H. Booske, R. J. Dobbs, C. D. Joye, C. L. Kory, S. Member, G. R. Neil, G. Park, J. Park, and R. J. Temkin, "Vacuum Electronic High Power Terahertz Sources," *IEEE Trans. Terahertz Sci. Technol.*, vol. 1, no. 1, pp. 54–75, 2011.

[8] J. S. Rieh, J. Yun, D. Yoon, J. Kim, and H. Son, "Terahertz InP HBT Oscillators," in *2018 IEEE International Symposium on Radio-Frequency Integration Technology, RFIT 2018*, 2018, pp. 1–3.

[9] A. Khalid, N. J. Pilgrim, G. M. Dunn, M. C. Holland, C. R. Stanley, I. G. Thayne, and D. R. S. Cumming, "A planar Gunn diode operating above 100 GHz," *IEEE Electron Device Lett.*, vol. 28, no. 10, pp. 849–851, 2007.

[10] W. Knap, S. Nadar, H. Videlier, S. Boubanga-Tombet, D. Coquillat, N. Dyakonova, F. Teppe, K. Karpierz, J. Łusakowski, M. Sakowicz, I. Kasalynas, D. Seliuta, G. Valusis, T. Otsuji, Y. Meziani, A. El Fatimy, S. Vandenbrouk, K. Madjour, D. Théron, and C. Gaquière, "Field effect transistors for terahertz detection and emission," *J. Infrared, Millimeter, Terahertz Waves*, vol. 32, no. 5, pp. 618–628, 2011.

[11] M. Sakhno, A. Golenkov, and F. Sizov, "Uncooled detector challenges: Millimeter-wave and terahertz long channel field effect transistor and Schottky barrier diode detectors," *J. Appl. Phys.*, vol. 114, no. 16, 2013.

[12] J. S. Rieh, D. Yoon, and J. Yun, "An overview of solid-state electronic sources and detectors for Terahertz imaging," *Proc. - 2014 IEEE 12th Int. Conf. Solid-State Integr. Circuit Technol. ICSICT 2014*, pp. 1–4, 2014.

[13] G. Dodel, "On the history of far-infrared (FIR) gas lasers: Thirty-five years of research and application," *Infrared Phys. Technol.*, vol. 40, no. 3, pp. 127–139, 1999.

[14] J.-F. Lampin, A. Pagies, G. Santarelli, J. Hesler, W. Hansel, R. Holzwarth, and S. Barbieri, "Quantum cascade laser-pumped terahertz molecular lasers: frequency noise and phase-locking using a 1560 nm frequency comb," *Opt. Express*, vol. 28, no. 2, p. 2091, 2020.

[15] R. Köhler, A. Tredicucci, F. Beltram, H. E. Beere, E. H. Linfield, A. G. Davies, D. A. Ritchie, R. C. Iotti, and F. Rossi, "Terahertz semiconductor-heterostructure laser," *Nature*, vol. 417, no. 6885, pp. 156–159, 2002.

[16] M. S. Vitiello, G. Scalari, B. Williams, and P. De Natale, "Quantum cascade lasers: 20 years of challenges," *Opt. Express*, vol. 23, no. 4, p. 5167, 2015.

[17] K. Zhong, W. Shi, D. G. Xu, P. X. Liu, Y. Y. Wang, J. L. Mei, C. Yan, S. J. Fu, and J. Q. Yao, "Optically pumped terahertz sources," *Sci. China Technol. Sci.*, vol. 60, no. 12, pp. 1801–1818, 2017.

[18] A. Rolland, G. Ducournau, G. Danion, G. Loas, M. Brunel, A. Beck, F. Pavanello, E. Peytavit, T. Akalin, M. Zaknoune, J. F. Lampin, F. Bondu, M. Vallet, P. Szriftgiser, D. Bacquet, and M. Alouini, "Narrow linewidth tunable terahertz radiation by photomixing without servo-locking," *IEEE Trans. Terahertz Sci. Technol.*, vol. 4, no. 2, pp. 260–266, 2014.

[19] K. Murasawa and T. Hidaka, "Generation and homodyne detection of continuous terahertz waves using single photoconductive antenna," *Jpn. J. Appl. Phys.*, vol. 49, no. 12, 2010.

[20] T. Ishibashi and H. Ito, "Uni-traveling-carrier photodiodes," *J. Appl. Phys.*, vol. 127, no. 3, 2020.

[21] S. Blin, R. Paquet, M. Myara, B. Chomet, L. Le Gratiet, M. Sellahi, G. Beaudoin, I. Sagnes, G. Ducournau, P. Latzel, J. F. Lampin, and A. Garnache, "Coherent and Tunable THz Emission Driven by an Integrated III-V Semiconductor Laser," *IEEE J. Sel. Top. Quantum Electron.*, vol. 23, no. 4, 2017.

[22] E. Castro-Camus and M. Alfaro, "Photoconductive devices for terahertz pulsed spectroscopy," *Photonics Res.*, vol. 4, no. 3, p. A36, 2016.

[23] X. C. Zhang and J. Xu, *Generation and Detection of THz Waves*. 2010.

[24] R. J. B. Dietz, B. Globisch, H. Roehle, D. Stanze, T. Göbel, and M. Schell, "Influence and adjustment of carrier lifetimes in InGaAs/InAlAs photoconductive pulsed terahertz detectors: 6 THz bandwidth and 90dB dynamic range," *Opt. Express*, vol. 22, no. 16, p. 19411, 2014.

[25] K. Peng, P. Parkinson, L. Fu, Q. Gao, N. Jiang, Y. N. Guo, F. Wang, H. J. Joyce, J. L. Boland, M. B. Johnston, H. H. Tan, and C. Jagadish, "Single GaAs/AlGaAs nanowire photoconductive terahertz detectors," *2014 Conf. Optoelectron. Microelectron. Mater. Devices, COMMAD 2014*, pp. 221–222, 2014.

[26] R. Yano, H. Gotoh, Y. Hirayama, S. Miyashita, Y. Kadoya, and T. Hattori, "Terahertz wave detection performance of photoconductive antennas: Role of antenna structure and gate pulse intensity," *J. Appl. Phys.*, vol. 97, no. 10, 2005.

[27] M. Tani, M. Herrmann, and K. Sakai, "Generation and detection of THz pulsed radiation with photoconductive antennas," *Meas. Sci. Technol.*, vol. 13, pp. 1739–1745, 2002.

[28] G. Niehues, S. Funkner, D. S. Bulgarevich, S. Tsuzuki, T. Furuya, K. Yamamoto, M. Shiwa, and M. Tani, "A matter of symmetry: terahertz polarization detection properties of a multi-contact photoconductive antenna evaluated by a response matrix analysis," *Opt. Express*, vol. 23, no. 12, p.

16184, 2015.

[29] A. Dreyhaupt, S. Winnerl, T. Dekorsy, and M. Helm, “High-intensity terahertz radiation from a microstructured large-area photoconductor,” *Appl. Phys. Lett.*, vol. 86, no. 12, pp. 1–3, 2005.

[30] P. J. Hale, J. Madeo, C. Chin, S. S. Dhillon, J. Mangeney, J. Tignon, and K. M. Dani, “20 THz broadband generation using semi-insulating GaAs interdigitated photoconductive antennas,” *Opt. Express*, vol. 22, no. 21, p. 26358, 2014.

[31] X. Ropagnol, M. Khorasaninejad, M. Raeiszadeh, S. Safavi-Naeini, M. Bouvier, C. Y. Côté, A. Laramée, M. Reid, M. A. Gauthier, and T. Ozaki, “Intense THz Pulses with large ponderomotive potential generated from large aperture photoconductive antennas,” *Opt. Express*, vol. 24, no. 11, p. 11299, 2016.

[32] M. Beck, H. Schäfer, G. Klatt, J. Demsar, S. Winnerl, M. Helm, and T. Dekorsy, “Impulsive terahertz radiation with high electric fields from an amplifier-driven large-area photoconductive antenna,” *Opt. Express*, vol. 18, no. 9, p. 9251, 2010.

[33] C. W. Berry, N. Wang, M. R. Hashemi, M. Unlu, and M. Jarrahi, “Significant performance enhancement in photoconductive terahertz optoelectronics by incorporating plasmonic contact electrodes,” *Nat. Commun.*, vol. 4, pp. 1610–1622, 2013.

[34] A. Jooshesh, V. Bahrami-Yekta, J. Zhang, T. Tiedje, T. E. Darcie, and R. Gordon, “Plasmon-Enhanced below Bandgap Photoconductive Terahertz Generation and Detection,” *Nano Lett.*, vol. 15, no. 12, pp. 8306–8310, 2015.

[35] S.-G. Park, Y. Choi, Y.-J. Oh, and K.-H. Jeong, “Terahertz photoconductive antenna with metal nanoislands,” *Opt. Express*, vol. 20, no. 23, p. 25530, 2012.

[36] S. H. Yang, M. R. Hashemi, C. W. Berry, and M. Jarrahi, “7.5% Optical-to-terahertz conversion efficiency offered by photoconductive emitters with three-dimensional plasmonic contact electrodes,” *IEEE Trans. Terahertz Sci. Technol.*, vol. 4, no. 5, pp. 575–581, 2014.

[37] N. T. Yardimci, S. H. Yang, C. W. Berry, and M. Jarrahi, “High-power terahertz generation using large-area plasmonic photoconductive emitters,” *IEEE Trans. Terahertz Sci. Technol.*, vol. 5, no. 2, pp. 223–229, 2015.

[38] K. Moon, I. M. Lee, J. H. Shin, E. S. Lee, N. Kim, W. H. Lee, H. Ko, S. P. Han, and K. H. Park, “Bias field tailored plasmonic nano-electrode for high-power terahertz photonic devices,” *Sci. Rep.*, vol. 5, pp. 1–9, 2015.

[39] S. Lepeshov, A. Gorodetsky, A. Krasnok, N. Toropov, T. A. Vartanyan, P. Belov, A. Alú, and E. U. Rafailov, “Boosting Terahertz Photoconductive Antenna Performance with Optimised Plasmonic Nanostructures,” *Sci. Rep.*, vol. 8, no. 1, pp. 1–7, 2018.

[40] F. D. J. Brunner and T. Feurer, “Antireflection coatings optimized for single-cycle THz pulses,” *Appl. Opt.*, vol. 52, no. 16, pp. 3829–3832, 2013.

[41] M. Nagel, C. Matheisen, and H. Kurz, *Novel techniques in terahertz near-field imaging and sensing*, no. Ic. Woodhead Publishing Limited, 2013.

[42] M. Kozub, K. Nishisaka, T. Maemoto, S. Sasa, K. Takayama, and M. Tonouchi, “Reflection Layer Mediated Enhancement of Terahertz Radiation Utilizing Heavily-Doped InAs Thin Films,” *J. Infrared, Millimeter, Terahertz Waves*, vol. 36, no. 5, pp. 423–429, 2015.

[43] H. Roehle, R. J. B. Dietz, H. J. Hensel, J. Böttcher, H. Künzel, D. Stanze, M. Schell, and B. Sartorius, "Next generation 1.5 μm terahertz antennas: mesa-structuring of InGaAs/InAlAs photoconductive layers," *Opt. Express*, vol. 18, no. 3, p. 2296, 2010.

[44] P. C. Gow, J. L. Carthy, S. A. Berry, and V. Apostolopoulos, "A radial double-metal bias-free THz emitter for coaxial cable transmission," in *2017 42nd International Conference on Infrared, Millimeter, and Terahertz Waves (IRMMW-THz)*, 2017.

[45] B. Ferguson and X. C. Zhang, "Materials for terahertz science and technology," *Nature Materials*, vol. 1, no. 1, pp. 26–33, 2002.

[46] D. Saeedkia, *Handbook of terahertz technolgy for imaging, sensing and comunications*. Elsevier, 2013.

[47] P. H. Siegel and R. J. Dengler, "Terahertz heterodyne imaging part I: Introduction and techniques," *Int. J. Infrared Millimeter Waves*, vol. 27, no. 4, pp. 465–480, 2006.

[48] J.-B. Perraud, "Reconstructions rapides d ' images en régime térahertz 3D," 2018.

[49] D. A. Shaghik Atakaramians, Shahraam Afshar V., Tanya M. Monro, "Terahertz dielectric waveguides," *Adv. Opt. Photonics*, vol. 6, pp. 293–339, 2014.

[50] F. Pavanello, F. Garet, M. B. Kuppam, E. Peytavit, M. Vanwolleghem, F. Vaurette, J. L. Coutaz, and J. F. Lampin, "Broadband ultra-low-loss mesh filters on flexible cyclic olefin copolymer films for terahertz applications," *Appl. Phys. Lett.*, vol. 102, no. 11, 2013.

[51] X. Liu, K. Fan, I. V. Shadrivov, W. J. Padilla, X. I. L. Iu, K. E. F. An, I. L. Y. A. V. S. Hadrivov, P. Adilla, W. J. Illie, X. Liu, K. Fan, I. V. Shadrivov, and W. J. Padilla, "Experimental realization of a terahertz all-dielectric metasurface absorber," *Opt. Express*, vol. 25, no. 1, p. 191, 2017.

[52] F. Friederich, E. Cristofani, C. Matheis, J. Jonuscheit, R. Beigang, and M. Vandewal, "Continuous wave terahertz inspection of glass fiber reinforced plastics with semi-automatic 3-D image processing for enhanced defect detection," *IEEE MTT-S Int. Microw. Symp. Dig.*, pp. 1–4, 2014.

[53] E. Cristofani, F. Friederich, S. Wohnsiedler, C. Matheis, J. Jonuscheit, M. Vandewal, and R. Beigang, "Nondestructive testing potential evaluation of a terahertz frequency-modulated continuous-wave imager for composite materials inspection," *Opt. Eng.*, vol. 53, no. 3, p. 031211, 2014.

[54] J. P. Guillet, M. Roux, K. Wang, X. Ma, F. Fauquet, H. Balacey, B. Recur, F. Darracq, and P. Mounaix, "Art Painting Diagnostic Before Restoration with Terahertz and Millimeter Waves," *J. Infrared, Millimeter, Terahertz Waves*, vol. 38, no. 4, pp. 369–379, 2017.

[55] H. Hirori, K. Yamashita, M. Nagai, and K. Tanaka, "Attenuated total reflection spectroscopy in time domain using terahertz coherent pulses," *Japanese J. Appl. Physics, Part 2 Lett.*, vol. 43, no. 10 A, pp. 43–46, 2004.

[56] M. Tani, Z. Jiang, and X.-C. Zhang, "Photoconductive terahertz transceiver," *Electron. Lett.*, vol. 36, no. 9, pp. 804–805, 2000.

[57] J. Pearce, H. Choi, D. M. Mittleman, J. White, and D. Zimdars, "Terahertz wide aperture reflection tomography," *Opt. Lett.*, vol. 30, no. 13, pp. 1653–1655, 2005.

[58] C. Jordens, N. Krumbholz, T. Hasek, N. Vieweg, B. Scherger, L. Bahr, M. Mikulics, and M. Koch,

"Fibre-coupled terahertz transceiver head," *Electron. Lett.*, vol. 44, no. 25, pp. 44–45, 2008.

[59] N. Vieweg, N. Krumbholz, T. Hasek, R. Wilk, V. Bartels, C. Keseberg, V. Pethukhov, M. Mikulics, L. Wetenkamp, and M. Koch, "Fiber-coupled THz spectroscopy for monitoring polymeric compounding processes," *Proc. SPIE*, vol. 6616, p. 66163M, 2007.

[60] S. Busch, T. Probst, M. Schwerdtfeger, R. Dietz, J. Palací, and M. Koch, "Terahertz transceiver concept," *Opt. Express*, vol. 22, no. 14, p. 16841, 2014.

[61] M. Tani, M. Watanabe, and K. Sakai, "Photoconductive twin dipole antennas for THz transceiver," *Electron. Lett.*, vol. 38, no. 1, p. 5, 2002.

[62] H. S. Bark, Y. Bin Ji, S. J. Oh, S. K. Noh, and T. I. Jeon, "Optical fiber coupled THz transceiver," in *IRMMW-THz 2015 - 40th International Conference on Infrared, Millimeter, and Terahertz Waves*, 2015, pp. 1–2.

[63] B. Globisch, R. J. B. Dietz, R. B. Kohlhaas, S. Nellen, M. Kleinert, T. Göbel, and M. Schell, "Fiber-coupled transceiver for terahertz reflection measurements with a 4.5 THz bandwidth," *Opt. Lett.*, vol. 41, no. 22, p. 5262, 2016.

[64] Y. Bin Ji, E. S. Lee, S.-H. Kim, J.-H. Son, and T.-I. Jeon, "A miniaturized fiber-coupled terahertz endoscope system," *Opt. Express*, vol. 17, no. 19, p. 17082, 2009.

[65] C. Jordens, N. Krumbholz, T. Hasek, N. Vieweg, B. Scherger, L. Bahr, M. Mikulics, and M. Koch, "Fibre-coupled terahertz transceiver head," *Electron. Lett.*, vol. 44, no. 25, 2008.

[66] B. You, J. Y. Lu, T. A. Liu, J. L. Peng, and C. L. Pan, "Subwavelength plastic wire terahertz time-domain spectroscopy," *Appl. Phys. Lett.*, vol. 96, no. 5, pp. 2008–2011, 2010.

[67] Y. Gao and R. Zoughi, "Millimeter Wave Reflectometry and Imaging for Noninvasive Diagnosis of Skin Burn Injuries," *IEEE Trans. Instrum. Meas.*, vol. 66, no. 1, pp. 77–84, 2017.

[68] S. Ayhan, S. Scherr, M. Pauli, and T. Zwick, "FMCW Radar in Oil-filled Waveguides for Range Detection in Hydraulic Cylinders," in *2012 9th European Radar Conference*, 2012, pp. 63–66.

[69] G. Goubau, "Surface waves and their application to transmission lines," *J. Appl. Phys.*, vol. 21, no. 11, pp. 1119–1128, 1950.

[70] M. Wächter, M. Nagel, and H. Kurz, "Frequency-dependent characterization of THz Sommerfeld wave propagation on single-wires," *Opt. Express*, vol. 13, no. 26, pp. 10815–10822, 2005.

[71] J. Bin Young, E. S. Lee, J. S. Jang, T.-I. Jeon, M. H. Kwak, and K.-Y. Kwang, "Guidance properties of metal wire waveguide by Terahertz pulse propagation," *J. Korean Phys. Soc.*, vol. 50, no. 5, pp. 1238–1242, 2007.

[72] K. R. Chu and P. Chow, "A theoretical study of terahertz surface plasmons on a cylindrical metal wire," *Phys. Plasmas*, vol. 24, no. 1, 2017.

[73] J. A. Deibel, N. Berndsen, K. Wang, D. M. Mittleman, N. C. J. Van Der Valk, and P. C. M. Planken, "Frequency-dependent radiation patterns emitted by THz plasmons on cylindrical metal wires," *Opt. Express*, vol. 14, no. 19, pp. 1715–1719, 2006.

[74] J. Zha, G. J. Kim, and T.-I. Jeon, "Enhanced THz guiding properties of curved two-wire lines," *Opt. Express*, vol. 24, no. 6, p. 6136, 2016.

[75] A. Markov and M. Skorobogatiy, “Two-wire terahertz fibers with porous dielectric support,” *Opt. Express*, vol. 21, no. 10, pp. 5344–5355, 2013.

[76] K. L. Wang and D. M. Mittleman, “Metal wires for terahertz wave guiding,” *Nature*, vol. 432, no. November, pp. 376–379, 2004.

[77] M. Awad, M. Nagel, and H. Kurz, “Tapered Sommerfeld wire terahertz near-field imaging,” *Appl. Phys. Lett.*, vol. 94, no. 5, pp. 3–6, 2009.

[78] J. P. Guillet, L. Chusseau, R. Adam, T. Grosjean, A. Penarier, F. Baida, and D. Charraut, “Continuous-wave scanning terahertz near-field microscope,” *Microw. Opt. Technol. Lett.*, vol. 53, no. 3, pp. 580–582, 2011.

[79] H. Cao and A. Nahata, “Coupling of terahertz pulses onto a single metal wire waveguide using milled grooves,” *Opt. Express*, vol. 13, no. 18, p. 7028, 2005.

[80] L. Chusseau and J.-P. Guillet, “Coupling and propagation of Sommerfeld waves at 100 and 300 GHz,” *J. Infrared, Millimeter, Terahertz Waves*, vol. 33, no. 2, pp. 174–182, 2012.

[81] J. A. Deibel, K. Wang, M. D. Escarra, and D. M. Mittleman, “Enhanced coupling of terahertz radiation to cylindrical wire waveguides,” *Opt. Express*, vol. 14, no. 1, pp. 511–518, 2006.

[82] T. I. Jeon, J. Zhang, and D. Grischkowsky, “THz Sommerfeld wave propagation on a single metal wire,” *Appl. Phys. Lett.*, vol. 86, no. 16, pp. 1–3, 2005.

[83] Y. Bin Ji, E. S. Lee, J. S. Jang, and T. I. Jeon, “Enhancement of the detection of THz Sommerfeld wave using a conical wire waveguide,” *Opt. Express*, vol. 16, no. 1, pp. 271–278, 2008.

[84] M. Wächter, M. Nagel, and H. Kurz, “Tapered photoconductive terahertz field probe tip with subwavelength spatial resolution,” *Appl. Phys. Lett.*, vol. 95, no. 4, pp. 1–4, 2009.

[85] R. Imai, N. Kanda, K. Konishi, and M. Kuwata-Gonokami, “Terahertz vector beam generation using segmented nonlinear optical crystals with three-fold rotational symmetry,” *Opt. Express*, vol. 20, no. 20, p. 21896, 2012.

[86] Z. Zheng, N. Kanda, K. Konishi, and M. Kuwata-Gonokami, “Efficient coupling of broadband terahertz radial beams to metal wires,” *Opt. Express*, vol. 21, no. 9, pp. 8433–8439, 2013.

[87] R. Menais and D. Grischkowsky, “THz interconnect with low-loss and low-group velocity dispersion,” *IEEE Microw. Wirel. Components Lett.*, vol. 11, no. 11, pp. 444–446, 2001.

[88] R. Mendis and D. Grischkowsky, “Undistorted guided-wave propagation of subpicosecond terahertz pulses,” *Opt. Lett.*, vol. 26, no. 11, p. 846, 2001.

[89] A. Bingham, Y. Zhao, and D. Grischkowsky, “THz parallel plate photonic waveguides,” *Appl. Phys. Lett.*, vol. 87, no. 5, pp. 10–13, 2005.

[90] S.-H. Kim, E. S. Lee, Y. Bin Ji, and T.-I. Jeon, “Improvement of THz coupling using a tapered parallel-plate waveguide,” *Opt. Express*, vol. 18, no. 2, p. 1289, 2010.

[91] J. Liu, R. Mendis, D. M. Mittleman, and N. Sakoda, “A tapered parallel-plate-waveguide probe for THz near-field reflection imaging,” *Appl. Phys. Lett.*, vol. 100, no. 3, pp. 98–101, 2012.

[92] M. Navarro-Cía, J. Wu, H. Liu, and O. Mitrofanov, “Generation of radially-polarized terahertz

pulses for coupling into coaxial waveguides," *Sci. Rep.*, vol. 6, no. December, pp. 1–8, 2016.

[93] J. Zhang and T. Y. Hsiang, "Dispersion characteristics of coplanar waveguides at subterahertz frequencies," 2006.

[94] Z. Zhou and K. L. Melde, "Development of a broadband coplanar waveguide-to-microstrip transition with vias," *IEEE Trans. Adv. Packag.*, vol. 31, no. 4, pp. 861–872, 2008.

[95] M. Naftaly and R. E. Miles, "Terahertz time-domain spectroscopy: A new tool for the study of glasses in the far infrared," *J. Non. Cryst. Solids*, vol. 351, no. 40–42, pp. 3341–3346, Oct. 2005.

[96] J. Anthony, R. Leonhardt, A. Argyros, and M. C. J. Large, "Characterization of a microstructured Zeonex terahertz fiber," *J. Opt. Soc. Am. B*, vol. 28, no. 5, p. 1013, 2011.

[97] J. Balakrishnan, B. M. Fischer, and D. Abbott, "Sensing the hygroscopicity of polymer and copolymer materials using terahertz time-domain spectroscopy," *Appl. Opt.*, vol. 48, no. 12, pp. 2262–2266, 2009.

[98] Y. S. Jin, G. J. Kim, and S. G. Jeon, "Terahertz dielectric properties of polymers," *J. Korean Phys. Soc.*, vol. 49, no. 2, pp. 513–517, 2006.

[99] A. W. Snyder and J. Love, *Optical waveguide theory*. Springer Science & Business Media, 2012.

[100] S. P. Jamison, R. W. McGowan, and D. Grischkowsky, "Single-mode waveguide propagation and reshaping of sub-ps terahertz pulses in sapphire fibers," *Appl. Phys. Lett.*, vol. 76, no. 15, pp. 1987–1989, 2000.

[101] R. Mendis and D. Grischkowsky, "Plastic ribbon THz waveguides," *J. Appl. Phys.*, vol. 88, no. 2000, pp. 4449–4451, 2000.

[102] L.-J. Chen, H.-W. Chen, T.-F. Kao, J.-Y. Lu, and C.-K. Sun, "Low-loss subwavelength plastic fiber for terahertz waveguiding," *Opt. Lett.*, vol. 31, no. 3, p. 308, 2006.

[103] J. Y. Lu, C. M. Chiu, C. C. Kuo, C. H. Lai, H. C. Chang, Y. J. Hwang, C. L. Pan, and C. K. Sun, "Terahertz scanning imaging with a subwavelength plastic fiber," *Appl. Phys. Lett.*, vol. 92, no. 8, pp. 2006–2009, 2008.

[104] C. Chiu, H. Chen, Y. Huang, Y. Hwang, W. Lee, H. Huang, and C. Sun, "All-terahertz fiber-scanning near-field microscopy," *Opt. Lett.*, vol. 34, no. 7, pp. 1084–1086, 2009.

[105] B. You, T.-A. Liu, J.-L. Peng, C.-L. Pan, and J.-Y. Lu, "A terahertz plastic wire based evanescent field sensor for high sensitivity liquid detection," *Opt. Express*, vol. 17, no. 23, pp. 20675–20683, 2009.

[106] B. Ung, M. Rozé, A. Mazhorova, M. Walther, and M. Skorobogatiy, "Suspended core subwavelength fibers for practical low-loss terahertz guidance," *Opt. InfoBase Conf. Pap.*, vol. 19, no. 10, pp. 1431–1433, 2011.

[107] H. Han, H. Park, M. Cho, and J. Kim, "Terahertz pulse propagation in a plastic photonic crystal fiber," *Appl. Phys. Lett.*, vol. 80, no. 15, pp. 2634–2636, 2002.

[108] M. Goto, A. Quema, H. Takahashi, S. Ono, and N. Sarukura, "Teflon Photonic Crystal Fiber as Terahertz Waveguide," *Japanese J. Appl. Physics, Part 2 Lett.*, vol. 43, no. 2 B, 2004.

[109] Y. Li, C. Wang, N. Zhang, C. Y. Wang, and Q. Xing, "Analysis and design of terahertz photonic crystal fibers by an effective-index method," *Appl. Opt.*, vol. 45, no. 33, pp. 8462–8465, 2006.

[110] D. K. Sharma, A. Sharma, and S. M. Tripathi, "Microstructured optical fibers for terahertz waveguiding regime by using an analytical field model," *Opt. Fiber Technol.*, vol. 39, no. September, pp. 55–69, 2017.

[111] M. Nagel, A. Marchewka, and H. Kurz, "Low-index discontinuity terahertz waveguides.," *Opt. Express*, vol. 14, no. 21, pp. 9944–54, 2006.

[112] A. Hassani, A. Dupuis, and M. Skorobogatiy, "Low loss porous terahertz fibers containing multiple subwavelength holes," *Appl. Phys. Lett.*, vol. 92, no. 7, pp. 2006–2009, 2008.

[113] S. Atakaramians, S. Afshar V., B. M. Fischer, D. Abbott, and T. M. Monro, "Porous fibers: a novel approach to low loss THz waveguides," *Opt. Express*, vol. 16, no. 12, p. 8845, 2008.

[114] S. Atakaramians, S. Afshar V., B. M. Fischer, D. Abbott, and T. M. Monro, "Low loss, low dispersion and highly birefringent terahertz porous fibers," *Opt. Commun.*, vol. 282, no. 1, pp. 36–38, 2009.

[115] S. Atakaramians, S. Afshar V., H. Ebendorff-Heidepriem, M. Nagel, B. M. Fischer, D. Abbott, and T. M. Monro, "THz porous fibers: design, fabrication and experimental characterization," *Opt. Express*, vol. 17, no. 16, p. 14053, 2009.

[116] S. Atakaramians, S. Afshar V., M. Nagel, H. K. Rasmussen, O. Bang, T. M. Monro, and D. Abbott, "Direct probing of evanescent field for characterization of porous terahertz fibers," *Appl. Phys. Lett.*, vol. 98, no. 12, pp. 2009–2012, 2011.

[117] A. Dupuis, J.-F. Allard, D. Morris, K. Stoeffler, C. Dubois, and M. Skorobogatiy, "Fabrication and THz loss measurements of porous subwavelength fibers using a directional coupler method," *Opt. Express*, vol. 17, no. 10, p. 8012, 2009.

[118] K. Nielsen, H. K. Rasmussen, P. U. Jepsen, and O. Bang, "Porous-core honeycomb bandgap THz fiber," *Opt. Lett.*, vol. 36, no. 5, p. 666, 2011.

[119] H. Bao, K. Nielsen, H. K. Rasmussen, P. U. Jepsen, and O. Bang, "Fabrication and characterization of porous-core honeycomb bandgap THz fibers," *Opt. Express*, vol. 20, no. 28, p. 29507, 2012.

[120] J. Fan, Y. Li, M. Hu, L. Chai, and C. Wang, "Design of Broadband Porous-Core Bandgap Terahertz Fibers," *IEEE Photonics Technol. Lett.*, vol. 28, no. 10, pp. 1096–1099, 2016.

[121] B. Ung, A. Mazhorova, A. Dupuis, M. Rozé, and M. Skorobogatiy, "Polymer microstructured optical fibers for terahertz wave guiding," *Opt. Express*, vol. 19, no. 26, p. B848, 2011.

[122] S. F. Kaijage, Z. Ouyang, and X. Jin, "Porous-core photonic crystal fiber for low loss terahertz wave guiding," *IEEE Photonics Technol. Lett.*, vol. 25, no. 15, pp. 1454–1457, 2013.

[123] R. Islam, G. K. M. Hasanuzzaman, M. S. Habib, S. Rana, and M. A. G. Khan, "Low-loss rotated porous core hexagonal single-mode fiber in THz regime," *Opt. Fiber Technol.*, vol. 24, pp. 38–43, 2015.

[124] M. S. Islam, J. Sultana, S. Rana, M. R. Islam, M. Faisal, S. F. Kaijage, and D. Abbott, "Extremely low material loss and dispersion flattened TOPAS based circular porous fiber for long distance terahertz wave transmission," *Opt. Fiber Technol.*, vol. 34, pp. 6–11, 2017.

[125] S. Rana, A. S. Rakin, M. R. Hasan, M. S. Reza, R. Leonhardt, D. Abbott, and H. Subbaraman, "Low loss and flat dispersion Kagome photonic crystal fiber in the terahertz regime," *Opt. Commun.*, vol. 410, no. October 2017, pp. 452–456, 2018.

[126] Z. WU, X. ZHOU, H. XIA, Z. SHI, J. HUANG, X. JIANG, and W. WU, "Low-loss polarization-maintaining THz photonic crystal fiber with a triple-hole core," *Appl. Opt.*, vol. 56, no. 8, pp. 2288–2293, 2017.

[127] M. D. S. Islam, J. A. Sultana, J. Atai, D. Abbott, S. Rana, and I. M. Rakibul, "Ultra low-loss hybrid core porous fiber for broadband applications," *Appl. Opt.*, vol. 56, no. 4, pp. 1232–1237, 2017.

[128] M. S. Islam, J. Sultana, M. Faisal, M. R. Islam, A. Dinovitser, B. W. H. Ng, and D. Abbott, "A modified hexagonal photonic crystal fiber for terahertz applications," *Opt. Mater. (Amst).*, vol. 79, no. March, pp. 336–339, 2018.

[129] J. Sultana, M. S. Islam, K. Ahmed, A. Dinovitser, B. W.-H. Ng, and D. Abbott, "Terahertz detection of alcohol using a photonic crystal fiber sensor," *Appl. Opt.*, vol. 57, no. 10, p. 2426, 2018.

[130] S. Rana, A. S. Rakin, H. Subbaraman, R. Leonhardt, and D. Abbott, "Low Loss and Low Dispersion Fiber for Transmission Applications in the Terahertz Regime," *IEEE Photonics Technol. Lett.*, vol. 29, no. 10, pp. 830–833, 2017.

[131] M. S. Islam, J. Sultana, A. Dinovitser, M. Faisal, M. R. Islam, B. W.-H. Ng, and D. Abbott, "Zeonex-based asymmetrical terahertz photonic crystal fiber for multichannel communication and polarization maintaining applications," *Appl. Opt.*, vol. 57, no. 4, p. 666, 2018.

[132] M. S. Islam, J. Sultana, A. A. Rifat, A. Dinovitser, B. Wai-Him Ng, and D. Abbott, "Terahertz sensing in a hollow core photonic crystal fiber," *IEEE Sens. J.*, vol. 18, no. 10, pp. 4073–4080, 2018.

[133] B. Bowden, J. a Harrington, and O. Mitrofanov, "Silver/polystyrene-coated hollow glass waveguides for the transmission of terahertz radiation.," *Opt. Lett.*, vol. 32, no. 20, pp. 2945–7, 2007.

[134] J. Harrington, R. George, P. Pedersen, and E. Mueller, "Hollow polycarbonate waveguides with inner Cu coatings for delivery of terahertz radiation.," *Opt. Express*, vol. 12, no. 21, pp. 5263–5268, 2004.

[135] M. Navarro-Cia, J. E. Melzer, J. A. Harrington, and O. Mitrofanov, "Silver-Coated Teflon Tubes for Waveguiding at 1-2THz," *J. Infrared, Millimeter, Terahertz Waves*, vol. 36, no. 6, pp. 542–555, 2015.

[136] D. Tian, H. Zhang, Q. Wen, Z. Wang, S. Li, Z. Chen, and X. Guo, "Dual cylindrical metallic grating-cladding polymer hollow waveguide for terahertz transmission with low loss," *Appl. Phys. Lett.*, vol. 97, no. 13, pp. 65–68, 2010.

[137] J. LI, K. NALLAPPAN, H. GUERBOUKHA, and M. SKOROBOGATIY, "Implementing Bragg mirrors in a hollow-core photonic-crystal fiber," *Opt. Express*, vol. 25, no. 4, pp. 4126–4144, 2017.

[138] J. Flannery, G. Bappi, V. Bhaskara, O. Alshehri, and M. Bajcsy, "Implementing Bragg mirrors in a hollow-core photonic-crystal fiber," *Opt. Mater. Express*, vol. 7, no. 4, pp. 207–210, 2017.

[139] B. Hong, S. Member, M. Swithenbank, N. Greenall, R. G. Clarke, N. Chudpooti, S. Member, P. Akkaraekthalin, N. Somjit, J. E. Cunningham, and I. D. Robertson, "Low-Loss Asymptotically Single-Mode THz Bragg Fiber Fabricated by Digital Light Processing Rapid Prototyping," *IEEE Trans. Terahertz Sci. Technol.*, vol. 8, no. 1, pp. 90–99, 2018.

[140] M. R. Hasan and S. Akter, “Extremely low-loss hollow-core bandgap photonic crystal fibre for broadband terahertz wave guiding,” *Electron. Lett.*, vol. 53, no. 11, pp. 741–743, 2017.

[141] M. A. Duguay, Y. Kokubun, T. L. Koch, and L. Pfeiffer, “Antiresonant reflecting optical waveguides in SiO2-Si multilayer structures,” *Appl. Phys. Lett.*, vol. 49, no. 1, pp. 13–15, 1986.

[142] D. Yin, J. P. Barber, A. R. Hawkins, and H. Schmidt, “Waveguide loss optimization in hollow-core ARROW waveguides,” *Opt. Express*, vol. 13, no. 23, p. 9331, 2005.

[143] N. . M. Litchinitser, A. K. Abeeluck, C. Headley, and B. J. Eggleton, “Antiresonant reflecting photonic crystal optical waveguides,” *Opt. Lett.*, vol. 27, no. 18, pp. 1592–1594, 2002.

[144] P. Rugeland, C. Sterner, and W. Margulis, “Visible light guidance in silica capillaries by antiresonant reflection,” *Opt. Express*, vol. 21, no. 24, p. 29217, 2013.

[145] J.-Y. Lu, C.-P. Yu, H.-C. Chang, H.-W. Chen, Y.-T. Li, C.-L. Pan, and C.-K. Sun, “Terahertz air-core microstructure fiber,” *Appl. Phys. Lett.*, vol. 92, no. 6, p. 064105, 2008.

[146] C. Lai, Y. Hsueh, H. Chen, Y. Huang, H. Chang, and C. Sun, “Low-index terahertz pipe waveguides,” *Opt. Lett.*, vol. 34, no. 21, pp. 3457–3459, 2009.

[147] D. Chen and H. Chen, “A novel terahertz waveguide: Polymer tube,” *Opt. Express*, vol. 18, no. 4, pp. 3762–3767, 2010.

[148] E. Nguema, D. Férachou, G. Humbert, J. Auguste, and J. Blondy, “Broadband terahertz transmission within the air channel of thin-wall pipe,” *Opt. Lett.*, vol. 36, no. 10, pp. 1782–1784, 2011.

[149] C. Lai, B. You, J. Lu, T. Liu, J. Peng, C. Sun, and H. Chang, “Modal characteristics of antiresonant reflecting pipe waveguides for terahertz waveguiding,” *Opt. Express*, vol. 18, no. 1, p. 309, 2010.

[150] B. You, J.-Y. Lu, C.-P. Yu, T.-A. Liu, and J.-L. Peng, “Terahertz refractive index sensors using dielectric pipe waveguides,” *Opt. Express*, vol. 20, no. 6, p. 5858, 2012.

[151] H.-Z. Chen, J.-Y. Lu, and B. You, “Terahertz endoscope based on anti-resonant reflecting hollow core waveguides,” *Opt. Soc. Am.*, vol. 2, no. c, 2011.

[152] B. You and J.-Y. Lu, “Remote and in situ sensing products in chemical reaction using a flexible terahertz pipe waveguide,” *Opt. Express*, vol. 24, no. 16, p. 18013, 2016.

[153] Y. Zhong, G. Xie, F. Mao, J. Ding, F. Yue, S. Chen, X. Lu, C. Jing, and J. Chu, “Thin-wall cyclic olefin copolymer tube waveguide for broadband terahertz transmission,” *Opt. Mater. (Amst).*, vol. 98, no. August, p. 109490, 2019.

[154] J. B. Sleiman, B. Bousquet, N. Palka, and P. Mounaix, “Quantitative Analysis of Hexahydro-1,3,5-trinitro-1,3,5, Triazine/Pentaerythritol Tetranitrate (RDX–PETN) Mixtures by Terahertz Time Domain Spectroscopy,” *Appl. Spectrosc.*, vol. 69, no. 12, pp. 1464–1471, Dec. 2015.

[155] J. B. Perraud, A. F. Obaton, J. Bou-Sleiman, B. Recur, H. Balacey, F. Darracq, J. P. Guillet, and P. Mounaix, “Terahertz imaging and tomography as efficient instruments for testing polymer additive manufacturing objects,” *Appl. Opt.*, vol. 55, no. 13, p. 3462, 2016.

[156] J.-B. Perraud, J.-P. Guillet, O. Redon, M. Hamdi, F. Simoens, and P. Mounaix, “Shape-from-focus for real-time terahertz 3D imaging,” *Opt. Lett.*, vol. 44, no. 3, p. 483, 2019.

[157] G. Ducournau, P. Szriftgiser, F. Pavanello, E. Peytavit, M. Zaknoune, D. Bacquet, A. Beck, T. Akalin, J.-F. Lampin, and J.-F. Lampin, "THz Communications using Photonics and Electronic Devices: the Race to Data-Rate," *J. Infrared, Millimeter, Terahertz Waves*, vol. 36, no. 2, pp. 198–220, 2015.

[158] G. Ducournau, F. Pavanello, A. Beck, L. Tohme, S. Blin, P. Nouvel, E. Peytavit, M. Zaknoune, P. Szriftgiser, and J. F. Lampin, "High-definition television transmission at 600 GHz combining THz photonics hotspot and high-sensitivity heterodyne receiver," *Electron. Lett.*, vol. 50, no. 5, pp. 413–415, 2014.

[159] G. Ducournau, P. Szriftgiser, A. Beck, D. Bacquet, F. Pavanello, E. Peytavit, M. Zaknoune, T. Akalin, and J. F. Lampin, "Ultrawide-bandwidth single-channel 0.4-THz wireless link combining broadband quasi-optic photomixer and coherent detection," *IEEE Trans. Terahertz Sci. Technol.*, vol. 4, no. 3, pp. 328–337, 2014.

[160] H. J. Song and T. Nagatsuma, "Present and future of terahertz communications," *IEEE Trans. Terahertz Sci. Technol.*, vol. 1, no. 1, pp. 256–263, 2011.

[161] N. M. Burford, M. O. El-Shenawee, C. B. O. Neal, and K. J. Olejniczak, "Terahertz Imaging for Nondestructive Evaluation of Packaged Power Electronic Devices," *Int. J. Emerg. Technol. Adv. Eng.*, vol. 4, no. 1, pp. 395–401, 2014.

[162] W. G. Yeo, N. K. Nahar, R. Lee, and J. L. Volakis, "New frontiers for commercial applications of terahertz," *Natl. Aerosp. Electron. Conf. Proc. IEEE*, pp. 5–8, 2011.

[163] G. Ok, H. J. Shin, M. C. Lim, and S. W. Choi, "Large-scan-area sub-terahertz imaging system for nondestructive food quality inspection," *Food Control*, vol. 96, pp. 383–389, 2019.

[164] A. Ren, A. Zahid, D. Fan, X. Yang, M. A. Imran, A. Alomainy, and Q. H. Abbasi, "State-of-the-art in terahertz sensing for food and water security – A comprehensive review," *Trends Food Sci. Technol.*, vol. 85, pp. 241–251, Mar. 2019.

[165] K. Krügener, E.-M. Stübling, R. Jachim, B. Kietz, M. Koch, and W. Viöl, "THz tomography for detecting damages on wood caused by insects," *Appl. Opt.*, vol. 58, no. 22, p. 6063, Aug. 2019.

[166] Q. Cassar, A. Chopard, F. Fauquet, J.-P. Guillet, M. Pan, J.-B. Perraud, and P. Mounaix, "Iterative Tree Algorithm to Evaluate Terahertz Signal Contribution of Specific Optical Paths within Multi-Layered Materials," *IEEE Trans. Terahertz Sci. Technol.*, 2019.

[167] M. Picot, H. Ballacey, J. P. Guillet, Q. Cassar, and P. Mounaix, "Terahertz Paint Thickness Measurements : from lab to automotive and aeronautics industry," *Apndt2017*, pp. 1–8, 2017.

[168] "TeraView | TeraCota – Terahertz Coating thickness analysis." [Online]. Available: https://teraview.com/teracota/.

[169] E. M. Kleist, C. L. Koch Dandolo, J. P. Guillet, P. Mounaix, and T. M. Korter, "Terahertz Spectroscopy and Quantum Mechanical Simulations of Crystalline Copper-Containing Historical Pigments," *J. Phys. Chem. A*, vol. 123, no. 6, pp. 1225–1232, 2019.

[170] C. L. K. Dandolo, J.-P. Guillet, X. Ma, F. Fauquet, M. Roux, and P. Mounaix, "Terahertz frequency modulated continuous wave imaging advanced data processing for art painting analysis," *Opt. Express*, vol. 26, no. 5, p. 5358, 2018.

[171] G. E. Tsydynzhapov, P. A. Gusikhin, V. M. Muravev, I. V. Andreev, and I. V. Kukushkin, "New

terahertz security body scanner," in *2018 43rd International Conference on Infrared, Millimeter, and Terahertz Waves (IRMMW-THz)*, 2018, pp. 1–1.

[172] K. M.C, T. P.F., C. B.E., C. A.J, F. A.J., and T. W.R., "Security applications of terahertz technology," in *Terahertz for Military and Security Applications*, 2003, vol. 5070, pp. 6–8.

[173] D. Markl, M. T. Ruggiero, and J. A. Zeitler, "Pharmaceutical applications of terahertz spectroscopy and imaging," *Eur. Pharm. Rev.*, vol. 21, no. 4, pp. 45–50, 2016.

[174] A. Al-Ibadi, J. Bou Sleiman, Q. Cassar, G. Macgrogan, H. Balacey, T. Zimmer, P. Mounaix, and J. P. Guillet, "Terahertz biomedical imaging: From multivariate analysis and detection to material parameter extraction," *Prog. Electromagn. Res. Symp.*, vol. Part F1343, pp. 2756–2762, 2017.

[175] E. Pickwell and V. P. Wallace, "Biomedical applications of terahertz technology," *J. Phys. D. Appl. Phys.*, vol. 39, no. 17, 2006.

[176] Q. Sun, R. I. Stantchev, J. Wang, E. P. J. Parrott, A. Cottenden, T. W. Chiu, A. T. Ahuja, and E. Pickwell-MacPherson, "In vivo estimation of water diffusivity in occluded human skin using terahertz reflection spectroscopy," *J. Biophotonics*, vol. 12, no. 2, pp. 1–10, 2018.

[177] Q. Cassar, A. Al-Ibadi, L. Mavarani, P. Hillger, J. Grzyb, G. MacGrogan, T. Zimmer, U. R. Pfeiffer, J.-P. Guillet, and P. Mounaix, "Pilot study of freshly excised breast tissue response in the 300 – 600 GHz range," *Biomed. Opt. Express*, vol. 9, no. 7, p. 2930, Jul. 2018.

[178] P. Doradla, C. Joseph, and R. H. Giles, "Terahertz endoscopic imaging for colorectal cancer detection: Current status and future perspectives," *Word J. Gastrointest. Endosc.*, vol. 9, no. 8, pp. 346–358, 2017.

[179] Y. Bin Ji, C. H. Park, H. Kim, S.-H. Kim, G. M. Lee, S. K. Noh, T.-I. Jeon, J.-H. Son, Y.-M. Huh, S. Haam, S. J. Oh, S. K. Lee, and J.-S. Suh, "Feasibility of terahertz reflectometry for discrimination of human early gastric cancers," *Biomed. Opt. Express*, vol. 6, no. 4, p. 1398, 2015.

[180] U. R. Pfeiffer, P. Hillger, R. Jain, J. Grzyb, T. Bucher, Q. Cassar, G. MacGrogan, J. Guillet, P. Mounaix, and T. Zimmer, "Ex Vivo Breast Tumor Identification: Advances Toward a Silicon-Based Terahertz Near-Field Imaging Sensor," *IEEE Microw. Mag.*, vol. 20, no. 9, pp. 32–46, 2019.

[181] D. L. I. Peytavit E, Lampin JF, Akalin T, "Integrated terahertz TEM horn antenna," *Electron. Lett.*, vol. 43, no. 2, pp. 73–75, 2007.

[182] R. O. S. Mith, A. F. J. Ooshesh, J. I. Z. Hang, and T. H. D. Arcie, "THz-TDS using a photoconductive free-space linear tapered slot antenna transmitter," vol. 25, no. 9, pp. 23466–23471, 2017.

[183] M. Nagel, C. Matheisen, S. Sawallich, H. Kurz, M. Nagel, C. Matheisen, S. Sawallich, and H. Kurz, "Photoconductive microprobe enabled on-chip and wafer- scale Terahertz sensing applications," *Adv. Photonics*, 2015.

[184] H. Yagi and S. Uda, "Projector of the Sharpest Beam of Electric Waves," in *Proceedings of the Imperial Academy*, 1926, vol. 2, no. 2, pp. 49–52.

[185] K. Han, Y. Park, H. Choo, and I. Park, "Broadband CPS-fed Yagi-Uda antenna," *Electron. Lett.*, vol. 45, no. 24, p. 1207, 2009.

[186] P. L. Chi and Y. C. Chou, "Planar Quasi-Yagi Antenna for Future 5G and WiGig Applications,"

2018 IEEE Antennas Propag. Soc. Int. Symp. Usn. Natl. Radio Sci. Meet. APSURSI 2018 - Proc., pp. 1213–1214, 2018.

[187] F. Pavanello, G. Ducournau, E. Peytavit, S. Lepilliet, and J. F. Lampin, "High-gain Yagi-Uda antenna on cyclic olefin copolymer substrate for 300-GHz applications," *IEEE Antennas Wirel. Propag. Lett.*, vol. 13, pp. 939–942, 2014.

[188] I. S. Maksymov, I. Staude, A. E. Miroshnichenko, and Y. S. Kivshar, "Optical yagi-uda nanoantennas," *Nanophotonics*, vol. 1, no. 1, pp. 65–81, 2012.

[189] N. Kaneda, W. R. Deal, Y. Qian, R. Waterhouse, and T. Itoh, "A Broad-Band Planar Quasi-Yagi Antenna," *IEEE Trans. Antennas Propag.*, vol. 50, no. 8, pp. 1158–1160, 2010.

[190] N. Kaneda, Y. Qian, and T. Itoh, "A broadband CPW-to-waveguide transition using quasi-Yagi antenna," in *IEEE MTT-S Digest*, 2002, pp. 617–620.

[191] H. K. Kan, R. B. Waterhouse, A. M. Abbosh, and M. E. Bialkowski, "Simple broadband planar CPW-fed quasi-Yagi antenna," *IEEE Antennas Wirel. Propag. Lett.*, vol. 6, pp. 18–20, 2007.

[192] T. Weiland, "A discretization model for the solution of Maxwell's equations for six-component fields," *Arch. Elektron. und Uebertragungstechnik*, vol. 31, pp. 116–120, 1977.

[193] C. A. Balanis, *Antenna theory : analysis and design*. John wiley \& sons, 2016.

[194] F. Friederich, K. May, B. Baccouche, C. Matheis, M. Bauer, J. Jonuscheit, M. Moor, D. Denman, J. Bramble, and N. Savage, "Terahertz Radome Inspection," *Photonics*, vol. 5, no. 1, p. 1, 2018.

[195] A. T. Local, O. Source, A. Maestrini, J. Ward, J. Gill, H. Javadi, E. Schlecht, G. Chattopadhyay, F. Maiwald, N. R. Erickson, and I. Mehdi, "A 1.7–1.9 THz Local Oscillator Source," *Ieee Microw. Wirel. Components Lett.*, vol. 14, no. 6, pp. 253–255, 2004.

[196] M. Abbasi, S. E. Gunnarsson, N. Wadefalk, R. Kozhuharov, J. Svedin, S. Cherednichenko, I. Angelov, I. Kallfass, A. Leuther, and H. Zirath, "Single-chip 220-GHz active heterodyne receiver and transmitter MMICs with on-chip integrated antenna," *IEEE Trans. Microw. Theory Tech.*, vol. 59, no. 2, pp. 466–478, 2011.

[197] K. B. Cooper, R. J. Dengler, N. Llombart, T. Bryllert, G. Chattopadhyay, E. Schlecht, J. Gill, C. Lee, A. Skalare, I. Mehdi, and P. H. Siegel, "Penetrating 3-D imaging at 4- and 25-m range using a submillimeter-wave radar," *IEEE Trans. Microw. Theory Tech.*, vol. 56, no. 12, pp. 2771–2778, 2008.

[198] J. Hasch, E. Topak, R. Schnabel, T. Zwick, R. Weigel, and C. Waldschmidt, "Millimeter-wave technology for automotive radar sensors in the 77 GHz frequency band," *IEEE Trans. Microw. Theory Tech.*, vol. 60, no. 3 PART 2, pp. 845–860, 2012.

[199] K. Schmalz, W. Winkler, J. Borngdiber, W. Debski, B. Heinemann, and J. C. Scheytt, "122 GHz ISM-band transceiver concept and silicon ICs for low-cost receiver in SiGe BiCMOS," *IEEE MTT-S Int. Microw. Symp. Dig.*, pp. 1332–1335, 2010.

[200] M. Pauli, B. Göttel, S. Scherr, A. Bhutani, S. Ayhan, W. Winkler, and T. Zwick, "Miniaturized Millimeter-Wave Radar Sensor for High-Accuracy Applications," *IEEE Trans. Microw. Theory Tech.*, vol. 65, no. 5, pp. 1707–1715, 2017.

[201] K. Schmalz, J. Borngräber, B. Heinemann, H. Rücker, and J. C. Scheytt, "A 245 GHz transmitter in

SiGe technology," *Dig. Pap. - IEEE Radio Freq. Integr. Circuits Symp.*, pp. 195–198, 2012.

[202] C. H. W. Ei, R. J. O. W. Eiblen, and C. U. R. M. Enyuk, "Negative curvature fibers," vol. 9, no. 3, pp. 504–561, 2017.

[203] L. Vincetti, "Numerical analysis of plastic hollow core microstructured fiber for Terahertz applications," *Opt. Fiber Technol.*, vol. 15, no. 4, pp. 398–401, 2009.

[204] L. Vincetti, "Single-mode propagation in triangular tube lattice hollow-core terahertz fibers," *Opt. Commun.*, vol. 283, no. 6, pp. 979–984, 2010.

[205] L. Vincetti and V. Setti, "Elliptical hollow core tube lattice fibers for terahertz applications," *Opt. Fiber Technol.*, vol. 19, no. 1, pp. 31–34, 2013.

[206] M. M. Nazarov, A. V. Shilov, K. A. Bzheumikhov, Z. C. Margushev, V. I. Sokolov, A. B. Sotsky, and A. P. Shkurinov, "Eight-Capillary Cladding THz Waveguide with Low Propagation Losses and Dispersion," *IEEE Trans. Terahertz Sci. Technol.*, vol. 8, no. 2, pp. 183–191, 2018.

[207] A. L. S. Cruz, V. A. Serrão, C. L. Barbosa, and M. A. R. Franco, "3D Printed Hollow Core Fiber with Negative Curvature for Terahertz Applications," *J. Microwaves, Optoelectron. Electromagn. Appl.*, vol. 14, no. July, pp. 45–53, 2015.

[208] L. D. van Putten, J. Gorecki, E. Numkam Fokoua, V. Apostolopoulos, and F. Poletti, "3D-printed polymer antiresonant waveguides for short-reach terahertz applications," *Appl. Opt.*, vol. 57, no. 14, pp. 3953–3958, 2018.

[209] G. K. M. Hasanuzzaman, S. Iezekiel, C. Markos, and M. S. Habib, "Hollow-core fiber with nested anti-resonant tubes for low-loss THz guidance," *Opt. Commun.*, vol. 426, no. ii, pp. 477–482, 2018.

[210] J. Sultana, S. Islam, C. M. B. Cordeiro, and A. Dinovitser, "Terahertz Hollow Core Antiresonant Fiber with Metamaterial Cladding," *Fibers*, vol. 8(2), no. 14, pp. 1–11, 2020.

[211] W. Lu, S. Lou, X. Wang, Y. Shen, and X. Sheng, "Demonstration of low-loss flexible fiber with Zeonex tube- lattice cladding for Terahertz transmission," in *2015 Optical Fiber Communications Conference and Exhibition (OFC)*, 2015, pp. 6–8.

[212] B. Bhushan and M. Caspers, "An overview of additive manufacturing (3D printing) for microfabrication," *Microsyst. Technol.*, vol. 23, no. 4, pp. 1117–1124, 2017.

[213] B. Zhang and H. Zirath, "Metallic 3-D Printed Rectangular Waveguides for Millimeter-Wave Applications," *IEEE Trans. Components, Packag. Manuf. Technol.*, vol. 6, no. 5, pp. 796–804, 2016.

[214] I. O. Saracho-Pantoja, J. R. Montejo-Garai, J. A. Ruiz-Cruz, and J. M. Rebollar, "Additive Manufacturing of 3D Printed Microwave Passive Components," *Emerg. Microw. Technol. Ind. Agric. Med. Food Process.*, 2018.

[215] D. Jahn, M. Weidenbach, J. Lehr, L. Becker, F. Beltrán-Mejía, S. F. Busch, J. C. Balzer, and M. Koch, "3D Printed Terahertz Focusing Grating Couplers," *J. Infrared, Millimeter, Terahertz Waves*, vol. 38, no. 6, pp. 708–716, 2017.

[216] S. F. Busch, M. Weidenbach, J. C. Balzer, and M. Koch, "THz Optics 3D Printed with TOPAS," *J. Infrared, Millimeter, Terahertz Waves*, vol. 37, no. 4, pp. 303–307, 2016.

[217] M. Weidenbach, D. Jahn, A. Rehn, S. F. Busch, F. Beltrán-Mejía, J. C. Balzer, and M. Koch, "3D

printed dielectric rectangular waveguides, splitters and couplers for 120 GHz," *Opt. Express*, vol. 24, no. 25, p. 28968, 2016.

[218] Z. Wu, W. Ng, M. E. Gehm, and H. Xin, "Terahertz electromagnetic crystal waveguide fabricated by polymer jetting rapid prototyping," *Opt. Express*, vol. 19, no. 5, pp. 3962–3972, 2011.

[219] S. Korobogatiy, "3D printed hollow core terahertz Bragg waveguides with defect layers for surface sensing applications," vol. 25, no. 4, pp. 309–322, 2017.

[220] J. Yang, J. Zhao, C. Gong, H. Tian, L. Sun, P. Chen, L. Lin, and W. Liu, "3D printed low-loss THz waveguide based on Kagome photonic crystal structure," *Opt. Express*, vol. 24, no. 20, p. 22454, 2016.

[221] S. Yang, X. Sheng, G. Zhao, Y. Wang, and Y. Yu, "Novel Pentagram THz Hollow Core Anti-resonant Fiber Using a 3D Printer," *J. Infrared, Millimeter, Terahertz Waves*, vol. 40, no. 7, pp. 720–730, 2019.

[222] A. L. S. Cruz, M. A. R. Franco, C. M. B. Cordeiro, G. S. Rodrigues, H. Osório, and L. E. Silva, "Exploring THz Hollow-Core Fiber Designs Manufactured by 3D Printing," vol. 00, no. c, pp. 2–6, 2017.

[223] A. Cruz, C. Cordeiro, and M. Franco, "3D Printed Hollow-Core Terahertz Fibers," *Fibers*, vol. 6, no. 3, p. 43, 2018.

[224] M. E. Layani-Tzadka, D. Krotkov, E. Tirosh, G. Markovich, and S. Fleischer, "Contact-free conductivity probing of metal nanowire films using THz reflection spectroscopy," *Nanotechnology*, vol. 30, no. 21, 2019.

[225] K. Wang and D. M. Mittleman, "Metal wires for terahertz wave guiding," *Nature*, vol. 432, no. 7015, pp. 376–379, 2004.

[226] Y. Cai, Z. Wang, R. Dias, and D. Goyal, "Electro Optical Terahertz Pulse Reflectometry - An innovative fault isolation tool," in *Proceedings - Electronic Components and Technology Conference*, 2010, pp. 1309–1315.

[227] K. Humphreys, J. P. Loughran, M. Gradziel, W. Lanigan, T. Ward, J. A. Murphy, and C. O'Sullivan, "Medical applications of terahertz imaging: a review of current technology and potential applications in biomedical engineering," *Conf Proc IEEE Eng Med Biol Soc*, vol. 2, pp. 1302–1305, 2004.

[228] M. Nagel, M. Först, and H. Kurz, "THz biosensing devices: Fundamentals and technology," *J. Phys. Condens. Matter*, vol. 18, no. 18, 2006.

[229] P. Doradla, K. Alavi, C. Joseph, and R. Giles, "Single-channel prototype terahertz endoscopic system," *J. Biomed. Opt.*, vol. 19, no. 8, 2014.

[230] P. Doradla, K. Alavi, C. S. Joseph, and R. H. Giles, "Flexible waveguide enabled single-channel terahertz endoscopic system," *Terahertz, RF, Millimeter, Submillimeter-Wave Technol. Appl. VIII*, vol. 9362, p. 93620D, 2015.

[231] H. Balacey, B. Recur, J.-B. Perraud, J. B. Sleiman, and P. Mounaix, "Advanced Processing Sequence for 3-D THz Imaging," *IEEE Trans. Terahertz Sci. Technol.*, vol. 6, no. 2, pp. 191–198, 2016.

[232] J. B. Perraud, J. B. Sleiman, B. Recur, H. Balacey, F. Simoens, J. P. Guillet, and P. Mounaix, "Liquid index matching for 2D and 3D terahertz imaging," *Appl. Opt.*, vol. 55, no. 32, pp. 9185–9192, Nov. 2016.

[233] W. R. Deal, K. Leong, V. Radisic, S. Sarkozy, B. Gorospe, J. Lee, P. H. Liu, W. Yoshida, J. Zhou, M. Lange, R. Lai, and X. B. Mei, "Low noise amplification at 0.67 THz using 30 nm InP HEMTs," *IEEE Microw. Wirel. Components Lett.*, vol. 21, no. 7, pp. 368–370, 2011.

[234] V. Radisic, K. M. K. H. Leong, X. Mei, S. Sarkozy, W. Yoshida, and W. R. Deal, "Power amplification at 0.65 THz using InP HEMTs," *IEEE Trans. Microw. Theory Tech.*, vol. 60, no. 3 PART 2, pp. 724–729, 2012.

[235] W. Deal, S. Member, X. B. Mei, K. M. K. H. Leong, V. Radisic, S. Member, S. Sarkozy, and R. Lai, "THz Monolithic Integrated Circuits Using InP High Electron Mobility Transistors," *IEEE Trans. Terahertz Sci. Technol.*, vol. 1, no. 1, pp. 25–32, 2011.

[236] W. R. Deal, K. Leong, A. Zamora, V. Radisic, and X. B. Mei, "Recent progress in scaling InP HEMT TMIC technology to 850 GHz," in *IEEE MTT-S International Microwave Symposium Digest*, 2014, pp. 1–3.

[237] M. Urteaga, M. Seo, J. Hacker, Z. Griffith, a. Young, R. Pierson, P. Rowell, a. Skalare, V. Jain, E. Lobisser, and M. J. W. Rodwell, "InP HBTs for THz frequency integrated circuits," *IPRM 2011 - 23rd Int. Conf. Indium Phosphide Relat. Mater.*, pp. 1–4, 2011.

[238] M. Urteaga, A. Carter, Z. Griffith, R. Pierson, A. Arias, P. Rowell, J. Hacker, and B. Brar, "THz Bandwidth InP HBT Technologies and Heterogeneous Integration with Si CMOS," *2016 IEEE Bipolar/BiCMOS Circuits Technol. Meet.*, pp. 35–41, 2016.

[239] S. Kang, D. Kim, M. Urteaga, and M. Seo, "State-of-the-art THz integrated circuits in InP HBT technologies," in *2017 IEEE International Symposium on Radio-Frequency Integration Technology, RFIT 2017*, 2017, pp. 25–27.

[240] T. Kraemer, I. Ostermay, T. Jensen, T. K. Johansen, F. J. Schmueckle, A. Thies, V. Krozer, W. Heinrich, O. Krueger, G. Traenkle, M. Lisker, A. Trusch, P. Kulse, and B. Tillack, "InP-DHBT-on-BiCMOS technology with fTfmax of 400/350 GHz for heterogeneous integrated millimeter-wave sources," *IEEE Trans. Electron Devices*, vol. 60, no. 7, pp. 2209–2216, 2013.

[241] L. Samoska, A. Fung, D. Pukala, P. Kangaslahti, R. Lai, S. Sarkozy, X. B. Mei, and G. Boll, "On-wafer measurements of S-MMIC amplifiers from 400-500 GHz," *IEEE MTT-S Int. Microw. Symp. Dig.*, pp. 1–4, 2011.

[242] A. Fung, L. Samoska, S. Member, D. Pukala, D. Dawson, P. Kangaslahti, M. Varonen, T. Gaier, C. Lawrence, G. Boll, R. Lai, and X. . B. Mei, "On-Wafer S-Parameter Measurements in the," *IEEE Trans. Terahertz Sci. Technol.*, vol. 2, no. 2, pp. 186–192, 2012.

[243] A. Fung, L. Samoska, M. Varonen, P. Kangaslahti, S. Sarkozy, and R. Lai, "A practical implementation of millimeter and submillimeter wave length on-wafer S-parameter calibration," *2014 39th Int. Conf. Infrared, Millimeter, Terahertz waves*, pp. 1–2.

[244] A. Rumiantsev, "RF Probe Technology ©," *IEEE Microwave Magazine*, no. December, pp. 46–58, 2013.

[245] M. F. Bauwens, N. Alijabbari, A. W. Lichtenberger, N. S. Barker, and R. M. Weikle, "A 1.1 THz

micromachined on-wafer probe," *IEEE MTT-S Int. Microw. Symp. Dig.*, pp. 6–9, 2014.

[246] E. M. Godshalk, "A V-Band Wafer Probe Using Ridge-Trough Waveguide," *IEEE Trans. Microw. Theory Tech.*, vol. 39, no. 12, pp. 2218–2228, 1991.

[247] E. M. Godshalk, J. Burr, and J. Williams, "An Air Coplanar Wafer Probe," pp. 70–75, 2007.

[248] N. Scott Barker, M. Bauwens, A. L. Erger, and R. Weikle, "Silicon-on-insulator substrates as a micromachining platform for advanced terahertz circuits," in *Proceedings of the IEEE*, 2017, vol. 105, no. 6, pp. 1105–1120.

[249] M. F. Bauwens, S. Member, L. Chen, C. Zhang, S. Member, A. I. Arsenovic, N. Alijabbari, A. W. Lichtenberger, N. S. Barker, R. M. W. Ii, and S. Member, "Characterization of Micromachined On-Wafer Probes for the 600-900 GHz Waveguide Band," *IEEE Trans. Terahertz Sci. Technol.*, vol. 4, no. 4, pp. 527–529, 2014.

[250] R. Campbell, M. Andrews, L. Samoska, and A. Fung, "Membrane Tip Probes for On-Wafer Measurements in the 220 to 325 GHz Band," in *18th International Symposium on space Terahertz Technology*, 2007, pp. 141–149.

[251] R. L. Campbell, M. Andrews, T. Lesher, and C. Wai, "220 GHz wafer probe membrane tips and waveguide-to-coax transitions," in *35th European Microwave Conference 2005 - Conference Proceedings*, 2005, vol. 2, pp. 1003–1006.

[252] C. Zhang, M. F. Bauwens, L. Xie, M. E. Cyberey, N. S. Barker, R. M. Weikle, and A. W. Lichtenberger, "A Micromachined Differential Probe for On-Wafer Measurements in the WM-1295 (140 — 220 GHz) Band," vol. 1295, no. c, pp. 1088–1090, 2017.

[253] Q. Yu, M. Bauwens, C. Zhang, A. W. Lichtenberger, R. M. W. Ii, and N. S. Barker, "Integrated Strain Sensor for Micromachined Terahertz On-Wafer Probe," in *2013 IEEE MTT-S International Microwave Symposium Digest (MTT)*, 2013, pp. 1–4.

[254] M. F. Bauwens, "Micromachined probes for on-wafer characterization of terahertz and submillimeter-wave components," in *2011 International Conference on Infrared, Millimeter, and Terahertz Waves*, pp. 1–2.

[255] R. M. Weikle, N. S. Barker, A. W. Lichtenberger, and M. F. Bauwens, "Micromachined Probes for On-Wafer Measurement of Millimeter- and Submillimeter-Wave Devices and Components," *2013 IEEE Glob. Conf. Signal Inf. Process.*, pp. 707–710, 2013.

[256] L. Chen, C. Zhang, T. J. Reck, C. Groppil, A. Arsenovic, A. Lichtenberger, R. M. Weikle, and N. S. Barker, "Terahertz Micromachined On-wafer Probes : Repeatability and Robustness," in *2011 IEEE MTT-S International Microwave Symposium*, pp. 1–4.

[257] K. Daffé, G. Dambrine, F. Von Kleist-retzow, and K. Haddadi, "RF Wafer Probing with Improved Contact Repeatability Using Nanometer Positioning," 2016, pp. 2–5.

[258] Q. Yu, M. Bauwens, A. W. Lichtenberger, R. M. Weikle, and N. S. Barker, "Measurement Uncertainty Characterization of Terahertz Large Wafer Probing," in *2014 IEEE MTT-S International Microwave Symposium (IMS2014)*, 2014, pp. 1–4.

[259] Q. Yu, M. F. Bauwens, C. Zhang, A. W. Lichtenberger, R. M. Weikle, and N. S. Barker, "Improved micromachined terahertz on-wafer probe using integrated strain sensor," *IEEE Trans. Microw. Theory Tech.*, vol. 61, no. 12, pp. 4613–4620, 2013.

[260] J. A. Byford and P. Chahal, "Broad-band dielectric probes for on-wafer characterization of terahertz devices," *Proc. - Electron. Components Technol. Conf.*, vol. 2018–May, pp. 2367–2373, 2018.

[261] C. Caglayan and K. Sertel, "Experimental Analysis of Repeatability and Calibration Residuals in On-Wafer Non-Contact Probing," *IEEE Trans. Microw. Theory Tech.*, vol. 65, no. 6, pp. 2185–2191, 2017.

[262] C. Caglayan and K. Sertel, "Noncontact On-Wafer Characterization of Submillimeter-Wave Devices and Integrated Circuits," *IEEE Trans. Microw. Theory Tech.*, vol. 64, no. 2, pp. 3911–3917, 2016.

[263] C. Caglayan, G. C. Trichopoulos, and K. Sertel, "Non-Contact Probes for On-Wafer Characterization of Sub-millimeter Wave Devices and Integrated," *IEEE Trans. Terahertz Sci. Technol.*, pp. 1–10, 2013.

[264] K. Sertel, "Automated Performance of On-wafer Calibration and Characterization Using Non-contact Probes," in *2019 92nd ARFTG Microwave Measurement Conference (ARFTG)*, 2019, pp. 1–4.

[265] Y. Cui and G. C. Trichopoulos, "Toward a terahertz quasi-optical vector network analyzer," in *2017 IEEE Antennas and Propagation Society International Symposium, Proceedings*, 2017, pp. 1511–1512.

[266] Y. Cui and G. C. Trichopoulos, "A Quasi-Optical Testbed for Wideband THz," *IEEE Trans. Terahertz Sci. Technol.*, vol. 9, no. 2, pp. 126–135, 2019.

[267] J. H. Lau, "Overview and outlook of through-silicon via (TSV) and 3D integrations," *Microelectron. Int.*, vol. 28, no. 2, pp. 8–22, 2011.

[268] F. Altmann and M. Petzold, "Innovative Failure Analysis Techniques for 3-D Packaging Developments," *IEEE Des. Test*, vol. 33, no. 3, pp. 46–55, 2016.

[269] Y. Li, P. K. M. Srinath, and D. Goyal, "A Review of Failure Analysis Methods for Advanced 3D Microelectronic Packages," *J. Electron. Mater.*, vol. 45, no. 1, pp. 116–124, 2015.

[270] F. Altmann, S. Brand, and M. Petzold, "Failure analysis techniques for 3d packages," *Proc. Int. Symp. Phys. Fail. Anal. Integr. Circuits, IPFA*, vol. 2018–July, pp. 1–8, 2018.

[271] O. Breitenstein, J. P. Rakotoniaina, F. Altmann, T. Riediger, and M. Gradhand, "New developments in IR lock-in thermography," *Proc. 30th ISTFA*, pp. 595–599, 2004.

[272] M. Xie, T. Begala, K. Kijkanjanapaiboon, and D. Goyal, "Innovations in Fault Isolation Methods for 3D Packages with 10X Improvement in Accuracy," *2016 IEEE 66th Electron. Components Technol. Conf.*, vol. 2, pp. 755–765, 2016.

[273] Q. Shi, Y. Chen, and P. Lai, "Advanced Fault Isolation Techniques for 3D Packaging," in *2016 IEEE 23rd International Symposium on the Physical and Failure Analysis ofIntegrated Circuits (IPFA)*, 2016, pp. 212–215.

[274] J. Gaudestad, V. Talanov, and M. Marchetti, "Opens localization on silicon level in a Chip Scale Package using space domain reflectometry," *Microelectron. Reliab.*, vol. 53, no. 9–11, pp. 1418–1421, 2013.

[275] W. Qiu, S. Tan, M. Tay, J. Gaudestad, and M. W. VV Talanov, "Non destructive open Fault isolation

in Flip Chip devices with SDR," pp. 332–336, 2013.

[276] J. Gaudestad and D. Vallett, "Magnetic Field Imaging for Non-Destructive 3D Package Fault Isolation," *Int. Symp. Microelectron.*, vol. 2014, no. 1, pp. 000635–000640, 2015.

[277] D. Abessolo-Bidzo, P. Poirier, P. Descamps, and B. Domengès, "Isolating failing sites in IC packages using time domain reflectometry: Case studies," *Microelectron. Reliab.*, vol. 45, no. 9–11, pp. 1639–1644, 2005.

[278] L. Cao, L. Tran, A. R. Prabhu, and M. Y. Tay, "Flip-chip package soft failure analysis and case studies using time domain reflectometry," vol. 1, no. 512, pp. 1–4, 2010.

[279] Teravie, "TeraView | Electro Optical Terahertz Pulse Reflectometry." [Online]. Available: https://teraview.com/eotpr/#tab%7C0. [Accessed: 23-Sep-2019].

[280] Teraview, "Introduction to EOTPR (Electro Optical Terahertz Pulse Reflectometry)." 2017.

Introduction in French

Situés entre deux domaines bien développés, à savoir les micro-ondes et l'infrarouge, les radiations térahertz ont attiré l'attention des observateurs pour leurs propriétés a priori séduisantes, parmi lesquelles on peut classer leur nature non ionisante, leur capacité à pénétrer à travers des matériaux optiquement opaques, ou encore leur sensibilité aux discontinuités diélectriques. Le développement des techniques spectroscopiques dans le régime du térahertz s'est progressivement étendu à l'imagerie, ce qui permet aujourd'hui aux domaines académique et industriel de réaliser un large panel de tests non destructifs allant du contrôle qualité à l'inspection de sécurité en passant par d'autres domaines comme la science du patrimoine.

Il est clair que les configurations des systèmes jouent un rôle important dans les utilisations pratiques, ce qui a un impact sur le champ d'application de la technologie térahertz. D'un point de vue pratique, un système de mesure du térahertz compact en mode réflexion plutôt qu'en géométrie de transmission est plus avantageux. Plus précisément, par rapport à la configuration de transmission qui impose des restrictions sur la forme et les propriétés d'un objet testé, une géométrie de réflexion est plus adaptée à une grande variété d'échantillons. Ceci étant dit, bien qu'elle soit plus susceptible d'être utilisée sur une grande variété d'objets, la complexité et la compréhension de la réponse qui accompagnent une configuration en mode réflexion est par conséquent plus élevée. En fait, les géométries de réflexion nécessitent généralement la mise en œuvre d'éléments quasi-optiques supplémentaires tels que des lentilles ou des séparateurs de faisceau. En plus d'induire des travaux supplémentaires pour obtenir un alignement correct le long du chemin de propagation, ces ajouts entravent les possibilités d'atteindre la compacité et l'intégration de tels systèmes.

Pour remédier à ce problème, la mise en œuvre de guides d'ondes térahertz est proposée dans le présent travail comme une solution prometteuse pour conduire les signaux d'interrogation vers la zone ciblée d'un échantillon. Une fois qu'un canal de communication unique sans optique est établi par un guide d'ondes entre l'émetteur-récepteur et l'échantillon, la structure des guides d'ondes stipule directement le chemin de propagation, ce qui réduit les difficultés d'alignement. La configuration de l'ensemble du système est simplifiée puisqu’aucun séparateur de faisceau ou lentille n'est nécessaire pour permettre le couplage. L'objectif principal du présent travail est de mettre en œuvre un système compact de réflectométrie guidée par ondes térahertz (TGR) après une sélection exigeante dans la vaste bibliothèque de composants existants.

Outre la construction d'un système TGR à des fins de détection et d'imagerie, les mesures au niveau des plaquettes/emballages dans la bande térahertz présentent un grand intérêt en raison du développement rapide des circuits intégrés monolithiques térahertz (TMIC). En effet, grâce aux progrès des technologies des semi-conducteurs et des techniques de conditionnement en 3D, de nombreux dispositifs à grande vitesse ont été proposés au cours de la dernière décennie. Pour vérifier et valider les nouveaux concepts avant la production en série, le processus de recherche et de développement des TMIC doit inclure des mesures sur plaquettes. Par rapport aux sources à ondes continues accordables classiques, un signal impulsionnel généré

par une source optoélectronique couvre une plus grande région de fréquence dans le spectre, ce qui permet d'obtenir les paramètres de diffusion dans une bande extra-large par une seule mesure. Non seulement le processus de mesure peut être simplifié par le déploiement d'une source optoélectronique, mais le coût de la plate-forme de mesure dans une gamme de fréquences extrêmement large peut également être réduit. Par conséquent, une partie de ce manuscrit est consacrée à la mise en œuvre d'un système de réflectométrie sur plaquette en utilisant une sonde RF sur plaquette en association avec un émetteur-récepteur large bande à double ACP. Comme il s'agit de la première tentative à délivrer un signal d'impulsion dans un échantillon sur plaquette, les principaux défis à relever sont de savoir comment coupler efficacement un signal d'impulsion dans un échantillon sur plaquette et comment interpréter le signal temporel en présence de modes de propagation plus élevés.

Compte tenu des objectifs susmentionnés, l'ensemble du manuscrit est composé de quatre chapitres qui sont décrits succinctement ci-après. Le premier chapitre offre une vue d'ensemble des développements de la technologie térahertz, y compris les progrès des dispositifs térahertz (sources, détecteurs et guides d'ondes), les configurations des systèmes et les applications. Par rapport à deux sources et détecteurs distincts, un émetteur-récepteur compact permet d'alléger la configuration du système en supprimant le séparateur ou le coupleur de faisceau utilisé pour séparer le faisceau incident et le faisceau réfléchi. Par conséquent, les études sur les émetteurs-récepteurs en térahertz sont passées en revue de manière approfondie. Afin de sélectionner un guide d'ondes approprié pour coopérer avec les émetteurs-récepteurs, un compte rendu général des progrès réalisés dans les guides d'ondes térahertz et de leurs applications est fourni. L'état des connaissances sur les guides d'ondes est divisé en deux parties : les guides d'ondes métalliques et les guides d'ondes diélectriques. En plus de leurs principes de fonctionnement et de leurs propriétés de propagation, la question du couplage, qui a fait l'objet d'études antérieures, est particulièrement examinée en détail.

Dans le deuxième chapitre, trois unités d'émission-réception sélectionnées, c'est-à-dire un émetteur-récepteur à double ACP sans lentille, un module FMCW basé sur la technologie III-V et un radar basé sur la technologie Si, sont testés séparément pour évaluer leurs performances. En particulier, les performances de l'émetteur-récepteur à double ACP, y compris sa bande de fréquence de fonctionnement et sa capacité d'imagerie, sont plus détaillées. Sur la base des études préliminaires, les guides d'ondes anti-résonants à noyau creux sont considérés comme un candidat approprié pour assurer la transmission du signal entre les émetteurs-récepteurs et un échantillon. Leurs bandes de transmission sont vérifiées par des mesures THz-TDS, correspondant à une bande de fréquence de fonctionnement optimisée de l'émetteur-récepteur à double ACP (de 400 GHz à 500 GHz), à la fois en mode transmission et en mode réflexion. La technique de fabrication additive (impression 3D), qui permet une chaîne de développement rapide et économique des guides d'ondes, est présentée à la fin de ce chapitre.

Le troisième chapitre présente les systèmes TGR construits et leurs performances correspondantes en tirant parti des émetteurs-récepteurs et des guides d'ondes susmentionnés. Selon l'unité émettrice-réceptrice choisie, ce chapitre est divisé en deux parties principales : (i) les systèmes de réflectométrie guidée par ondes térahertz en mode impulsionnel (TGR-P), et (ii) les systèmes de réflectométrie guidée par ondes térahertz en mode FMCW (TGR-FMCW). En ce qui concerne les systèmes TGR-P, deux guides d'ondes diélectriques à noyau creux sélectionnés sont testés pour établir un canal de communication unique sans optique entre l'émetteur-récepteur à double ACP et un échantillon. En plus de la caractérisation de la forme

d'onde dans le domaine temporel, les applications d'imagerie et de détection des systèmes sont également délimitées. Alors que le système TGR-G exploitant un guide d'ondes à noyau creux en silice de 3 mm de diamètre affiche un pouvoir de résolution d'environ 700 µm, les autres systèmes TGR-G comprenant un guide d'ondes en plastique de 6 mm de diamètre affichent le potentiel de détection de la profondeur des liquides. En ce qui concerne les systèmes TGR-FMCW, la tête SynView à 100 GHz et la puce émettrice-réceptrice du radar au silicium à 122 GHz sont testées séparément avec un guide d'onde creux en plastique. L'effet fantôme indésirable est ensuite corrigé par l'intégration d'une lentille hémisphérique supplémentaire de terminaison, ce qui permet d'améliorer la capacité d'imagerie. En plus des installations et des applications expérimentales, des recherches sur les propriétés du champ à l'intérieur du système sont menées à l'aide de la simulation 3D pleine onde, ce qui permet d'analyser les comportements de propagation des ondes le long du guide d'ondes. Les paramètres tels que l'efficacité du couplage, les modes de propagation, la gamme dynamique sont évalués et discutés.

Le dernier chapitre, plus prospectif, commence par présenter le développement rapide de la TMIC, offrant le contexte du besoin croissant de mesures sur plaquettes. Différentes méthodes permettant d'améliorer la fiabilité et la répétabilité des mesures sur plaquette à haute fréquence sont passées en revue, notamment l'approche de contrôle du déplacement en Z et les sondes sans contact. Outre les mesures sur les plaquettes, la détection des défauts au niveau de l'emballage a bénéficié des progrès des dispositifs optoélectroniques. La technique EOTPR exploitant des dispositifs PCA avec une sonde RF, est particulièrement détaillée. Inspirées par le système EOTPR, deux sondes RF dans la bande de fréquences de 140-220 GHz et 330 GHz à 500 GHz sont déployées séparément pour diriger un signal d'impulsion du double émetteur-récepteur PCA vers un échantillon sur la plaquette. Les deux configurations du système donnent lieu à des signaux de forme annulaire, et les origines des réflexions sont discutées.

Les travaux présentés dans ce manuscrit ont été réalisés dans le cadre d'une collaboration qui a rassemblé plusieurs équipes de recherche. La mise en œuvre et l'analyse des systèmes de réflectométrie térahertz guidée ont été réalisées dans le laboratoire de l'IMS sous la supervision du Dr. Patrick Mounaix et du Dr. Jean-Paul Guillet, tandis que les mesures sur plaquette ont été effectuées sous la direction du Dr. Sébastien Fregonese (Bordeaux, France). Les guides d'ondes à paroi mince à noyau creux ont été fournis par le Dr. Georges Humbert de l'Institut de recherche XLIM (Limoges, France). La conception et la fabrication des guides d'ondes à courbure négative imprimés en 3D ont été réalisées par le professeur Cristiano M.B. Cordeiro de l'UNICAMP (Brésil) et Marcos A. R. Franco de l'IEAv (Brésil).

AUTHOR CONTRIBUTION

Journal papers

1. **Guided terahertz pulse reflectometry with double photoconductive antenna**

Mingming Pan, Quentin Cassar, Frédéric Fauquet, Georges Humbert, Patrick Mounaix, and Jean-Paul Guillet, *Appl. Opt.* 59, 1641-1647,2020.

2. **Iterative Tree Algorithm to Evaluate Terahertz Signal Contribution of Specific Optical Paths Within Multilayered Materials**

Q. Cassar, A. Chopard, F. Fauquet, J. Guillet, M. Pan, J. Perraud and P. Mounaix, *IEEE Transactions on Terahertz Science and Technology*, vol. 9, no. 6, pp. 684-694, Nov. 2019.

3. **Guided Reflectometry Imaging Unit using Millimeter Wave FMCW Radars**

M. Pan, A. Chopard, F. Fauquet, P. Mounaix and J. Guillet, *IEEE Transactions on Terahertz Science and Technology*, 2020. (doi: 10.1109/TTHZ.2020.3008330.)

4. **Teragogic: Open source platform for low cost millimeter wave sensing, terahertz imaging and control (submission)**

Adrien Chopard, Frederic Fauquet, Jing Shun Goh, Mingming Pan, Anton Simonov, Olga Smolyanskaya, Patrick Mounaix and Jean-Paul Guillet, *IEEE Transactions on Industrial Electronics*, submission in April 2020.

Conferences and communication

1. **Guided terahertz FMCW radars for reflectometry probing purposes (Poster)**

Chopard, M. Pan, F. Fauquet, J. P. Guillet and P. Mounaix***, in*** *9th International Workshop on Terahertz Technology and Applications*, Kaiserslautern, German, 2019.

2. **Study of a THz Hollow-core Fiber for Sample Reflectance Analysis (Poster)**

Mingming Pan, Cristiano MB Cordeiro, Frédéric Fauquet, Patrick Mounaix, Gildo S Rodrigues, Marcos AR Franco, Jean-Paul Guillet, in *2019 44th International Conference on Infrared, Millimeter, and Terahertz Waves (IRMMW-THz)*, Paris, France, 2019, pp. 1-1.

3. **THz imaging with a hollow core waveguide (Oral)**

M. Pan, J.-P. Guillet, G. Humbert, F. Fauquet, D. Lewis and P. Mounaix, *in 2019 French-German THz Conference*, Kaiserslautern, German, 2019.

4. Comparative study of terahertz waveguide in reflective mode configuration (Oral)
M. Pan, J.-P. Guillet, G. Humbert, F. Fauquet, D. Lewis and P. Mounaix, *in 2018 43rd International Conference on Infrared, Millimeter, and Terahertz Waves (IRMMW-THz)*, Nagoya, Japan, 2018, pp. 1-2.

5. Réflectométrie dans le domaine temporel pour l'optique guidée terahertz. (Poster)
ED SPI day, Bordeaux, France, 15 march 2018.

6. Guided terahertz pulsed reflectometry: a remote probe for near-field imaging (Oral)
Mingming Pan, Frédéric Fauquet, Dean Lewis, Frédéric Darracq, Patrick Mounaix, and Jean-Paul Guillet, *Proc. SPIE 10531, Terahertz, RF, Millimeter, and Submillimeter-Wave Technology and Applications XI, 105310L,* 14 March 2018.

7. Guided terahertz waves in reflection mode (Poster)
M. Pan, J.-P. Guillet, F. Fauquet, D. Lewis and P. Mounaix, in *GDR NanoTeraMIR*, Montpelier, France, 2017.

8. Guided terahertz pulsed reflectometry simulation with near field probe (Oral)
M. Pan, J.-P. Guillet, F. Fauquet, D. Lewis, M. Patrick, *in 2017 42nd International Conference on Infrared, Millimeter, and Terahertz Waves (IRMMW-THz)*, Cancun, Mexico, 2017, pp. 1-2.